Warm Forming Behaviour of ZEK100 and AZ31B Magnesium Alloy Sheet

by

Mariusz Boba

A thesis
presented to the University of Waterloo
in fulfilment of the
thesis requirement for the degree of
Master of Applied Science
in
Mechanical Engineering

Waterloo, Ontario, Canada, 2014

I hereby declare that I am the sole author of this thesis. This is a true copy of the thesis, including any required final revisions, as accepted by my examiners.

I understand that my thesis may be made electronically available to the public.

ABSTRACT

The current research addresses the formability of two magnesium sheet alloys, a conventional AZ31B and a rare earth alloyed ZEK100. Both alloys had a nominal thickness of 1.6 mm. Both Limiting Dome Height (LDH) and Cylindrical Cup Draw experiments were performed between room temperature and 350°C. To examine the effect of sheet directionality and anisotropy, LDH experiments were performed in both the sheet rolling and transverse directions. In addition, strain measurements were performed along both sheet orientations of the cylindrical cup and LDH specimens for which the geometry is symmetric.

The LDH tests were used to study the formability of ZEK100 and AZ31B (O and H24 tempers) magnesium alloy sheet between room temperature and 350°C. At room temperature, AZ31B-O and AZ31B-H24 exhibit limited formability, with dome heights of only 11-12 mm prior to the onset of necking. In contrast, the dome heights of ZEK100 at room temperature reached 29 mm (a 140% improvement over AZ31B). Increasing the temperature above 200°C did not affect the relative ranking of the three sheet samples, however it did reduce the magnitude of the difference in dome heights. The rare earth alloyed ZEK100 had pronounced benefits at intermediate temperatures, achieving an LDH of 37 mm at 150°C; this dome height was only reached by AZ31B at a much higher temperature of 250°C.

To further characterize the formability of ZEK100, forming limit curves (FLCs) were developed from the LDH tests in both the rolling and transverse directions. Comparisons to AZ31B were made at selected temperatures. Surface strain data was collected with an *in situ* digital image correlation (DIC) system incorporating two cameras for stereo observation. Results from these experiments further highlighted the enhanced formability relative to AZ31B over the entire temperature range between room temperature and 350°C, with the most dramatic improvements between room temperature and 150°C. The plane strain forming limit (FLC_0) for ZEK100 at 150°C was 0.4 which equals that of AZ31B at 250°C. At higher temperatures (300°C), the two alloys exhibited similar performance with both achieving similar dome heights at necking of 37 mm (AZ31B) and 41 mm (ZEK100).

To round out the investigation of ZEK100 for industrial applications, cylindrical cup deep drawing experiments were performed on ZEK100 sheet between 25°C and 250°C under isothermal and non-isothermal conditions. Draw ratios of 1.75, 2.00 and 2.25 were considered to examine the effects of draw ratio on draw depth. The effect of sheet anisotropy during deep drawing was investigated by measuring the earring profiles, sheet thickness and strain distribution along both the rolling and transverse directions. Isothermal test results showed enhanced warm temperature drawing performance of ZEK100 over AZ31B sheet; for example, a full draw of 203.2 mm (8") blanks of ZEK100 was achieved with a tool temperature of 150°C, whereas a tool temperature of 225°C was needed to fully draw AZ31B-O blanks of this diameter. Non-isothermal deep draw experiments showed further improvement in drawability with significantly lower tooling temperatures required for a full cup draw using ZEK100. ZEK100 achieved a full draw of 228.6 mm (9") blanks with a die and blank holder temperature of 150°C and a cooled punch (25°C) while the same size blank of AZ31B required a die and blank holder temperature 225°C and a cooled punch (150°C). Temperature process windows were developed from the isothermal and non-isothermal results to show a direct comparison of drawing behaviour between ZEK100 and AZ31B.

Overall, ZEK100 offers significantly improved forming performance compared to AZ31B, particularly at temperatures below 200°C. This lower temperature enhanced formability is attractive since it is less demanding in terms of lubricant requirements and reduces the need for higher temperature tooling.

ACKNOWLEDGEMENTS

I would like to express my sincere gratitude to my supervisor Professor Michael Worswick for the opportunity to work within his research group and complete a Master's degree. His knowledge, guidance and support, throughout my graduate studies, have been invaluable and are greatly appreciated. I would also like to thank Professor Warren Poole, the MagNET theme leaders, and the NSERC Magnesium Strategic Research Network, for creating this opportunity and providing support in this research. I am grateful for the collaboration and support from General Motors of Canada through Dr. Raja K. Mishra and Dr. Jon T. Carter. Their insight, knowledge and discussions have proven to be invaluable in my growth as an engineer. The ongoing efforts of the above individuals and groups show a true commitment to the pursuit of knowledge to further research in academia and industry. Their work and the opportunities they provide countless students are a testament to the state of research in Canada and its representation on world scale. I am grateful to have been a small part of it.

I would like to thank Reza Bagheriasl, José Imbert, Srihari Kurukuri, Nima Panahi, and Dariush Ghaffari Tari for all their various roles and discussions that ranged from everything including r-values, digital image correlation problems all the way to 'oh no my hard drive crashed'. I thank the entire research group for making my graduate studies an enjoyable process.

I would like to thank the many laboratory technicians who truly make the work and experiments possible through their tireless efforts in helping create and maintain the laboratory work stations. They are the backbone of the research group that bring research efforts to reality. Thank-you to Eckhard Budziarek for his untiring efforts and patience during my many, many experimental setups and re-setups on the warm forming press, Richard Gordon and Tom Gawel for their assistance in their labs and Andy Barber and Neil Griffett for developing and coding a reliable and strong warm forming press. I believe that my experiments and educational errors truly tested the robustness of all their work. Thank you to the administrative staff of the Mechanical Engineering Department, especially Laurie Wilfong who helped me

many times process all the paper work for travel reimbursements and was always there to answer administrative questions. I would also like to thank Debbie Burgess from UBC for her tremendous efforts in organizing the many excellent collaborative workshops that I had the pleasure of participating in.

Finally, I would like to thank my mom Danuta and my dad Tadeusz, my fiancé (edit: July 6, 2013: wife) Isabelle Glinka and her family. Each of you has been there from the beginning of my Master's journey and has shared in both the challenges and successes. Your continually unwavering support and patience has encouraged and sustained me throughout my 'back to school' endeavour. I am blessed to be surrounded by such a loving family. Dziękuję Wam bardzo, od serca, za pomoc w dorastaniu akademickim i życiowym.

Thank you.

To my Mother and Father

Danuta and Tadeusz Boba

TABLE OF CONTENTS

LIST OF FIGURES

LIST OF TABLES

1 INTRODUCTION

Over the past several years fuel economy has become a key focus and the subject of much research in the automotive industry. Spurred by rising fuel prices, public demand and increasingly stringent governmental standards, car manufacturers are striving to lower vehicle fuel consumption. Various approaches have proven effective, including improvements in power train design and vehicle aerodynamics, but among the most promising is the study into new lighter materials in an effort to reduce the overall mass of the vehicle. Indeed, investigations have shown that a significant portion of a vehicle's total fuel consumption is related to its mass (Abu-Farha et al., 2012) and research into the successful forming performance of light weight materials will have a direct benefit for automotive manufacturers looking to increase fuel efficiency and meet future federal fuel economy standards.

1.1 Automotive Industry Trends in Vehicle Materials and Weight

Today's vehicle is composed of various materials whose purposes range from structural to cosmetic. Figure 1.1 presents the United States Automotive Materials Partnership (USAMP) breakdown of the material distribution of an average vehicle by weight, almost two thirds of which is comprised of steel and cast iron. Most of this is for structural loading and impact safety, some of which could potentially be replaced by lighter materials that would reduce overall weight without compromising the structural integrity of the vehicle. The present study investigates the formability characteristics and behaviour of an alternative material, magnesium sheet alloy, which is currently under consideration as a candidate for automotive applications.

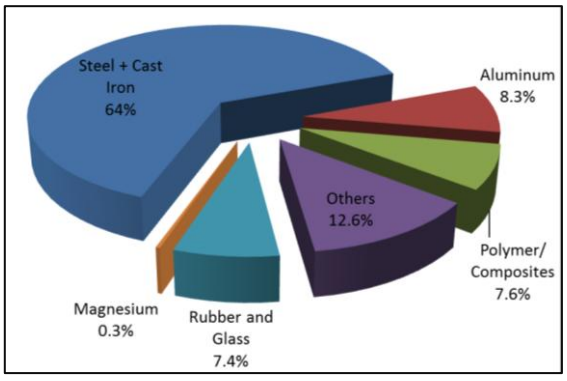

Figure 1.1: Material distribution for an average North American vehicle (USCAR, 2006).

The weight of a vehicle has been affected by both economic conditions and consumer trends over the past forty years (Lutsey et al., 2010). In light of the Oil Crises of the mid-1970s and the subsequent wildly fluctuating fuel prices of the late-1970s and early-1980s, the United States government (followed by other nations including Canada) imposed strict fuel-economy standards on automotive manufacturers. To meet these requirements the industry redesigned their vehicles, which achieved a 21% reduction in vehicle weight by 1980 (Figure 1.2).

Yet by 1987 vehicle weight was back on the rise, driven chiefly by consumer demands for more options and increased safety standards. Options such as power windows, power seats, air conditioning, air-bags, etc. eventually became part of the base model and were joined by many other optional features as new technologies were developed. These consumer add-ons increased vehicular mass to the point where current cars and trucks are on average the same weight as they were in 1975 (Figure 1.2).

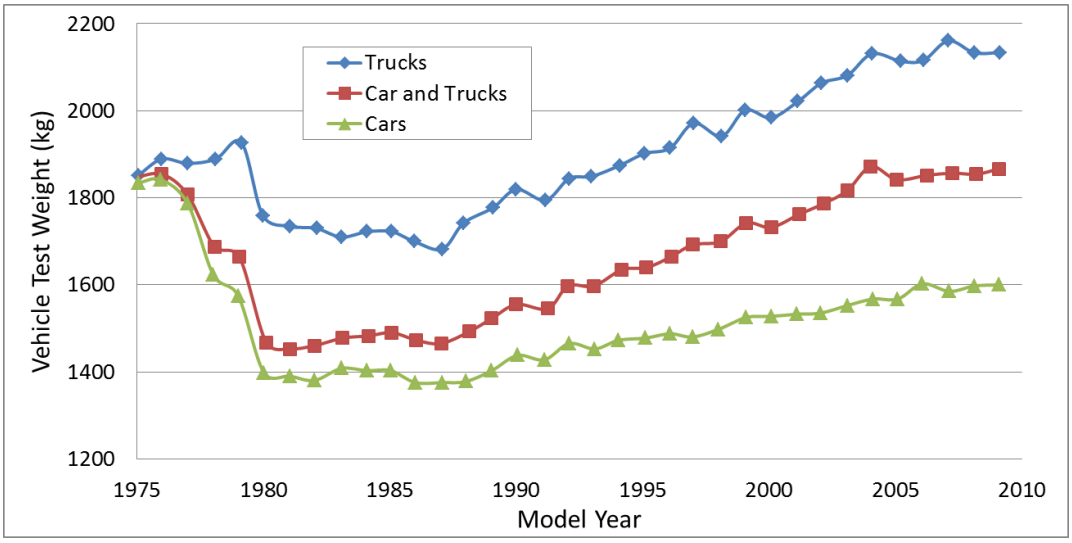

Figure 1.2: Vehicle weight trends from 1975 to 2009 (Lutsey et al., 2010).

With vehicle weight rising, the U.S. government has mandated improved fuel efficiency (6.9 L/100km (34.1 MPG) by 2016, *versus* the currently required 8.2 L/100 (28.8 MPG)) Cheah (2010). At the same time consumers are demanding both excellent fuel-economy and maximal optional features (including safety features) forcing auto manufacturers to look for alternative lightweight materials. Studies have shown that every 10% reduction in a vehicle's curb weight

reduces its expected fuel consumption by 5-7% (Cheah, 2010). In light of such a relationship between vehicular mass and fuel-efficiency, as well as the aforementioned consumer and governmental demands, it is necessary to look to other types of alloys to find the necessary weight savings which currently cannot be met by today's conventional steel, cast iron and aluminum alloys.

Magnesium is viewed as a potential light weight replacement for conventional steel alloys since it is 77% lighter than steel and 35% lighter than aluminum. Magnesium alloys (with a density of 1.738g/cm^3) also have a high strength-to-weight ratio. Further research is needed, however, to address the manufacturing issues of magnesium alloys, such as their poor formability during stamping, and in-service performance issues such as poor corrosion resistance and brittle fracture under high strain rate crash conditions (Parrish et al., 2012). Presently, the majority of magnesium alloys used in automobile components are processed by die casting, which has limited the application of Mg alloys to components that have less stringent mechanical requirements such as fatigue strength or ductility (Doege et al., 2001a). There is, however, widespread interest in research to develop formable wrought magnesium alloys which would extend their possible application to include outer and inner body panels. Such applications will require development of manufacturing techniques and understanding of the process parameters required to fabricate magnesium alloy components. A 2006 report issued by USAMP entitled "Magnesium Vision 2020" points to the promise of Magnesium alloys (USCAR, 2006). Investigating the realities of magnesium as an alternative material in automotive production, and highlighting the benefits of magnesium while also recognizing its limitations, the report concluded that magnesium is a material well-suited for use in strategic areas of a vehicle where its benefits outweigh its limitations.

Current commercial automotive applications of wrought Mg alloys center around AZ31B (96.5% Mg, 2.8% Al, 0.7% Zn, Balance, Mn, Fe), which shows very good formability in the temperature range between 200°C and 300°C. General Motors, for one, succeeded in hot gas blow-forming an experimental decklid inner panel from AZ31B based on dies and processes used in commercial applications (Figure 1.3a) (Min et al., 2012b). Eventually the AZ31B

decklid was applied as a production component in the company's Cadillac CTS model (Figure 1.3b) (Alderman, 2013).

Figure 1.3: a) Experimental decklid inner panel formed by hot gas blow-forming process on AZ31B (Min et al., 2012b), b) GM's Cadillac CTS (Photo: Hogan, 2008).

Continued development of magnesium alloy sheet has led to the production of rare-earth alloyed ZEK100 (Mg 98 wt.%, zinc 1 wt.%, Nd 0.5 wt.%, Zr 0.5 wt.%). The main differentiating compositional element is Neodymium (Nd), whose addition as the rare-earth alloying element has led to improved formability. ZEK100 has drawn the attention of researchers because it has shown enhanced formability performance compared to AZ31B. Kurukuri et al. (2012a) conducted characterization work on both ZEK100 and AZ31B showing that ZEK100 provides better elongation than AZ31B. These results suggest that the ZEK100 alloy may be formed at lower temperatures than those required for AZ31B. Ghaffari Tari et al. (2013) have also demonstrated that non-isothermal deep drawing techniques offer a significant benefit to extend the drawability of AZ31B. No such investigation has yet been conducted for ZEK100.

The objectives of the present research are to investigate the formability and drawability of ZEK100 magnesium alloy sheet and to compare this performance to that of current commercial AZ31B sheet. Limiting dome height experiments were performed on ZEK100 under isothermal conditions ranging from 25°C to 350°C. The results from these experiments were used to create forming limit diagrams for ZEK100 in both the rolling and transverse sheet directions. Selected temperatures were used to compare the formability of ZEK100 to AZ31B.

The drawability of ZEK100 was investigated through experimental deep drawing of ZEK100 magnesium alloy sheet under both isothermal and non-isothermal conditions in the temperature range of 25-250°C. The effect of Draw Ratio (DR) on draw depth was investigated by using specimens with draw ratios of 1.75, 2.00 and 2.25. The effect of temperature and temperature gradients on material anisotropy was examined by means of the measured earring profiles, thickness profiles and strain measurements. Finally, temperature process windows for ZEK100 were developed to summarize the drawability of ZEK100 in relation to AZ31B-O. These process windows show temperature as a function of tooling temperature *versus* punch temperature for both isothermal and non-isothermal conditions.

What follows in the remainder of this chapter is a review of the literature relevant to this study. The first area is the characteristics of magnesium alloy sheet and their expected formability behaviour. Thereafter follows a review of known techniques for measuring material formability and drawability. Limiting Dome Height (LDH) testing is discussed along with its use in developing Forming Limit Diagrams (FLD). Finally, the chapter concludes with a review of recent research on AZ31B and ZEK100 involving the effects of isothermal and non-isothermal forming, material texture and anisotropy to establish the current level of understanding for these materials.

1.2 Magnesium Alloy Sheet

Uniaxial stress-strain curves offer a good indication of the formability characteristics of a material by showing the amount of work hardening and elongation a particular material is capable of achieving. A useful variation of the stress-strain curve for comparing different materials, shown in Figure 1.4, is the plotting of a material's elongation as a function of yield strength, which represents a mechanical performance window. Figure 1.4 clearly illustrates how AZ31B and ZEK100 (large red region) compare to conventional steels (grey region), magnesium-die casting (blue region), higher strength steel sheet (large orange region) and aluminum sheet (green region). Magnesium rolled sheets show more elongation than die-cast magnesium material, more than the majority of aluminum sheets, but less than conventional steel sheet. When one considers the density differences between these alloys and the specific

properties, (magnesium has a density of 1.74 g/cm^3, aluminum 2.78 g/cm^3 and steel 7.8 g/cm^3), magnesium becomes a potential candidate for replacement of certain steel components. The results found in this figure also suggest that ZEK100 will outperform AZ31B due to their relative elongation performance.

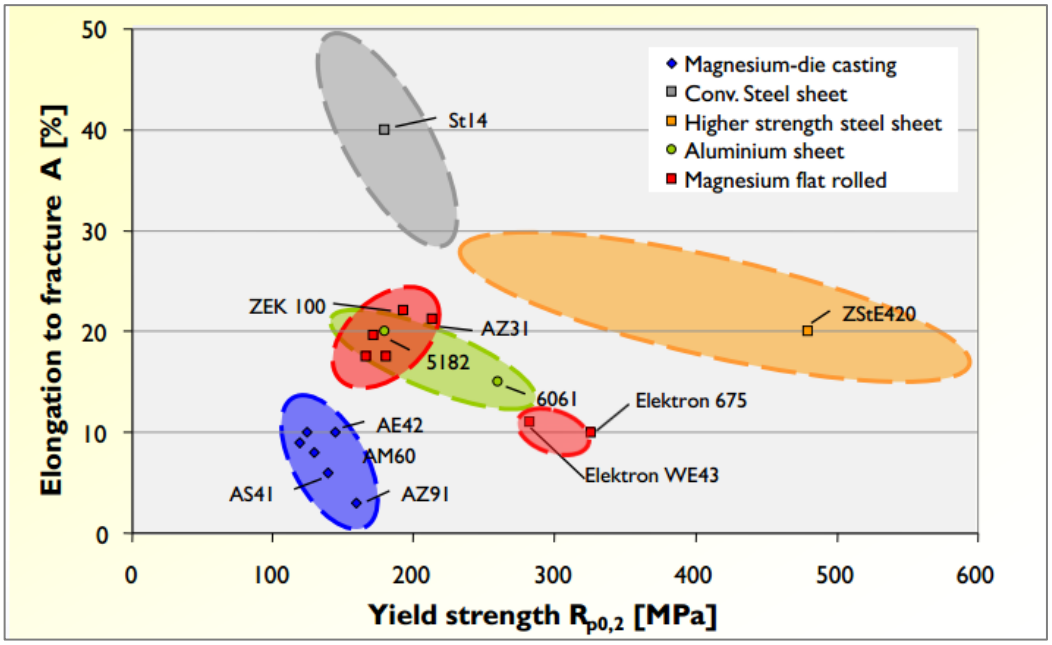

Figure 1.4: Comparison of Mechanical Properties of Magnesium Alloys. (Alderman, 2013).

It is commonly recognized that current commercial magnesium alloy sheet possesses poor formability at room temperature because of its hexagonal close-packed (HCP) structure (Lee et al., 2002). Formability of a material is determined by the crystal structure's ability to deform along its slip systems. A slip system consists of a slip plane and a slip direction which, for HCP materials, is shown in Figure 1.5 (Motyka et al., 2012). For magnesium alloys, only four independent slip systems are active at room temperature, requiring activation of twinning to accommodate low temperature deformation (Lou et al., 2007; Yoo, 1981; Koike et al., 2003). HCP materials show many forms of twinning, however deformation twinning, such as extension twinning, on pyramidal planes is the dominant one (Wang, 2007; Staroselsky, 2003).

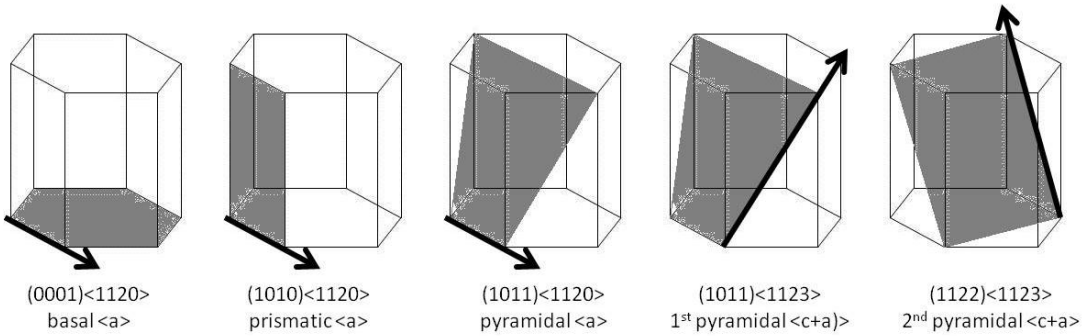

Figure 1.5: HCP slip systems (Doege et al., 2001b).

From Figure 1.5 the first three slip systems from the left (basal <a>, prismatic <a>, and pyramidal <a>) provide a relatively easy slip system at room temperature compared to the two rightmost slip systems (1st pyramidal <c+a> and 2nd pyramidal <c+a>). This makes room temperature or warm temperature formability difficult since five independent slip systems are required for plastic deformation, according to the von Mises criterion, requiring twinning to support deformation (Khosravani and Scott, 2013). Twinning occurs when the crystal lattice becomes reoriented in response to an applied force and a mirror image of the lattice is created, as shown in Figure 1.6a (Wong, 2006). The amount of deformation able to be accommodated by twinning is quite limited and further complications can result from the tension-compression asymmetry associated with twinning (Lou et al., 2007). Wrought magnesium alloy sheet also exhibits a strong basal texture which makes material thinning difficult (Lou et al., 2007) and leads to strong room temperature anisotropy (Agnew et al., 2001, Styczynski et al., 2004; Jeong and Ha, 2007). As a result, the room temperature formability of magnesium sheet is inherently low (Zhang et al., 2007) and considerable effort has been made to address the warm formability of magnesium alloy sheet. Particular focus has been made on commercial AZ31B, in light of its higher formability under warm forming conditions (Chen et al, 2003b) and higher drawability at temperatures above 250°C (Chen et al., 2003a; Ambrogio et al., 2007; Ghaffari Tari et al., 2013).

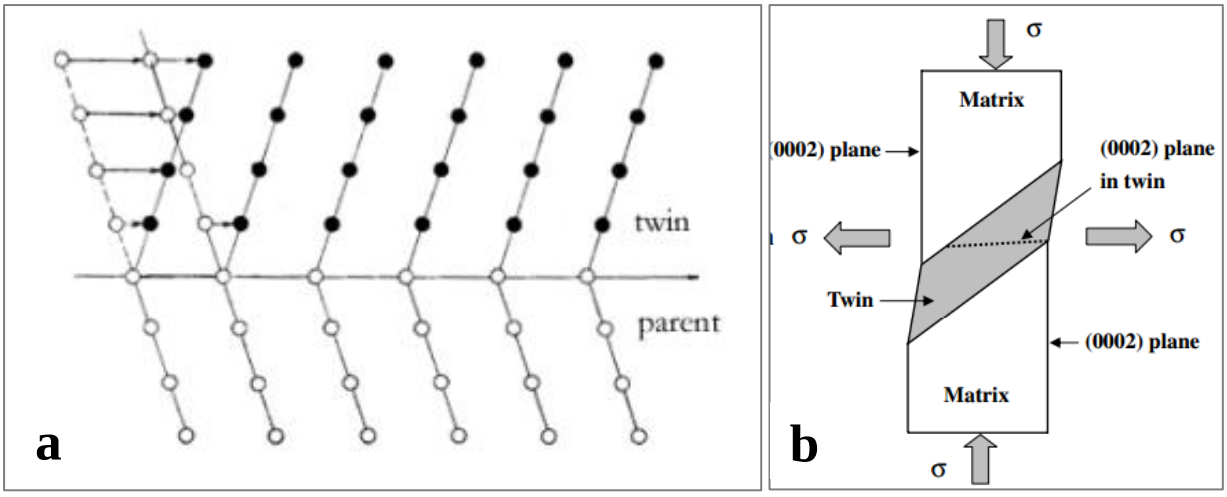

Figure 1.6: a) Twinning of crystal lattice during shearing (Wong, 2006), b) Deformation for pyramidal twinning (Wang, 2007).

1.3 ZEK100 and AZ31B Magnesium Alloys

The magnesium sheet alloys considered in this research include ZEK100 and AZ31B, the latter being the most commonly used commercial magnesium alloy sheet (Min et al., 2012a). ZEK100 is a more recent commercial offering with a nominal composition of Zn at 1 wt% and a 0.12 wt% addition of Nd, a rare-earth element. While such additions generally result in a weakened material texture, the full effects of rare-earth additions on formability still require further detailed investigation (Bohlen et al., 2006). The alloy composition of AZ31B and ZEK100 is shown in Table 1.1.

Table 1.1: Chemical Composition of AZ31B and ZEK100 (wt%)

Material	Al	Zn	Mn	Ca	Cu	Fe	Ni	Si	Zr	Re(Nd)	Others	Mg
AZ31B[1]												
min	2.5	0.7	0.2	---	---	---	---	---	---	---	---	---
max	3.5	1.3	1.0	0.04	0.05	0.0005	0.005	0.05	---	---	0.3	Balance
ZEK100[2]												
min	---	1.0	---	---	---	---	---	---	0.2	0.12	---	---
max	---	1.5	---	---	0.008	0.004	0.001	---	0.5	0.22	0.3	Balance

[1]Obtained from Magnesium Elektron Material Specification sheet
[2]Obtained from General Motors Material ZEK100 Specification Sheet, April 26, 2010

1.3.1 Material Texture

On a microscopic level, metallic sheet material consists of a tightly packed arrangement of crystals which make up a crystal lattice. In the case of magnesium alloys, the individual crystals within the HCP crystal structure can take on various orientations. Material texture is used as a measure and a description of distribution of crystal orientations present within a crystalline material, as illustrated in Figure 1.7. A strong material texture is one where the crystals are predominantly oriented in one direction, as shown in Figure 1.7a, while a weak texture is one with crystals oriented in random directions (Figure 1.7b).

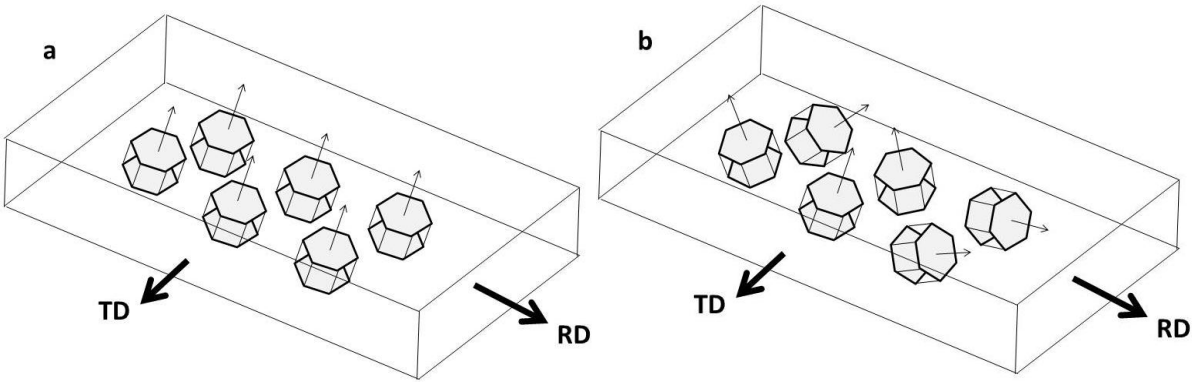

Figure 1.7: Material texture a) Strong basal texture b) weakened texture.

While previous work has demonstrated that acceptable automotive component quality can be achieved during warm forming of AZ31B sheet, the elevated temperature requirement adds cost and complexity to manufacturing processes. Recent studies have investigated the addition of rare-earth alloying elements to Mg in an effort to alter or reduce the strong basal texture of wrought magnesium sheet (Bohlen et al., 2006, 2007; Hantzsche et al., 2010). These studies have demonstrated that rare-earth additions, such as Yttrium (Y), can result in a weakened as-rolled texture and increased formability. Bohlen et al. (2007) also report that grain size refinement, through Zirconium (Zr) additions, further increase ductility and lead to an increase in both the compressive and tensile yield strengths (Bettles, 2005). Stanford (2012) found that the addition of rare-earth Gadolinium (Gd) caused significantly faster material recrystallization than in AZ31B in post-deformation static annealing, resulting in a weaker recrystallization texture.

ZEK100 sheets have a more random texture distribution (Figure 1.88b) compared to AZ31B (Figure 1.88a). These figures also show a much weaker texture intensity factor (TIF) for ZEK100 from the basal planes (002) indicating a reduced texture (Min et al., 2012a; Bohlen et al., 2006), compared to that of AZ31B which shows a strong reflection from basal planes (002).

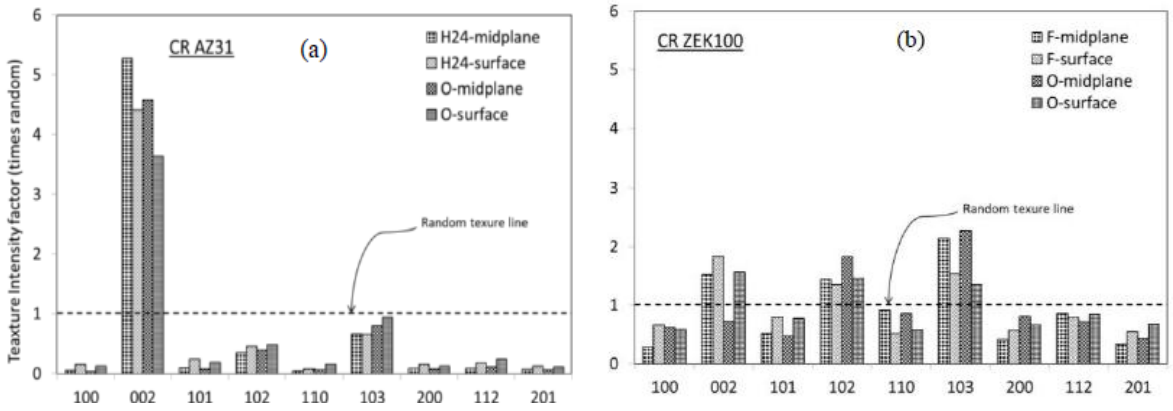

Figure 1.8: Texture intensity factors at sheet surface and sheet mid-plane for a) AZ31B and b) ZEK100 (Min et al., 2012a).

ZEK100 has a weakened texture due to its rare-earth (RE) additions compared to AZ31B (Figure 1.9) and a finer grain size, both of which factors have been hypothesized to increase formability (Bohlen et al., 2007).

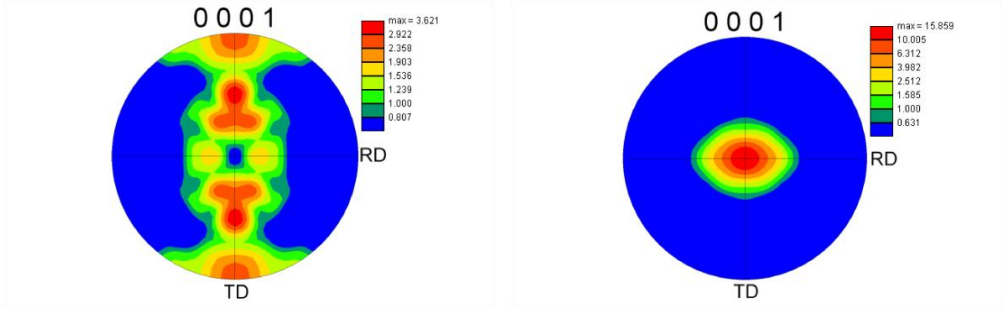

(a) ZEK100 sheet (b) AZ31B sheet

Figure 1.9: Pole figures of initial textures for (a) ZEK100 and (b) AZ31B.

Considering the studied material is a rolled sheet, the directionality of the rolled sheet material is of importance, namely the rolling direction (RD) and transverse direction (TD). Examination

of Figure 1.9 reveals that the ZEK100 alloy exhibits a much lower basal texture intensity compared to AZ31B (3.6 versus 13.9, respectively) and a considerably greater spreading of the texture along the transverse direction (TD). In contrast, the AZ31B pole figure shows a strong basal texture with slight tilting of the c-axis distribution towards the rolling direction (RD). This difference in texture is illustrated schematically in Figure 1.10. For AZ31B, the majority of crystal c-axes (shown with the red arrow) are perpendicular to the sheet surface with slight tilting in the rolling direction (Figure 1.10a). In contrast, ZEK100 exhibits a more random distribution of the c-axes along the transverse direction (Figure 1.10b), with little tilting in the rolling direction. The grain size of the analyzed materials was 15.3 μm for ZEK100, whereas the AZ31B grain size was 4.2 μm (Min et al., 2012a). The room and elevated temperature constitutive behaviour of ZEK100 and AZ31B are reported in Kurukuri (2013a-b).

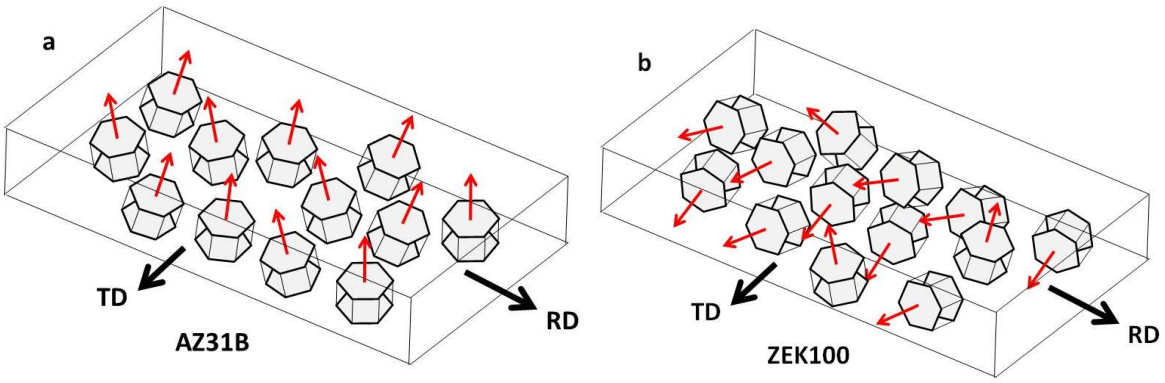

Figure 1.10: Material texture a) AZ31B (strong texture) b) ZEK100 (weakened texture).

1.3.2 Stress – Strain Response

Investigations of the stress-strain response of AZ31B (Kurukuri et al. 2014a) (Figure 1.11) have found that the tensile flow curves have a downward concave shape, due to the alloy's predominant crystallographic slip in tension, and a positive strain rate sensitivity for both the rolling and transverse directions. The yield stress for the entire strain rate range is higher along the TD than in the RD with all specimens failing without any necking (Kurukuri et al. 2014a).

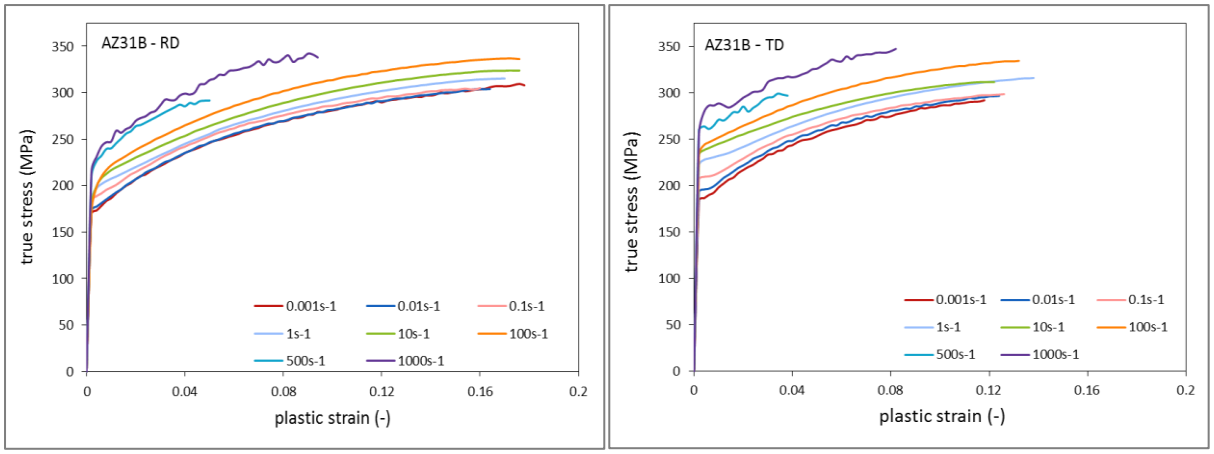

Figure 1.11: True stress vs. effective plastic strain for AZ31B in RD and (Kurukuri et al., 2013a).

Similar investigations for ZEK100 (Kurkuri et al., 2013b) (Figure 1.12) have found a rather different characteristic in the strain rate sensitivity between RD and TD loading. Along RD there is a strong rate sensitivity of the yield stress whereas along the TD , the yield strength is essentially rate insensitive but the work hardening rate increases with increasing strain rates (Kurkuri et al., 2013b). The TD is also considerably more ductile than the RD as discussed by Kurukuri et al. (2013b).

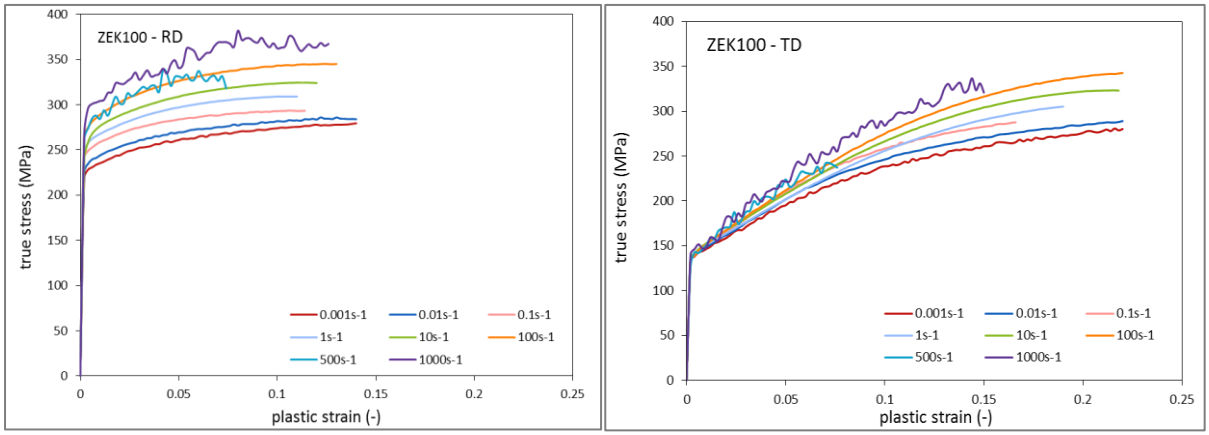

Figure 1.12: True stress vs. effective plastic strain for AZ31B in RD and (Kurukuri et al., 2013b).

Tension-compression comparisons were conducted by Kurukuri et al. (2013a) which showed that AZ31B sheet exhibits a strong tension-compression asymmetry in both the rolling and transverse sheet directions as shown in Figure 1.13. Conversely, there is only minor asymmetry

in the yield strength in the transverse direction for the ZEK100 sheets and a strong asymmetry exhibited in the rolling direction compared to what was observed in AZ31B sheet.

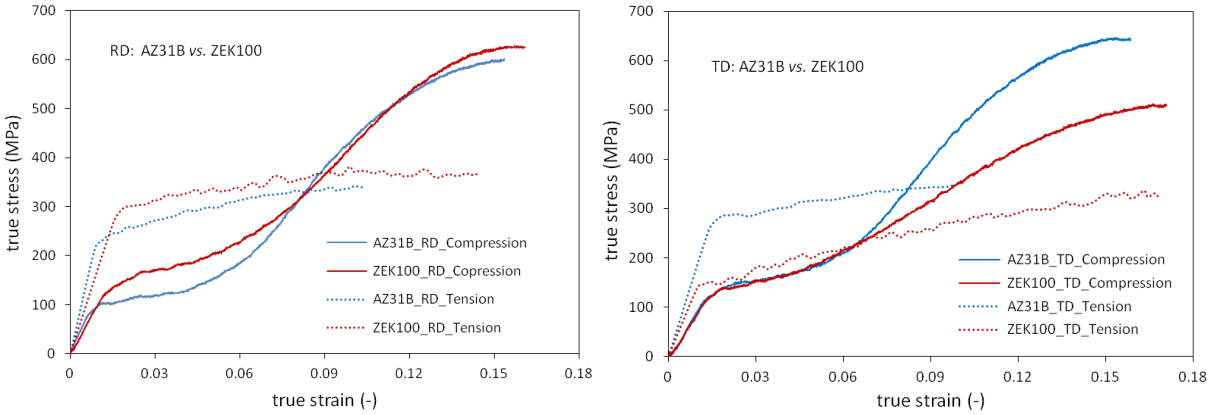

Figure 1.13: Tension-Compression asymmetry of ZEK100 and AZ31B (Kurukuri et al., 2013a).

1.4 Temperature Effects on Formability

At elevated temperatures, non-basal <c+a> slip systems are activated (Doege et al., 2001b; Agnew and Duygulu, 2005) thereby allowing ductility to increase. Developments in magnesium alloy sheet production, furthermore, have tailored the material to improve elevated temperature formability and these have been the focus of recent studies. Ghaffari Tari et al. (2013) have researched the formability of AZ31B through cylindrical deep draw experiments. This work demonstrated significant improvements in formability of AZ31B at elevated temperatures, especially in non-isothermal cases where the punch temperature was lower than the die and blank holder temperature. Abu-Farha et al. (2012) conducted experiments on AZ31B using pneumatic stretching that focused on the equi-biaxial tension behaviour of the material. Comparisons were made between Twin-Rolled Cast (TRC) sheets and Direct Chill (DC) cast sheets and the study demonstrated that sheets produced by the TRC method outperform the DC cast sheets. The low ductility of the sheet at room temperature was explained by the alloy's strong crystallographic texture. Experiments conducted by Mukai et al. (2001) showed that a reduction of grain size in AZ31B alloy resulted in longer elongation to failure by more than 40%.

Antoniswamy et al. (2013) developed ZEK100 FLDs between temperatures of 300 to 450°C, shown in Figure 1.14, and found that ZEK100 has greater formability over AZ31B, attaining up to 60% higher major strain at fracture for all tested strain paths, temperatures and strain rates.

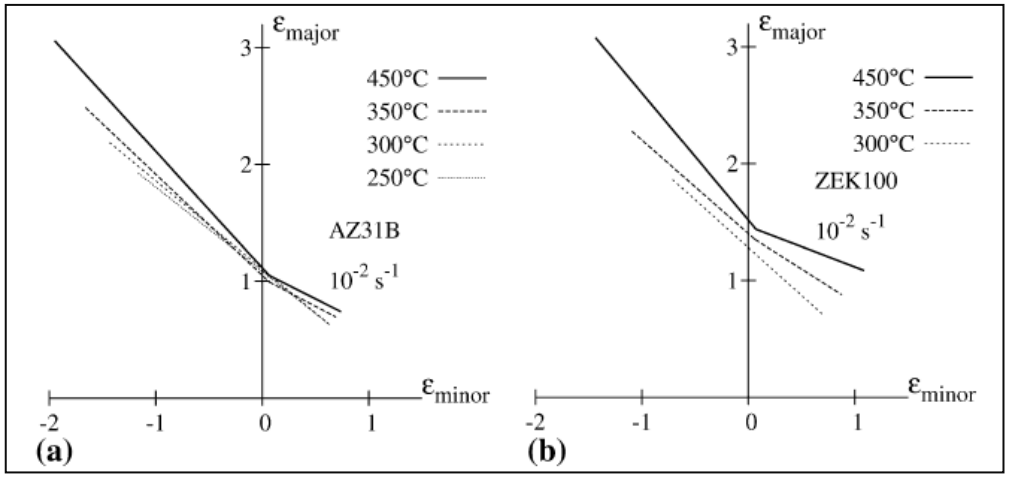

Figure 1.14: Forming limit curves for a) AZ31B and b) ZEK100 between 300 and 450°C (Antoniswamy et al., 2013)

Three-point bending of ZEK100 at room temperature was investigated by Aslam, et al. (2013) with ZEK100 material characterization showing improved room temperature and warm temperature formability over AZ31B (Min et al., 2012a and 2012b; Kurukuri et al., 2013a and 2013b). Min et al. 2012b showed this by observing the elongation of both AZ31B and ZEK100 between both rolling and transverse direction shown in Figure 1.15. ZEK100 exhibited greater total elongation, especially in the transverse sheet direction.

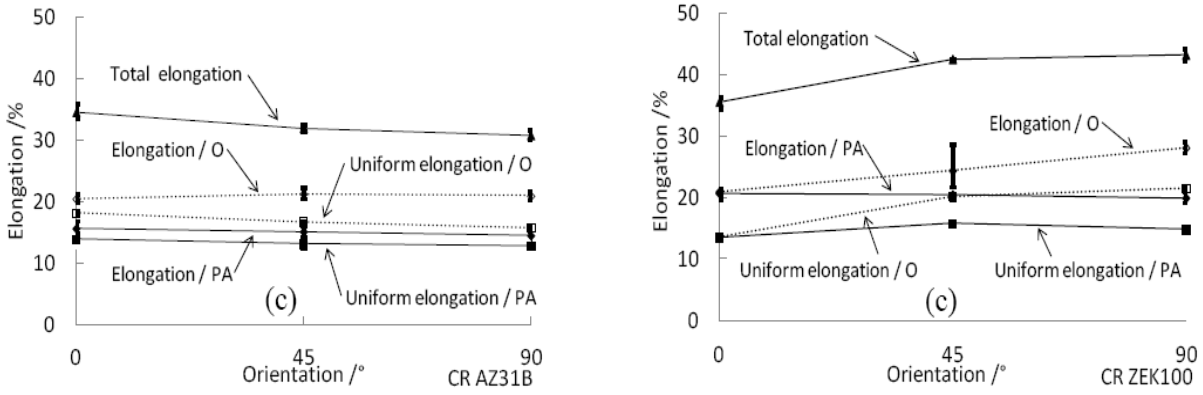

Figure 1.15: Elongation of AZ31B and ZEK100 (Min et al. 2013b)

In general, these studies report that the optimal formability and drawability within the "warm temperature range" is reached around 250°C. As such, recent works have focused on warm deep drawing behaviour of AZ31B (Chen et al., 2003a; Ambrogio et al., 2007; Zhang et al. 2007; Ghaffari Tari et al., 2013). The work of Chen et al. (2003a) involved deep drawing of square cups using AZ31B with comparisons made to results obtained from simulation models. The work concluded that the optimal drawing temperature for drawing 0.5 mm AZ31B sheet is 200°C with good performance of simulation models shown in Figure 1.16.

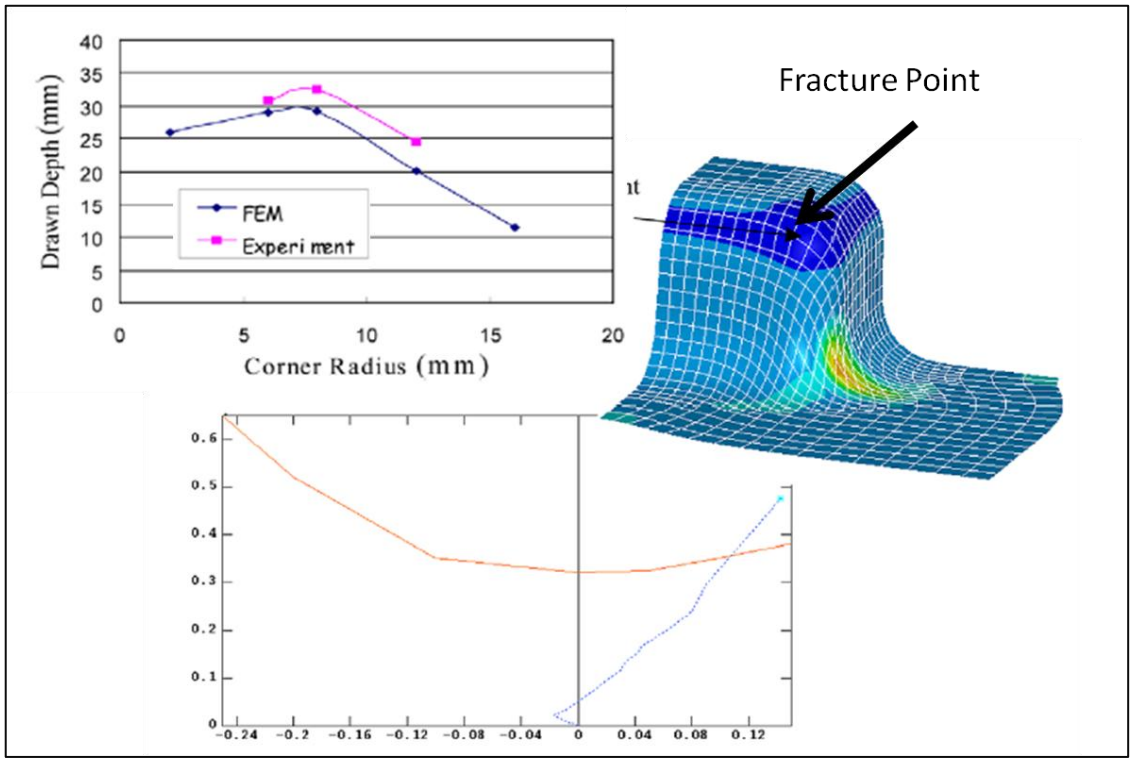

Figure 1.16: Simulation results of deep drawn AZ31B square cups

Non-isothermal deep drawing, in particular, has been shown to result in enhancements in forming behaviour for magnesium alloys. (Palumbo et al., 2007; Palaniswamy et al., 2004; Kaya et al., 2008; Ghaffari Tari et al., 2013). Most research work on deep drawing has been focused on AZ31B with very little work performed on ZEK100.

1.5 Limiting Dome Heights (LDH) and Forming Limit Diagrams (FLD)

Research in this thesis focuses on the characterization of formability and drawability of sheet material hence the techniques and methods of quantifying the performance are reviewed here.

Forming Limit Diagrams (FLDs) are a well-accepted method of presenting the limits of formability for a material under nominally monotonic load paths (as shown in Figure 1.17). The forming limit curve (FLC) presents the limiting major strain as a function of minor strain (strain state) prior to the onset of necking. This description of material behaviour was first given by Hill (1952) for uni-axial tension strains while Marciniak (1973) described the process for equi-biaxial tensile strains as a strain concentration where a defect or “groove” occurs in the material. The maximum strain of a material prior to the onset of the "groove" or necking is used to establish the limiting strain values for both major and minor strain. When the major vs. minor limiting strains are plotted on a graph, a forming limit curve is created, as shown in Figure 1.17. A number of specimen geometries are tested in order to produce different states of strain. These include uni-axial tension, plane strain, and equi-biaxial tension strain. The uni-axial tension strain state consists of tensile strains along the major axis with compressive strains along the minor axis. This strain state can be produced by a deep notched blank, as shown in Figure 1.17 (blank number 1). The plane strain state consists of tensile strain along the major axis and zero (or minimal strain) along the minor axis. This strain state can be produced by a shallow notched blank as shown in Figure 1.17 (blank number 3). To obtain an intermediate tensile strain an intermediate notched blank is required, as shown in Figure 1.17 (blank number 2). Finally, the equi-biaxial strain state consists of a material stretch condition where both major and minor axes experience equal or close to equal tensile strains. This strain state is achieved with a square blank. To obtain a variety of biaxial strain states (minor strain less than major strain) the form of lubrication can be varied between no lubrication and various lubricated conditions in which the ratio of minor strain to major strain can be controlled by the degree of lubricants.

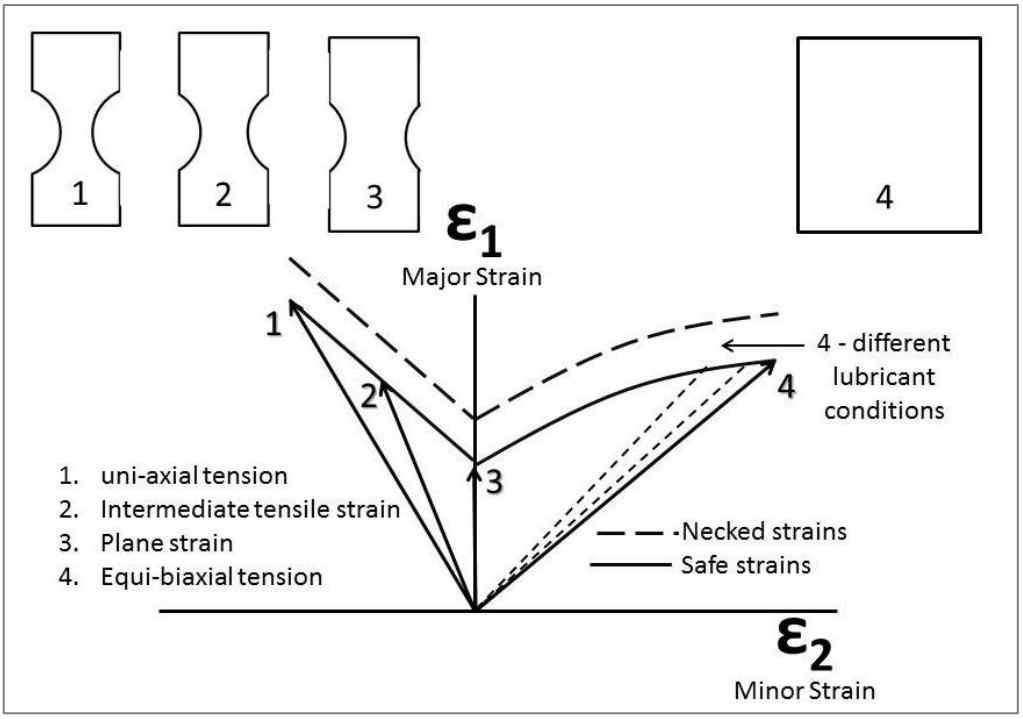

Figure 1.17: Components of a Forming Limit Diagram.

For most forming limit curves a single monotonic strain path is considered. A strain path is the history of strain states experienced during a forming operation. A strain state is the ratio between major and minor strain. Figure 1.17 shows four strain paths depicted as straight lines while in reality the strain path often appears as an upward concave curve. By altering the strain path (history of strain states) the forming characteristics of the material are affected, including various conditions of localization (necking), twin activity, and failure behaviour (Khosravani and Scott, 2013). The limiting strain of a material is, therefore, path dependent. This means that the history of major and minor strains is important for repeatability and comparison purposes (Stoughton, 2000). For example, Kleemola et al. (1980a) showed that in multi-stage forming operations, the effects of the strain path for each stage must be taken into account when assessing formability using an FLD. There are a large number of FLDs published in the literature for a range of materials, however several experimental factors must be considered when conducting direct comparisons of forming limit curves from different sources since each FLC is somewhat dependent on the testing procedures, equipment used, the strain measuring methods and the criteria for determining the limiting strains (Hijazi et al., 2004). FLCs based on strain measurements remain the most used industrial metric for quantifying the performance

of a material even though stress-based FLCs have been shown to provide a path independent material performance metric (Stoughton, 2000; Min et al. 2013). However stress-based FLCs are very difficult to apply on the shop floor.

The current study presents FLDs developed by using hemispherical dome tests utilizing a hemispherical punch, as proposed by Ghosh and Hecker (1975) and known as Limiting Dome Height (LDH) experiments. Using this method, Ghosh and Hecker showed that out-of-plane experiments result in higher limiting strains than those obtained from in-plane experiments, principally due to the presence of curvature and friction effects that act to strengthen the material (Gosh and Hecker, 1974). The LDH method of formability testing provides out-of-plane deformation tests suitable for measuring strains using a Digital Image Correlation (DIC) system. Successful work using DIC to measure material strains has been demonstrated by Brunet et al. (1998), Hijazi et al. (2004) and Bagheriasl (2012a), for example.

Chen et al. (2003b) conducted experiments on deep drawing of square cups with AZ31B and obtained stress-strain curves and FLCs at elevated temperatures from these experiments, shown in Figure 1.18, demonstrating good performance and elongation at temperatures above 200°C.

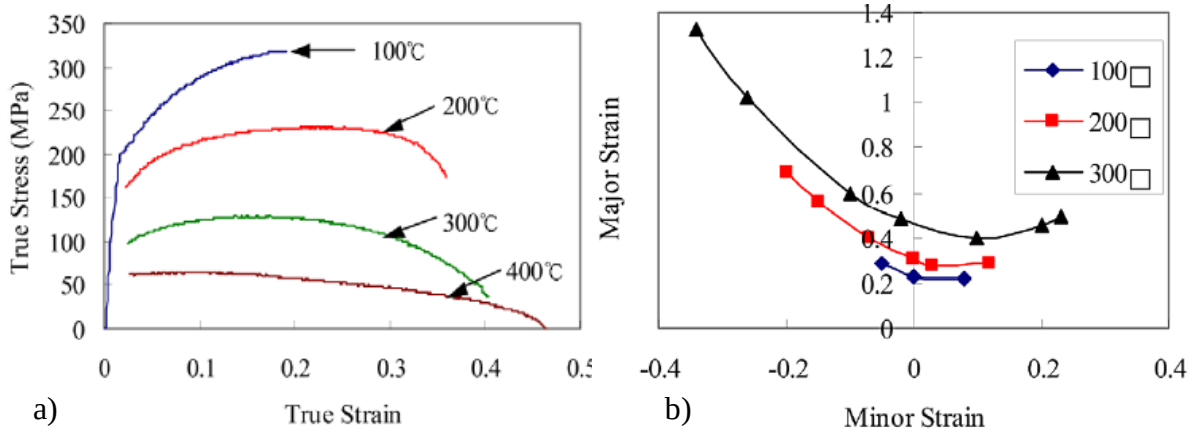

Figure 1.18: AZ31B experimental results a) stress-strain curves b) FLC at elevated temperatures (Chen et al. 2003b).

The work of Min et al. (2013) has focused on developing an analytical method for FLD prediction for ZEK100 and achieved good results by applying the orthotropic Barlat-Lian yield criterion as shown in Figure 1.19.

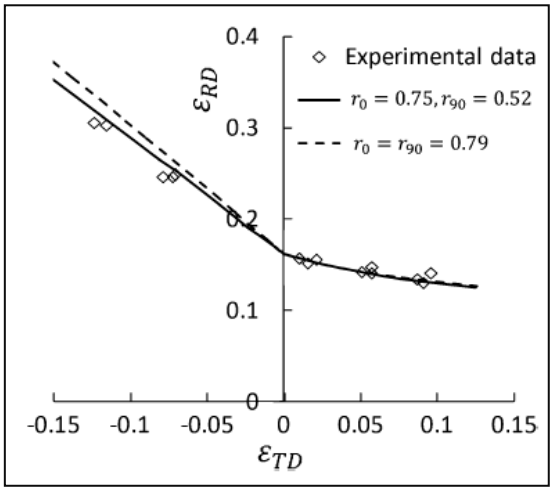

Figure 1.19: Comparison of prediction results between models based on yield criterion (Min et al., 2013)

Low to warm temperature FLCs for AZ31B were developed by Kim et al. (2008) using a hydraulic press with a hemispherical punch showing promising results in the warm temperature range of room temperature to 100°C shown in Figure 1.20.

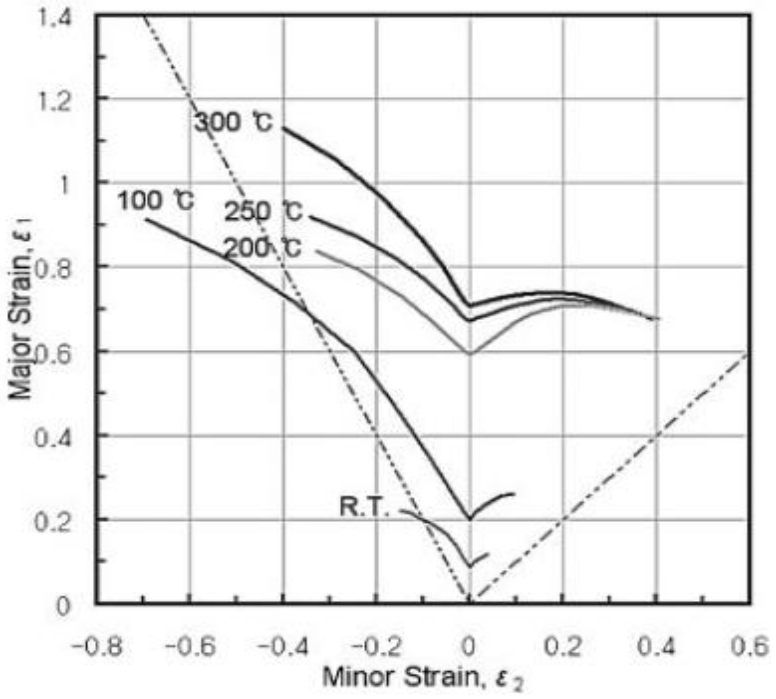

Figure 1.20: FLCs for AZ31B (0.5 mm thick) for room temperature, 100°C, 200°C, 250°C, 300°C (Kim et al. 2008)

1.5.1 Digital Image Correlation (DIC)

The measurement of material strain has always been an integral component of mechanical testing. Several methods exist for such measurement, including extensometers (for 2D deformation), the circle grid technique (Keeler, 1968; Kim et al., 2008; Min et al., 2013) and digital image correlation (DIC) optical techniques (Hijazi et al., 2004). The latter two are the most commonly used for large deformation tests on sheet material (both 2D and 3D deformation) similar to those conducted for the study at hand. The method of DIC is based on using two stereoscopic cameras that each capture an image, which are then processed using computer software that measures the difference between the two images (i.e. the parallax) and renders a 3-dimentional representation (much like what the human eyes do). The setup can be seen in Figure 1.21. By recording a series of images starting with an un-deformed specimen and ending with a fully deformed specimen the DIC system is able to measure the movement of points on the surface of the material. In the case of mechanical deformation, the movement of points directly relates to the strain measurements of the material. The forming limit curves developed in this study are based on the measurements obtained from the DIC system. A more detailed discussion of DIC related to the present research project is given in Section 2.3.5.

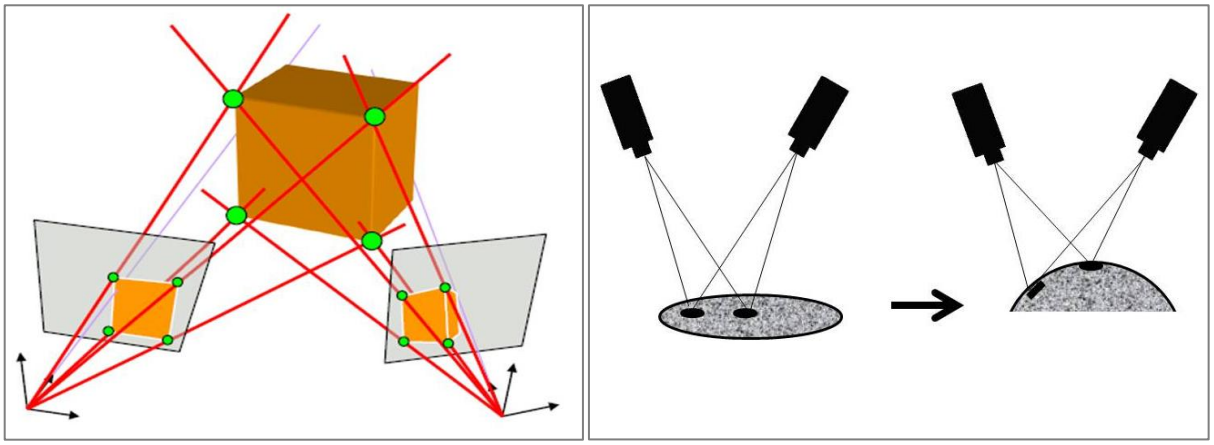

Figure 1.21: Digital Image Correlation: Stereo Camera for 3D triangulation (Correlated Solutions).

1.6 Current Research

Research-to-date on formability of Mg sheet has focused primarily on AZ31B and its positive results have led to the limited adoption of the alloy at the production level in the automotive

industry. As yet, the mechanical characteristics of the rare-earth alloyed ZEK100 magnesium alloy sheet have received very little attention. There is very little past research in the areas of forming limit characterization in the low to warm temperature regime (room temperature to 300°C) and the drawability of ZEK100 for any temperature conditions. The present study aims to address these deficiencies by developing forming limit curves for ZEK100 from room temperature to 350°C in both the rolling and transverse direction and comparing it with AZ31B at selected temperatures. In addition, this study investigates the drawability of ZEK100 under both isothermal (100°C to 250°C) and non-isothermal conditions (punch: 25°C to 200°C and die: 100°C to 250°C). The ultimate goal of this research is to broaden the understanding of the potential benefits of rare-earth additions and improved (weakened) texture through experimental observations of LDH and Cylindrical Cup Draw experiments on a rare earth-alloyed magnesium sheet.

The balance of this thesis presents the methods and findings of these investigations. Chapter 2 lays out the experimental methods and experiments performed in the current research, including descriptions of the apparatus and treatments of the control parameters. Chapter 3 treats the nuances of processing the experimental data, including detailed discussions of inherent or potential experimental errors and the steps required to account for or mitigate error. Chapters 4 and 5 present and discuss, respectively, the results of the formability and drawability experiments. Chapter 6 provides a summary and conclusions stemming from this study and finally, Chapter 7 recommends related areas of future work that have been indentified throughout the progress of the current study.

2 EXPERIMENTS AND EXPERIMENTAL METHODS

This chapter presents the experimental methods used to conduct the current research. Formability and drawability of as-received ZEK100 magnesium alloy sheet was investigated under isothermal and non-isothermal conditions and compared to that of AZ31B-O. The conducted experiments included: Limiting Dome Height (LDH) experiments, with specimens cut in both the rolling and transverse directions, and Cylindrical Cup Draw experiments. A detailed description of the parameters and methodology used in the experiments is provided in the following sections.

2.1 Experimental Apparatus

All limiting dome height and deep drawing experiments were conducted on a hydraulic press, as seen in Figure 2.1, with a 60 ton blank holder capacity and a 75 ton punch capacity. The tooling setup is interchangeable depending on the type of experiments. The experiments contained in this thesis involved two different tooling setups: the Limiting Dome Height (LDH) experiment and the Cylindrical Cup Draw experiment, in which material stretching and drawing behaviour were examined, respectively.

Figure 2.1: Experimental Setup; Hydraulic Press (left), computer control rack (right).

2.1.1 Limiting Dome Height Tooling

Limiting Dome Height experiments were conducted with a vertically moving blank holder situated above the blank, a fixed die and hemispherical punch with the force being applied to the top of the blank. The tooling setup for the LDH experiments is shown in Figure 2.2. The die and blank holder incorporate a set of lock-beads to remove or minimize any effect of material drawing. Each component of the toolset contained heating cartridges capable of heating the tooling to 400°C under proportional-integral-derivative (PID) control. The punch and blank holder motion and applied force were controlled using MTS servo controllers with program signals generated via a custom LabView program. The punch velocity during all LDH testing was set at 1 mm/sec. A more detailed geometric description of the lock-bead and shim placement is presented later in this chapter in Section 2.3.3, along with the blank holder forces used for the tests.

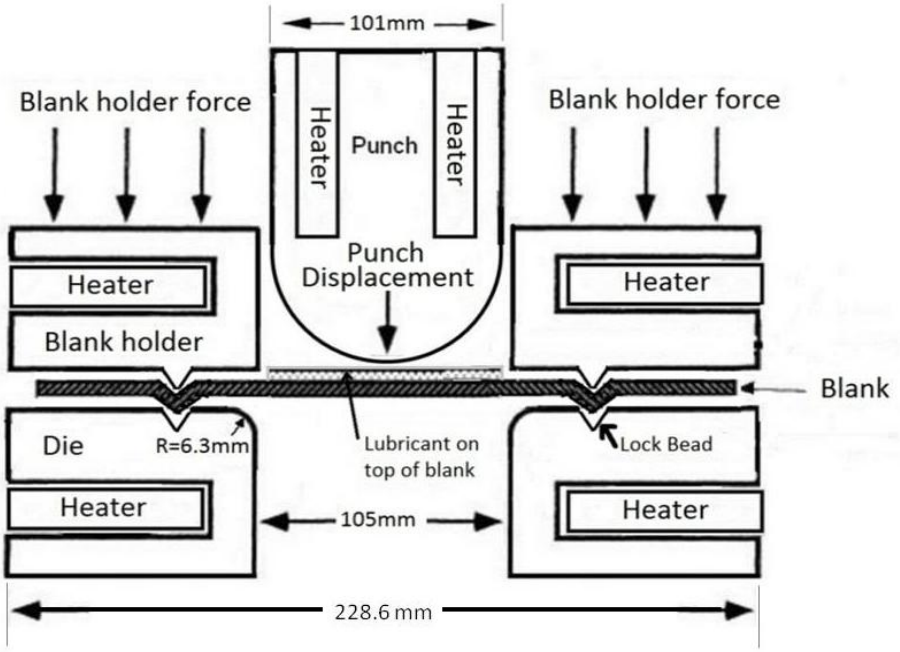

Figure 2.2: Dome punch tooling with lock-beads.

2.1.2 Deep Draw Tooling

The Cylindrical Cup Draw tooling is illustrated in Figure 2.3. The die and blank holder are smooth circular plates to allow for drawing of material into the die opening. The tooling was heated via embedded cartridge heaters. The cylindrical punch was optionally heated with embedded cartridge heaters or cooled with flowing water via water channels within the punch. The punch and blank holder movement and applied force were controlled using MTS servo controller with program signals generated via a LabView program. The punch speed was set to 4 mm/s for all Cylindrical Cup Draw experiments.

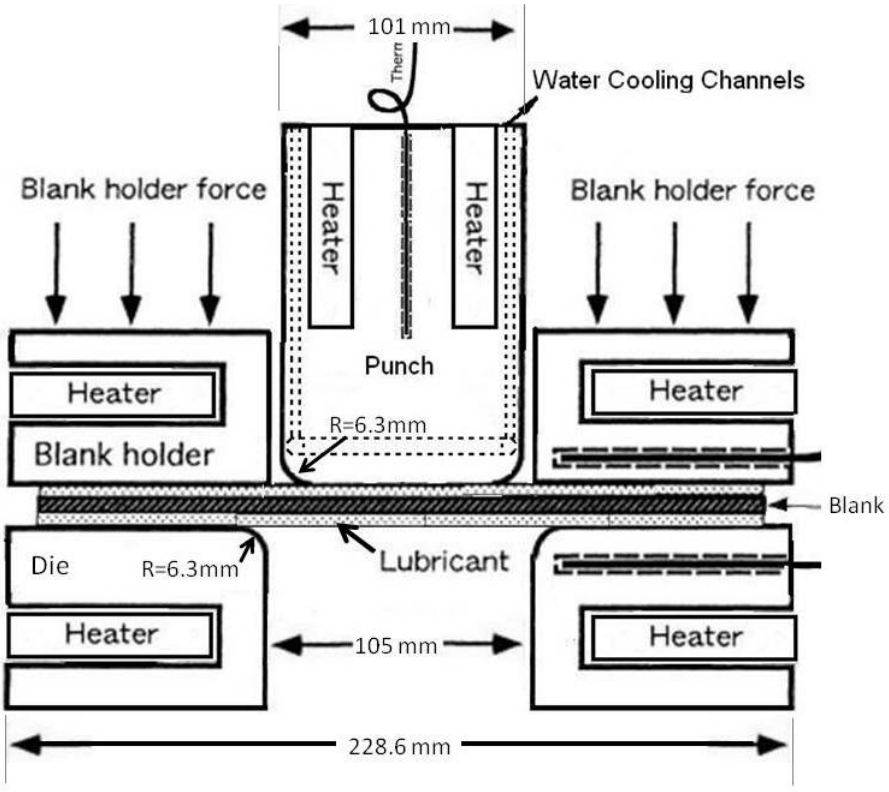

Figure 2.3: Deep draw punch tooling with smooth dies.

2.2 Material and Experimental Conditions

Single processed batches of as-received ZEK100 and AZ31B-O (some LDH tests also used AZ31B-H24) were used throughout all experiments contained within this thesis. The chemical composition of the ZEK100 and AZ31B-O magnesium alloy sheet can be seen in Table 1.1:

Chemical Composition of AZ31B and ZEK100 (wt%), shown earlier is Section 1.3. A series of experiments were conducted on AZ31B-O to act as a baseline to which the performance of the ZEK100 alloy could be compared. The alloy AZ31B-O is a hot rolled and fully annealed material. The ZEK100 was tested in an "as-fabricated" or F temper. Both the ZEK100 and AZ31B-O had a nominal sheet thickness of 1.6 mm. An exhaustive series of material characterization experiments were performed on the same alloys (same lots) considered in the current experiments by Kurukuri et al. (2013a,b). The uniaxial stress-strain response is shown in Figures 1.11 - 1.13 (Kurukuri et al., 2013a,b).

2.2.1 Lubrication

All testing was conducted with 0.07 mm Polytetrafluoroethylene (PTFE) film, commonly known as Teflon, as a lubricant. For the LDH experiments, Teflon was placed between the punch and the blank, but not in the die-blank holder (clamping) region of the tooling. For the deep drawing experiments, Teflon was used between all blank-tooling interfaces. Teflon offers a low coefficient of friction (0.05 – 0.10 based on ASTM Standard D1894) and allows for an acceptable melting point of 327°C based on ASTM Standard D3418. Bagheriasl et al. (2012a) have measured the room temperature coefficient of friction for Teflon film in conjunction with an AA3003 alloy and obtained a value of 0.043. Elevated temperature friction coefficients are not available. The use of Teflon allowed for experimental consistency and reduced pick-up of material on the punch surface which would create frictional variability and therefore affect the repeatability of experiments.

Teflon, as a lubrication material, is typically not readily employed in industrial production processes due to the complexity of its implementation in production and added expense. Dry film lubricants, however, are applied in liquid form and dried on to the surface of the material to be formed and are easily incorporated into typical production processes. A parallel investigation was conducted to compare the frictional effects between Teflon and a dry film lubricant (Forge Ease AL 278 from FUCHS). The results based on deep drawing of 203 mm blanks at various temperatures, presented in Figure 2.4, show the measured load-displacement response for the punch. The punch force was marginally larger for the dry film lubricant compared to Teflon by up to approximately 5% for all tested temperatures.

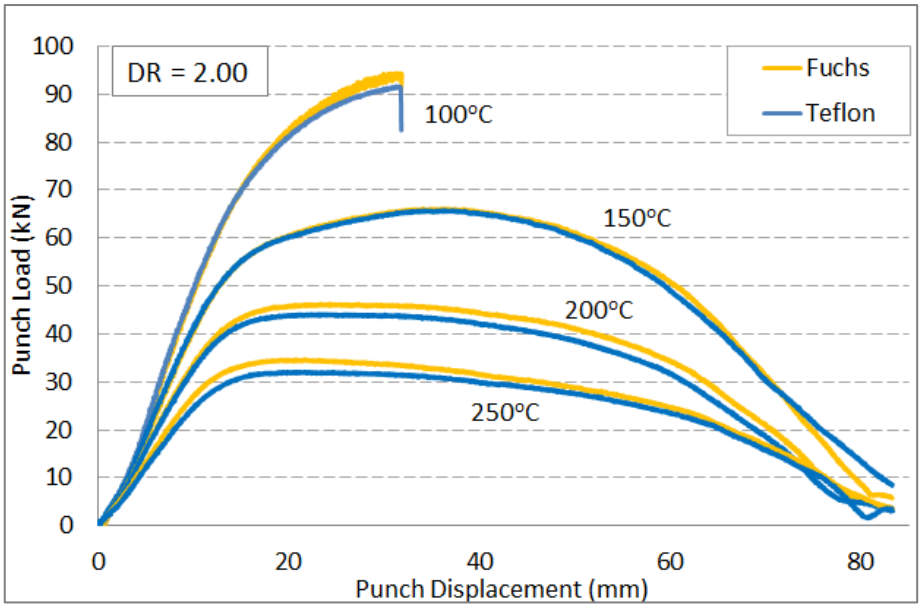

Figure 2.4: Punch load vs. displacement for LDR comparison of Teflon and Forge Ease AL 278 (FUCHS) dry lubricant.

2.3 Limiting Dome Height Experiments

Limiting Dome Height experiments were performed to obtain a quantifiable formability performance measure between ZEK100, AZ31B-O and AZ31B-H24. These experiments involved stretching a sheet over a hemispherical punch, as proposed by Ghosh and Hecker (1975). In each test, a sheet specimen is stretched over a hemispherical punch (or dome) until necking and eventually failure/fracture occurs. The dome height of the stretched sample is recorded as the Limiting Dome Height for the particular material. Two sets of LDH tests were conducted for this thesis. The first involved using only square 203 x 203 mm blanks to obtain the maximum height of domes prior to failure. The punch-load vs. punch displacement data was used to detect the onset of failure for the initial set of LDH tests. The second set of tests involved a range of specimen sizes, as described in Section 2.3.1 and used digital image correlation to measure surface strains on deformed specimens. Failure was defined as the onset of necking, as detected using the DIC strain measurements, described in Section 3.2.3. These experiments were utilized to construct forming limit curves for a range of temperatures.

2.3.1 LDH Specimen Geometry

Limiting Dome Height experiments were performed to measure the formability of ZEK100 as well as develop forming limit curves. LDH experiments were conducted using the specimen geometry described in ISO/DIS 12004-2 (2006) and consisted of the four geometries shown below in Figure 2.5. LDH results were obtained by forming square 203 x 203 mm blanks, while Forming Limit Curves were determined using all four specimen geometries including: a square 203 x 203 mm blank and three notched blanks of 25.4 mm (1”), 50.8 mm (2”), and 76.2 mm (3”) in width at their narrowest point. Specimens were cut with their major axis oriented along either the sheet rolling direction (RD) or transverse direction (TD) to investigate the effects of anisotropy.

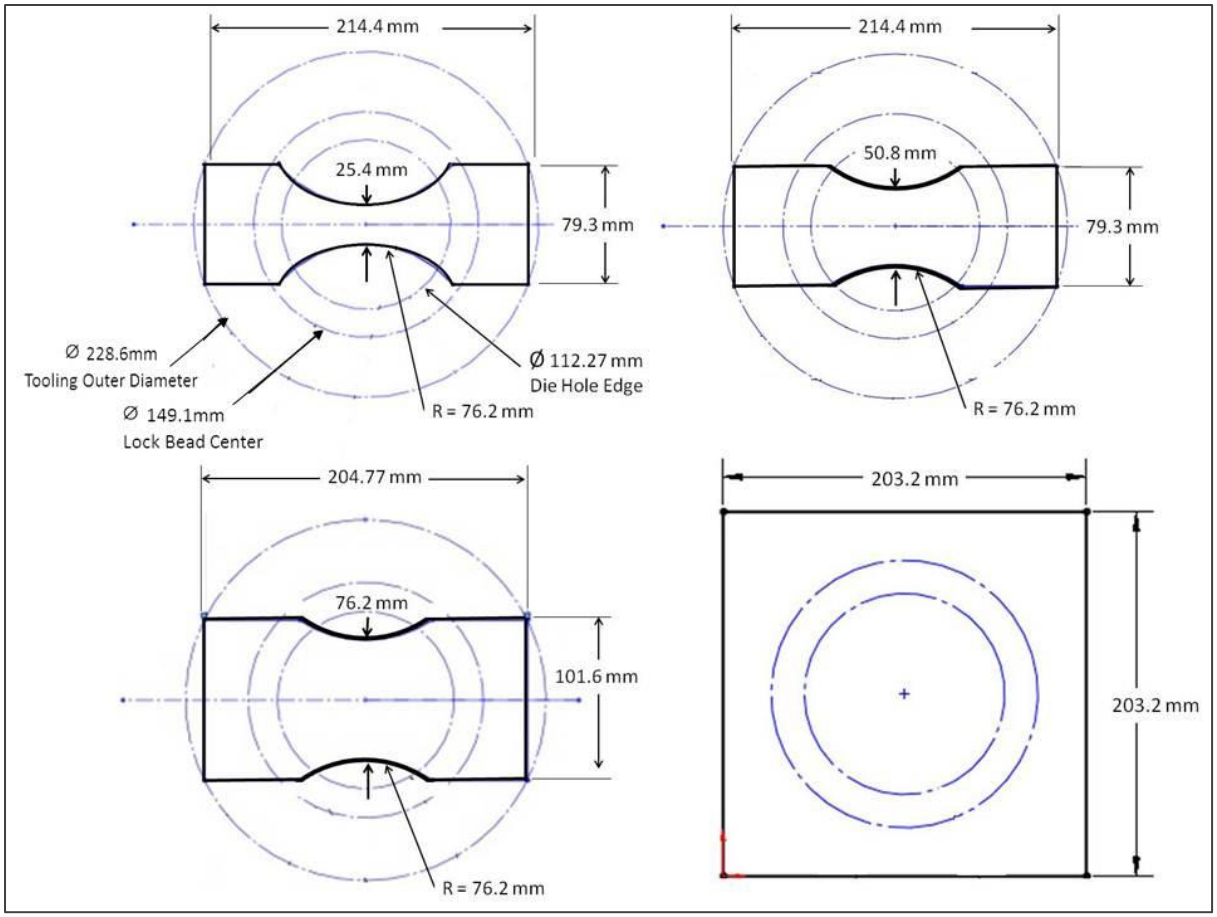

Figure 2.5: Specimen geometry used in the LDH experiments.

2.3.2 LDH Temperature Control

Experiments were conducted to determine the time required for the blank to achieve thermal equilibrium at each test temperature for LDH experiments. Prior to testing, the toolset was heated to the selected temperature which was confirmed with a thermocouple. Following this, the blank was placed onto the die and then clamped by the blank holder. The punch was then lowered to engage the blank with an applied displacement of 1 mm. The blank and toolset were then given time to reach the equilibrium temperature, as shown in Figure 2.6. The timing curves begin from the moment at which the punch is positioned above the blank, at which point the LabView program begins recording of the blank temperature *via* a thermocouple attached to the surface of the blank midway between the center and the edge of the die opening. This temperature data and heat up time information was used to ensure a repeatable starting point during the LDH testing procedure for duplicating the heating cycles. Note that the heating curves shown in Figure 2.6 do not start at the same temperature since there was a temperature rise between the moment the blank holder was closed and the final positioning the punch prior to forming. It was found that within 90 seconds the recorded temperature of the blank began to stabilize and achieve quasi-equilibrium after 120 seconds of heating time for temperatures between 50°C and 200°C. To attain desired blank temperatures of 250°C and 300°C a longer heat time of 6 minutes was necessary.

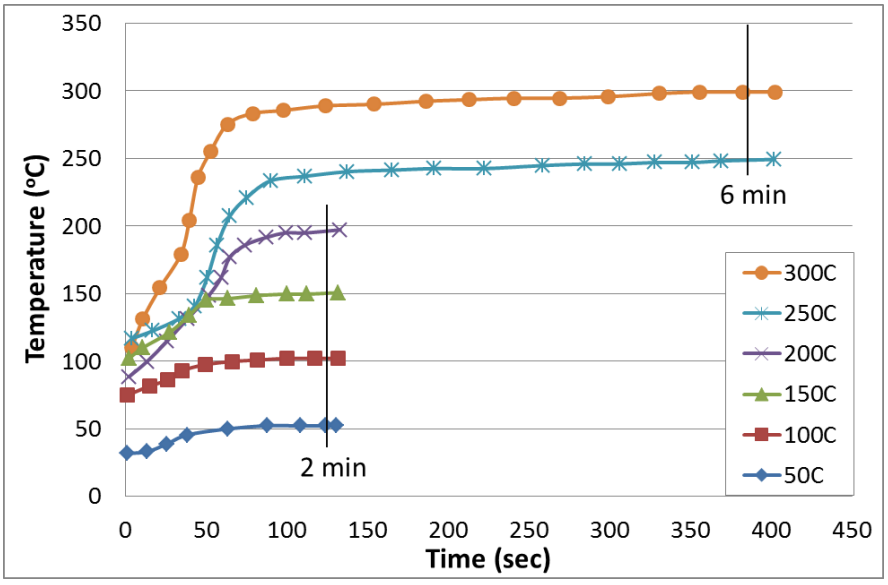

Figure 2.6: Time of heating profile for a 203 x 203 mm square blank.

2.3.3 LDH Binder Force

The required binder force needed to be determined prior to performing the warm LDH experiments. Preliminary tests resulted in undesired failures of the blank due to tearing at the lock-bead or wrinkling of the blank within the flange area. These failures may be prevented by adjusting the binder force and/or the lockbead penetration. A series of experiments were performed to determine appropriate binder forces for each temperature condition and blank geometry. The blank holder force (BHF) was selected using the following criteria: 1) sufficiently high to prevent the specimen from drawing into the dome while removing wrinkling of the blank in the flange area and 2) sufficiently low to not cause fracture within the lock-bead. For the 203 x 203 mm square blanks, a BHF of 66 kN was used for temperatures up to 200°C. The force was reduced to 33 kN for the 250-350°C samples. The notched samples were prone to tearing at the lock-bead, so a shim/spacer was installed between the sheet and tooling to reduce the lock-bead penetration (Figure 2.7). A BHF of 88 kN was used for all temperatures where a shim was involved to ensure a sufficient clamping force to control draw-in. A detailed listing of blank holder forces and use of spacers is shown in Table 2.1. Changes in the blank holder force did not affect the ability to compare the results from these experiments since the major role of the blank holder in these experiments was to restrict the movement of the blank in such a way that it did not draw into the punch opening, allowing only deformation over the punch.

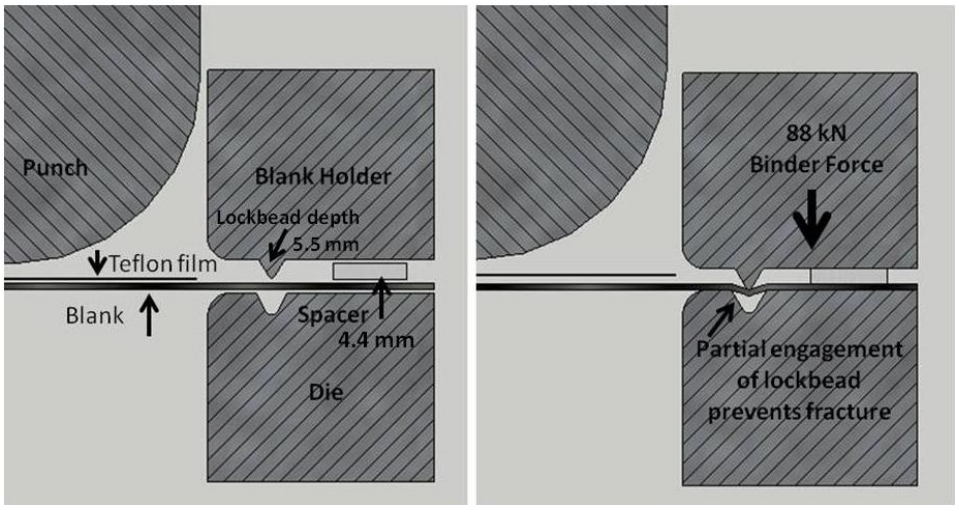

Figure 2.7: Die and blank holder lock-bead engagement with spacer.
Blank holder disengaged (left), engaged (right)

Table 2.1: Blank holder forces for all FLD experiments

Specimen	Blank Holder Force (kN)	Temperature (°C)	Reason
203x203 mm	66	RT - 200	Good results
203x203 mm	33	250 - 350	Force reduced to prevent tearing at lock-bead
50.8 and 76.2 mm	88	RT - 350	Spacer of 4.4 mm placed between die and blank holder outside of lock-bead to prevent tearing at lock-bead
25.4 mm	66	RT	Spacer of 4.4 mm placed between die and blank holder outside of lock-bead to prevent tearing at lock-bead
25.4 mm	88	50 - 350	Spacer of 4.4 mm placed between die and blank holder outside of lock-bead to prevent tearing at lock-bead

2.3.4 LDH Experimental Method

Both sets of experiments required heating of the tooling to isothermal conditions. Prior to each test the tooling was heated to the test temperature and allowed sufficient time to reach an equilibrium temperature and become stable. The temperature level was monitored *via* a thermocouple prior to performing each test.

The selected temperatures for the first set of LDH experiments were room temperature (RT), 150, 200, 250, and 300°C. The second set of tests used for development of FLDs was performed at RT, 50, 100, 150, 200, 250, 300, 350°C. The punch speed was kept constant at 1 mm/sec for each experiment.

Each LDH experiment consisted of loading the blank into the press and running the LabView program as follows:

1) Engage the blank holder to a predetermined blank holder force and lock-bead penetration (see Table 2.1)
2) Lower the hemispherical punch to engage the blank, apply a displacement of 1 mm.
3) Allow adequate heating time to reach desired temperature (Figure 2.6).
4) Start recording DIC data collection system (for FLC data).
5) Advance the punch until failure of stretched dome occurs.
6) Stop recording by DIC collection system (for FLC data).

Tests at each temperature for all geometries were repeated three times to account for the experimental scatter and check for repeatability of the results. Table 2.2 shows the final count of successfully formed and analyzed specimens using the DIC system. Some specimens failed DIC analysis since the speckle pattern flaked off during testing and, as a result, did not provide adequate strain data.

Table 2.2: Forming Limit Diagram experimental matrix

ZEK100 Rolling Direction.	RT	50	100	150	200	250	300	350
203x203mm (8"x8")	3	3	3	3	3	2	3	3
25.4mm (1")	3	3	3	3	3	3	3	3
50.8mm (2")	2	3	3	3	3	3	3	3
76.2mm (3")	3	3	3	3	3	3	3	3

ZEK100 Transverse Direction	RT	50	100	150	200	250	300	350
203x203mm (8"x8")	3	3	3	3	3	2	3	3
25.4mm (1")	2	3	3	3	3	3	3	3
50.8mm (2")	3	3	3	3	3	3	3	2
76.2mm (3")	3	3	3	3	3	3	3	3

AZ31B Rolling Direction	RT	50	100	150	200	250	300	350
203x203mm (8"x8")	2				2	3		
25.4mm (1")	2				3	3		
50.8mm (2")	3				3	3		
76.2mm (3")	2				3	3		

2.3.5 Digital Image Correlation System for Data Collection

In situ strain measurement was performed using two CCD cameras (Figure 2.8a) to capture stereo images of speckled samples during deformation after which digital image correlation (DIC) analysis (Figure 2.8b) was used to generate the forming strain history. The DIC system allows for adjusting processing parameters of subset size and step at the beginning of each analysis. The subset size of the DIC system denotes the number of pixels that is used for comparison. This corresponds approximately to a size of 2.5 mm on the surface of the blank which is comparable to the size of the grid used in the circle grid technique used for measuring strain in the deep draw experiments (where direct observation of the surface during testing was not possible). The step size for processing the DIC data corresponds to the resolution of the

analysis. A step size of 1 means that correlation analysis is performed on every pixel in the area of interest while a step size of 7 means that the analysis will be performed on every 7th pixel in the area of interest. Adjusting the subset size and the step size allowed for a balance between accuracy and processing speed. For the DIC analysis performed on the current work, a subset size of 31 pixels and step size of 7 pixels was used since it provided a satisfactory projection error. The DIC system recorded the deformation history for each sample from which the strains were calculated and the onset of necking was determined, as described in Section 3.2.1. Images were collected every 300 ms for the duration of the test for all experiments.

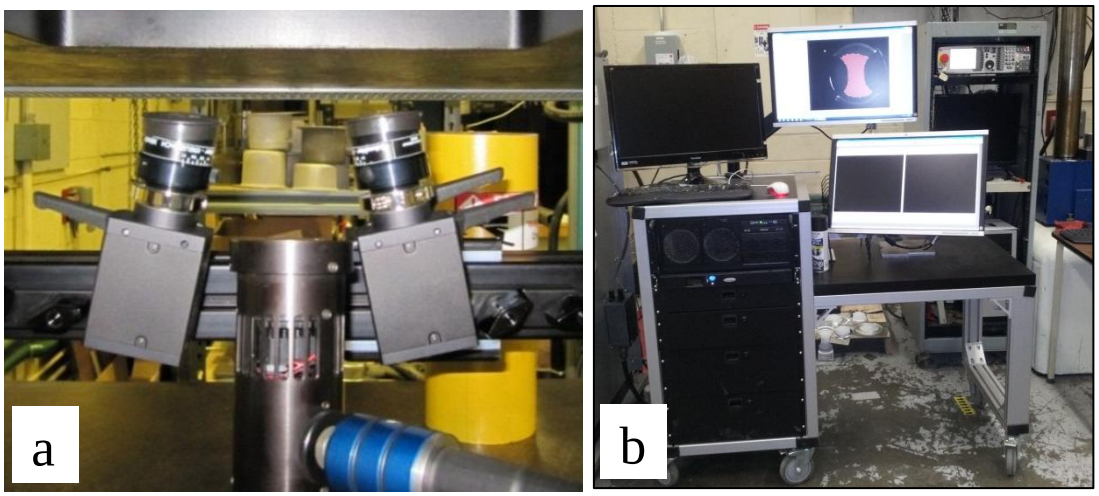

Figure 2.8: a) DIC cameras mounted under toolset b) DIC computer control rack.

2.3.5.1 Sample Preparation

The DIC cameras observe geometrical changes on the surface of interest. To accomplish this, the area of interest was speckled to provide a high contrast image between randomly distributed black dots against a white background. Typically this is done by painting the area with white paint and then speckling the surface with a spray of black dots. This method was used for the surface preparation of the AZ31B-O material. The dual paint method, however, was not suitable for ZEK100, since it resulted in peeling or flaking of the paint at temperatures above 100°C. An alternative method was developed for ZEK100, which involved lightly sandblasting the area of interest with a 300 grit sand blasting powder resulting in a white/grey matte surface (instead of white paint). This light surface finish was then speckled with a black

spray paint that was applied from a distance of approximately 60 cm with the aid of a pressurized air nozzle. The resulting pattern, shown in Figure 2.9, was found to be suitable for high temperature testing and measurements using the DIC system.

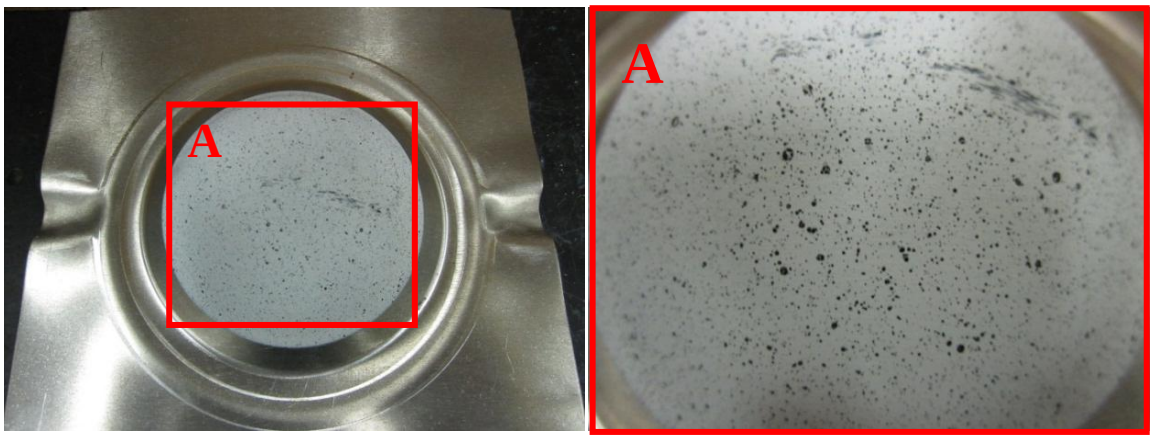

Figure 2.9: Speckled ZEK100 sample using sandblast and speckle method.

2.4 Cylindrical Deep Draw Experiments

2.4.1 Deep Draw Specimen Geometry

Blanks for deep drawing experiments consisted of circular disks cut from ZEK100 magnesium alloy sheet with a nominal thickness of 1.6 mm. The edge of the circular blank was de-burred. To investigate the effects of draw ratio, the disks were cut to 177.8 mm (7”), 203.2 mm (8”), 228.6 mm (9”), providing draw ratios (DRs) of 1.75, 2.00, and 2.25, respectively. Draw ratio is the ratio of original blank size to punch diameter; e.g. a blank size of 203.2 mm (8") drawn with a 101.6 mm (4") punch results in a DR of 2.00.

2.4.2 Deep Draw Temperature Control

Tests were conducted to determine the time for blanks to reach the desired temperature as well as to observe the temperature distribution on the blank for both isothermal and non-isothermal deep drawing tests. Temperatures were monitored with a hand held thermocouple and probe. Heating times were consistent with those reported earlier for LDH temperature control (Section 2.3.2), as expected. Prior to each test using different temperatures, the heating time and temperature were verified to ensure consistent conditions.

2.4.3 Deep Draw Binder Force

Binder forces for all isothermal and non-isothermal draws were determined to provide good depth of draw. The procedure for determining the binder force for the Cylindrical Cup Draw tests involved lowering the binder force until a full draw of the material or until failure at the punch tip occurred with the onset of wrinkling at the flange. The selected forces for the isothermal tests were 24 kN for 177.8 mm (7”), 60 kN for 203.8 mm (8”) blanks, and 60 kN for 228.6 mm (9”) blanks. Binder forces for the non-isothermal experiments that provided good depth of draw for tested DRs are given in Tables 2.3-5.

Table 2.3: Binder forces used for 177.8 mm (7”) blanks in non-isothermal drawing.

Die Temp (°C)							
270		48kN			48kN	48kN
250	24kN					
200	24kN					
150	24kN	24kN	24kN	24kN		
100	24kN	24kN	24kN			
50						
25						
	25	50	100	150	200	250

Punch Temp. (°C)

Table 2.4: Binder forces used for 203.2 mm (8”) blanks in non-isothermal drawing.

Die Temp (°C)						
270		63kN				63kN
250	60kN					60kN
200	60kN				60kN	
150	60kN	60kN	60kN	60kN		
100						
50						
25						
	25	50	100	150	200	250

Punch Temp. (°C)

Table 2.5: Binder forces used for 228.6 mm (9”) blanks in non-isothermal drawing.

Die Temp (°C)							
270						80kN
250	60k					
200	60k	60kN				
150	60k	60kN	60kN			
100						
50						
25						
	25	50	100	150	200	250

Punch Temp. (°C)

2.4.4 Deep Draw Experimental Method

Deep drawing experiments were conducted using the deep drawing tooling shown in Section 2.1.2. ZEK100 sheets with a nominal thickness of 1.6mm were used for all experiments using three different sized blanks to achieve draw ratios (DRs) of 1.75, 2.00, and 2.25. Isothermal experiments were performed with blank temperatures ranging from 100°C to 270°C. Non-isothermal experiments were also performed in which the punch temperature was varied from 25°C to 200°C and the die and blank holder temperature was varied from 100°C to 270°C.

Each deep draw experiment consisted of loading the circular blank into the press and running the LabView program as follows:

1) Engage the blank holder to a predetermined blank holder force (see Table 2.3 - 2.5)
2) Lower the cylindrical punch to rest on the blank.
3) Allow adequate heating time to reach desired temperature.
4) Move the punch until failure occurs or full draw is achieved. (Punch displacement was reduced as necessary for interrupted tests to determine earring profiles, thickness profiles, etc.)

3 PROCESSING OF EXPERIMENTAL DATA

3.1 Limiting Dome Height Experiments

In the limiting dome height experiments, the specimens utilized for FLD determination were deformed to failure and the point of necking was detected using strain measurements obtained from a digital image correlation (DIC) system. This was the most favorable method since it is difficult to accurately determine the necking point from punch load vs. punch displacement data as shown in Figure 3.1.

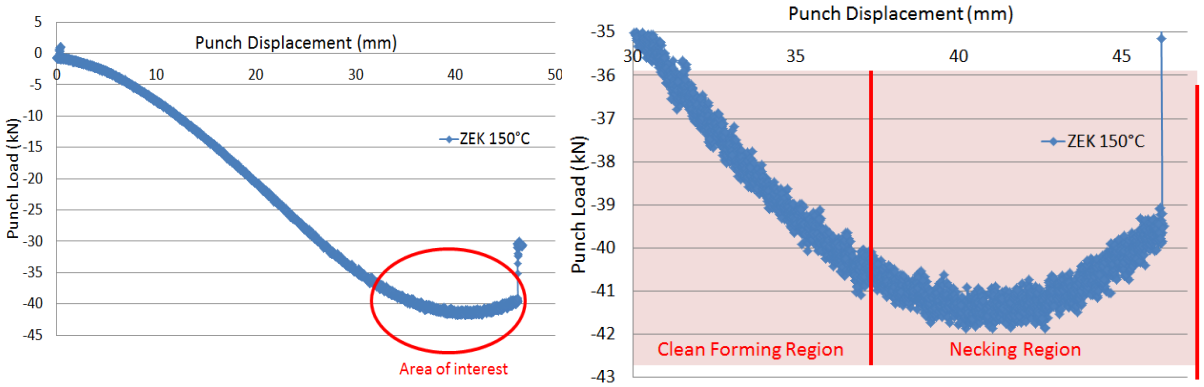

Figure 3.1: Punch load vs. displacement curve showing (left) the response associated with necking.

3.2 Forming Limit Curve Experiments

3.2.1 Processing of Experimental Data

Using the DIC system, strain measurements were collected for each specimen during testing. The data collected provides histories of measured major and minor strain across the surface of the speckled region of the specimen. Each experiment was conducted until failure of the material. For the equi-biaxial (203 mm square) and plane strain (76 mm dog bone) specimens, the failure occurred near the center of the specimen/test area by localized necking as typically occurs in sheet metal operations formed under multi-axial states of stress (Kleemola et al., 1980a). Specimens for uniaxial and near uniaxial (25 and 51 mm dog bones) failed off center, mid-way between the specimen center and edge or nearer the edge. The edge failures are attributed to damage effects at the edge induced by the shearing method used to create the

specimen. The effects of this damage are discussed later in Section 3.2.4. Strain data was selected at points near the fracture, as shown in a typical plot of measured strain contours in Figure 3.2.

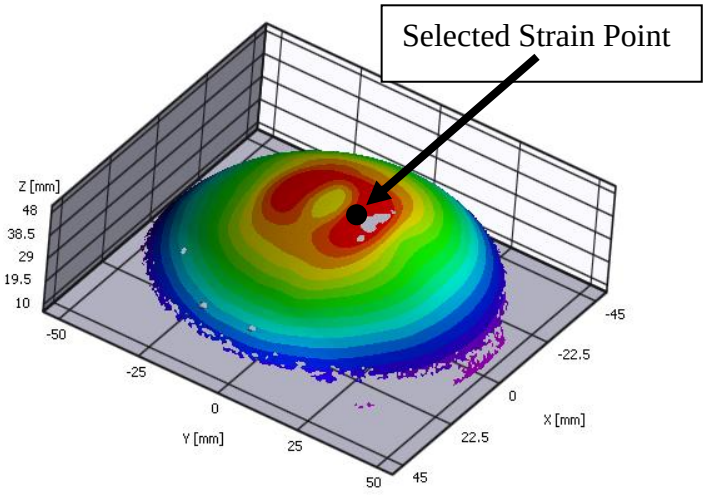

Figure 3.2: Strain visualization of a fracture image: equi-biaxial strain point.

The selected points were used to extract the representative major and minor strain histories for each specimen from its un-deformed state to its final fractured state in incremental steps recorded every 300 ms, creating a series images comprising strain measurements for each step in the deformation history, as shown in Figure 3.3

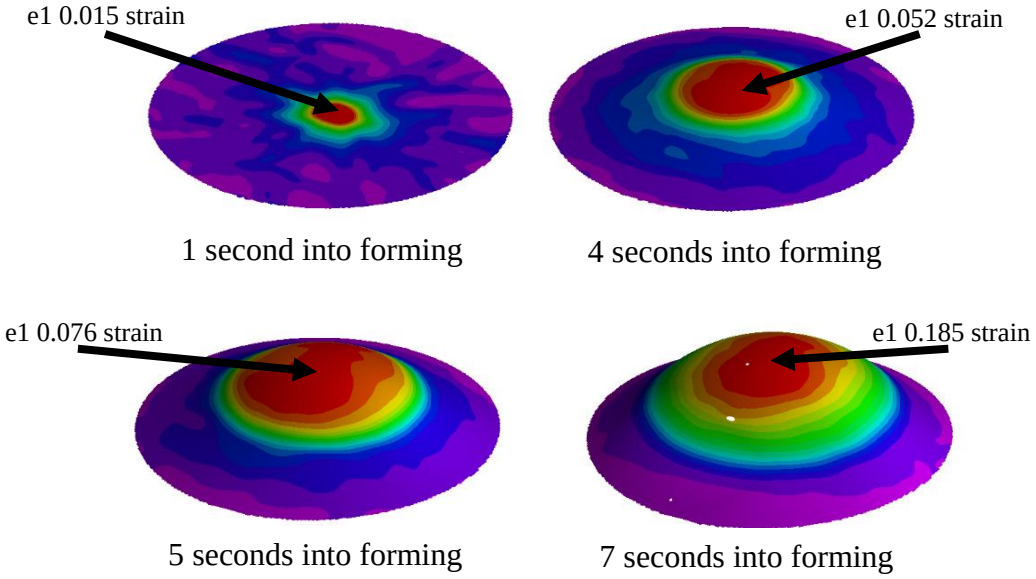

Figure 3.3: Incremental strain contour plots from DIC system.

The major and minor strain histories for the selected point were extracted and plotted for each incremental strain image collected by the DIC system; the resulting histories of major and minor strain are shown in Figure 3.4.

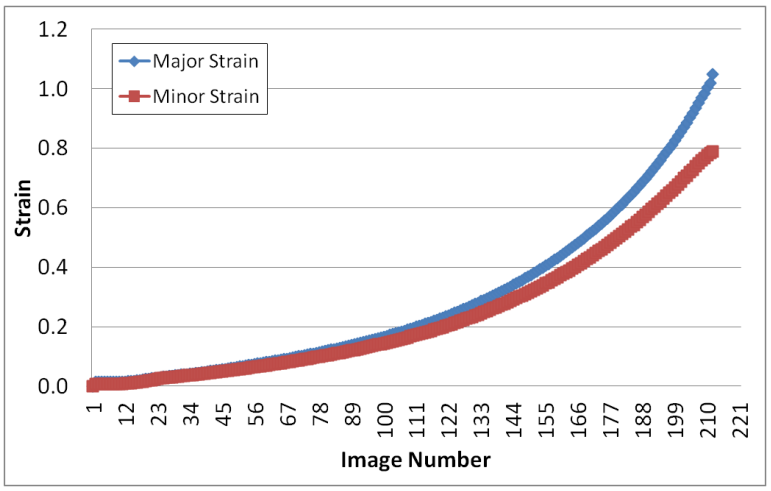

Figure 3.4: Strain history for selected point on a deformed 203 mm square blank at 200°C.

The measured major versus minor strain can be plotted on a forming limit diagram (FLD) to generate a strain path history. The final point prior to necking on the strain path corresponds to a limit strain point on the material forming limit curve. The strain paths and limit strains from all specimens are used to generate the material forming limit curve (FLC). Figure 3.5 shows recorded strain path histories for ZEK100 RD samples tested at 200°C, as determined using the DIC system. Results are shown for the three repeat tests for each condition and illustrate the degree of variation in the actual strain paths. The largest variation in strain path is seen for the biaxial (203 x 203 mm) samples; however, the exact cause of this variation is not known. All four strain paths exhibit an increase in slope with increasing strain; this behaviour is most pronounced for the narrower notched samples.

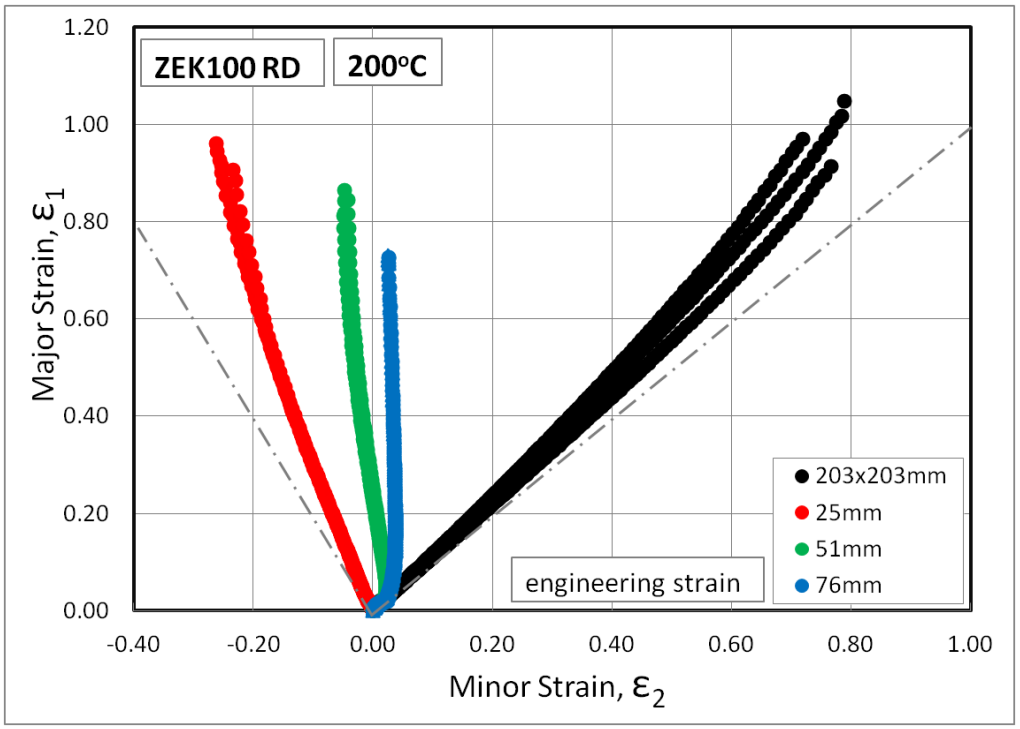

Figure 3.5: Strain paths to failure, ZEK100 specimens collected at 200°C.

3.2.2 Effect of refractive heat waves on DIC measurements

Measurements taken using image based systems may be prone to the effects of refractive heat waves during experiments at high temperatures. An analysis was performed to understand and quantify the amount of noise in the measured strain that may be introduced in a heated experiment. To investigate the possible effect of 'heat waves' and associated refraction of light waves at high temperatures, strain measurements were taken using the DIC system for three test cases. For all cases strain measurements were collected from a static experiment for 10 seconds. Strain measurements were collected along a line on the specimens' surface from the center of the specimen to the edge of the die as illustrated in Figure 3.6.

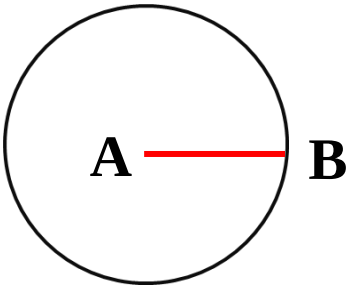

Figure 3.6: Line of interest for refractive heat wave test.

The first case was an un-deformed specimen at room temperature to provide a baseline and determine the experimental noise present within the DIC system in the absence of heat waves. The second case was that of an un-deformed specimen at 250°C. The last case was a deformed sample at 250°C. Comparing cases 2 and 3 to case 1, showed the effect of the refractive heat waves on the strain measurements from the DIC system.

Figure 3.7 shows the baseline measurements of case 1 at room temperature for an un-deformed specimen. The plot shows a scatter plot of measured major strain collected at room temperature every 300 ms along the line depicted in Figure 3.6 with point A, on the left, being the center of the blank and point B, on the right, being the edge of the test area on the blank. On this plot a value of zero would indicate no error since the specimen is not undergoing deformation and the measured strain should be zero. Any non-zero values indicate the presence of noise/error. The error in measured strain at room temperature was approximately 0.02% strain over the 10 second period which is judged to be quite small.

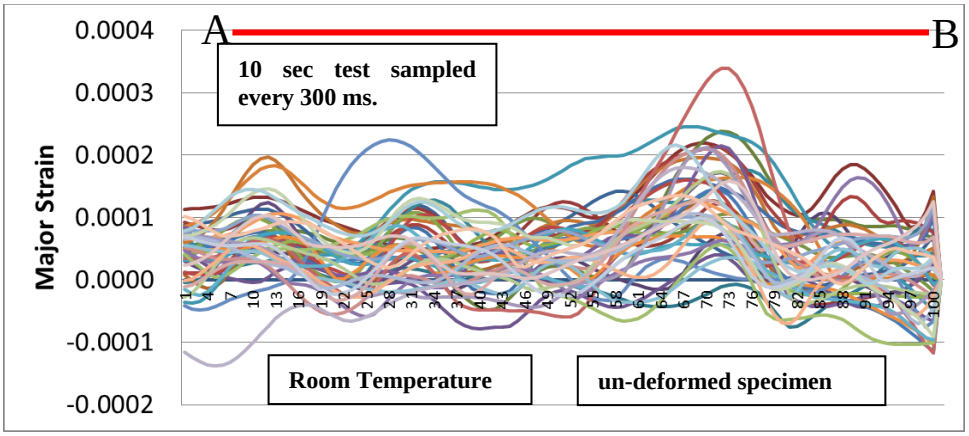

Figure 3.7: Major Strain Noise of DIC at RT, AZ31B 203 mm square specimen.

The results of the second case for which strain measurements were collected on an un-deformed specimen at 250°C are shown in Figure 3.8. The measured strains for this case fluctuated by up to 0.06% strain relative to the actual strain of zero, with most strain error occurring at the center and the edge of the test area. The addition of heat caused an increase in the error in measured strain of approximately 0.04% strain. This amount of noise may be neglected.

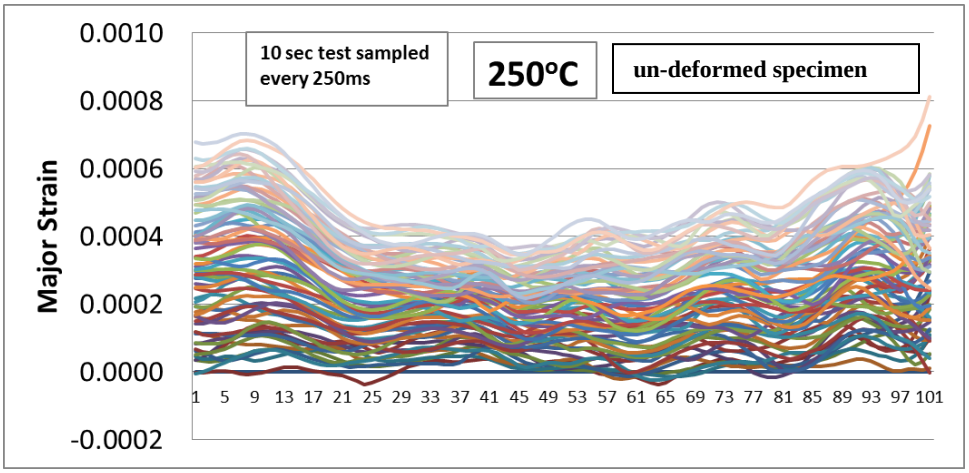

Figure 3.8: Major Strain Noise at 250°C, ZEK100 203 mm square un-deformed specimens.

The final case, shown in Figure 3.9, involved measuring the strain fluctuations on a deformed specimen at 250°C. This case showed the largest level of noise of up to 0.17% strain with the largest error occurring near the edge of the test area with the measured "strain" at the center of the blank being approximately 0.03%. In all the above cases, the highest noise experienced by the DIC system was less than 0.2% which occurred near the edge of the test area. It can be concluded that the effects of refractive heat waves on the strain measurement results using DIC are negligible for this experimental setup. All strain measurements for FLD construction are obtained from near the center of test area, which experienced up to 0.06% strain noise associated with heat waves and may be neglected in determining the final strain measurements. However, other sources of errors may be present. The negligible effect of the refractive heat waves on the DIC measurements may be attributed to the current experimental setup of the DIC cameras in relation to the heated toolset. The heated toolset is situated above the cameras, thus allowing the refractive heat waves to rise without significant distortion to the image.

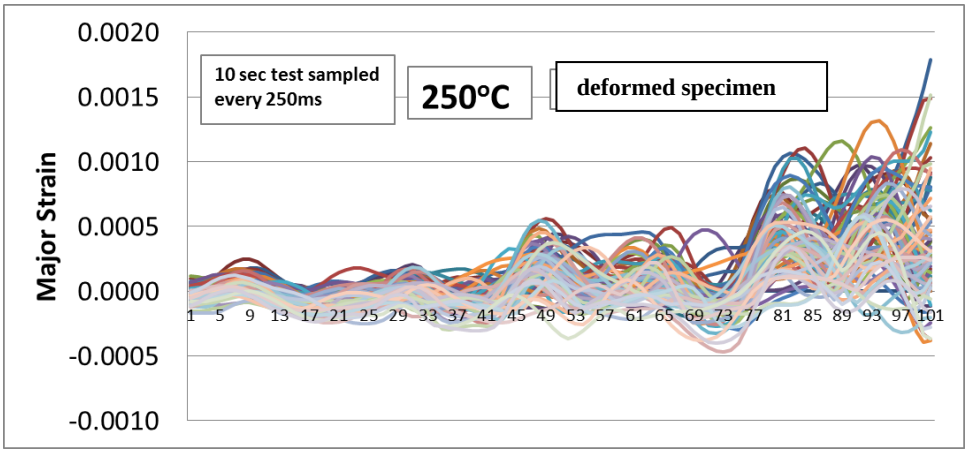

Figure 3.9: Major Strain Noise at 250°C, ZEK100 203 mm square deformed specimen.

3.2.3 Determination of Safe Limit Strain

Each strain path shown in Figure 3.5 describes the strain history from an initially un-deformed specimen to the last DIC image prior to fracture. The major and minor strain from this final image is the largest strain that the material is able to achieve prior to fracture. At this point the material has undergone severe necking and is well beyond its limit strain (the safe strain just prior to the onset of necking). The strain path of each specimen in Figure 3.5 contains strains at which the material is either un-necked or necked. In the un-necked state the material is accommodating the applied forces by gradually distributing the strains across the material compared to the necked state where strain localization has occurred, rendering the material mechanically unstable. The safe limit strain is contained within each strain path and is located at a point prior to the onset of localized necking. Several methods exist for determining the safe limit strain. Experiments conducted by Veerman et al. (1971) showed that the limit strain may be determined by examining the change in slope of a strain path (Kleemola et al., 1980a); while Marciniak et al. (1973) showed that limit strains can be determined from changes in the strain rate. Ghosh and Hecker (1974) showed that the limit strains can be identified from the strain gradient and the strain path. In the current study, safe limiting strains were determined from changes in the rate of both major and minor strain. Figure 3.10a and Figure 3.11a show histories of major and minor strain, respectively, for the point at which necking occurs in a square 203 mm (8”) blank. In Figure 3.10a and Figure 3.11a, the plots show, respectively, the major and minor strain history, of a selected point, as recorded for each DIC image (collected

every 300 ms). Figure 3.10b and Figure 3.11b show a corresponding pseudo strain rate history in which the incremental change in strain from subsequent DIC images is plotted. Since image numbers are used to show the progression the change in strain and not time, this is termed a "pseudo strain rate". Observing the pseudo strain rate made it possible to distinguish between the safe strains and the necked strains, as shown in Figure 3.10b and Figure 3.11b by observing the change in the pseudo strain rate. In Figure 3.10b, the major strain increment increases at the point of necking while in Figure 3.11b, the increment in minor strain no longer increases or becomes smaller. This method was used for all other geometries with similar observations of changes in pseudo strain rate.

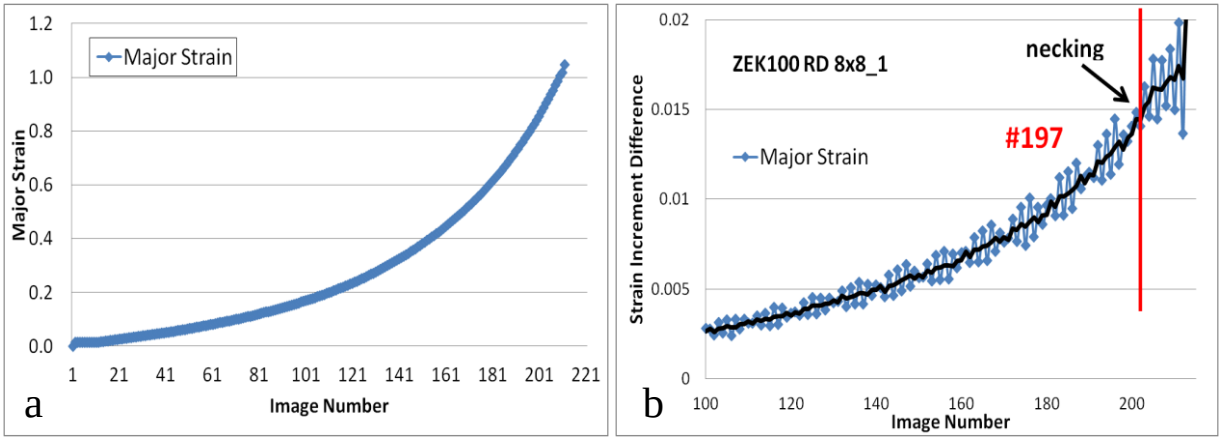

Figure 3.10: Strain Measurements for ZEK100 203x203m 200°C a) Incremental Peak Major Strain b) Difference in Incremental Peak Major Strain.

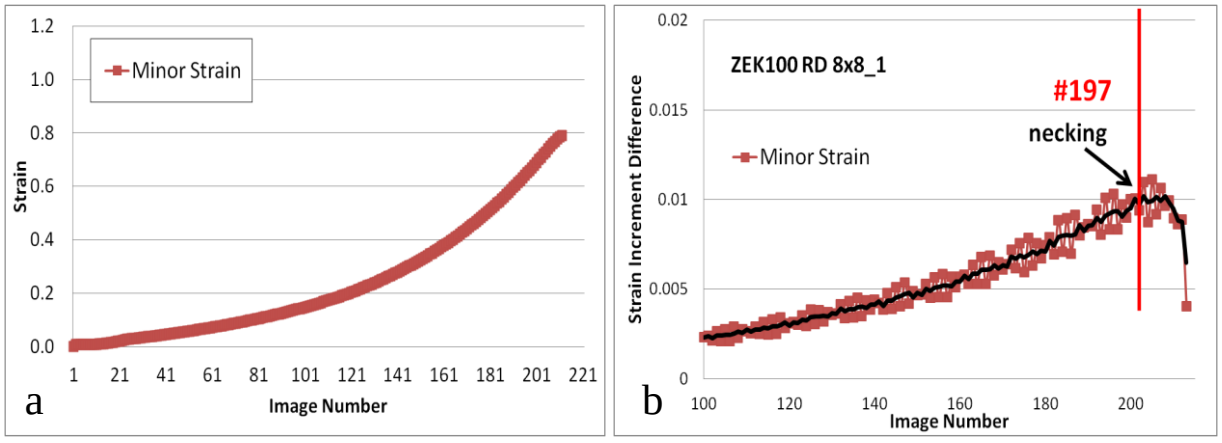

Figure 3.11: Strain Measurements for ZEK100 203x203 mm 200°C a) Incremental Peak Minor Strain b) Difference in Incremental Peak Minor Strain.

3.2.4 Edge Damage Effect on Failure Location

An edge damage effect on the 25 and 51 mm dog bone samples became apparent during testing. The damage was induced on the specimen during sample preparation in which the specimen edges were sheared into the desired geometry followed by de-burring of the cut edges, in keeping with commercial stamping practice. The process of shearing imposes severe work hardening and damage along the sheared edge as discussed by Boljanovic (2004). The effect of sheared edge damage and work hardening along the sheared edge is well established for conventional/high strength steel and aluminum alloys, resulting in lower limiting strain. (Scheib et al., 2008; Levy and Van Tyne, 2008, 2011; Pathak et al., 2013); however, this effect has not been examined for magnesium alloys to the author's knowledge. Close examination of the onset of necking within the notched samples was performed using the recorded images of the DIC analysis from which it was determined that failure initiated at the sheared edge for most if not all of the notched samples. Figure 3.12 shows an example of the failure initiation process for a notched 51 mm wide sample tested at 200°C. A sharp notch forms at the left edge of the sample in the image (Figure 3.12a) which then triggers a neck that propagates across the width of the sample (Figure 3.12b). (Note that necking in the biaxial 203 x 203 mm and plane strain 76 mm notched samples initiated within the bulk of the sheet, away from the edge.) This observation indicates that the formability within the bulk of the material away from the sheared edge may be higher than the limit strains on the draw side of the FLCs measured in the current work. On-going work (Panahi, 2013) is considering machined samples in an effort to isolate the sheared edge effect for this material.

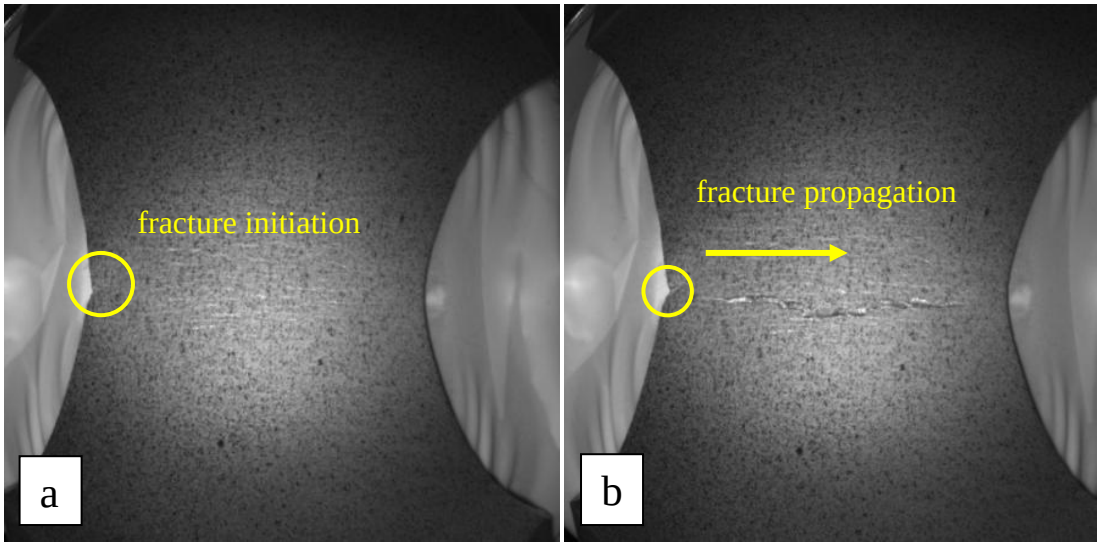

Figure 3.12: Effect of edge crack, 51 mm sample a) edge fracture initiation b) edge fracture propagation.

3.2.5 Punch Depth Experimental Scatter

Mechanical experiments introduce a factor of variability in measured results. It is important to understand the magnitude and sources of this variability to help interpret the results or to mitigate them through experimental techniques. To reduce experimental variation all specimens were cut from one batch of sheet material rolled to a nominal thickness of 1.6 mm. The effects of friction between the punch and the specimen were reduced and maintained constant by using Teflon sheet for all experiments. The Teflon acted as a consistent lubricant and also prevented material pick-up on the punch surface where, due to friction, material deposits from the specimen would accumulate on the punch surface if the punch and specimens were in direct contact. Figure 3.13 shows the scatter for three repeat experiments for each specimen geometry and temperature. Scatter is taken here as the difference between the measured punch depth and the mean punch depth for each geometry/temperature. The graph presents the results for experiments conducted at 100°C and 200°C. The results show that temperature did not have a significant effect on scatter in the results. The 203 mm square blank showed the largest scatter in maximum punch depth, however, this error may be neglected as it is +/- 0.9 mm at its largest.

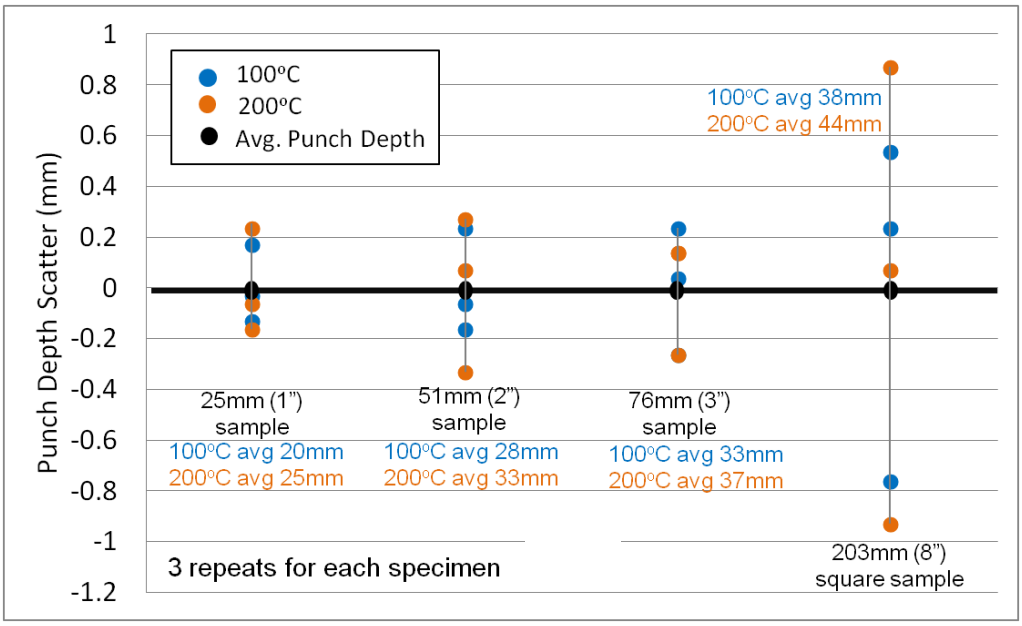

Figure 3.13: Experimental scatter for all specimen geometries at 100°C and 200°C with average punch depth at fracture shown.

3.2.6 Strain Measurement Scatter

Strain measurements were conducted with a DIC system. This system provides a consistent and objective approach to measuring strains in deformed samples. Investigations into the causes of scatter in limit strains in LDH tests have been conducted by Van Minh et al. (1974) who suggested that the variability in the forming limits is not significantly dependent on experimental error but indeed it reflects the properties of the material. Figure 3.14 shows the scatter in major and minor strain for three repeat experiments conducted at 100°C and 200°C for all specimen geometries. The measured strain had an experimental scatter of up to +/- 0.08% strain for experiments conducted at 200°C. There was less scatter, up to 0.05%, observed at 100°C. In both temperature cases, the major strain showed more scatter than the minor strain measurements and in each case is small enough to be considered negligible.

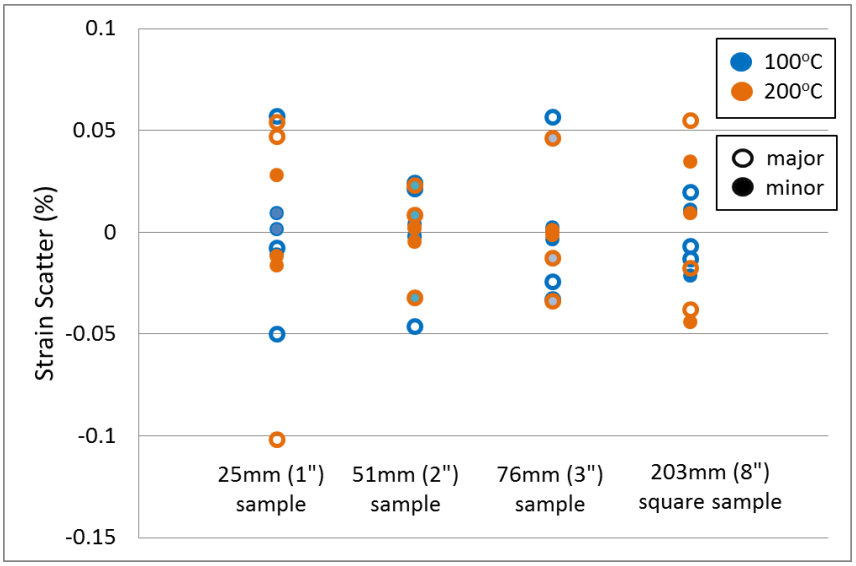

Figure 3.14: Experimental scatter in measured safe limiting strains at 100°C and 200°C.

3.3 Deep Draw Experiments

3.3.1 Strain Measurements using Chemically Etched Circle Grids

For deep draw experiments, direct observation of the specimen surface is impossible, so strain measurements were obtained using the circle grid method. Circle grids of 2.00 mm were chemically etched using a Canada Stamp 125A electrolyte and an applied AC electrical current to a gridded circle mask. The circle mask was oriented on the specimen to allow for measurements to be taken along both the rolling and transverse directions. The results of the etching may be seen in Figure 3.15. The strain was measured using a custom in-house image analysis software which determined the lengths of the major (d_2) and minor (d_1) axes of the elliptical deformed circle grids measured using the outer edge of the ellipse. The largest factor affecting accuracy of this method of strain measurements was the quality of the etched edge. Etching quality for this material was not ideal and resulted in a reliable accuracy of +/-0.01 mm which is as expected of the conventional strain circle technique and within ASTM E2218-02 standards (Ozturk et al., 2009)

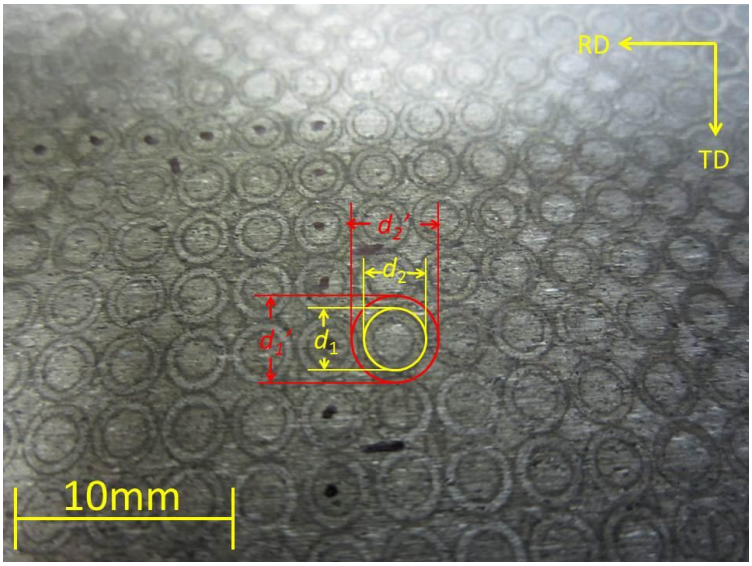

Figure 3.15: Circle gridded ZEK100 blank.

3.3.2 Temperature Distribution on Heated Blank

To observe the temperature distribution across the surface of the heated blank, a thermal camera was used to record an infrared (IR) image. The infrared thermal camera operates by measuring the amount of infrared radiation leaving the surface of the blank. This measurement is tied to material emissivity which is a measure of the ability of a surface to emit energy by radiation. The infrared thermal camera offers a good representation of relative temperatures within an image, thus making it a good tool for obtaining a good visual representation of the temperature distribution of the blank. To observe the temperature distribution, the tooling was allowed to heat up to 250°C. Once a stable temperature was reached a blank was inserted into the press followed by the closing of the blank holder and bringing the punch to just touch the blank. After the pre-determined 6 min of heating time (Figure 2.6) a thermal image was taken to record the temperature distribution across the blank, shown in Figure 3.16.

Figure 3.16a shows the blank with the cooler press frame shown as the outer circular rim in blue and the heated blank in orange/red. Figure 3.16b shows a closer view of region A, from Figure 3.16a, focusing on the center of the blank. The images show that the temperature at the central region of the blank lies in the range 251-257°C while at the outer edges of the blank the temperature reached 261°C. Independent measurements with a thermocouple indicated a temperature of 252°C at the center of the blank and 256°C at the outer edge of the blank. Both

temperature measurement methods showed a variation in blank temperature of 10°C and 4°C for the thermal camera and thermocouple methods, respectively. For each subsequent experiment a thermocouple was used to ensure the correct test temperature existed at the blank center.

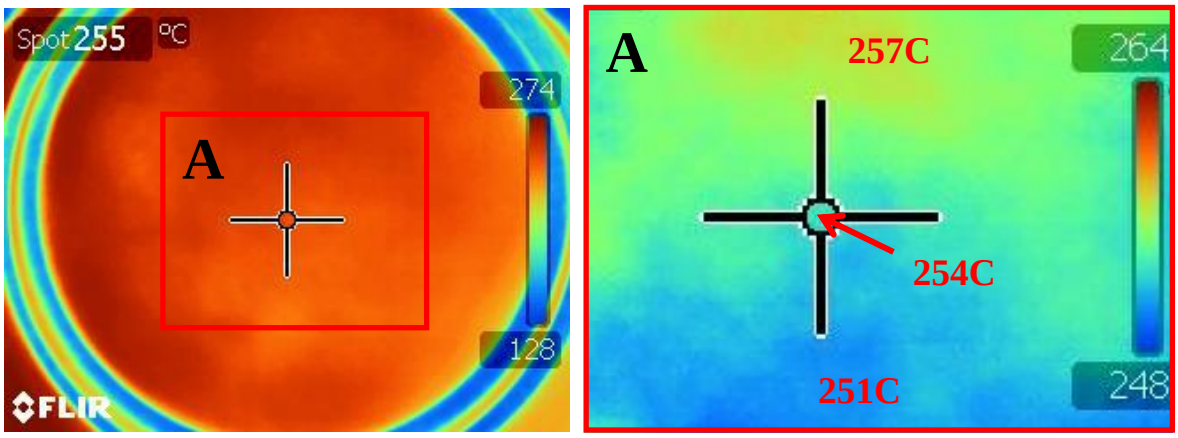

Figure 3.16: (a) Infrared image of blank with die and (b) close up of region A.

3.3.3 Thickness Profile

Cross-sectional thickness measurements from as-formed cups were taken in both the rolling and transverse directions using a digital Vernier caliper. The cups were cut into quarter sections along each axis and the edges were de-burred. Measurements were taken at 10 mm intervals starting at the center of the cup along the surface length of the cup with the interval decreasing to 5 mm near and on the radius of the specimen, as shown in Figure 3.17

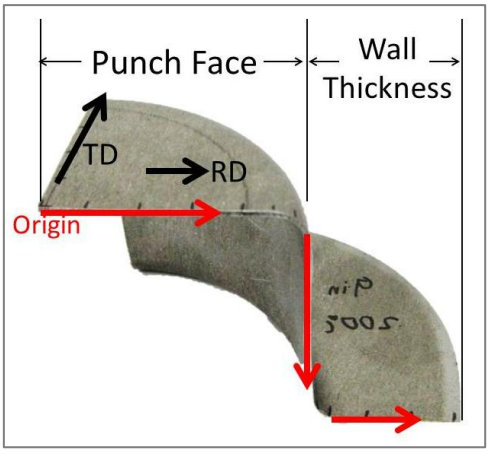

Figure 3.17: Sectioned cups for thickness measurements.

3.3.4 Earring Profile

Earring profiles were obtained for both isothermal and non-isothermal deep draw experiments. Measurements were divided into two deep drawing cases: cups achieving a full draw and cups drawn to fracture. For cases in which the cup was able to achieve a full draw, subsequent tests were interrupted at a punch depth that was 20 mm prior to a full draw depth in order to leave sufficient flange area for earring profile measurements. For cases in which the cup fractured, subsequent tests were interrupted at a punch depth that was 3 mm prior to the fracture depth. The result of forming with these criteria was a set of test specimens comprising a flange section with visible earring that was subsequently used to obtain earring profile measurements.

Measurements of earring profiles were obtained by creating a high-contrast photographic image of the formed blank coloured in white against a black background, as shown in Figure 3.18a. This high-contrast image was then processed through image processing software which binarized the image (Fiji: http://fiji.sc/wiki/index.php/Fiji), creating an image file containing only white and black pixels (Figure 3.18b). The software extracted the edge between the black background and white specimen. This resulted in an image of an extracted line representing the edge of the specimen showing the earring of the formed blank as seen in the example of an earring profile image of Figure 3.18c. Following this, the image was processed by another program (getpixels.exe) that determined the distance from the blank center to the earring line in the image starting from 0°, pointing to the rolling direction to the right (Figure 3.18c) and moving counter-clockwise to complete the profile from 0° to 360°.

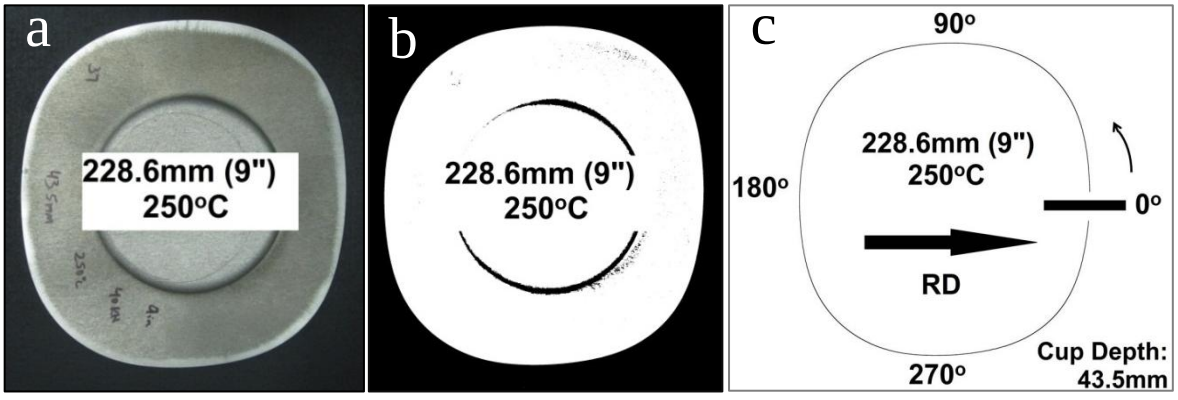

Figure 3.18: a) top view image of specimen b) binary image c) processed image of edge of specimen.

To quantify earring, the average distance from the center of the blank to the blank edge is first calculated as an "average radius". This average radius is then subtracted from the measured radial distances around the blank periphery to obtain a relative measure of the amount of earring in the blank, as shown in Figure 3.19

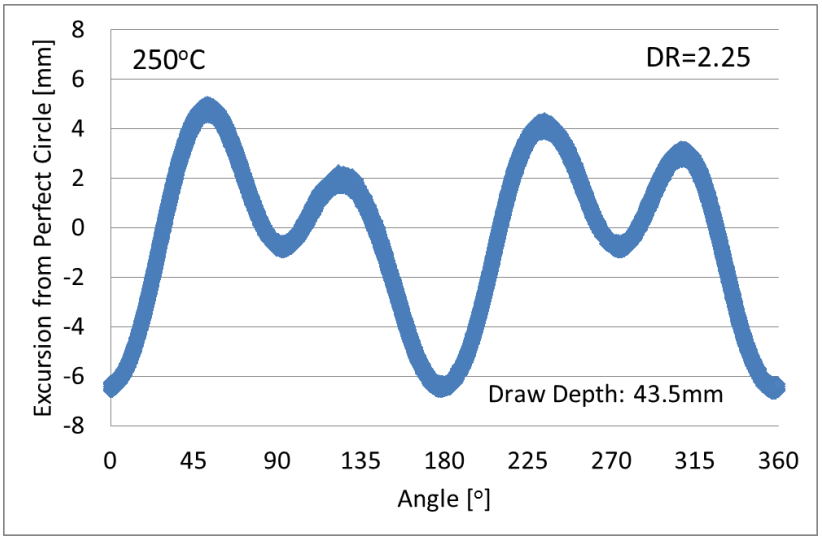

Figure 3.19: Example of deep drawn cup earring profile.

3.3.5 Deep Drawing Experimental Scatter

Each condition was repeated at least twice while some conditions were repeated 3 or 4 times depending on the need of formed or fractured samples for measurements where cutting of drawn blanks was required. Repetition of tests was done to determine the consistency of results and scatter due to material and experimental variability. Figure 3.20 and Figure 3.21 show the scatter in the load-displacement response for blanks with DR = 2.25 drawn at 200 and 250°C, respectively. At 200°C a cup was drawn to fracture at 57 mm and the three subsequent cups were interrupted 3 mm prior to fracture. The punch loads for all four tests were within 0.75 kN of each other. At 250°C, the cups that were drawn to fracture all failed at 45.5mm +/- 1 mm punch depth with a difference of 2 kN in punch load.

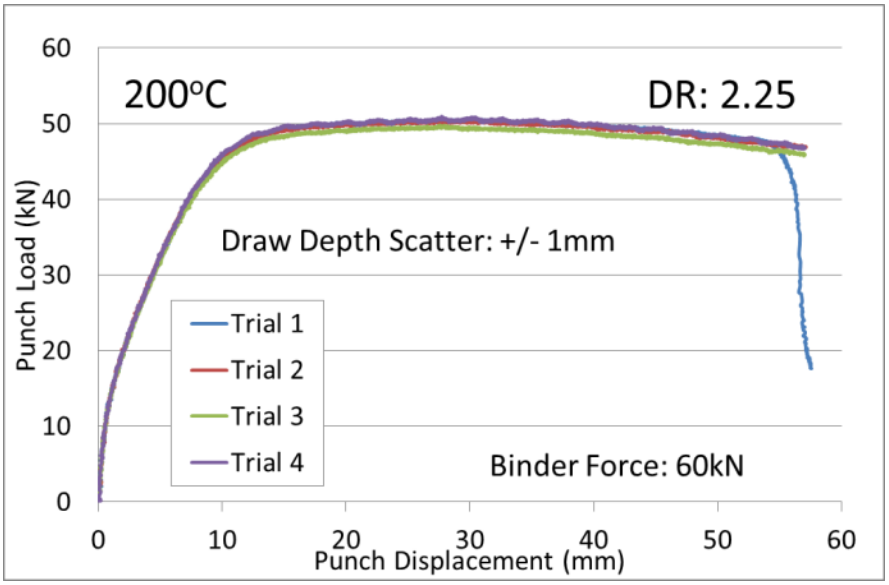

Figure 3.20: Scatter plot: DR = 2.25, drawn at 200°C.

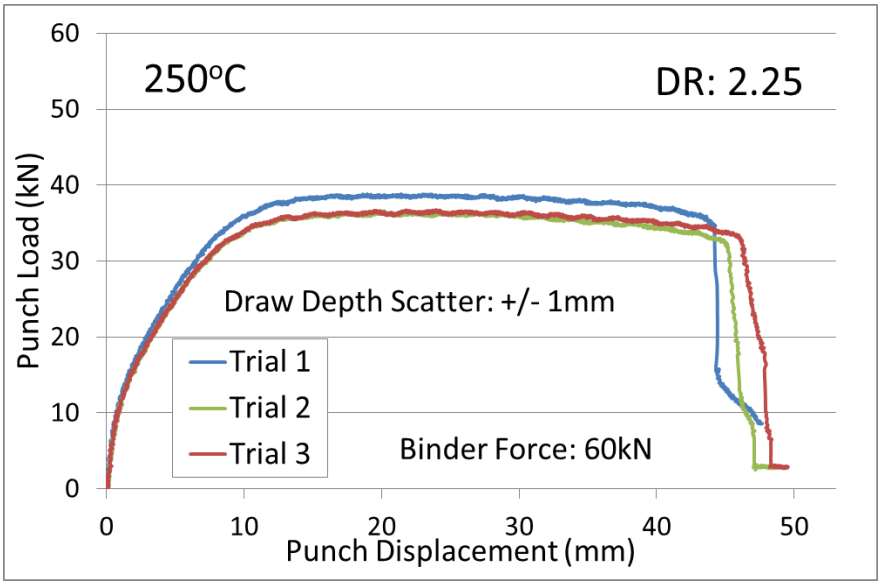

Figure 3.21: Scatter plot: DR = 2.25, drawn at 250°C.

4 FORMABILITY RESULTS

Experimental results for the Limiting Dome Height tests are presented in this chapter. Dome heights at fracture for ZEK100 and AZ31B (O and H24 temper) at elevated temperatures are presented in the first section since these experiments were conducted and processed independently from the experiments used to develop the forming limit curves (FLCs), which are presented in the latter portion of this chapter. FLC results were obtained for isothermal conditions from room temperature to 350°C in both the rolling and transverse direction.

4.1 Measured Limiting Dome Heights

ZEK100 exhibits significantly higher room temperature formability relative to AZ31B-O and AZ31B-H24, as seen in Figure 4.1 in which samples were stretched until failure. The increase is most likely attributed to the grain refinement brought on by the addition of Zr (Bohlen et al., 2007) and the weakened texture resulting from the rare-earth addition of Nd. As temperature increases, the dome heights for all three alloys increase, as can be seen in Figure 4.1 - 4.4. This increase is attributed to the enhanced slip activity available at elevated temperature.

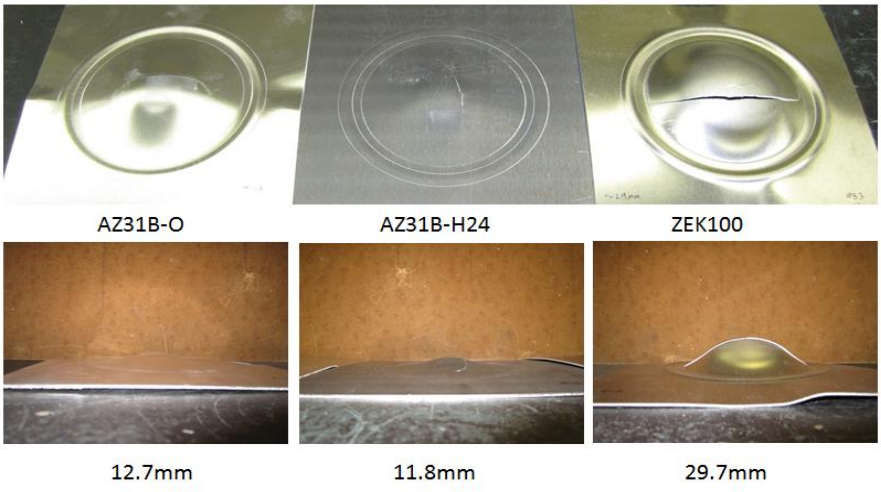

Figure 4.1: Room temperature LDH at fracture.

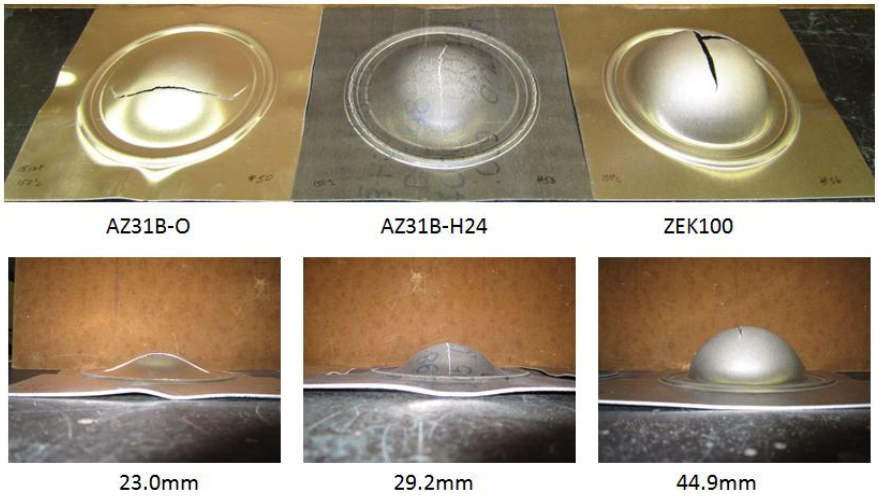

Figure 4.2: 150°C LDH at fracture.

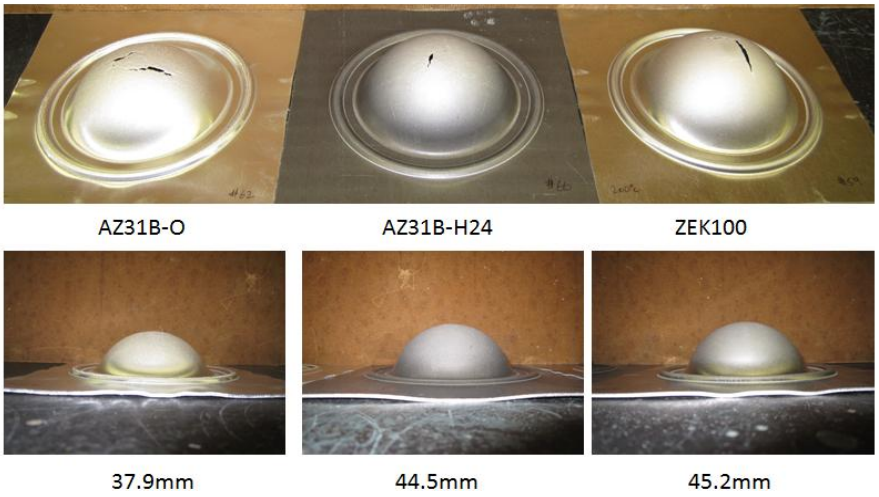

Figure 4.3: 200°C LDH at fracture.

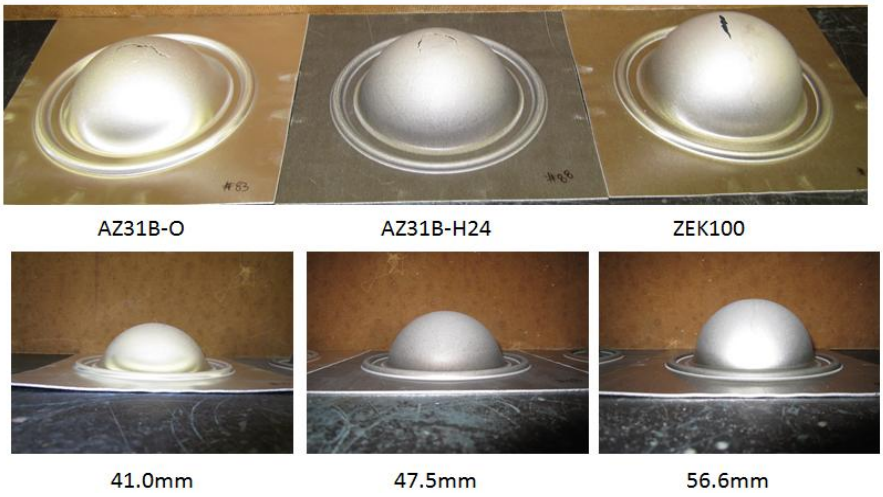

Figure 4.4: 300°C LDH at fracture.

4.1.1 Punch Force vs. Displacement for ZEK100 vs. AZ31B-O

Figure 4.5 shows the measured load-displacement response for ZEK100 and AZ31B-O for each temperature. As expected, the load levels drop with temperature for both alloys. The AZ31B shows a much lower dome height at room temperature; however the difference in the dome height between the ZEK100 and AZ31B sheets is reduced at higher temperatures. A full set of punch force vs. punch displacement graphs for individual temperature conditions is available in Appendix B. The oscillation of the load data is attributed to noise within the load cell and the data acquisition system, as well as the rather low measured load range, which is less than 8% of the press force capacity.

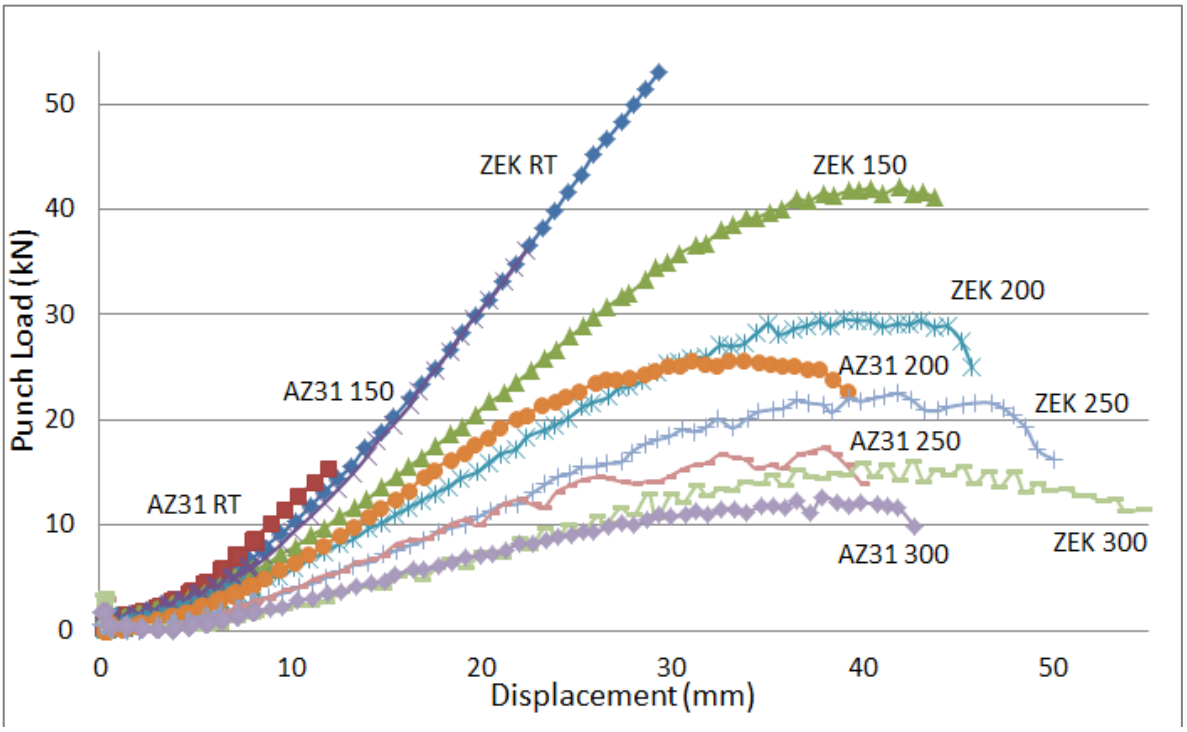

Figure 4.5: Load vs. displacement for dome height experiments ZEK100 vs. AZ31B (200 mm x 200 mm blanks).

Direct comparisons were conducted between ZEK100 and AZ31B for narrower, notched blanks at room temperature, 200, and 250°C. Figure 4.6 shows the comparison of the two materials in terms of the punch load vs. punch displacement for experiments on the 76.2 mm (3") specimens. This graph shows that ZEK100 exhibited higher elongation at room temperature, whereas above 200°C both materials attained a similar punch depth.

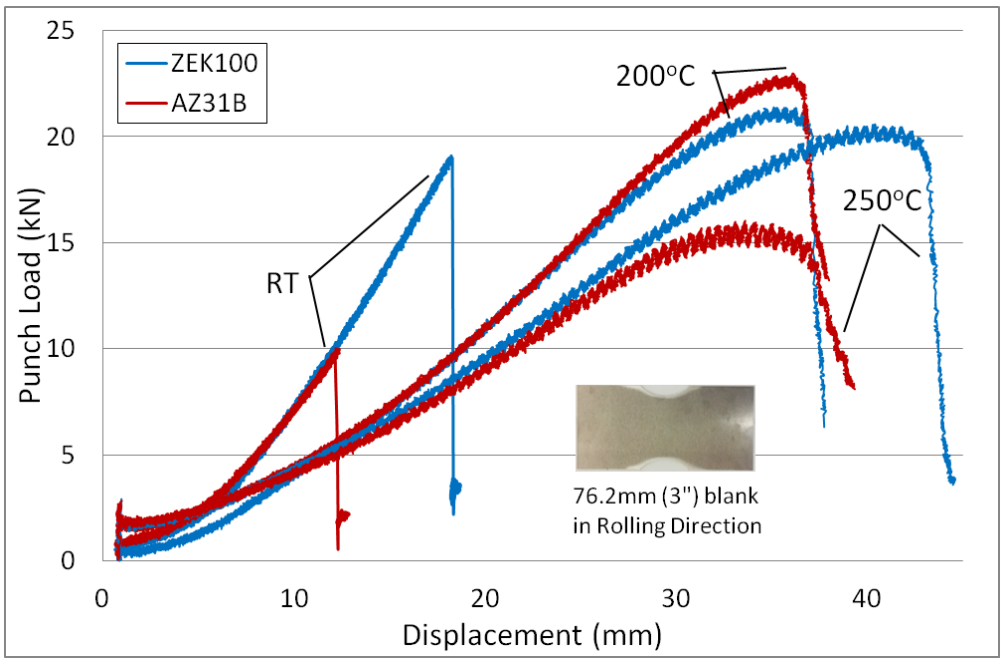

Figure 4.6: Punch Load vs. Punch Displacement plot comparing ZEK100 and AZ31B at RT, 200, and 250°C.

4.1.2 Comparison of LDH up to Necking for ZEK100 vs. AZ31B-O

Limiting Dome Heights for 203 mm (8") square samples were measured for AZ32B (O and H24 tempers) and ZEK100. It was observed that at room temperature, AZ31B-O and AZ31B-H24 exhibited very little necking and simply fractured, while ZEK100 displayed necking prior to fracture. Shown in Figure 4.7, the achievable maximum dome height for ZEK100 is higher than for AZ31B-O and AZ31B-H24 throughout the temperature range between room temperature and 300°C. At room temperature ZEK100 reaches a dome height of 29 mm at the onset of necking, whereas AZ31B-O and AZ31B-H24 reach 12 mm at the onset of necking. At 150°C ZEK100 continues to have a significantly higher dome height at necking of 37 mm in comparison to 22 and 29 mm for AZ31B-O and AZ31B-H24, respectively. As temperature is increased to 200°C and to 300°C, the maximum dome height appears to saturate. The relative ranking of the three alloys remains the same, with the necking limit of ZEK100 reaching a saturation value of 40 mm for temperatures of 200°C and above. AZ31B-O and AZ31B-H24 achieve similar necking dome height values: 34 mm and 36 mm for AZ31B-O at 200°C and 250°C, respectively, while AZ31B-H24 reaches a necking dome height of 38 mm and 40 mm

at 200°C and 250°C, respectively. At 300°C, the ZEK100 formability increases slightly to 41 mm at necking.

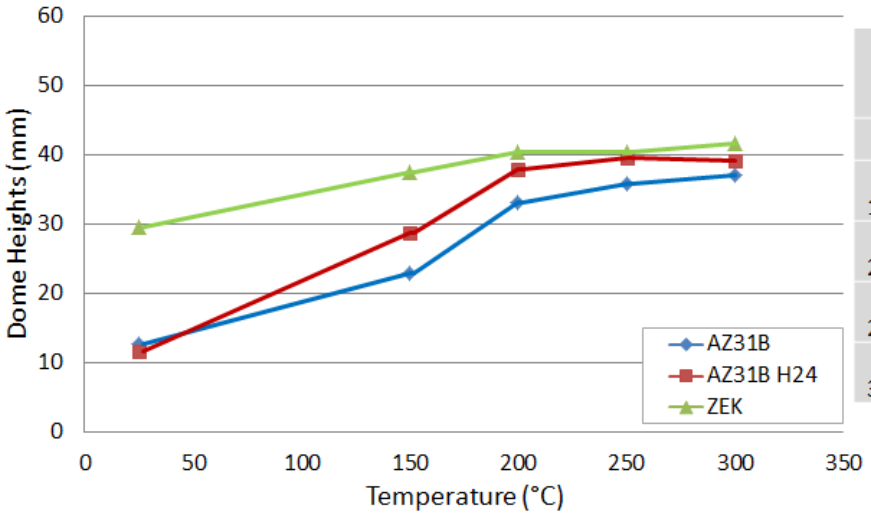

	AZ31B (mm)	AZ31B H24 (mm)	ZEK (mm)
25°C	12.6	11.6	29.47
150°C	22.8	28.8	37.43
200°C	33.17	37.93	40.43
250°C	35.8	39.63	40.43
300°C	36.97	39.07	41.56

Figure 4.7: LDH results at necking, 203 mm square blank, 1.6 mm sheet with Teflon.

ZEK100 has shown significant anisotropy between the rolling and transverse sheet direction (Kurukuri et al., 2013b). To investigate this phenomenon, 76.2 mm (3") samples were cut with the major strain axis oriented along the sheet rolling and transverse directions. Figure 4.8 shows the punch load vs. displacement for experiments conducted with the 76.2 mm (3") specimens at room temperature, 100°C, 200°C and 300°C. The lower temperature samples exhibit a more brittle response with sudden unloading at failure, whereas the elevated temperature samples exhibit a more gradual necking and unloading. In each case the transverse direction attained a larger punch displacement compared to specimens cut in the rolling direction and required a lower punch force. This behaviour is consistent with observations by Kurukuri et al. (2013a) who found that RD tensile samples exhibit higher strength with less work hardening and elongation compared to the transverse direction.

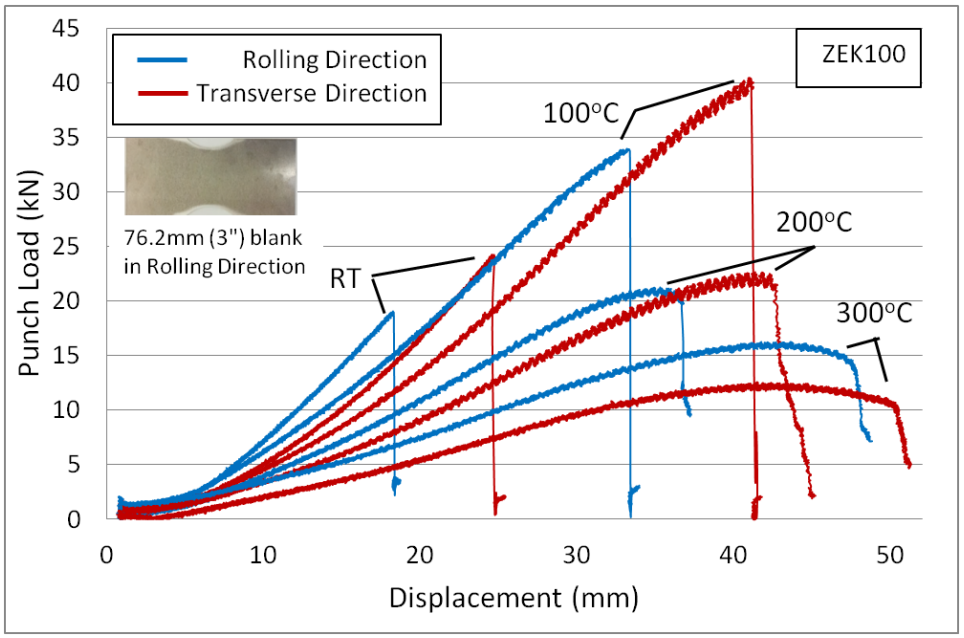

Figure 4.8: Punch load vs. punch displacement curves for rolling and transverse direction of 76 mm (3") specimen.

4.1.3 Discussion

The formability of ZEK100 has been shown to be superior to that of AZ31B as a result of weakened texture compared to AZ31B. At room temperature, ZEK100 shows the greatest improvement in formability by a factor of 2.3 on dome height compared to AZ31B. At 150°C ZEK100 maintains better formability by a factor of 1.6 compared to AZ31B. As the temperature is further increased above 200°C, the difference in formability between the alloys is reduced, with ZEK100 exhibiting dome heights that are 10% higher than that of AZ31B.

The high temperature behaviour of all three sheet materials/tempers is believed to be influenced by dynamic recrystallization as well. The data, taken together, points to the fact that slip mechanisms dominate during limiting dome height testing, with weakened texture favoring higher dome height in ZEK100 sheets at low temperature and increased slip activity at elevated temperature in all samples resulting in nearly identical home height values.

4.2 Measured Forming Limit Curves

4.2.1 ZEK100 Forming Limit Strains

The forming limit diagram for all of the ZEK100 RD and TD experiments is shown in Figures 4.9 and 4.10. The forming limit curve for each temperature has been drawn through the mid-point of the "safe" strains for each test condition. An alternative approach to constructing the FLC is to draw the "safe" line through the lowest measured safe strain; however, the scatter bands are drawn through the corresponding range in measured major strain for each condition from which this alternate FLC can be constructed. The forming limit data reveals a very strong dependence upon temperature, as expected. The performance of the ZEK100 under warm forming conditions is considered to be quite good. At 300°C, which corresponds to the upper end of conventional warm forming temperatures, the lowest major strain occurs near the plane strain condition (referred to herein as the near-FLC_0 strain) and exceeds 0.7. At a relatively low temperature for warm forming at 100°C, the near-FLC_0 strain is just below 0.4. This value compares well to the room temperature plane strain formability limit of AA2024 (26% strain for 1.25 mm sheet at FLC_0) as reported by Hijazi et al. (2004) and that of drawing quality steel (35% strain at FLC_0) as reported by Fracz and Stachowicz (2012).

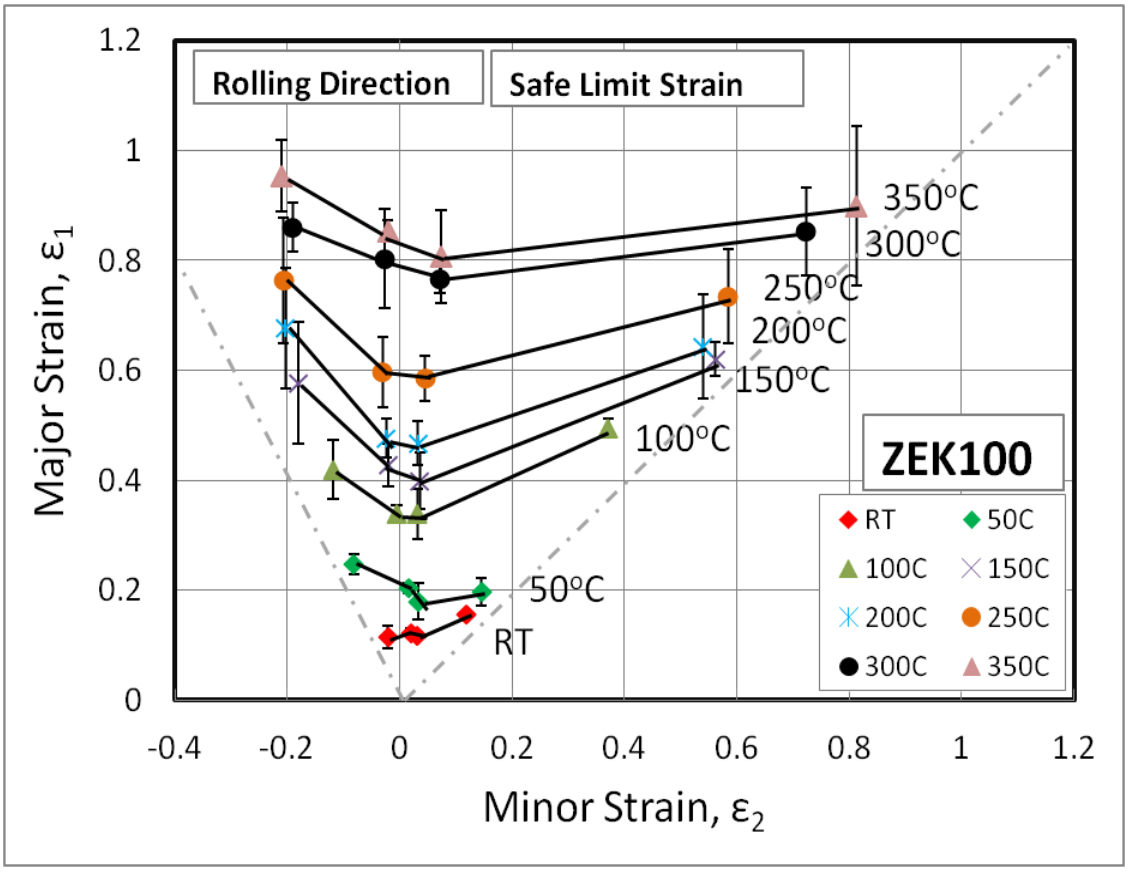

Figure 4.9: FLD for ZEK100 in RD at RT, 50, 100, 150, 200, 250, 300, and 350°C. The symbols correspond to the median measured safe strain for each condition, while the scatter bands indicate the range in measured safe major strain from the repeat experiments (in most cases three repeats, see Table 2.2).

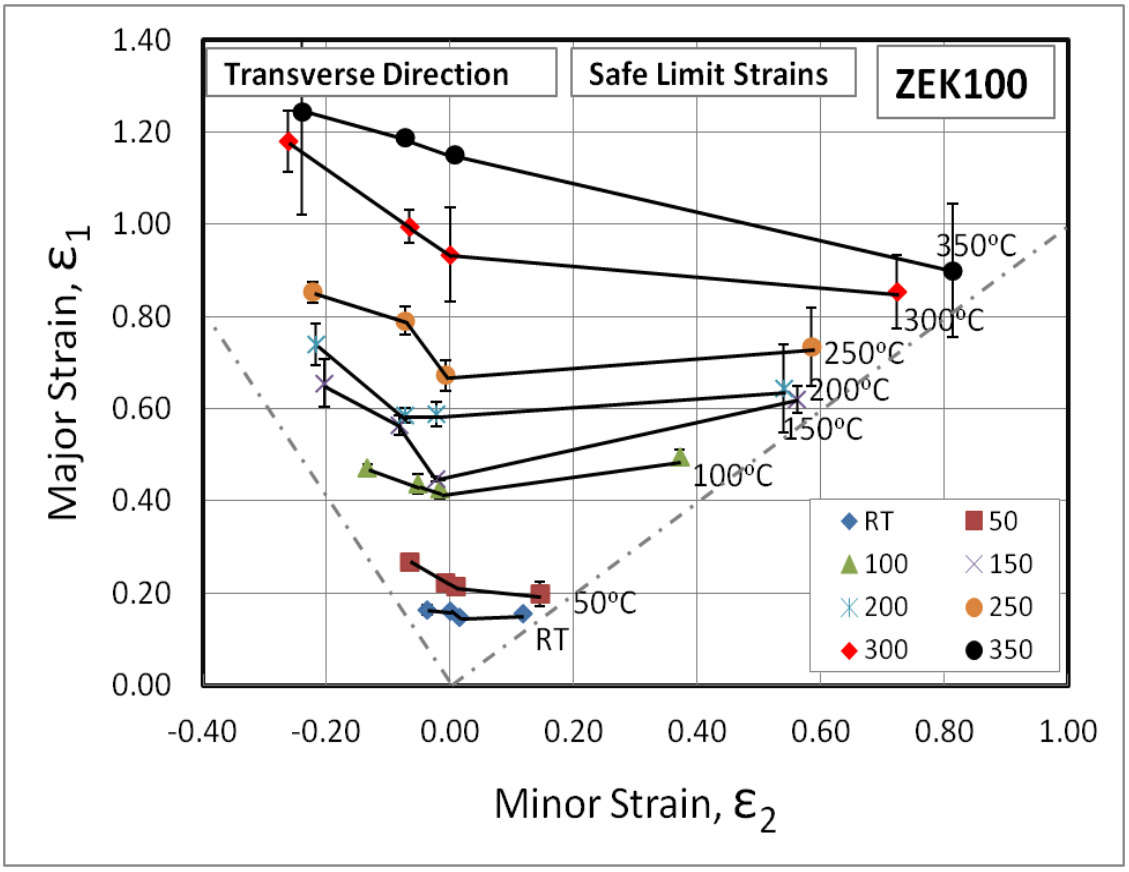

Figure 4.10: FLD for ZEK100 in TD at RT, 50, 100, 150, 200, 250, 300, and 350°C. The symbols correspond to the median measured safe strain for each condition, while the scatter bands indicate the range in measured safe major strain from the repeat experiments (in most cases three repeats, see Table 2.2).

4.2.2 Rolling vs. Transverse Direction

The effect of specimen orientation for the ZEK100 alloy is shown in Figure 4.11. FLCs are plotted for both the RD and TD oriented samples at RT, 100, 200 and 300°C. A full list for all tested temperatures is available in Appendix K. The material exhibits a significant level of anisotropy in the measured forming limit response, with the RD FLCs lying below the corresponding TD data for all cases. This trend is consistent with the measured LDH data (Figure 4.8) in which the TD 76 mm width samples exhibited the highest dome heights. As discussed in Section 1.3.2, Kurukuri et al. (2013a) have shown that TD uniaxial tensile samples exhibit lower yield strength, higher work hardening rates and greater ductility, all of which is consistent with the higher formability observed in the current formability data. The TD (versus RD) mechanical behaviour reported by Kurukuri et al. (2013a) and the enhanced TD

formability in the current FLC data can also be attributed to the greater spreading of the basal texture seen in Figure 1.9a.

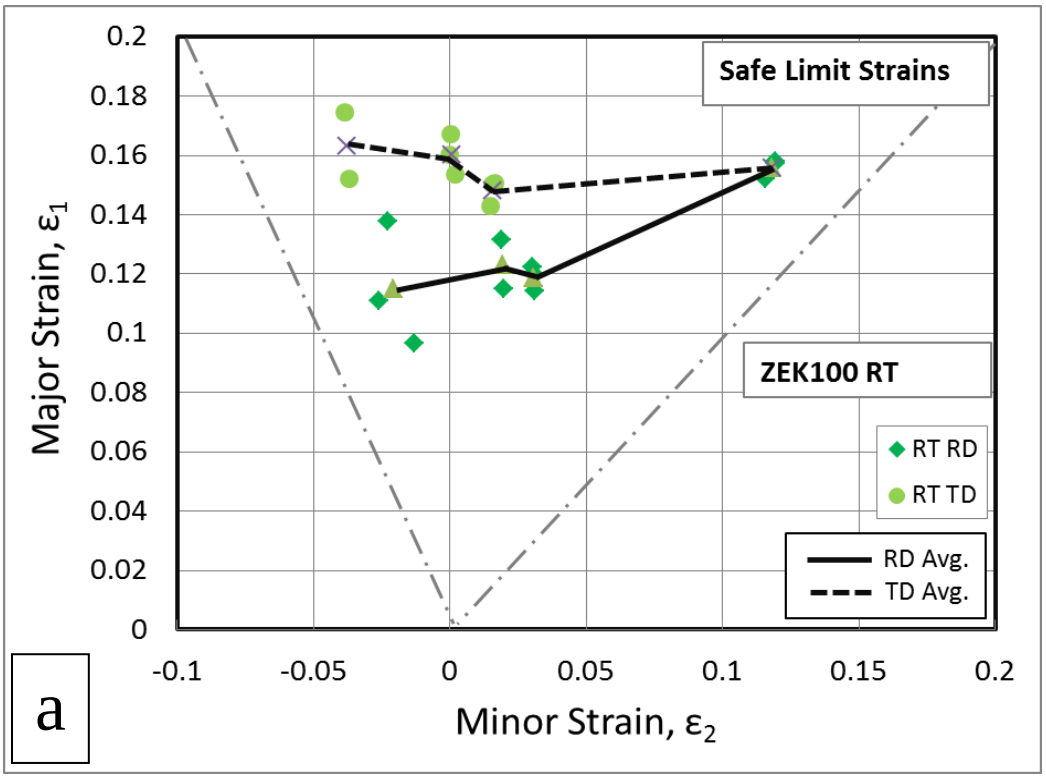

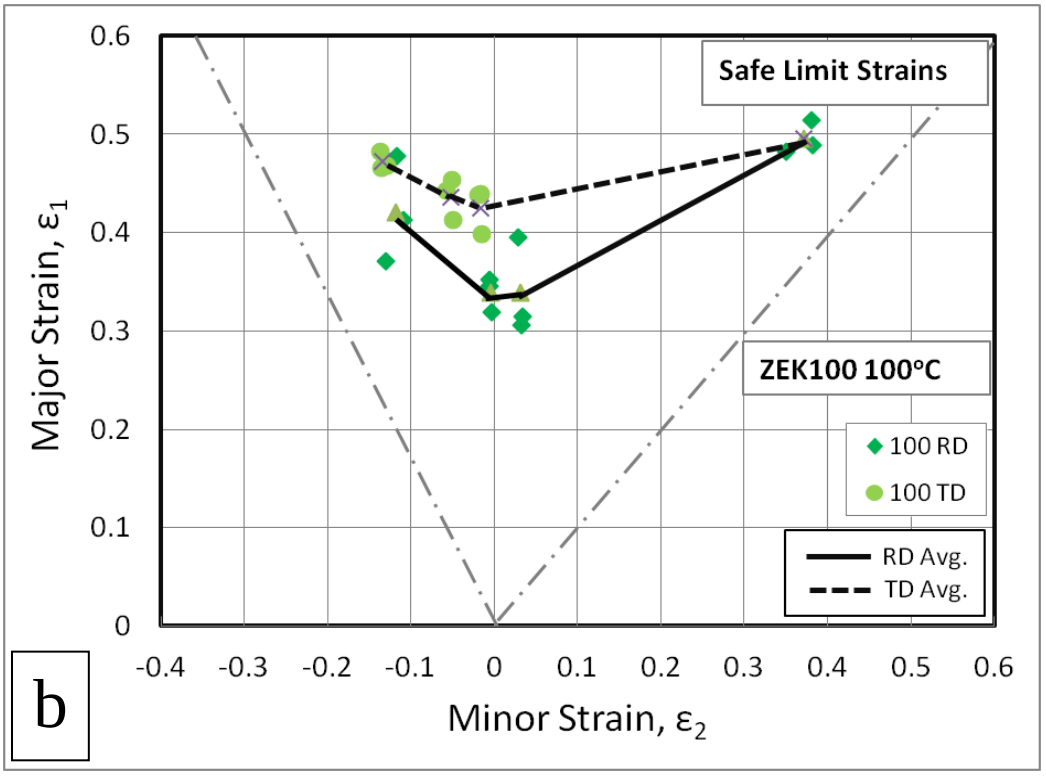

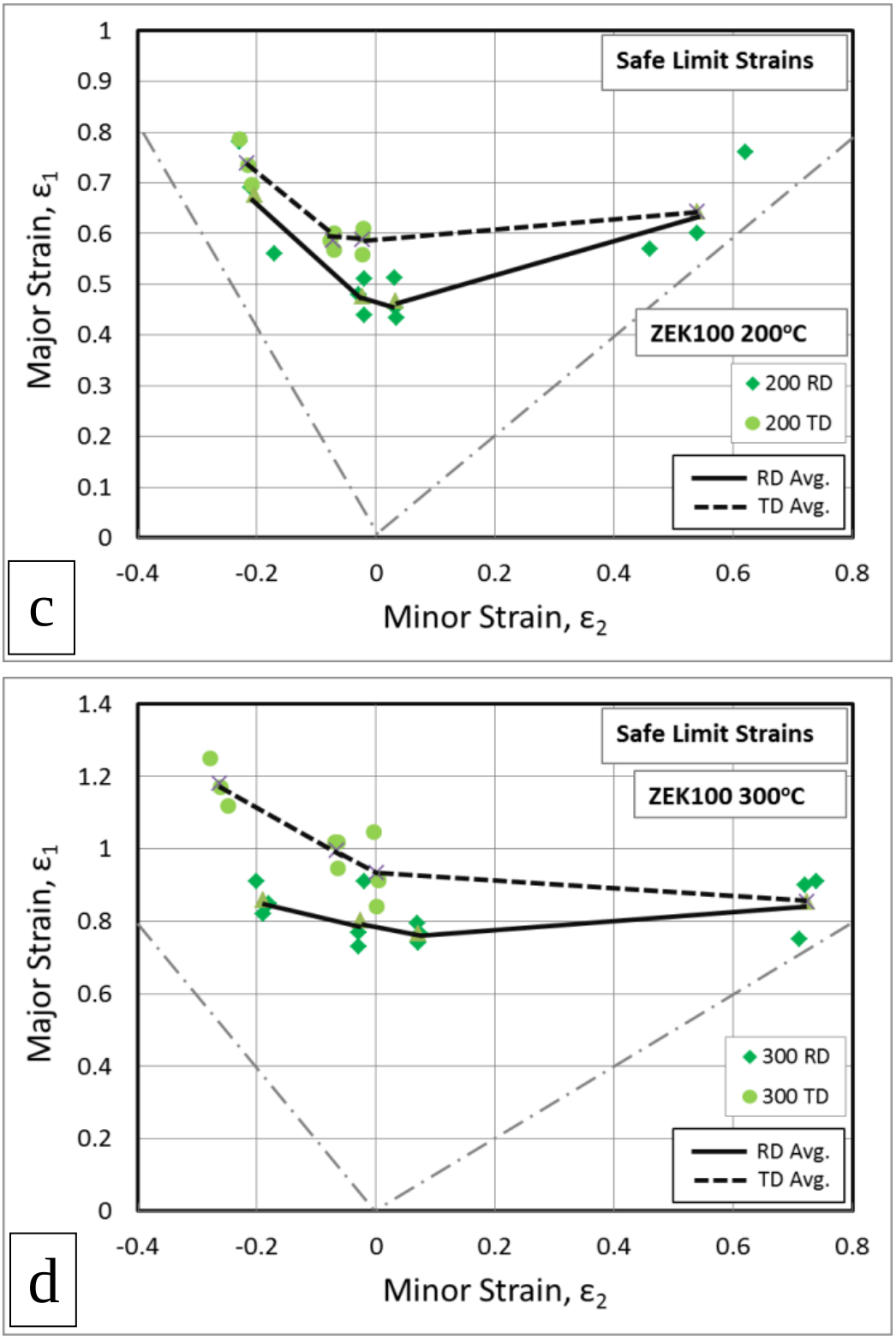

Figure 4.11: RD *versus* TD forming limit curves at a) room temperature, b) 100°C, c) 200°C and d) 300°C.

4.2.3 FLD Comparison: ZEK100 vs. AZ31B

Figure 4.12 serves to compare the forming limits of ZEK100 and AZ31B. The results show a higher FLC for ZEK100 at all tested temperatures compared to AZ31B. At 200°C both materials fail at similar punch depths of 36 mm as seen in Figure 4.6, whereas in the FLD in Figure 4.12, ZEK100 achieves a safe major strain at near-FLC_0 of 0.46 while AZ31 achieves a safe major strain of 0.32. What may be interpreted from this case is that AZ31B begins necking earlier than ZEK100. The earlier onset of necking in AZ31B is then further magnified at the higher temperature of 250°C, where ZEK100 attains a safe limiting major strain at near-FLC_0 of 0.58, while AZ31B attains a safe limiting strain of 0.39. This may be attributed to the higher number of available slip systems in ZEK100 brought on by its more random texture compared to AZ31B. This would allow ZEK100 to accommodate higher strains prior to the onset of localized necking of the material.

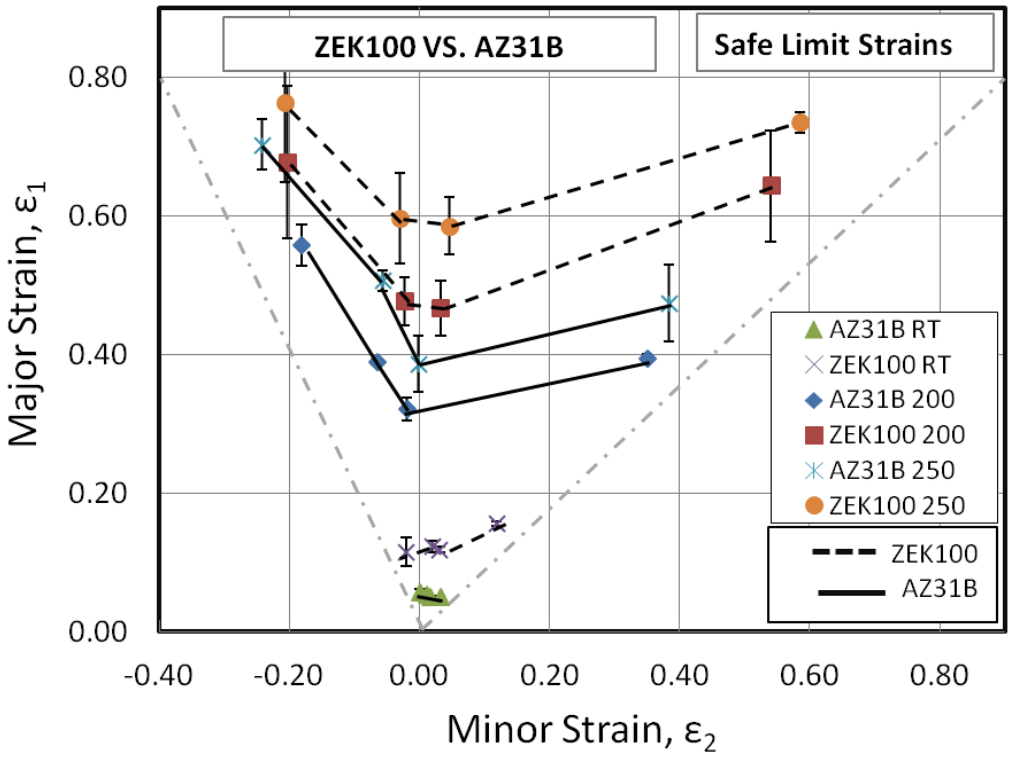

Figure 4.12: FLD comparing ZEK100 (RD) and AZ31B (RD) at RT, 200, and 250°C.

The enhanced formability of ZEK100 versus AZ31B is further examined in Figure 4.13 which shows the near-FLC_0 as a function of temperature for all conditions tested. At elevated

temperatures (200-250°C), the ZEK100 RD samples exhibited a near-FLC_0 that was on average 49% higher than the corresponding AZ31B value. Interestingly, the near-FLC_0 strain for ZEK100 (RD) at 150°C (0.40) is roughly equal to the near-FLC_0 strain for AZ31B at 250°C (0.39).

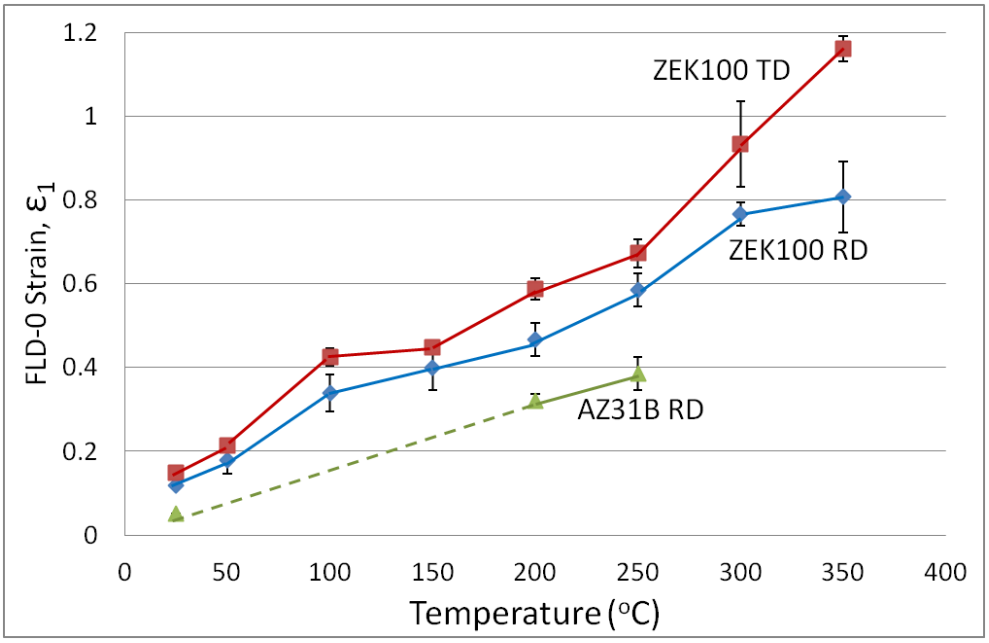

Figure 4.13: FLC_0 vs. temperature, comparing ZEK100 (RD, TD) and AZ31B (RD).

4.2.4 Low to Warm Temperature Comparison ZEK100 vs. AZ31B

A striking feature of the ZEK100 sheet examined in this work is the rather good formability at temperatures of 100 - 200°C which is below the commonly used temperature (>200°C) range needed for warm forming of magnesium alloy sheet. In contrast, AZ31B does not begin to exhibit good formability until temperatures of 200°C are reached. The behaviour of these alloys in this "lukewarm" temperature regime below 200°C can be examined by considering Figure 4.14 which shows forming limit curves for temperatures up to 150°C from the current work and from other studies of AZ31B by Kim et al. (2008) and Khosravani and Scott (2013). Direct comparison with the current work and the other studies is confounded by differences in punch speed and material thickness, for example, Kim et al. (2008) considered 0.5 mm material, but a much slower punch speed of 0.1 mm/s, whereas Khosravani and Scott (2013) studied a somewhat higher thickness (2.0 mm) and used lower punch speeds (0.3-0.6 mm/s).

The work by Khosravani and Scott (2013) considered forming temperatures between 50 and 125°C and resulted in rather low formability limits compared to the current work. It is important to note that Khosravani and Scott (2013) used LDH tests for the biaxial limit strains and uniaxial tensile tests to construct the left side of the FLC. Kim et al. (2008) conducted LDH tests for all points of the FLC in the same manner as the current work, but used grid deformation for strain measurements, whereas the current worked used DIC measurements. These changes in test methods and strain measurements may result in differing limit strains. In addition, a lower punch speed results in higher limiting strains, for example, thereby having an increasing effect on the overall FLC at elevated temperature, as reported by Naka et al. (2001) for aluminum-magnesium alloys. Despite these differences in test methodology, the study by Khosravani and Scott (2013) serves to demonstrate the rather poor low temperature ductility of AZ31B which is consistent with the current results.

More importantly, the current work has determined that a significant forming process window exists for ZEK100 in the 100-200°C temperature regime. This lower temperature process window is important because it reduces blank and tooling pre-heat temperature requirements and also greatly increases the range of lubricants that can be used for warm forming of this alloy.

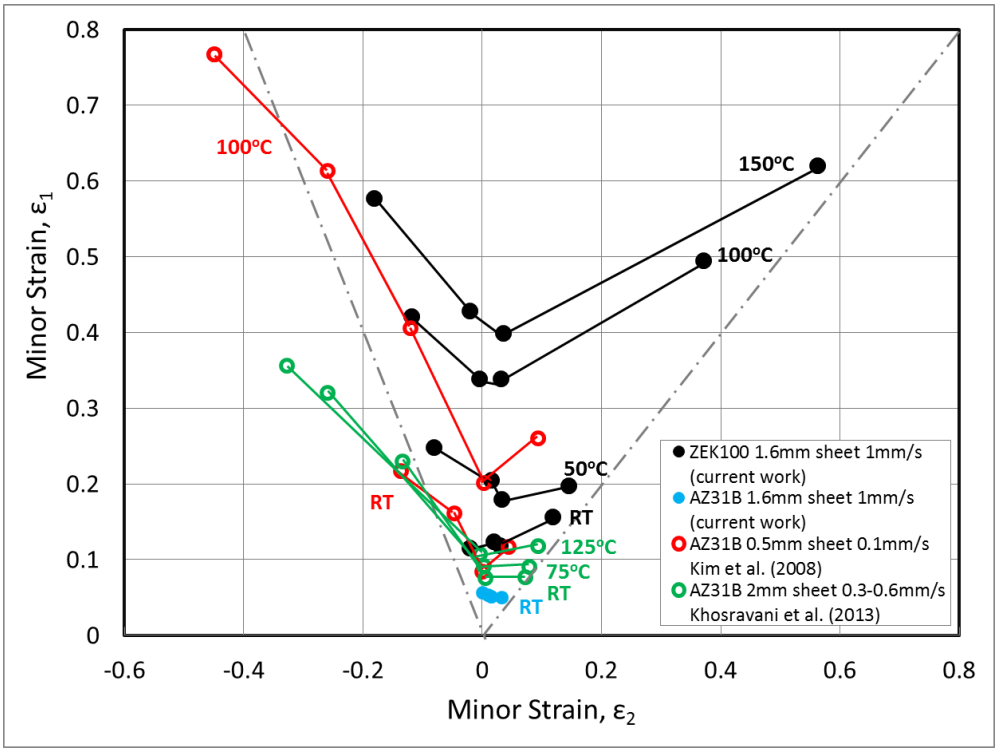

Figure 4.14: Low/warm temperature FLD comparing ZEK100 and AZ31B at RT, 100, and 150°C.

Much of the formability gains exhibited by ZEK100 relative to AZ31B is hypothesized to be attributed to the reduced basal texture intensity, spreading of the basal axes along the TD direction (Figure 1.9), and a relatively small grain size. Bohlen et al. (2006) have attributed such texture softening in ZE10 sheet, which is similar to the current ZEK100, to rare-earth additions. The resulting spreading of the basal texture away from the sheet normal direction (Figure 1.9a) increases the availability of basal (easy) slip systems promoting enhanced low temperature formability. As temperature increases, non-basal slip becomes active for both alloys tested; however, ZEK100 maintains superior formability relative to AZ31B. The ZEK100 does exhibit a high degree of anisotropy in terms of the measured LDH and formability for TD- and RD- oriented samples. This effect is again attributed to the anisotropy seen in the initial texture (Figure 1.9a) in which a higher degree of spreading of the c-axis tilt is observed for the TD versus the RD, making for easier slip along the TD. Kurukuri et al. (2013a) have shown that this results in lower initial yield strength, higher hardening rate and higher ductility along the TD, all of which are conducive to higher formability as seen in this work.

5 DRAWABILITY RESULTS

The deep draw experiments are presented and discussed using metrics including: earring behaviour (anisotropy), strain and material thickness profiles, and drawability. The effects of isothermal and non-isothermal temperature conditions were investigated for each of the preceding metrics. Finally, a process window is developed showing the temperature conditions for successful drawing of ZEK100 and is compared to that of AZ31B.

5.1 Isothermal Deep Drawing

Blanks were drawn under isothermal conditions in which the die, blank holder and punch were heated to uniform temperatures of 100, 150, 200, and 250°C. The load-displacement response for drawing blanks with a draw ratio (DR) equal to 2.00 and 2.25 are shown in Figure 5.1 and Figure 5.2, respectively. The smaller draw ratio (2.00) exhibited better drawability than the larger draw ratio (2.25). With DR = 2.00, cups were drawn to a full depth of 80 mm for all tested temperatures except for 100°C. The blanks with DR = 2.25 (Figure 5.2), however, resulted in fractures for all temperature conditions, with cup depths of 24.8, 45, 57 and 45.5 mm at temperatures of 100, 150, 200, and 250°C, respectively. All cups fractured at the punch tip as seen in Figure 5.3. Increasing the temperature beyond 200°C resulted in a lower cup depth. This is thought to be due to excessive softening of the material at the punch tip. A complete set of data for all isothermal tests and draw ratios conducted for this thesis is available in Appendix C.

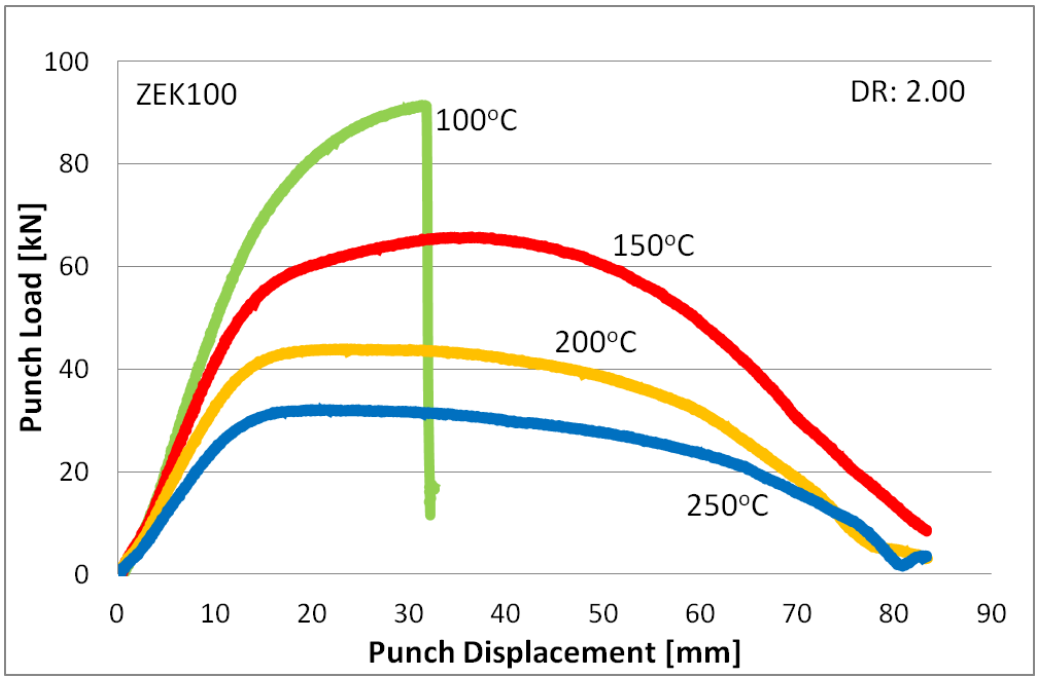

Figure 5.1: Isothermal draw of DR = 2.00, Binder Force: 60 kN.

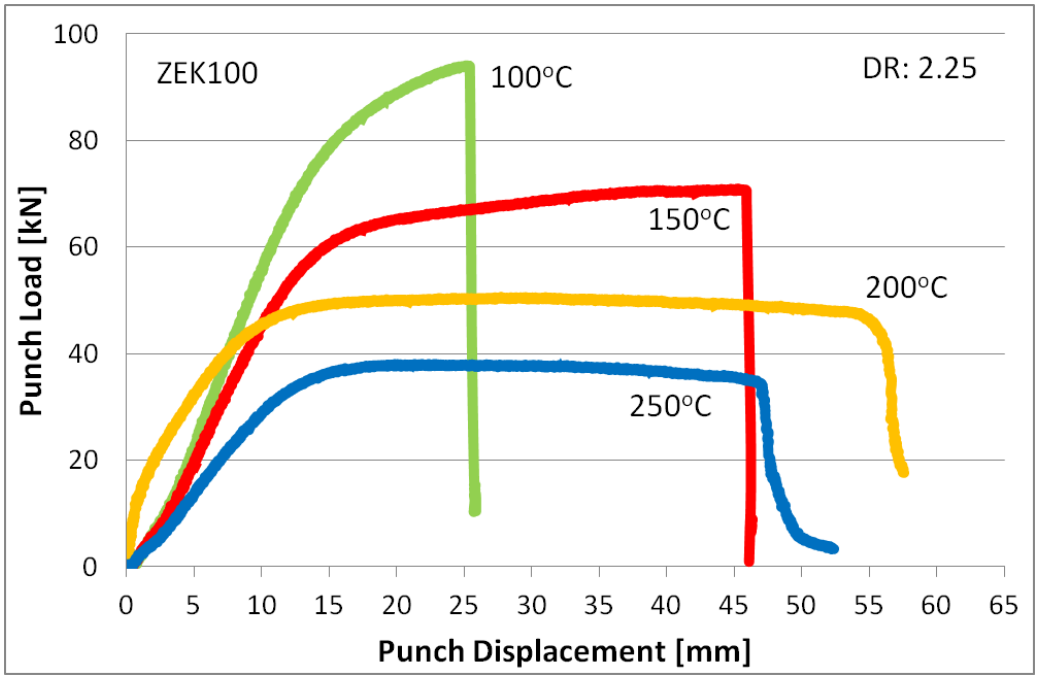

Figure 5.2: Isothermal draw of DR = 2.25, Binder Force: 60 kN.

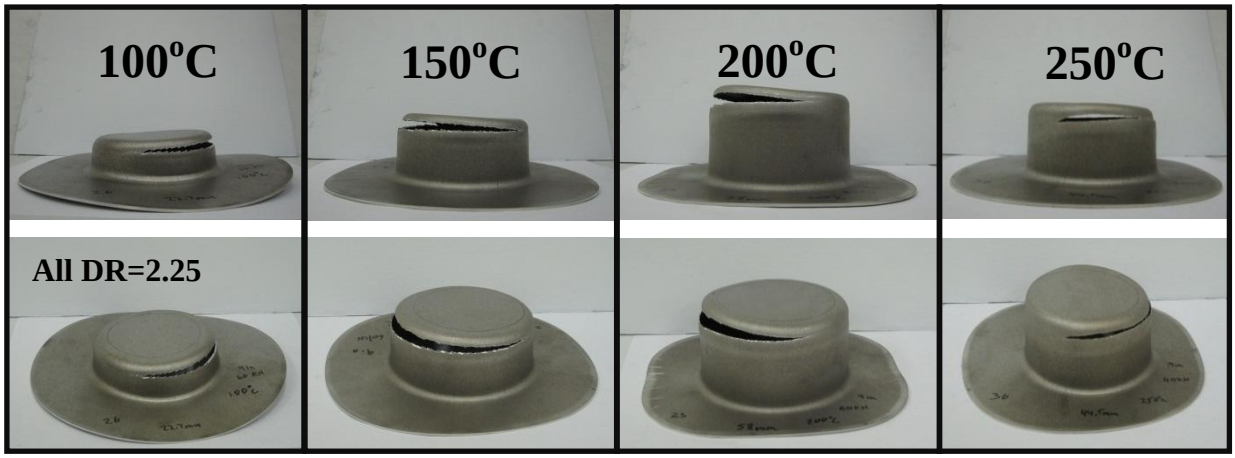

Figure 5.3: Deep drawn ZEK100 cups formed under isothermal conditions.

A comparison of punch load *versus* punch displacement at 200°C between ZEK100 and AZ31B is shown in Figure 5.4. With DRs of 2.00 and 2.50, both materials exhibit similar behaviour; both fully draw with DR = 2.00 and fracture with DR = 2.25. AZ31B experiences higher punch loads in both cases.

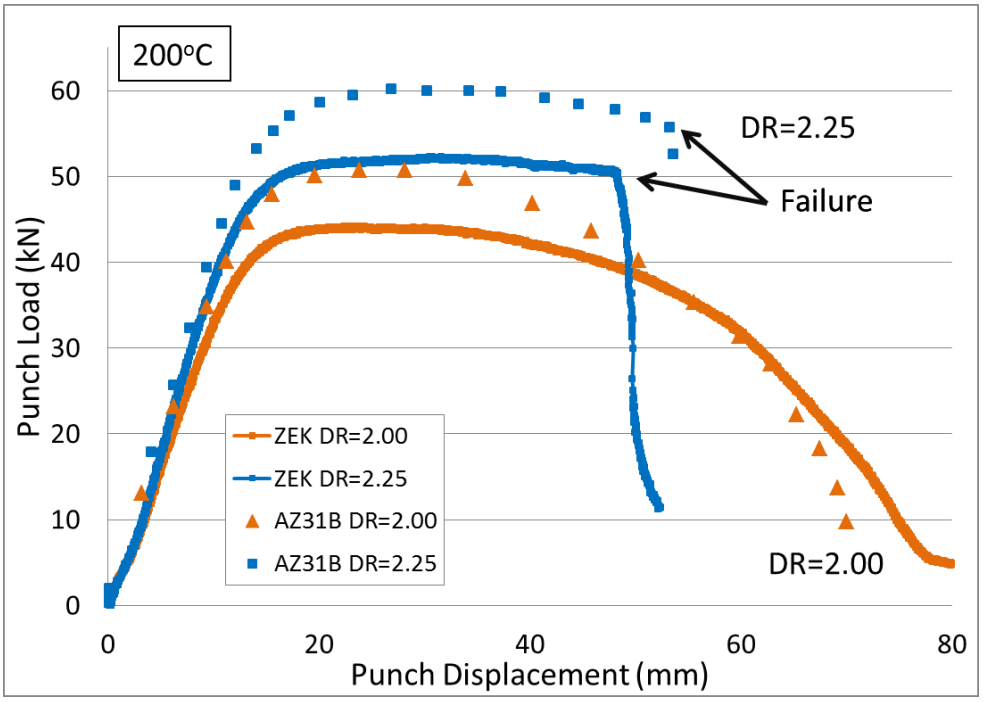

Figure 5.4: Punch Load vs. Punch Displacement comparison between ZEK100 and AZ31B

5.2 Non-isothermal Deep Drawing

Cups were deep drawn with an imposed temperature difference between the punch and the die/blank holder. Ghaffari Tari et al. (2013) presented similar experiments on AZ31B showing that lowering the punch temperature, relative to the die and blank holder, proved advantageous in forming deeper/full depth cups. Analogous temperature conditions were applied to ZEK100 with similar benefits. To illustrate the benefits of non-isothermal forming, Figure 5.5 shows the measured punch force *versus* punch displacement response for blanks with a DR of 2.25, flange temperature of 150°C, and punch temperature ranging from 150°C (isothermal case) down to 25°C. The isothermal case shows drawing until fracture at the punch radius at a depth of 45 mm. Reducing the temperature to 100°C in the punch region increases the strength of the blank in the punch area sufficiently enough such that the load in the sidewall of the cup may be supported, thus increasing the draw depth. Reducing the punch temperature further to 50°C and 25°C also resulted in fully drawn cups.

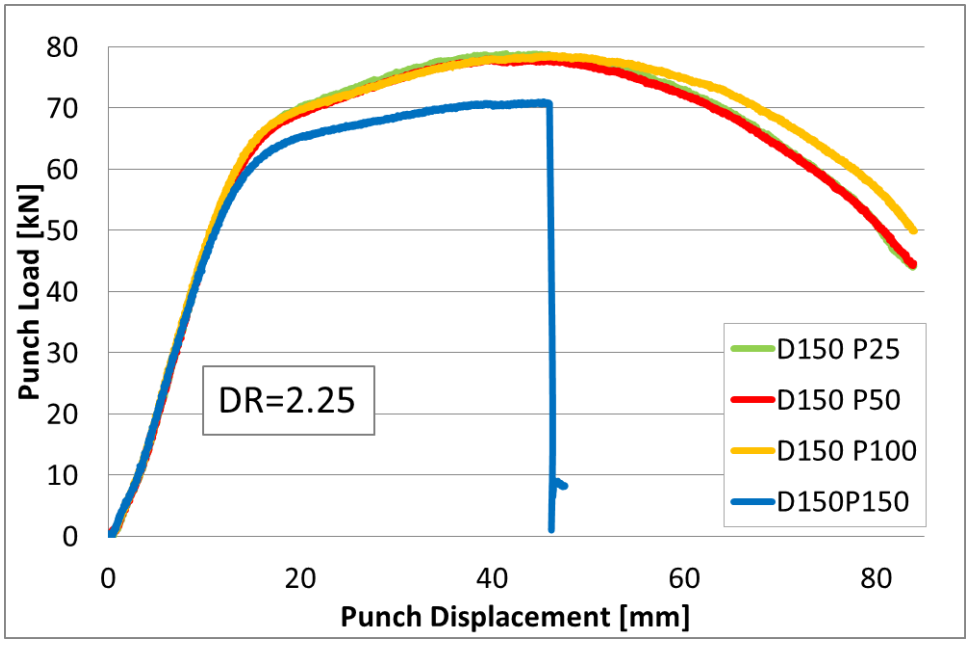

Figure 5.5: Effect of Punch Temperature Die: 150°C, Punch: 25-150°C.

The effect of varying the temperature in the flange region can be examined using Figure 5.6. Plotted is the measured punch load *versus* punch displacement response for die and blank holder temperatures in the range 150°C to 250°C, a punch temperature of 25°C, and a DR of

2.25. It can be seen from the figure that all of the blanks achieved a full draw. As the die and blank holder temperature is increased from 150°C to 250°C, the maximum punch load for each drawn cup decreases from 78 to 44 kN, respectively. A complete set of data for all non-isothermal tests and draw ratios conducted for this thesis is available in Appendix D.

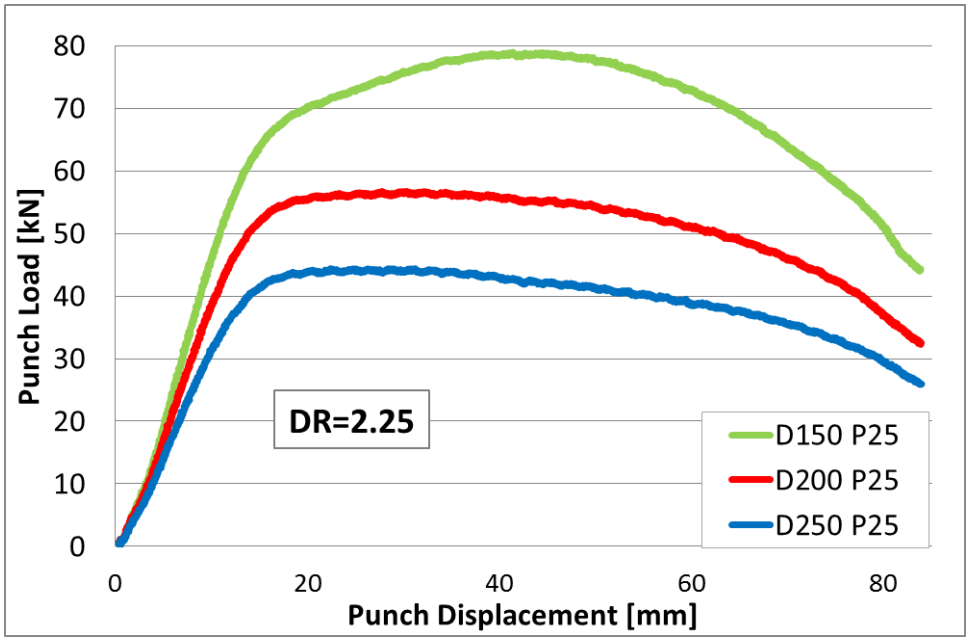

Figure 5.6: Effect of Die and Blank Holder Temperature Punch: 25°C, Die: 150-250°C.

5.3 Earring Behaviour of ZEK100

The deep drawing of ZEK100 resulted in an uneven cup rim. This behaviour is due to the anisotropy of the material and is often quantified by means of earring profiles in which the number of ears, their location in relation to the sheet rolling direction and their amplitude (Kurukuri, 2010) is characterized. For an orthotropic material, the earring profile between 0° and 90° should mirror the profile between 90° and 180° with respect to the 90° axis. Any changes from this arrangement are normally attributed to alignment of the center of the blank and the center of the die and punch (Chung and Shah, 1992).

The earring profiles obtained from the ZEK100 experiments appear to fall in between the shapes of an ideal square and an ideal circle. Figure 5.7 shows a cup drawn at 250°C with a DR

= 2.25 and the resulting measured earring profile. The RD is horizontal in Figure 5.7a. The earring profile was centered at the geometric center of the formed blank. At approximately 0°, 180° (and 360°) (rolling direction) the distance from the center of the blank to the edge of the blank should be the same due to symmetry. At approximately 90° and 270° (transverse direction) the distance to the center should also be equal due to symmetry and thus the earring measurements between angles 0° – 180° and 180° – 360° should also be similar. The difference in the height of the peaks at 45° and 135° and subsequently 225° and 315° may be due to a slight misalignment of the blank holder and die. Overall a good symmetry has been achieved with the current setup.

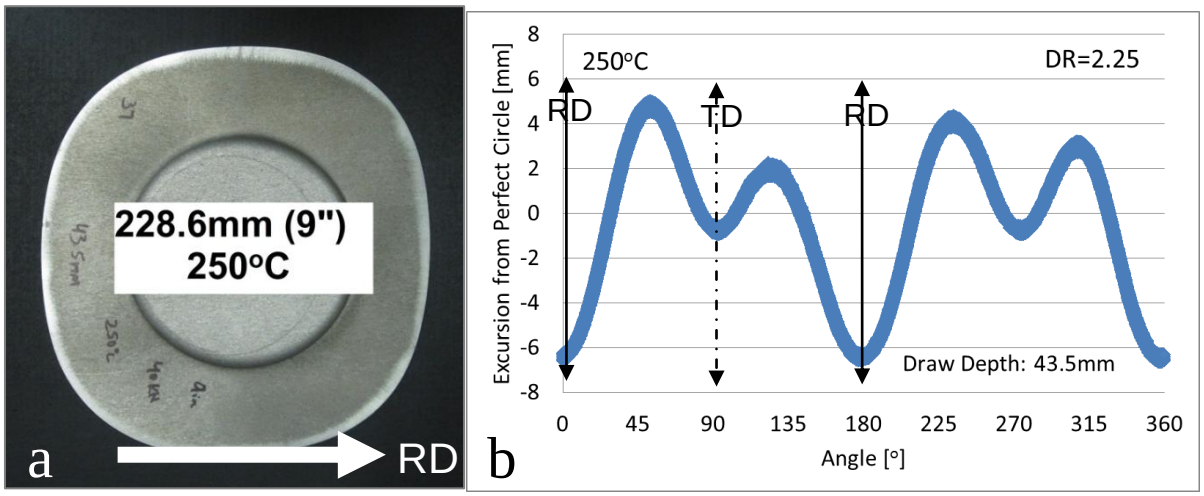

Figure 5.7: a) top view of image for earring profile analysis b) Earring profile obtained from a blank with DR = 2.25 at 250°C.

5.4 Isothermal Earring Profile

Blanks with DR = 2.25 were formed in interrupted tests to 3 mm prior to fracture for isothermal tests from 100°C to 250°C. The draw heights for the blanks were 21.8, 42, 54, and 42.5 mm at draw temperatures of 100, 150, 200, and 250°C, respectively. Figure 5.8 shows the resulting earring profiles (note that a negative "excursion from perfect circle" implies more draw-in relative to positive values). The nominal flange diameters for the deep drawn cups in Figure 5.8 were 205, 186, 157, 187 mm at test temperatures of 100, 150, 200, 250°C, respectively. At the lower temperature of 100°C, the least earring is present as expected since the lower temperature provides the least formability allowing for only a 21 mm cup height.

Conversely the most formable isothermal temperature was observed at 200°C with a cup height of 54 mm which, as expected, resulted in the largest earring profile. At a temperature of 250°C the cup height was reduced to 42.5 mm which resulted in an earring profile similar to that observed at 150°C. The first and largest peak occurred at approximately +/- 45° to the RD for all cases. The most amount of draw-in occurs along the rolling direction and the draw-in along the TD direction is also relatively high. The lowest draw-in occurs along the 45°orientation. At this point it is unclear which aspects of the material anisotropy are controlling the earring response and further analysis is recommended for future work. The trends in earring response do not change significantly with temperature, just the magnitudes which tend to correlate with draw depth resulting flange diameter. A full set of data from the earring profile measurements for all isothermal tests and draw ratios conducted for this thesis is available in Appendix E.

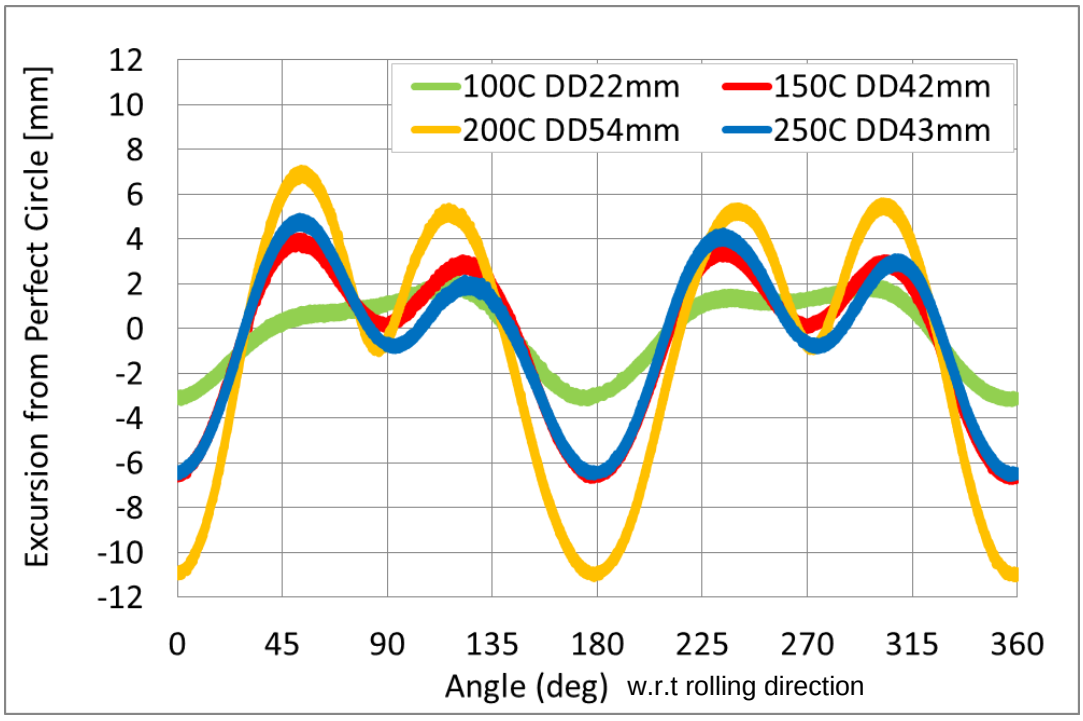

Figure 5.8: Isothermal Earring Profile DR = 2.25.

5.5 Non-isothermal earring profiles

The effect of temperature gradient on the ZEK100 drawability was investigated by forming with varying temperatures for the die/blank holder and punch. In the first case, as seen in

Figure 5.9, the die and blank holder temperature was held constant at 150°C while the punch temperature was increased from 25°C to 100°C. All formed cups achieved a full draw depth of 84 mm, so the earring profile tests were interrupted at 20 mm (at 64 mm) prior to full draw to leave a flange area sufficient for earring measurements, as described in Section 3.3.4. Varying the punch temperature and keeping the flange temperature constant had very little effect on the resulting earring profile. This is expected since most of the deformation occurs near the flange region.

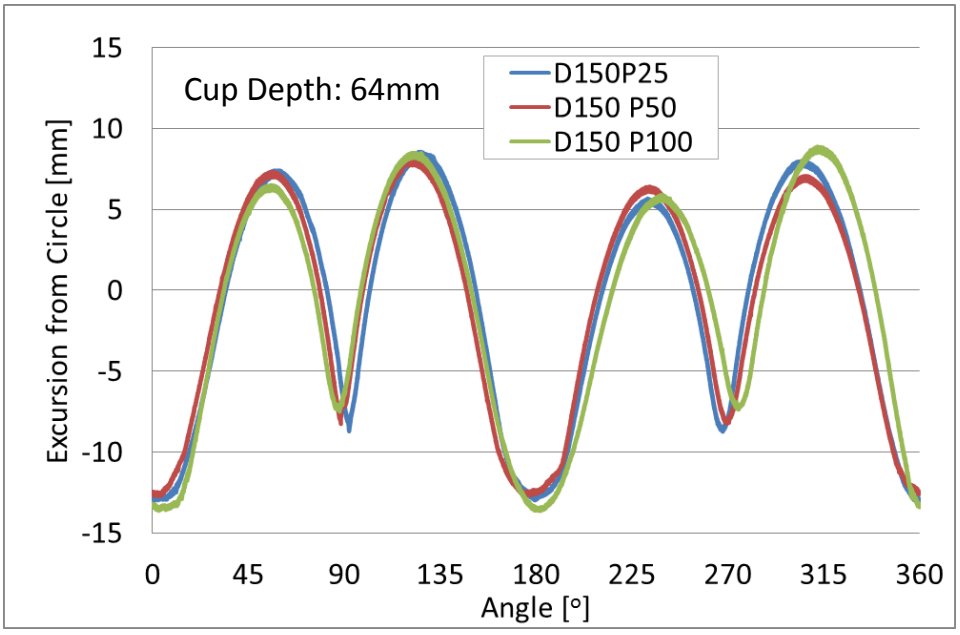

Figure 5.9: Non-isothermal earring profile: Die Temperature held constant at 150°C.

In contrast, if the punch temperature was held constant, earring was reduced somewhat when the die and blank holder temperature were increased, as seen in Figure 5.10, in which the cups were drawn to the same depth of 64 mm. This behaviour suggests that the degree of anisotropy decreases as temperature increases. The overall trends in measured earring were similar for the isothermal and non-isothermal deep draw cases. A complete set of data for the earring profile measurements for all non-isothermal tests and draw ratios conducted for this thesis is available in Appendix F.

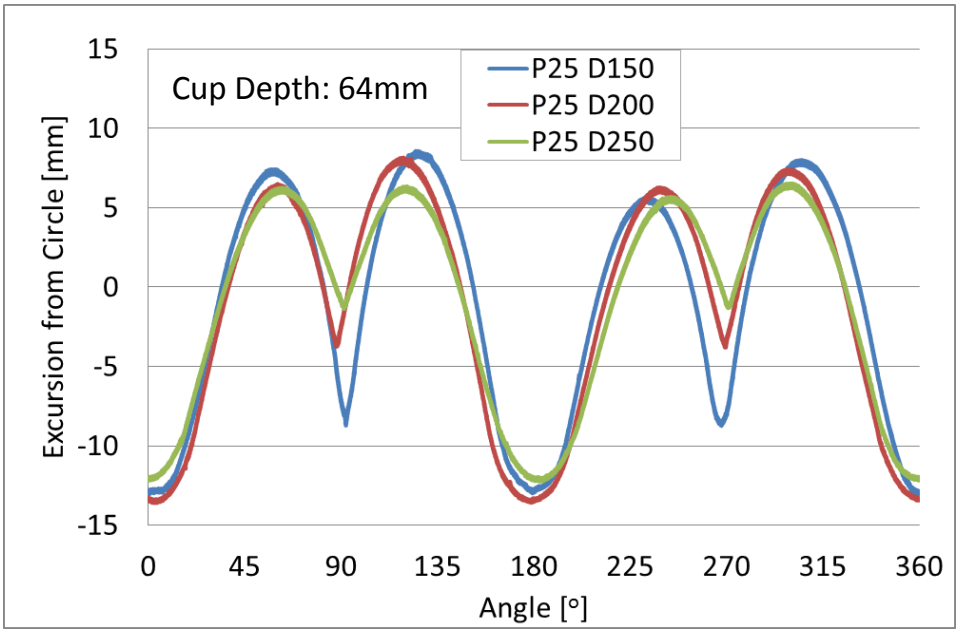

Figure 5.10: Non-isothermal earring profile: Punch Temperature held constant at 25°C.

5.6 Effect of Temperature on Strain and Thickness Distributions within Isothermal ZEK100 Deep Drawn Cups

The previous sections have demonstrated that increasing overall blank temperature, as well as increasing the difference in temperature between the die and punch, allows for better drawability of magnesium alloys. It is important to characterize how the temperature within a blank affects the thickness and strain distributions within the as-drawn cups. This section presents such data for cups drawn under isothermal conditions, while the non-isothermal results are presented in the following section.

ZEK100 blanks of DR = 2.25 were drawn at temperatures of 100, 150, 200, 250°C in which the tests were interrupted at 3 mm prior to fracture (Figure 5.11), resulting in varying cup heights due to the forming limits at different temperatures leaving more or less material in the flange area. The thickness measurements were taken starting at the center of the cup at the punch face and progressing along the surface to the edge of the flange in 10 mm increments (5 mm increments were used near to and on the punch radius). All measurements were taken from one of the three deep draw samples for each temperature condition.

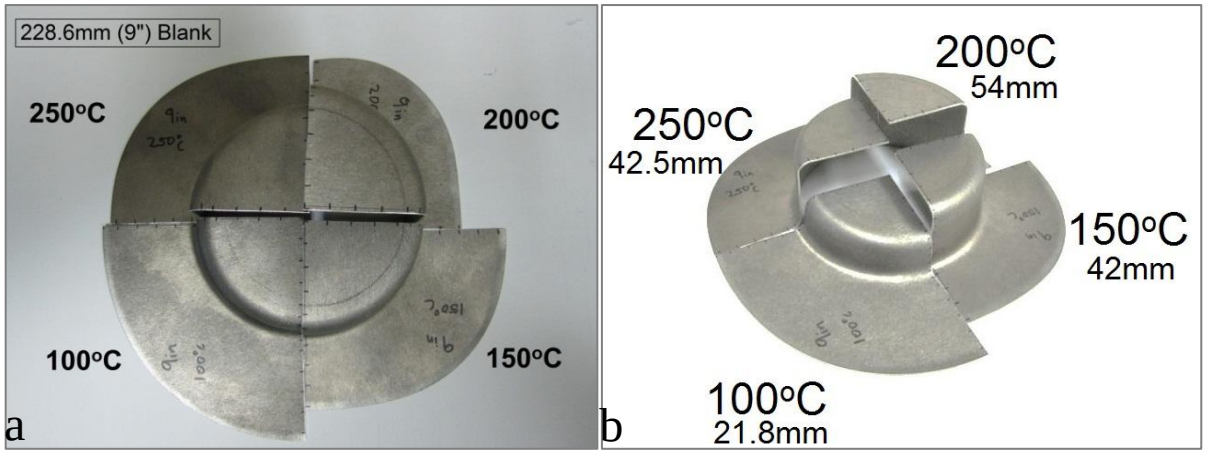

Figure 5.11: (a) Top view of cup sections drawn at 100, 150, 200 and 250°C. (b) Specimens interrupted 3 mm prior to the fracture draw depth for DR = 2.25 cups drawn at 100, 150, 200 and 250°C.

All specimens experienced significant thickening in the flange and cup wall sections, as shown in Figure 5.12. The amount of wall thickening increased with increasing temperature (and draw depth) up to 250°C when compared to thickness at the punch face. As the temperature is increased, the punch face experiences greater amounts of thinning. As shown in Figure 5.12, the average punch face thickness for the rolling direction was 1.42, 1.32, 1.3 and 1.12 mm for draw temperatures of 100, 150, 200, 250°C, respectively. The lowest thickness was observed at the punch radius for all temperatures and the punch radius becomes thinner with increasing temperature. The highest temperature condition (250°C) at the punch radius results in the largest thinning (excessive strains) causing earlier fracture compared to cups drawn at 200°C. Blanks formed at 150 and 250°C, which achieved a comparable draw depth, show a similar thickness profile with the latter experiencing more thinning than the former, especially at the punch radius (located approximately 50 mm from the center of the blank). It is important to note that the same blank holder force was used for all of the isothermally drawn cups, which may account for the higher degree of thinning and lower cup depth at fracture for the cups drawn at 250°C. At higher temperatures, the material strength decreases yet the frictional resistance remains approximately constant for a constant blank holder force; hence, earlier failure results. The blank holder force for the experiments in the current work was optimized for the lowest drawing temperatures to provide the deepest draw depth with no visible wrinkling of the flange and henceforth maintained as a constant blank holder force for all test temperatures. It should be possible to optimize the blank holder force to improve the draw

depth for each temperature condition; however, this was judged beyond the scope of the current work.

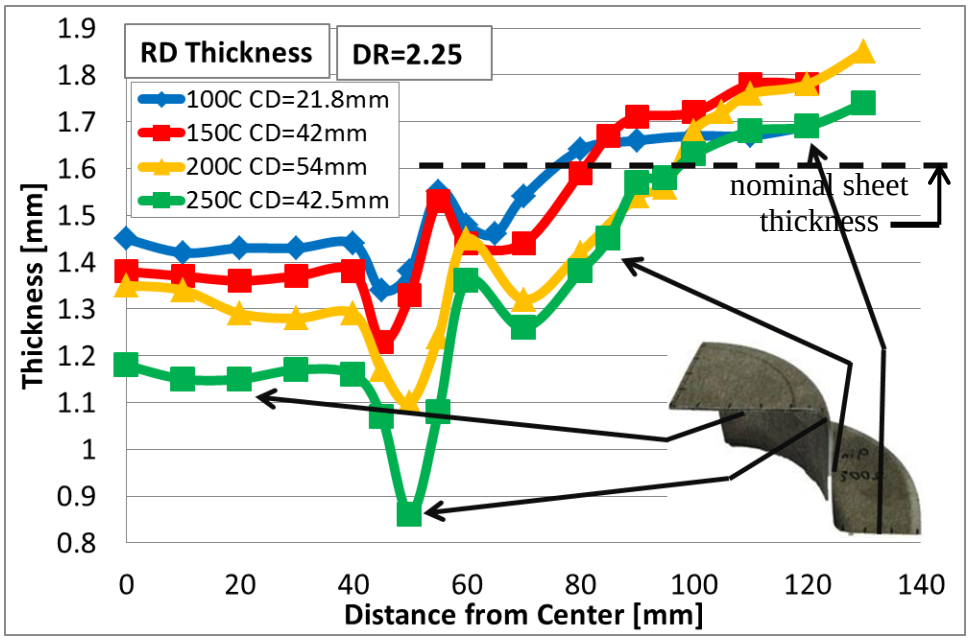

Figure 5.12: Isothermal Thickness Profile DR = 2.25 in Rolling Direction at various temperatures.

Measurements of major and minor strain were taken from the as-drawn samples with DR = 2.25 using the circle grid method. Samples were drawn to just before fracture as described above. Measurements were taken from the cup center along both the rolling and transverse direction toward the edge of the flange. The strain measurements were plotted against the measured FLCs (from Section 4.2.1) corresponding to the temperature at which the cup was drawn. The results are plotted in Figure 5.13 for forming temperatures of 100, 150, 200, 250°C.

The measured strains within the cups increase with draw temperature (and draw depth) as expected. All isothermal draws resulted in premature fracture leading to the measurements being taken from cups interrupted at 3 mm prior to fracture depth. The results show that the strains within the cups, for all temperature cases, are very close to the forming limit strain. The largest critical strains were observed at the punch radius and in the cup wall between the punch and die profile radii (region B and D). Forming at higher temperatures (above 150°C) allowed

for significantly more drawing of material while sustaining higher strains. The draw at 200°C resulted in the highest cup depth of 54 mm which may be explained by the lower strains experienced in the flange region thus lowering the strains experienced along the punch radius. The mostly positive strains observed in Figure 5.13 a,b,c, and d may be attributed to the constant (and relatively high) binder force used for the deep draw tests. The relatively high binder force may have contributed to less drawing of material from the flange area and caused more stretching of material at the punch face as observed later in Section 5.6.1.

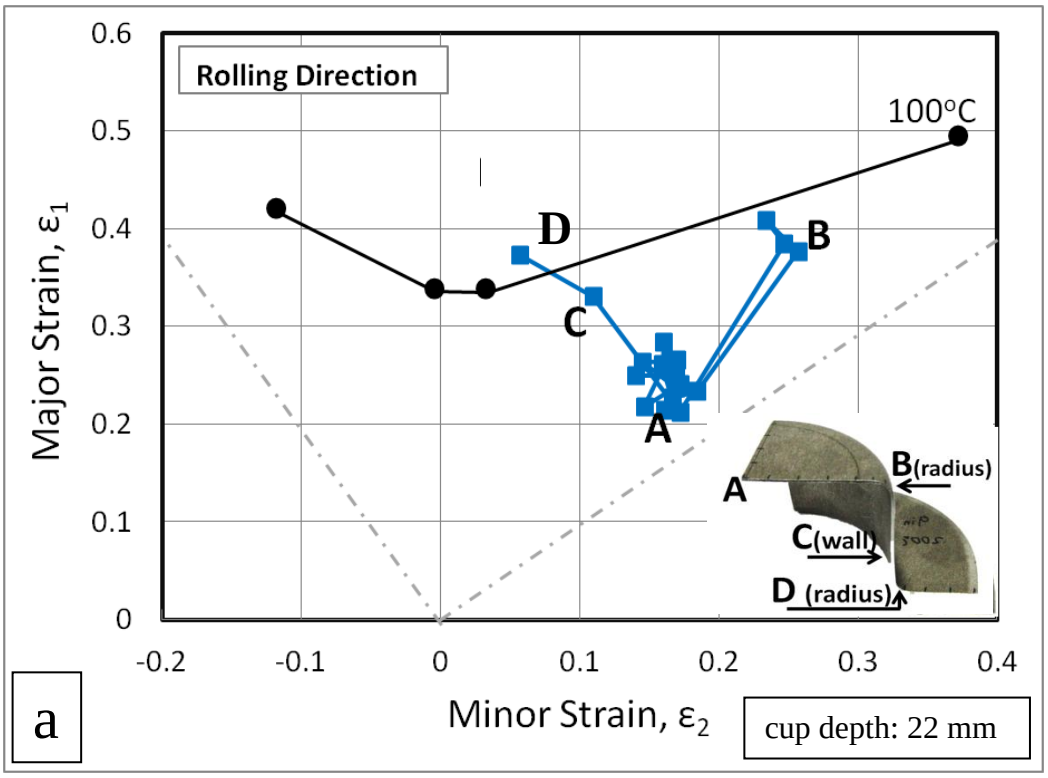

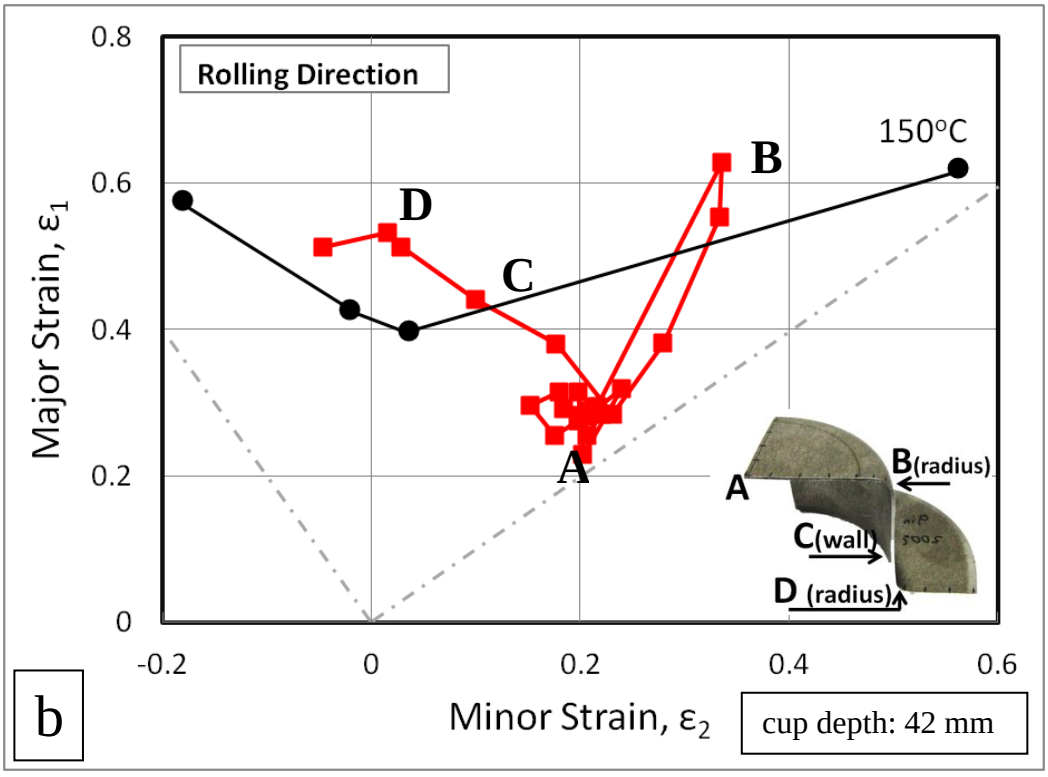
Rolling Direction
150°C
B
D
C
A
B(radius)
A
C(wall)
D (radius)
0.8
0.6
0.4
0.2
0
-0.2
0
0.2
0.4
0.6
Major Strain, ε1
Minor Strain, ε2
b
cup depth: 42 mm

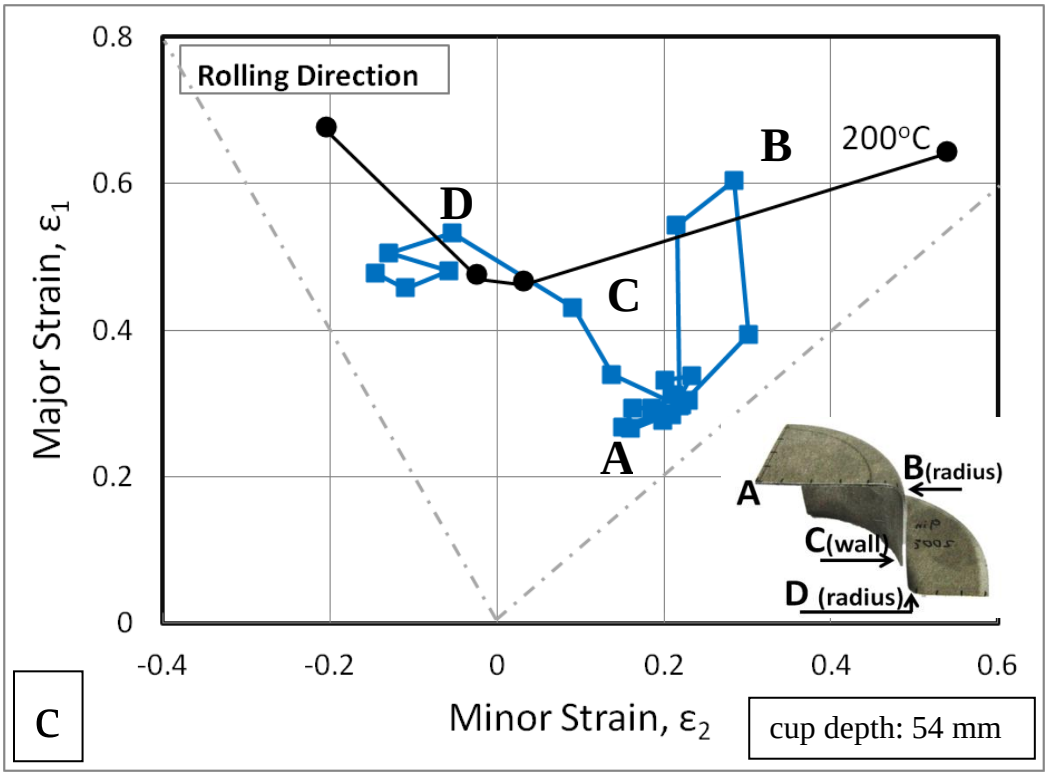
Rolling Direction
200°C
B
D
C
A
B(radius)
A
C(wall)
D (radius)
0.8
0.6
0.4
0.2
0
-0.4
-0.2
0
0.2
0.4
0.6
Major Strain, ε1
Minor Strain, ε2
c
cup depth: 54 mm

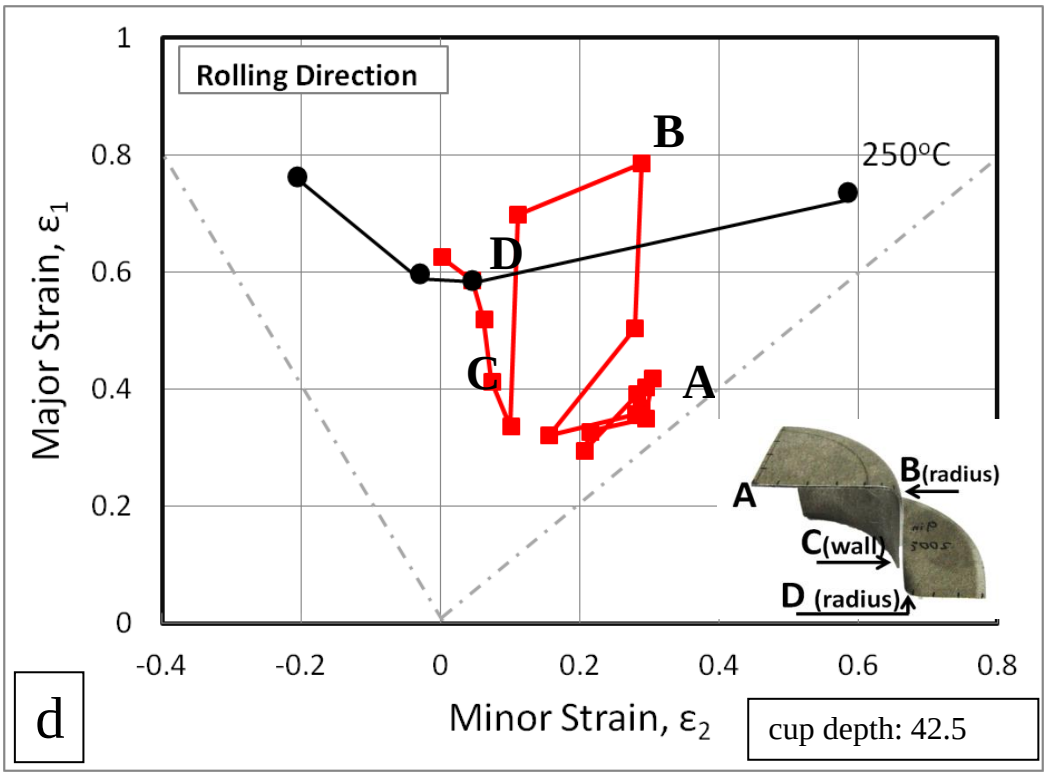

Figure 5.13: Isothermal deep draw of DR = 2.25 strains compared with forming limit curves for: a) 100°C b) 150°C c) 200°C and d) 250°C

All isothermal deep draw experiments showed anisotropic behaviour. The punch face experienced stretching in both the rolling and transverse directions and thus thinning due to tensile strains in all directions occurred across the punch face. Figure 5.14 shows a comparison of the thinning measured along the rolling and transverse directions at 150°C and 250°C. The as-received nominal thickness of the tested material was 1.6 mm as indicated in Figure 5.14 by the dashed line. Similar draw depths of 42 and 42.5 mm were achieved at both temperatures of 150°C and 250°C. This similarity allows for a direct comparison between these two temperatures showing that more thinning is present at the punch face and less thickening of the cup wall occurs as the temperature is increased. (The reader is cautioned that the blank holder force was held constant for this test series which is likely the cause of the increased thinning at 250°C.) At 150°C, the transverse direction appears to resist thinning more than the rolling direction. In the cup wall and flange regions, the in-plane anisotropy is manifest as the transverse direction experiencing less thickening than the rolling direction. The degree of anisotropy is reduced with increasing temperature. A complete set of data with the strain and

thickness measurements for all isothermal tests and draw ratios conducted for this thesis are available in Appendix G and H, respectively.

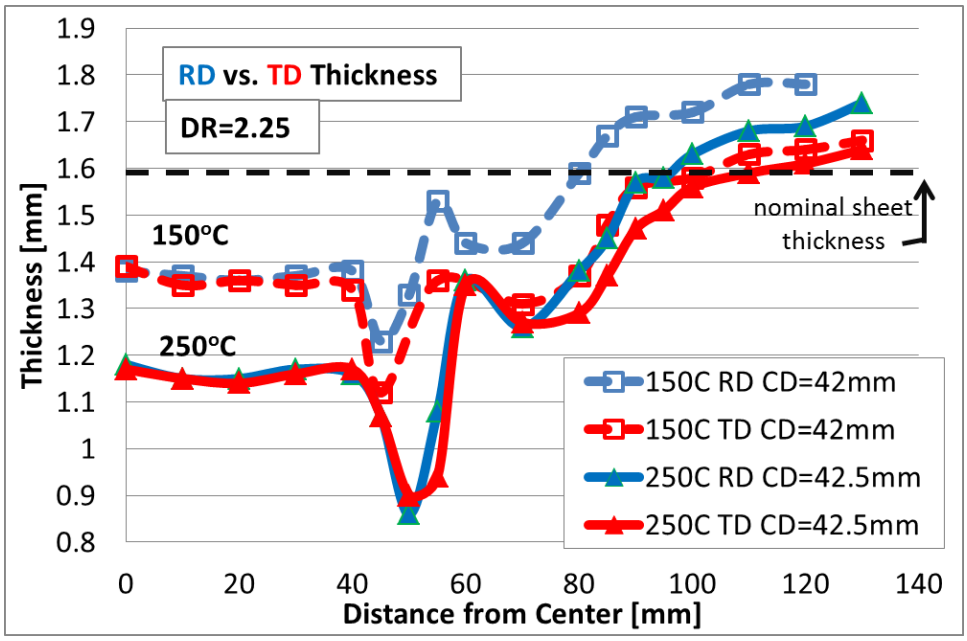

Figure 5.14: Rolling vs. Transverse Direction Isothermal Thickness Profile DR = 2.25.

5.6.1 Effect of Draw Ratio on Predicted Thickness Distribution

The effect of draw ratio on the predicted thinning was investigated using three draw ratios of 1.75, 2.00 and 2.25 that were deep drawn at 100°C. The cups were drawn to fracture achieving cup heights of 50 mm (full draw), 31 mm, and 25 mm for DRs of 1.75, 2.00 and 2.25 respectively, as shown in Figure 5.15. As the DR increased more thinning of the punch face was observed while the draw depth at fracture was reduced. This trend indicates that with a small DR there was more drawing of material, whereas with a large DR mainly stretching at the punch face occurred with only minimal drawing of material. These results may be explained by the added resistance imparted by the larger material area clamped in the flange region and the additional force required to draw the material in from the flange area at high DR.

Additional work would be necessary to explore the effects of binder force for the higher temperature isothermal cases to determine whether more deformation of the flange, resulting in

possibly deeper draws, can be obtained without wrinkling in the flange. As the material was drawn into the die cavity the thickness of the material increased relative to the amount of cup depth achieved.

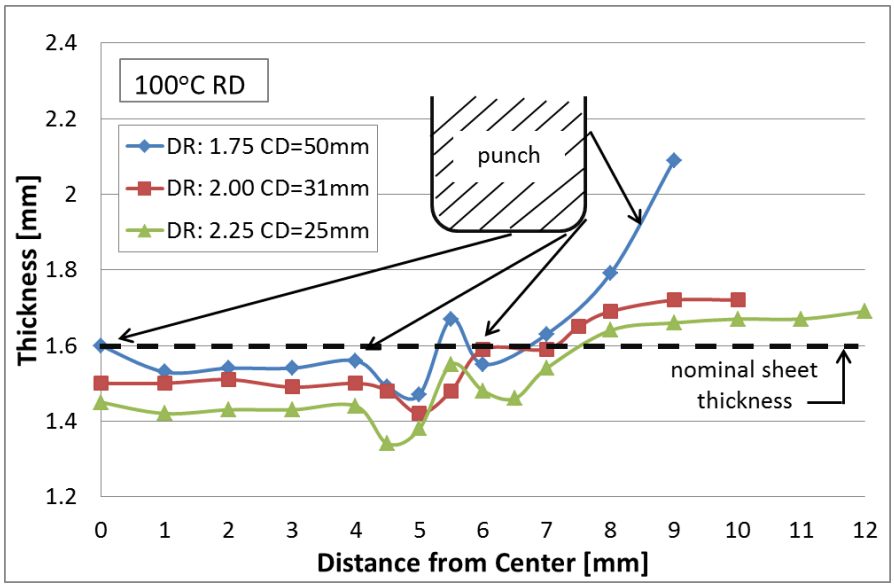

Figure 5.15: Draw ratio effect on draw thickness profile at 100°C.

At a higher temperature of 150°C the trends remain the same, as shown in Figure 5.16. A major difference with the increase in temperature is observed with the DR = 2.00 case. The thinning of the punch face remains similar for both 100 and 150°C (Figure 5.15 and 5.16), while the thermally softened material in the flange area allows for more draw-in of the flange and thickening in the punch wall.

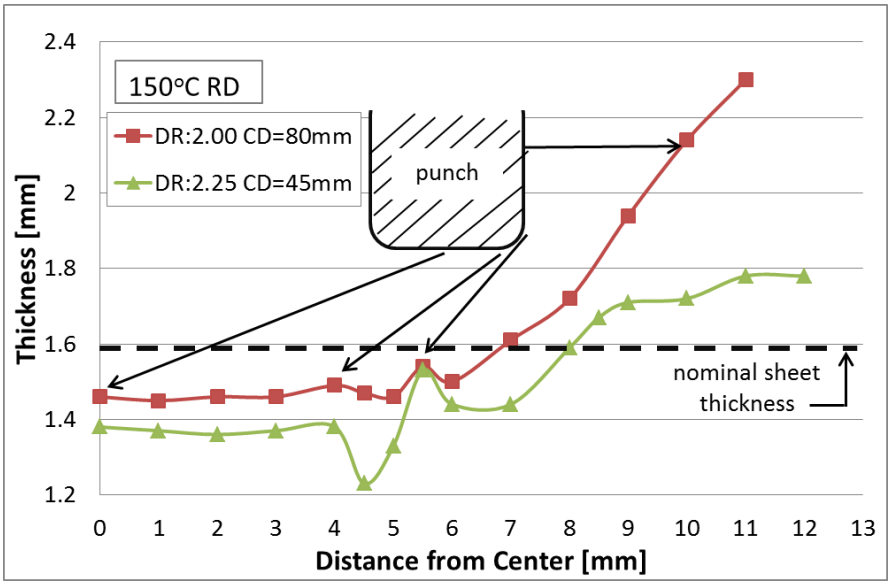

Figure 5.16: Draw ratio effect on draw thickness profile at 150°C.

5.7 Non-Isothermal Thickness Profile and Strain Profiles

The most favorable forming conditions were achieved by prescribing a lower punch temperature in relation to the die and blank holder temperature. The effects of varying the temperature between the punch and die on the thickness and strain distributions were investigated by using two scenarios whereby in the first case the die and blank holder temperature was held constant at 150°C and the punch temperature was varied from 25, 50 and 100°C. In the second case the punch temperature was held constant at 25°C while the die and blank holder temperature was varied from 150, 200, 250°C. Each DR (1.75, 2.00, and 2.25) was formed under the same conditions and all blanks achieved a full draw. Similar to isothermal forming, the common observable trend was that the transverse direction experiences noticeably less thickening of the punch wall.

The non-isothermal results presented in Figure 5.17 show the effects of varying the punch temperature between 25, 50 and 100°C while maintaining the die and blank holder temperature at 150°C. In this case there are no discernible effects on formability other than slightly less thinning of the material at the punch face and punch radius with a lower punch temperature. A spinoff benefit that may be derived from this forming behaviour is the lower manufacturing

costs that may result from lower tooling temperatures. The isothermal case is shown for reference and reveals a much higher degree of thinning at the punch nose region.

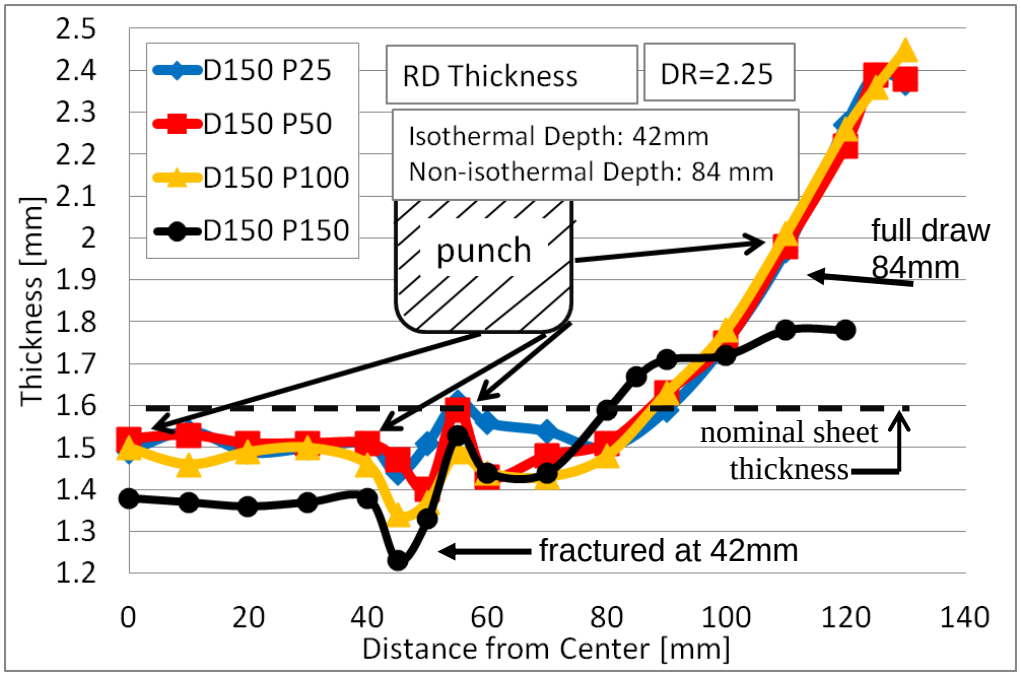

Figure 5.17: Non-Isothermal Thickness Profile along RD, Die: 150°C, Punch: 25, 50, 100°C.

In the opposite scenario in which the die and blank holder temperature was increased and the punch temperature held constant, there was very little difference in the thickness profiles for all tested die and blank holder temperatures at 150, 200, 250°C. This was due to a softer material in the blank holder region which allowed for more drawing of material.

Figure 5.18 serves to compare measured strains from two non-isothermal forming experiments to the forming limit curves presented in Chapter 4. In both draw cases, the flange area was maintained at a higher temperature (150°C) compared to the punch temperature (100°C and 25°C). The low punch temperatures significantly reduce the strains along the punch bottom and the critical punch nose region to lie below the low temperature forming limit curves. At the same time, the strains in the flange region remain safely below the forming limit for the higher temperature flange. A set of data showing strain and thickness measurements for all non-

isothermal tests and draw ratios conducted for this thesis is available in Appendix I and J, respectively.

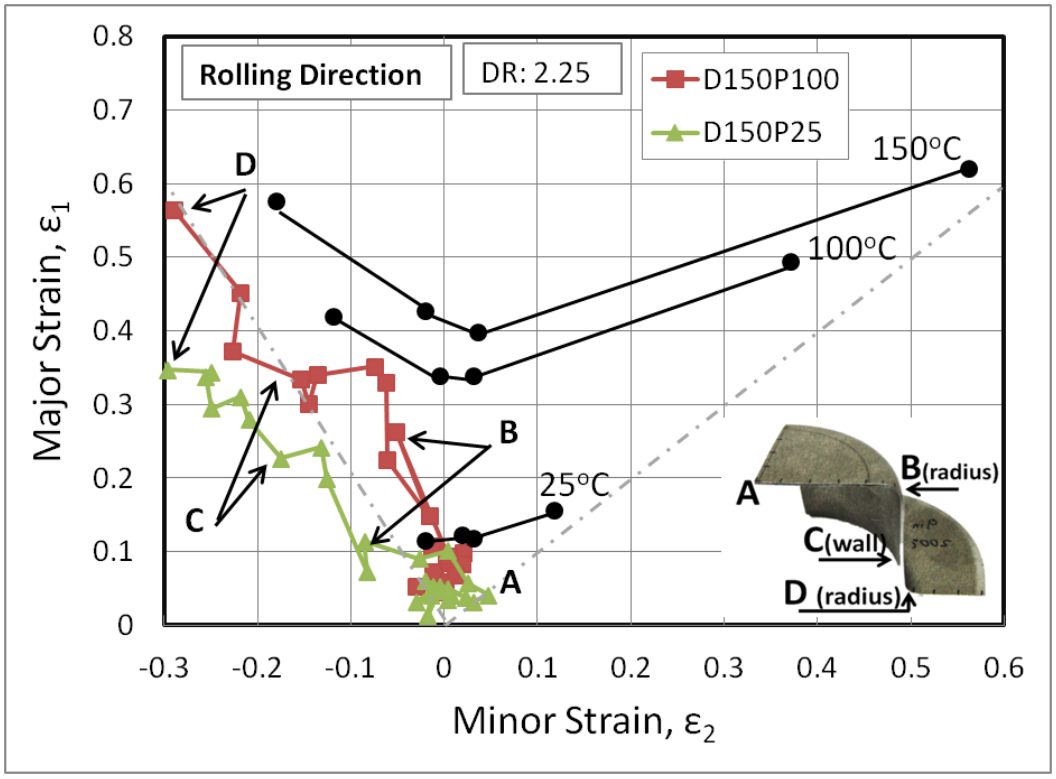

Figure 5.18: Non-isothermal deep draw strains of DR = 2.25 compared with forming limit curves for: a) 100°C b) 150°C c) 200°C and d) 250°C

5.8 Thermal Process Window for ZEK100

The drawability of ZEK100 was experimentally characterized *via* measuring the punch load *vs.* punch displacement for each circular blank under various isothermal and non-isothermal temperature conditions. Tables 5.1 - 5.3 show the temperature conditions, between 25 and 250°C, under which blanks were formed into deep drawn cups. An additional temperature of 270°C for the die was tested as a direct comparison to work performed on AZ31B by Ghaffari Tari et al. (2013). Tests began at the top right temperature combination in the table and progressed down towards the temperature combinations on the left. Once a fracture was observed, the binder force was reduced to allow for easier drawing until wrinkling was observed. In each of the respective tables the green blocks indicate a full draw and red blocks

indicate cups that fractured during the draw. The value within the block shows the binder force between the die and the blank holder.

Table 5.1: 177.8 mm (7”) Blank DR = 1.75.

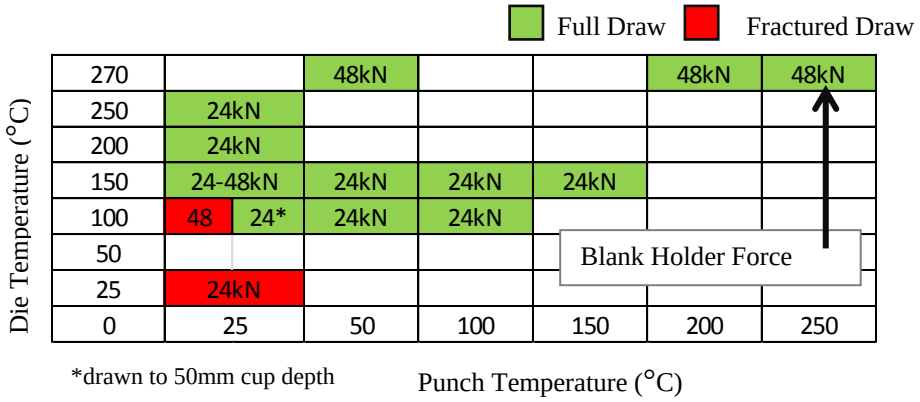

Table 5.2: 203.2 mm (8”) Blank DR = 2.00.

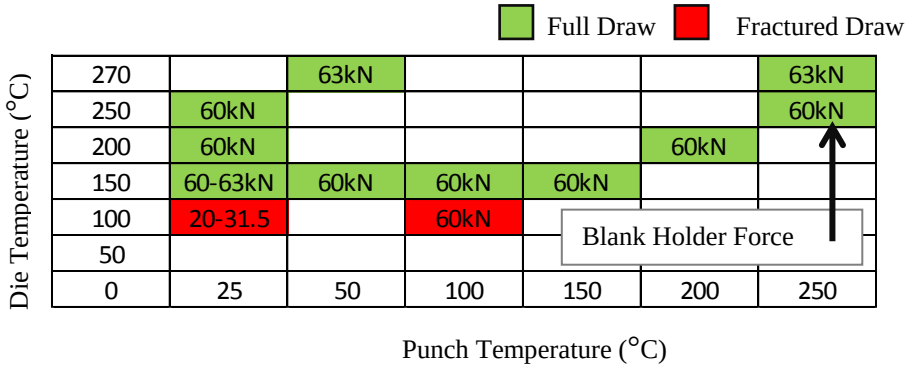

Table 5.3: 228.6 mm (9”) Blank DR = 2.25.

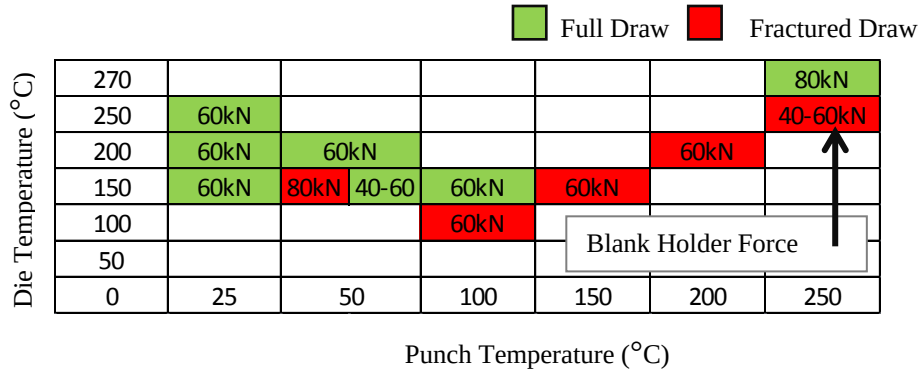

Combining the results of the isothermal and non-isothermal experiments, a thermal process window was created to summarize the results. Figure 5.19 shows the temperature conditions for the die/blank holder and the punch that achieve a full draw of ZEK100 (denoted by solid black circles) and versus fractured cups (denoted by 'x'). Figures 5.19(a) and (b) show results for DRs of 2.25 and 2.00, respectively. A process window for blanks with DR 1.75 is not shown since all experiments resulted in a full draw for all isothermal and non-isothermal temperatures tested between 100°C and 270°C.

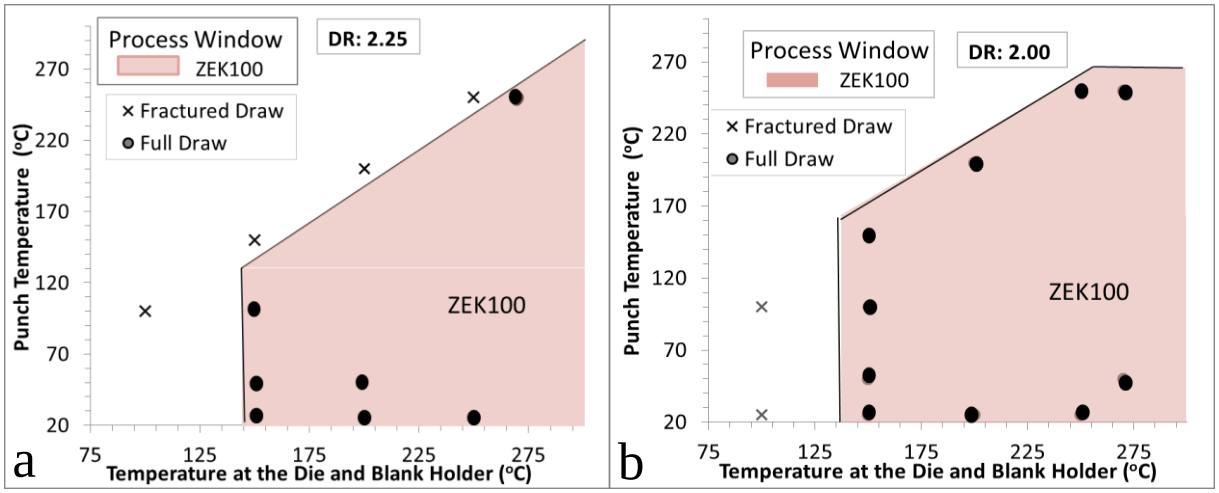

Figure 5.19: Toolset Temperature Window for blanks a) DR = 2.25 and b) DR = 2.00.

Ghaffari Tari et al. (2013) developed thermal process windows for AZ31B-O for DR = 2.25 blanks drawn at various non-isothermal conditions. A direct comparison to ZEK100 is possible and is presented in Figure 5.20. The full drawn samples within the noted ellipse are positioned vertically according to punch temperature during the test; however, it should be noted that the temperature at the center of the blank is higher than the set punch temperature for the non-isothermal cases and therefore, the corresponding points would be shifted up but remain within the ellipse. The main conclusions that may be drawn is that the thermal process window for ZEK100 is substantially larger than that of AZ31B-O and that ZEK100 can be drawn at much lower temperatures. This lower temperature process window translates into shorter heating times, lower heating costs and lower lubricant requirements for production of components using ZEK100 *versus* AZ31B.

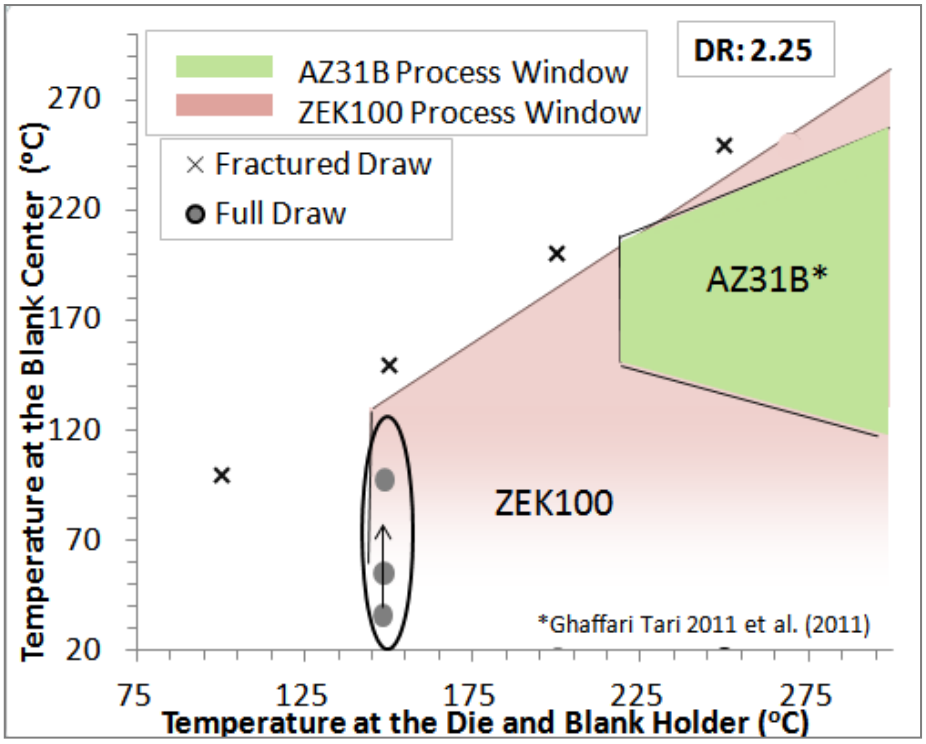

Figure 5.20: Thermal Process Window for blank DR = 2.25 ZEK100 vs. AZ31B.

6 CONCLUSIONS

The following conclusions are drawn from this research:

1. The limiting dome height (LDH) experiments have demonstrated the superior formability of ZEK100 over AZ31B, particularly for temperatures below 200°C. At a temperature of 150°C ZEK100 achieved a dome height 60% higher than that of AZ31B. The plane strain forming limit (FLC_0) for ZEK100 at 150°C was 0.4 which equals that of AZ31B at 250°C. At higher temperatures (300°C), the two alloys exhibited similar performance with both achieving similar dome heights at necking of 37 mm (AZ31B) and 41 mm (ZEK100).

2. ZEK100 has shown significant improvements in drawability compared to AZ31B, with the largest benefit observed in non-isothermal deep draw tests. Fully drawn cups of ZEK100 were achieved with a die and blank holder temperature of 150°C and a blank center temperature well below 100°C. Full draws for AZ31B required a die and blank holder temperature of 225°C and a blank center temperature of 150°C.

3. A significant level of anisotropy was present in all of the ZEK100 experiments, as observed in the strain distributions and earring present in the deep drawing experiments. ZEK100 exhibited the highest draw-in along the RD orientation and the least draw-in along the 45° orientation.

4. Strong anisotropy was also observed in the forming limit strains with respect to sheet orientation. Notched samples cut in the transverse direction and formed at room temperature experienced 33% higher dome heights than samples cut in the rolling direction. Increasing the temperature above 150°C led to a reduction in the amount of anisotropy resulting in only a 14% difference between RD and TD dome heights. At 200°C, the transverse sheet orientation exhibited higher limit strains than the rolling direction with FLC_0 values of 0.6 and 0.45 for TD- and RD- oriented samples, respectively.

7 FUTURE WORK

Continued research work on forming behaviour is needed to support application of this material in production settings. Further characterization of the anisotropic effects is necessary for efficient die manufacturing and blank geometry design, whereas the favourable non-isothermal temperature conditions for forming have been shown to be well aligned with current manufacturing processes. The following is some future work that has been identified from the current research:

1. A closer examination of limiting draw ratios for isothermal temperatures as well as earring profiles through optimization of blank holder forces for each drawing temperature.

2. An investigation into improving the limiting draw ratio with tooling optimization by varying the punch and die profile radii.

3. Examine the variation in limit strains due to edge damage imposed by shearing process used to create the notched specimens.

4. Investigate which aspects of the material mechanical response are controlling the earring behaviour of ZEK100.

5. Apply the current results to finite element models for simulation of warm forming processes.

REFERENCES

Abu-Farha, F., Verma, R., Hector Jr., L.G., 2012. High Temperature Composite Forming Limit Diagrams of Four Magnesium AZ31B Sheets Obtained by Pneumatic Stretching, Journal of Materials Processing Technology, vol. 212, is. 6, pp. 1414-1429.

Albuţ, A, 2009. The Sheet Thickness Effect on Springback Amplitude of a U-Shaped Part made from Tailor Welded Strips. The Annals of "dunarea De Jos" University of Galati Fascicle V, Technologies in Macine Building, ISSN 1221-4566.

Alderman, M, 2013. The Lightest Structural Metal in Automotive. Presented by Magnesium Elektron at the Niche Vehicle Network. March 19, 2013.

Agnew S.R., Yoo M.H., Tomé C.N. 2001. Application of Texture Simulation to Understanding Mechanical Behaviour of Mg and Solid Solution Alloys Containing Li or Y, Acta Materialia, 12/3; 49, no. 20, pp. 4277-4289.

Agnew, S. & Duygulu, Ö., 2005. Plastic Anisotropy and the Role of Non-Basal Slip in Magnesium Alloy AZ31B, International Journal of Plasticity, 21, pp. 1161-1193.

Ambrogio, G., Bruni, C., Bruschi, S., Filice, L., Ghiotti, A., Simoncini, M., 2007. Characterization of AZ31B Magnesium Alloy Formability in Warm Forming Conditions, Proceedings Esaform 2007, Lyon, France.

Antoniswamy, A.R., Carpenter, A.J., Carter, J.T., Hector Jr. L.G., Taleff, E.M., 2013. Forming-Limit Diagrams for Magnesium AZ31B and ZEK100 Alloy Sheets at Elevated Temperatures. Journal of Materials Engineering and Performance. vol. 22, pp. 3389–3397

Aslam, I., Li, B., McClelland, Z., Horstemeyer, S.J., Maa, Q., Wang, P.T., Horstemeyer, M.F., 2013, Three-Point Bending Behaviour of a ZEK100 Mg Alloy at Room Temperature. Materials Science & Engineering A. vol. 590, pp. 168-173.

ASTM Designation: E2492-07, 2012. Standard Test Method for Evaluating Springback of Sheet Metal Using the Demeri Split Ring Test, reapproved.

Bagheriasl, R., 2012a. Formability of Aluminum Alloy Sheet at Elevated Temperature. Doctoral Thesis for the University of Waterloo.

Bagheriasl, R., Ghavam, K., Worswick, M.J., 2012b. Formability Improvement with Independent Die and Punch Temperature Control, International Journal of Material Forming.

Bettles, C.J., Gibson, M.A., 2005. Current Wrought Magnesium Alloys: Strengths and Weaknesses. Journal of Materials, pp. 46-49, May 2005.

Boba, M., Worswick, M.J., Mishra, R.K., Carter, J.T., 2012. Formability of AZ31B and ZEK100 Magnesium Alloy Sheets at Elevated Temperatures, Magnesium Conference 2012, Vancouver July 2012.

Bohlen, J., Dobran, P., Garcia, E.M., Chmelik, F., Lukac, P., Letzig, D., Kainer, K.U., 2006. The Effect of Grain Size on the Deformation Behaviour of Magnesium Alloys Investigated by the Acoustic Emission Technique, Advanced Engineering Materials, vol. 8, no. 5.

Bohlen, J., Nurnberg, M.R., Senn, J.W., Letzig, D., Agnew, S.R., 2007. The Texture and Anisotropy of Magnesium-Zinc-Rare Earth Alloy Sheets, Acta Materialia 55, pp. 2101-2112.

Boljanovic, V., 2004. Sheet Metal Forming Processes and Die Design, Industrial Process Inc.

Brunet, M., Mguil, S., Morestin, F., 1998. Analytical and Experimental Studies of Necking in Sheet Metal Forming Processes. Journal of Materials Processing Technology. vol.80-81. pp. 40-46.

Cheah, L.W., 2010. Cars on a Diet: The Material and Energy Impacts of Passenger Vehicle Weight Reduction in the U.S., Submitted to the engineering systems division in partial fulfillment of the requirements for the degree of Doctor of Philosophy in engineering systems at the Massachusetts Institute of Technology.

Chen F., Huang, T., 2003a. Formability of Stamping Magnesium-Alloy AZ31 Sheets. Journal of Materials Processing Technology, vol. 142, pp. 643-647.

Chen F., Huang, T., Chang, C.K., 2003b. Deep drawing of square cups with magnesium alloy AZ31 sheets. International Journal of Machine Tools & Manufacture vol. 43 pp.1553–1559

Chung, K., Shah, K., 1992. Finite Element Simulation of Sheet Metal Forming for Planar Anisotropic Metals, International Journal of Plasticity, Vol. 8, pp. 453-476.

Dilmee, M., Halkaci, H. S., Ozturk, F., Livatyali, H., Yigit, O., 2012. Effects of Sheet Thickness and Anisotropy on Forming Limit Curves of AA2024-T4, International Journal of Advanced Manufacturing Technology, DOI 10.1007/s001 70-012-4684-0.

Doege, E., Droder, K., 2001a. Sheet Metal Forming of Magnesium Wrought Alloys – Formability and Process Technology, Journal of Materials Processing Technology 115, p9. 14-19.

Doege, E., Droder, K., 2001b. Mechanical Properties of Structures of Semi-finished Products Joined to Aluminum Foams, Journal of Materials Processing Technology, vol. 115, is. 1, pp.20-24.

Fracz, W., Stachowicz, F., 2012. Determination of Forming Limit Diagram of Zinc Electro-Galvanized Steel Sheets, Journal of Metallurgy, 51(2) 161-165.

General Motors Material ZEK100 Specification Sheet, April 26, 2010.

Ghaffari Tari, D., Worswick, M.J., Winkler, S., 2013. Experimental Studies of Deep Drawing of AZ31B Magnesium Alloy Sheet Under Various Thermal Conditions, Journal of Materials Processing Technology, vol. 213, pp. 1337-1347.

Ghosh, A.K., Hecker, S.S., 1974. Stretching Limits in Sheet Metals: In-Plane Versus Out of Plane Deformation, Metallurgical Transactions, vol. 5, pp. 2161.

Ghosh, A.K., Hecker, S.S., 1975. Failure of Thin Sheets Stretched Over Rigid Punches, Journal of Metallurgical and Materials Transactions A, vol. 6, no. 5, p. 1065-1074.

Hantzsche, K., Bohlen, J., Wendt, J., Kainer, K.U., Yi, S.B., Letzig, D., 2010. Effect of Rare Earth Additions on Microstructure and Texture Development of Magnesium Alloy Sheets, Scripta Materialia 63, pp. 725-730.

Hijazi, A., Yardi, N., Madhavan, V., 2004. Determination of Forming Limit Curves Using 3D Digital Image Correlation and In-Situ Observation, Proceedings of SAMPE.

Hill, R., 1952. Journal of the Mechanics and Physics of Solids. Vol.1, pp.19.

Hogan, M., 2008. Photo from http://www.automotiveaddicts.com/1073/2009-cadillac-cts-v-already-on-ebay#prettyPhoto

ISO 12004-2, 2006. Metallic Materials – Sheet and Strip – Determination of Forming Limit Curves – Part 2: Determination of Forming Limit Curves in Laboratory, ISO TC 164/SC 2.

Jeong H.T., Ha T.K., 2007. Texture Development in a Warm Rolled AZ31 Magnesium Alloy, Journal of Materials Processing Technology, 6/12; 187-188:559-561.

Jérusalem, A., Fernández, A., Pérez-Prado, M.T., 2010. Continuum modeling of {10-12} twinning in a Mg-3%Al-1%Zn rolled sheet. Revista De Metalurgia, vol. 46, pp.133-137

Kaya, S., Spampinato, G., Altan, T., 2008. An Experimental Study on Non-Isothermal Deep Drawing Process Using Aluminum and Magnesium Alloys. Journal of Manufacturing Science and Engineering, vol. 130, no. 6, p. 11.

Keeler, S., 1968. Circular Grid System - A Valuable Aid for Evaluating Sheet-metal Formability", Society of Automobile Engineers, TP # 680092.

Khosravani, A., Scott, J., 2013. Twinning in Magnesium Alloy AZ31B Under Different Strain Paths at Moderately Elevated Temperatures, International Journal of Plasticity, Col 45 pp. 160-173.

Kim, H.J., Choi, S.C., Lee, K.T., Kim, H.Y., 2008. Experimental Determination of Forming Limit Diagram and Springback Characteristics of AZ31B Mg Alloy Sheets at Elevated Temperatures, Materials Transactions, vol. 49, no. 5, pp. 1112 to 1119.

Kleemola, H.J., Kumpulainen, J.O., 1980a. Factors Influencing The Forming Limit Diagram: Part I – The Experimental Determination of The Forming Limits of Sheet Steel, Journal of Mechanical Working Technology, vol. 3 pp. 289-302.

Kleemola, H.J., 1980b. Factors Influencing the Forming Limit Diagram: Part II – Influence of Sheet Thickness, Journal of Mechanical Working Technology, vol. 3, pp. 303-311.

Koike J., Kobayashi T., Mukai T., Watanabe H., Suzuki M., Maruyama K., 2003. The Activity of Non-Basal Slip Systems and Dynamic Recovery at Room Temperature in Fine-Grained AZ31B Magnesium Alloys. Acta Materialia, 4/18; 51(7), pp. 2055-2065.

Kurukuri, S., 2010. Simulation of Thermally Assisted Forming of Aluminum Sheet, Doctoral Thesis for the University of Twente.

Kurukuri, S., Ghaffari-Tari, D., Worswick, M.J., Carter, J.T., Mishra, R.K., 2012a. Dynamic Characterization of AZ31B and ZEK100 Magnesium Alloy Sheets, In: Magnesium Conference 2012. International Conference on Magnesium Alloys and Their Applications, Vancouver, BC, Canada, p. 6.

Kurukuri, S., Bardelcik, A., Worswick, M.J., Mishra, R.K., Carter, J.T., 2012b. High Strain Rate Characterization of ZEK100 Magnesium Rolled Alloy Sheet, EPJ Web of Conferences, Vol. 26, 01042.

Kurukuri, S., Worswick, M.J., Ghaffari Tari, D., Mishra, R.K., Carter, J.T., 2013a. Rate Sensitivity and Tension-Compression Asymmetry in AZ31B Magnesium Alloy Sheet, accepted in Phil. Trans. A.

Kurukuri, S., Worswick, M.J., Mishra, R.K., Carter, J.T., 2013b. Constitutive behaviour of commercial grade ZEK100 magnesium alloy sheet over wide range of strain rates, under review in Met. Trans. A.

Laurent, H., Greze, R., Manach, P.Y., Coer, J., 2009. Springback of an Aluminum Alloy in Warm Forming Conditions Using the Split-Ring Test, 7th EUROMECH Solid Mechanics Conference.

Lee, S., Chen, Y., Wang, J., 2002. Isothermal Sheet Formability of Magnesium Alloy AZ31 and AZ61, Journal of Materials Processing Technology 124, pp. 19-24.

Levy, B.S., Van Tyne, C.J., 2008. Failure During Sheared Edge Stretching, ASM International, 17:842-848, 1059-9405.

Levy, B.S., Van Tyne, C.J., 2011. Review of the Shearing Process for Sheet Steels and its Effect on Sheared Edge Stretching, ASM International, 1059-9405.

Lou, X.Y., Li M., Boger R.K., Agnew S.R., Wagoner R.H. (2007), Hardening Evolution of AZ31B Mg Sheet. International Journal of Plasticity, vol. 1; 23, no. 1, pp. 44-86.

Lutsey, N., 2010. Review of Technical Literature and Trends Related to Automobile Mass-Reduction Technology, Institute of Transportation Studies, University of California, Davis.

Marciniak, Z., Kuczynski, K., 1973. Limit Strains in the Processes of Stretch-Forming Sheet Metal, International Journal of Mechanical Sciences, vol. 15 pp. 789-800.

Min, J., Cao, Y., Carter, J.T., Verma, R., 2012a, Comparison of Tensile Properties and Crystallographic Textures of Three Magnesium Alloy Sheets, Magnesium Technology.

Min, J., Cao, Y., Carter, J.T., Verma, R., 2012b. Tensile Properties of Three Preform-Annealed Magnesium Alloy Sheet, Magnesium Technology.

Min, J., Hector Jr. L.G., Lin, J., Carter, J.T., 2013. Analytical Method for Forming Limit Diagram Prediction with Application to a Magnesium ZEK100-O Alloy. Journal of Materials Engineering and Performance. vol. 22, pp. 3324–3336.

Motyka, M., Kubiak, K., Sieniawski, J., Ziaja, W., 2012. Hot Plasticity of Alpha Beta Alloys, Titanium Alloys - Towards Achieving Enhanced Properties for Diversified Applications, Dr. A.K.M. Nurul Amin (Ed.), ISBN: 978-953-51-0354-7, InTech, DOI: 10.5772/34806.

Mukai, T., Yamanoi, M., Watanabe, H., Higashi, K., 2001. Ductility Enhancement in AZ31B Magnesium Alloy by Controlling its Grain Structure, Scripta Materialia , vol. 45, p. 89.

Naka, T., 2001. The Effects of Temperature and Forming Speed on the Forming Limit Diagram for Type 5083 Aluminum-Magnesium Alloy Sheet, Journal of Materials Processing Technology 113, pp. 648-653.

Ozturk, F., Dilmec, M., Turkoz, M., Ece, R.E., Halkaci, H.S., 2009. Grid Marking and Measurement Methods for Sheet Metal Formability. 5th International Conference and Exhibition on Design and Production of Machines and Dies/Molds. June 18-21, 2009, Kusadasi, Turkey.

Palaniswamy, H., Ngaile, G., Altan, T., 2004. Finite Element Simulation of Magnesium Alloy Sheet Forming at Elevated Temperatures. Journal of Material Processing Technology, vol. 146, pp. 52-60.

Palumbo, G., Sorgente, D., Tricarico, L., Zhang, S. H., Zheng, W. T., 2007. Numerical and Experimental Investigation on the Effects of the Heating Strategy and the Punch Speed on the Warm Deep Drawing of Magnesium Alloy AZ31. Journal of Materials and Processing Technology, vol. 191, pp. 342-346.

Panahi, N., 2013. Work in progress, University of Waterloo.

Pathak, N., Butcher, C., Worswick, M., 2013. Influence of the Sheared Edge Condition on the Hole Expansion of Dual Phase Steel, proceedings IDDRG 2013, Zurich, Switzerland.

Parrish, A., Rais-Rohani, M., Najafi, A., 2012. Crashworthiness Optimization of Vehicle Structures with Magnesium Alloy Parts, International Journal of Crashworthiness, pp. 1-23.

Scheib, S., Satkulvanich, P., Altan T., 2008. Examining Edge Cracking in Hole Flanging of AHSS Part II: Modeling and Blanking, Stamping Journal, FMA Publication.

Stanford, N., 2012. The Effect of Rare Earth Elements on the Behaviour of Magnesium-Based Alloys: Part 2 – Recrystallization and Texture Development, Materials Science & Engineering A, http://dx.doi.org/10.1016/j.msea.2012.10.084

Staroselsky, A., Anand, L., 2003. A Constitutive Model for HCP Materials Deforming by Slip and Twinning: Application to Magnesium Alloy AZ31B. International Journal of Plasticity. vol. 19, pp. 1843–1864.

Stoughton, T.B., 2000. A General Forming Limit Criterion for Sheet Metal Forming. International Journal of Mechanical Sciences vol. 42, 1-27.

Styczynski A., Hartig C., Bohlen J., Letzig, D., 2004. Cold rolling textures in AZ31 wrought magnesium alloy, ScriptaMaterialia, vol. 4;50, no. 7:943-947.

USCAR, 2006. Magnesium Vision 2020: A North American Automotive Strategic Vision for Magnesium, USAMP.

Van Minh, H., Sowerby, R., Duncan, J.L., 1974. Variability of Forming Limit Curves, International Journal of Mechanical Sciences, vol. 16, pp. 31-44.

Veerman, C., Hartman, L., Peels, J., Neve, P., 1971. Determination of Appearing and Admissible Strains in Cold-Reduced Sheets. Sheet Metal Industries 687 – 694.

Wang, Y.N., Huang, J.C., 2007. The Role of Twinning and Untwinning in Yielding Behaviour in Hot-Extruded Mg–Al–Zn Alloy, Acta Materialia, vol. 55, pp. 897 – 905.

Wong, S.L., 2006. Deformation Twinning: Mechanisms and Their Role in Crystal Plasticity Models. ftp://ftp.ccmr.cornell.edu/tmp/410/MS&E%20410/Papers/Wong.pdf

Yoo M., 1981. Slip, Twinning, and Fracture in Hexagonal Close-Packed Metals, Metallurgical and Materials Transactions A, 03/01; 12 (3):409-418.

Zhang, S.H., Zhang, K., Xua, Y.C., Wang, Z.T., Xua, Y., Wang, Z.G., 2007. Deep-drawing of Magnesium Alloy Sheets at Warm Temperatures. Journal of Materials Processing Technology. vol. 185, pp. 147–151.

APPENDIX A: SPECIMEN GEOMETRY

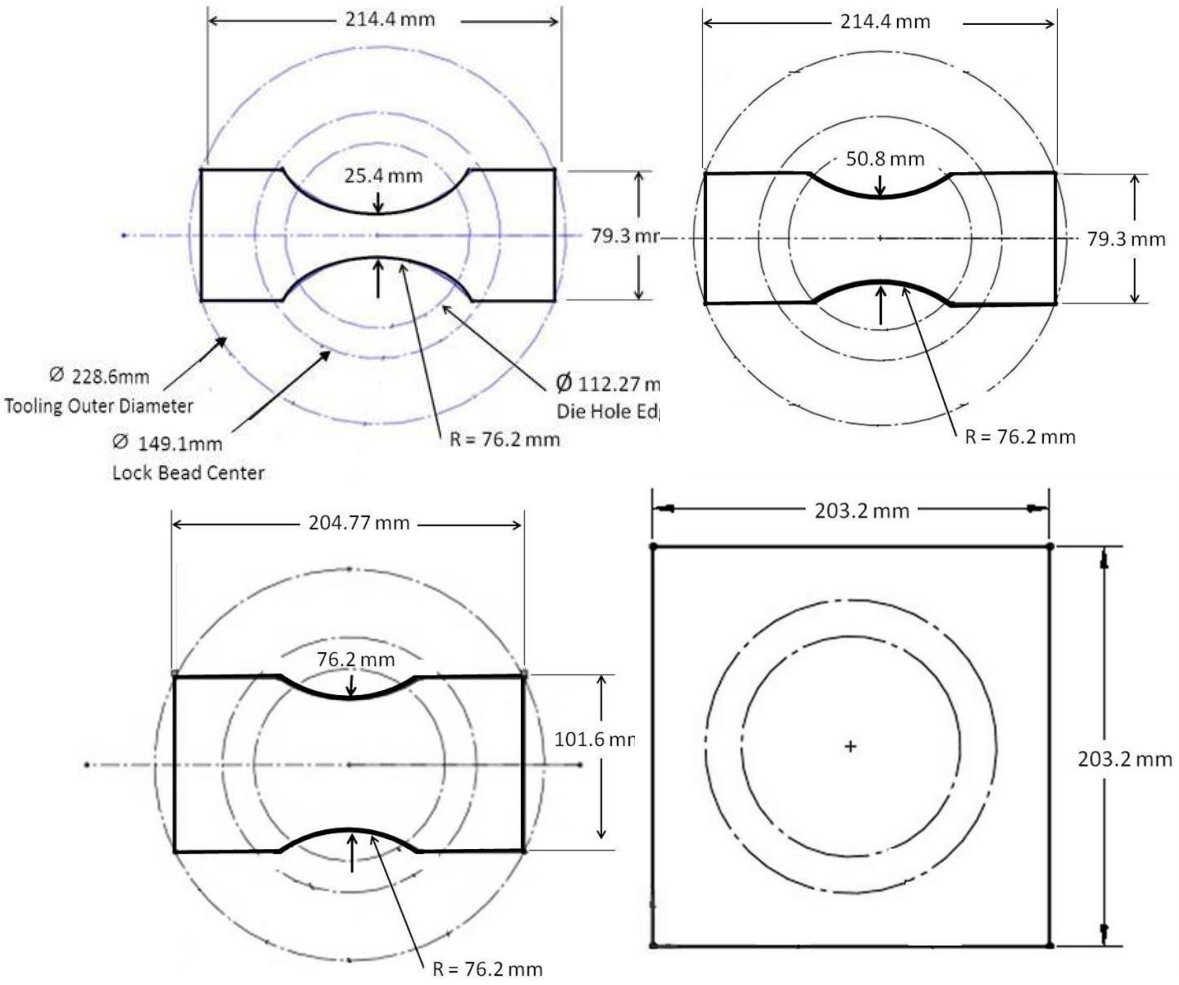

APPENDIX B: ISOTHERMAL LDH PUNCH FORCE VS. PUNCH DISPLACEMENT FOR ZEK100 AND AZ31B

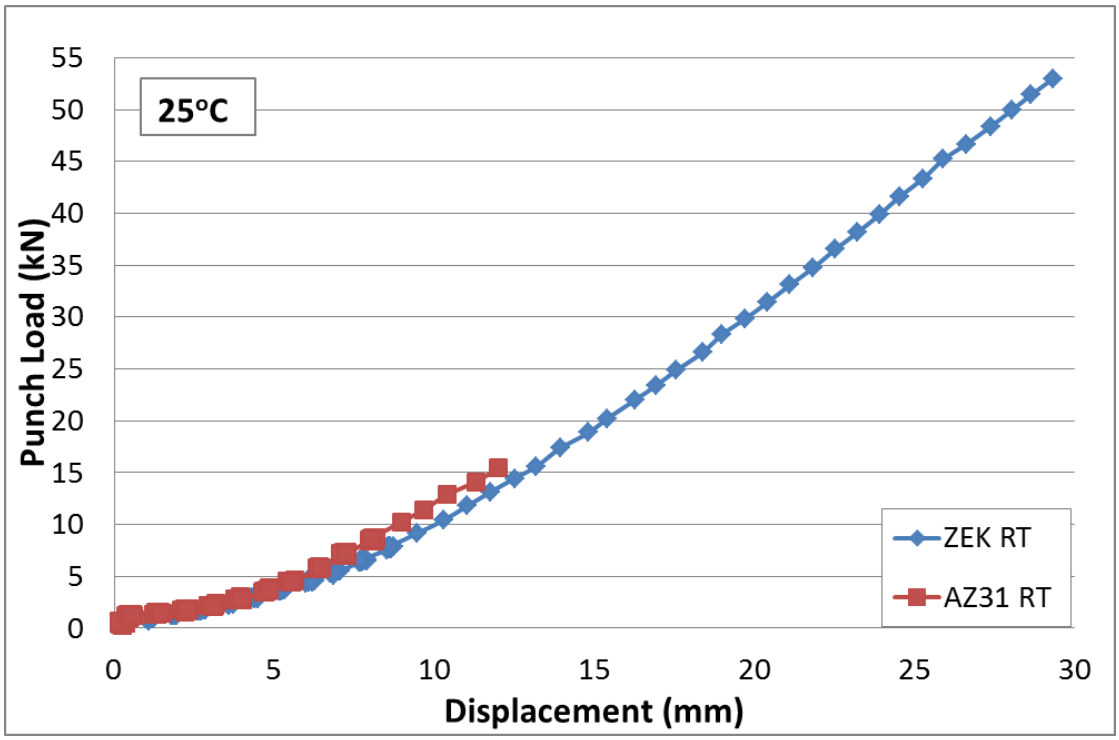

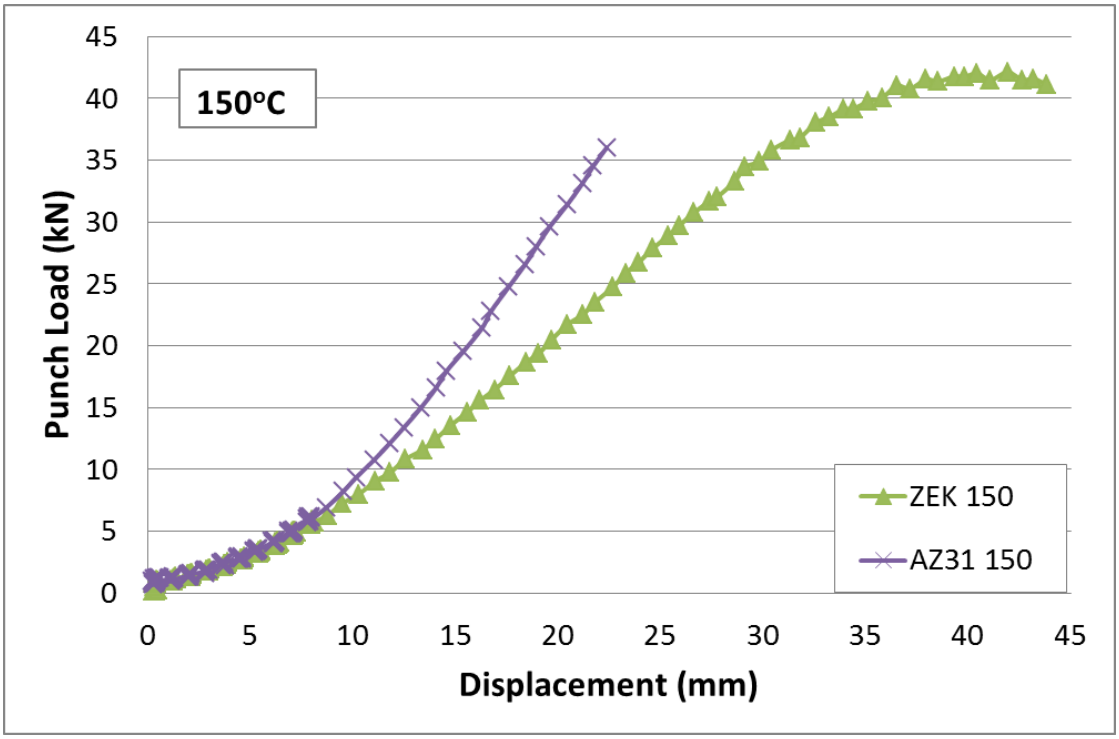

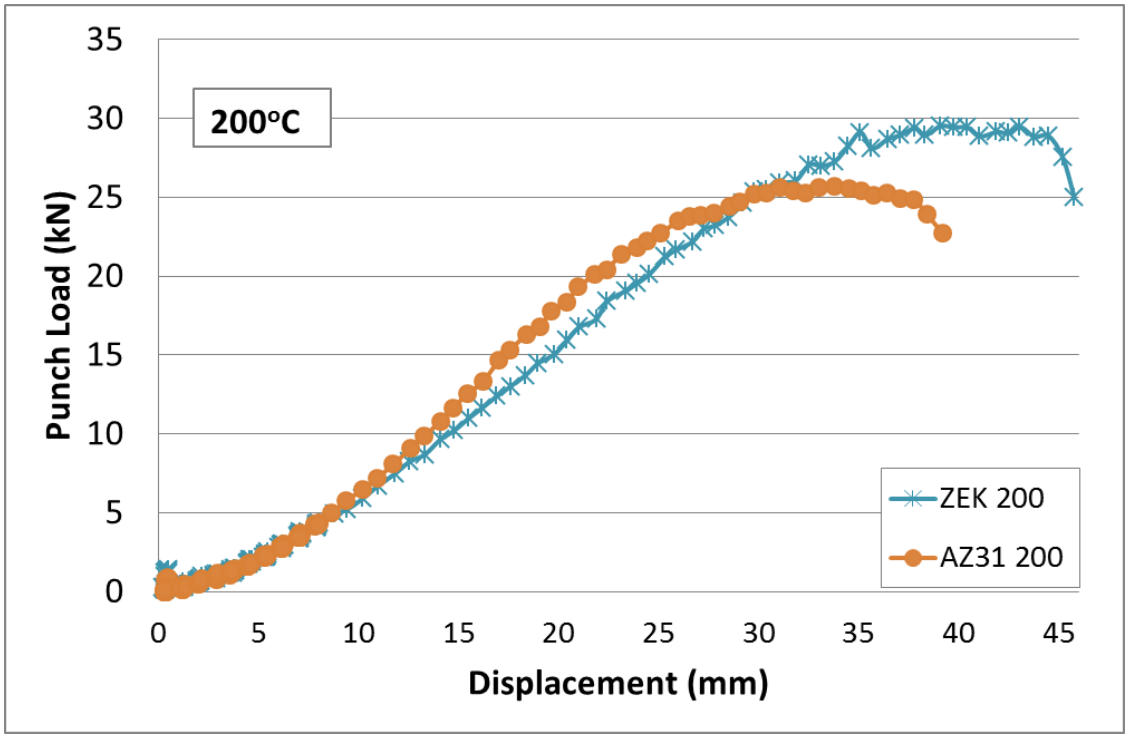
200°C
Punch Load (kN)
Displacement (mm)
ZEK 200
AZ31 200
0
5
10
15
20
25
30
35
40
45

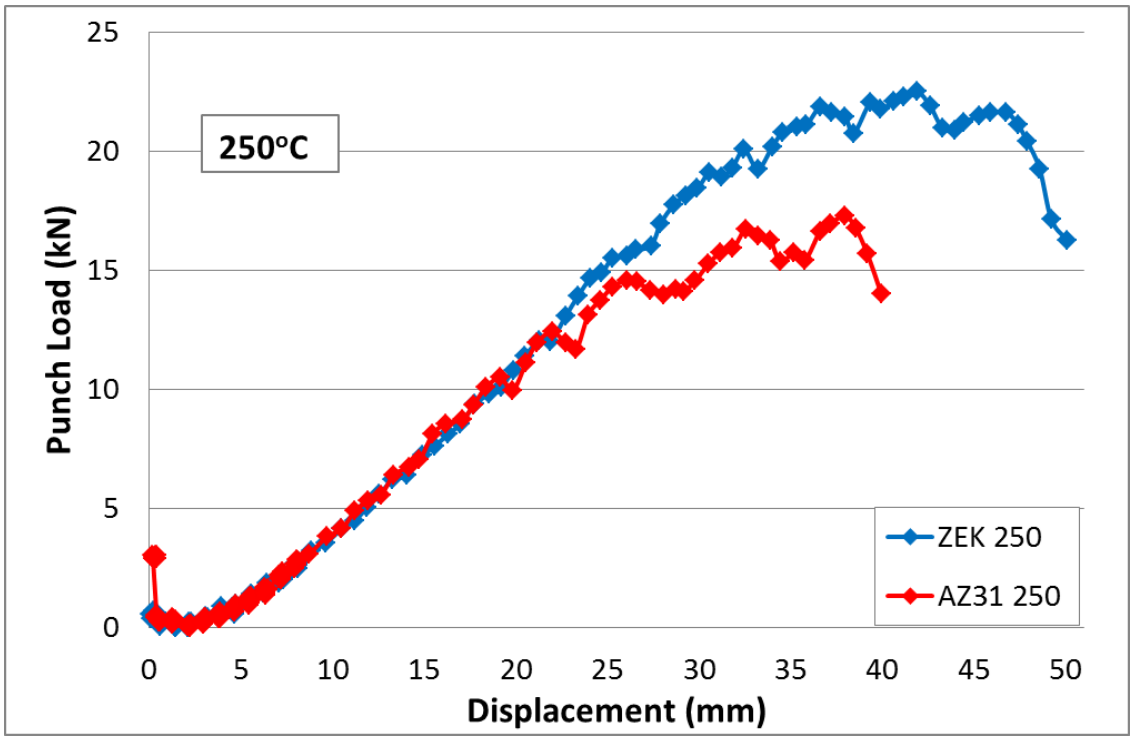
250°C
Punch Load (kN)
Displacement (mm)
ZEK 250
AZ31 250
0
5
10
15
20
25
30
35
40
45
50

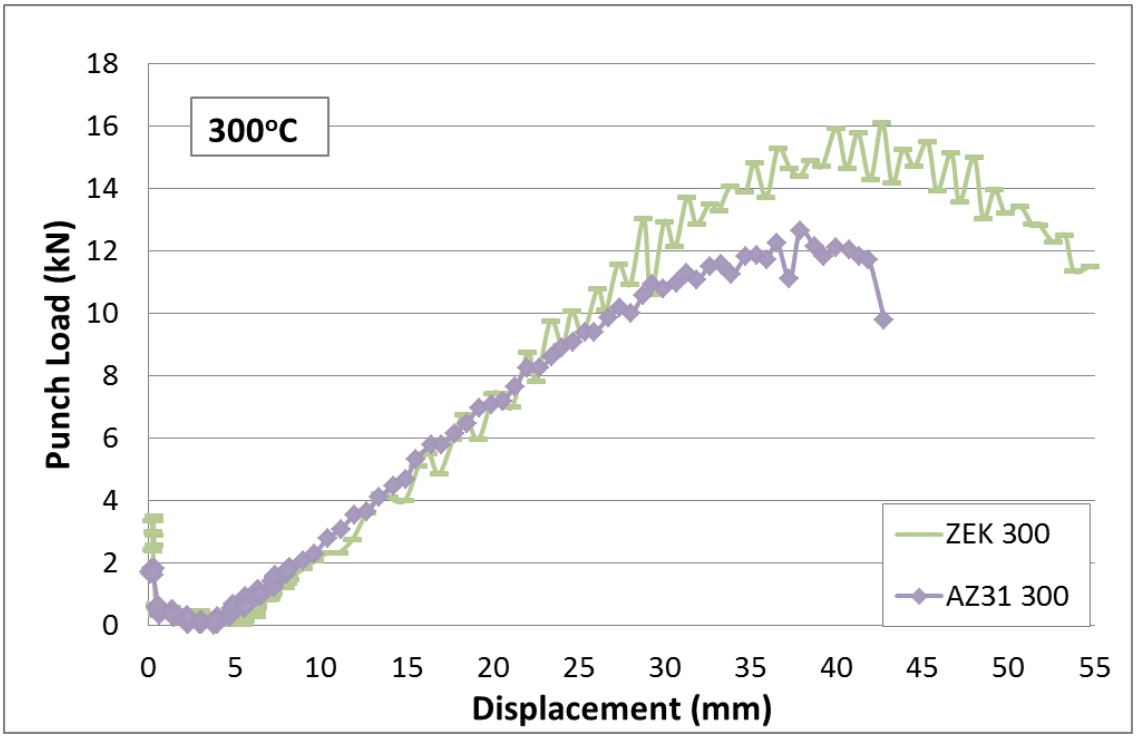
300°C
Punch Load (kN)
Displacement (mm)
ZEK 300
AZ31 300

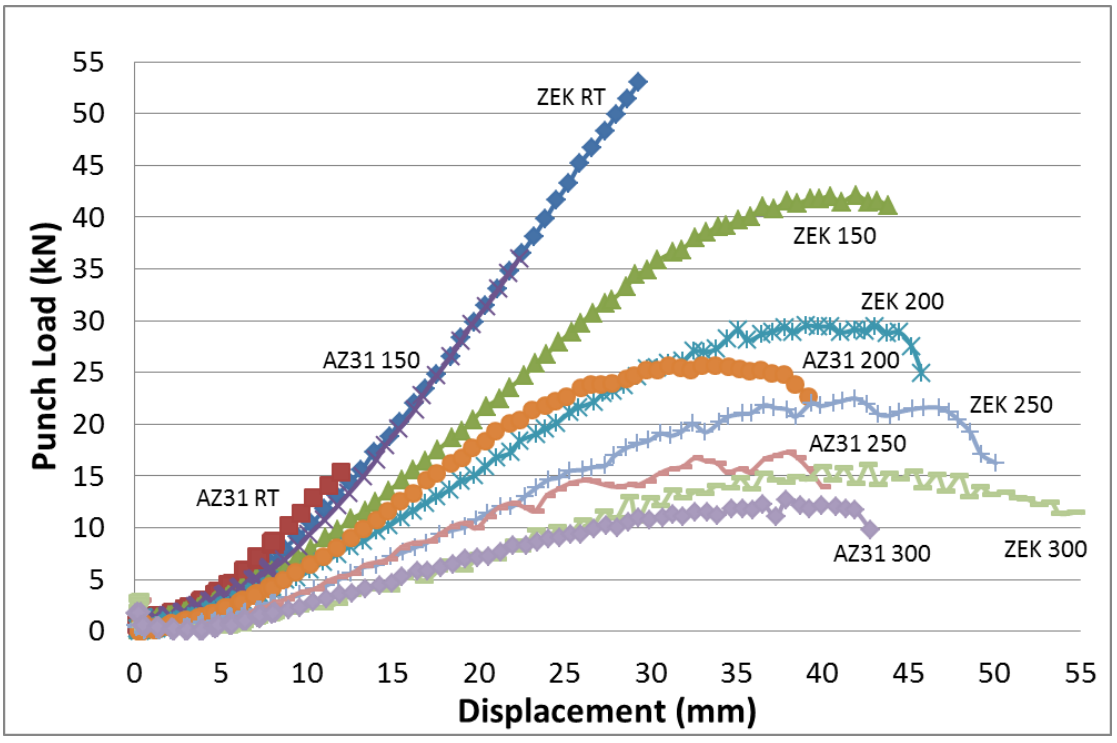
Punch Load (kN)
Displacement (mm)
ZEK RT
ZEK 150
ZEK 200
ZEK 250
ZEK 300
AZ31 150
AZ31 200
AZ31 250
AZ31 300
AZ31 RT

APPENDIX C: ISOTHERMAL DEEP DRAWING PUNCH FORCE VS. PUNCH DISPLACEMENT FOR ZEK100

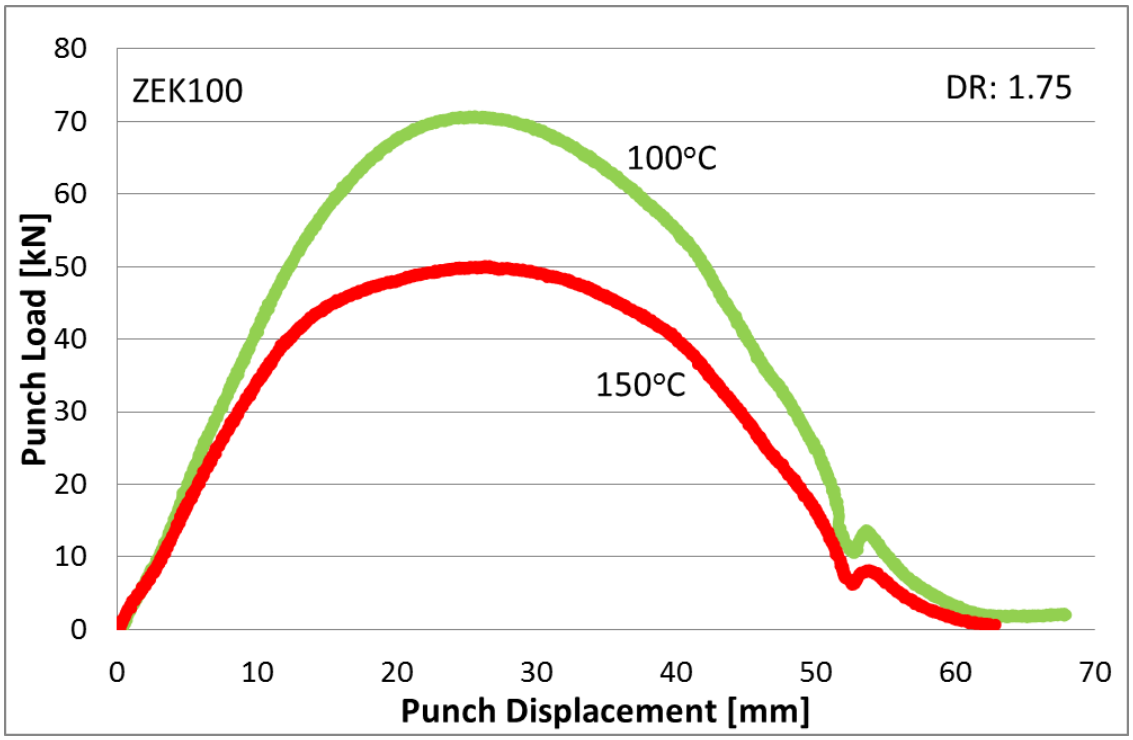

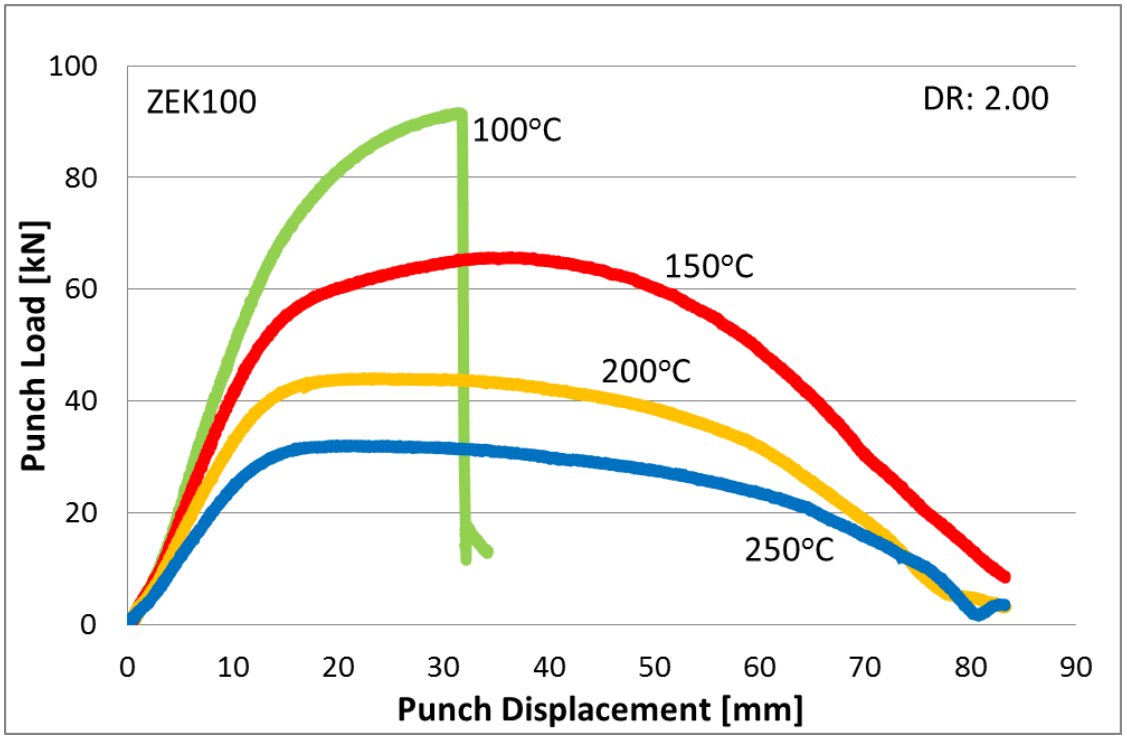

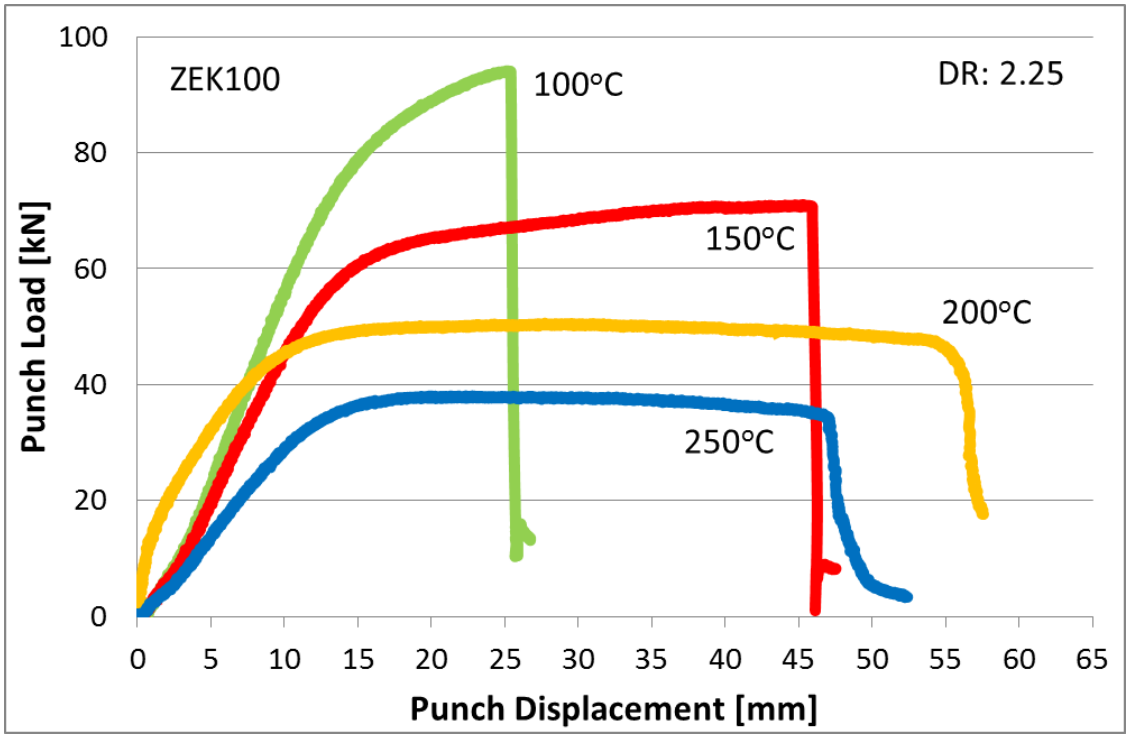
ZEK100
100°C
DR: 2.25
150°C
200°C
250°C
Punch Load [kN]
Punch Displacement [mm]
0
20
40
60
80
100
0
5
10
15
20
25
30
35
40
45
50
55
60
65

APPENDIX D: NON-ISOTHERMAL DEEP DRAWING PUNCH FORCE VS. PUNCH DISPLACEMENT FOR ZEK100

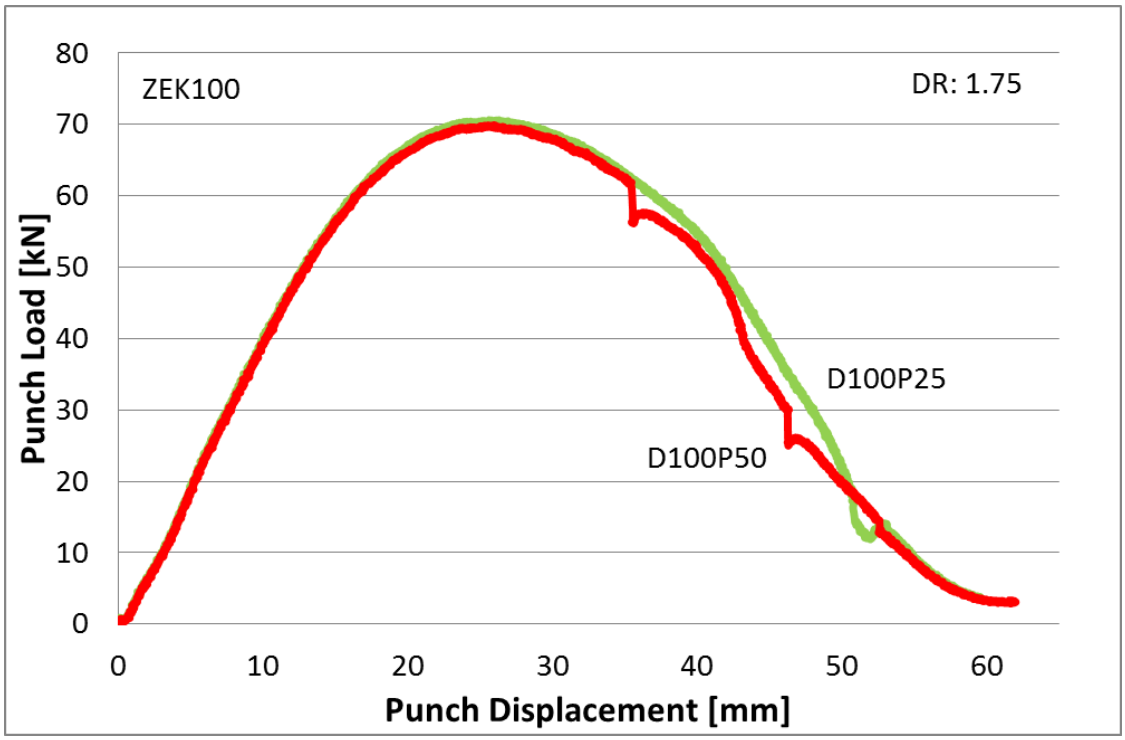

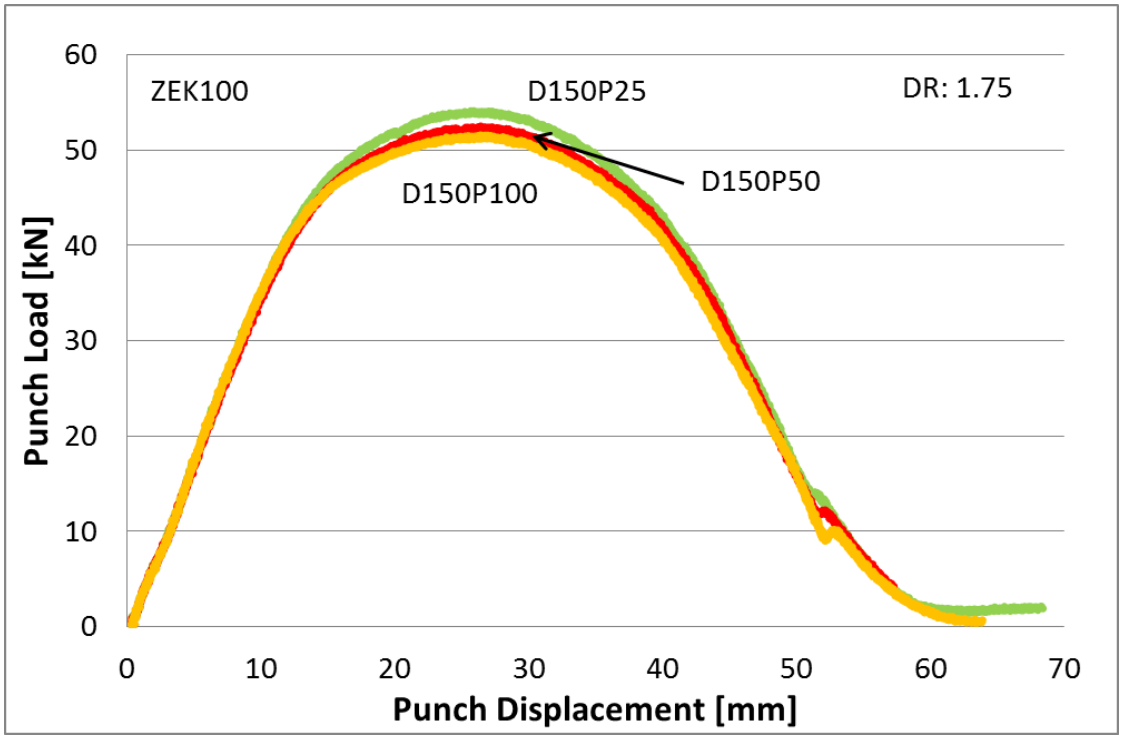

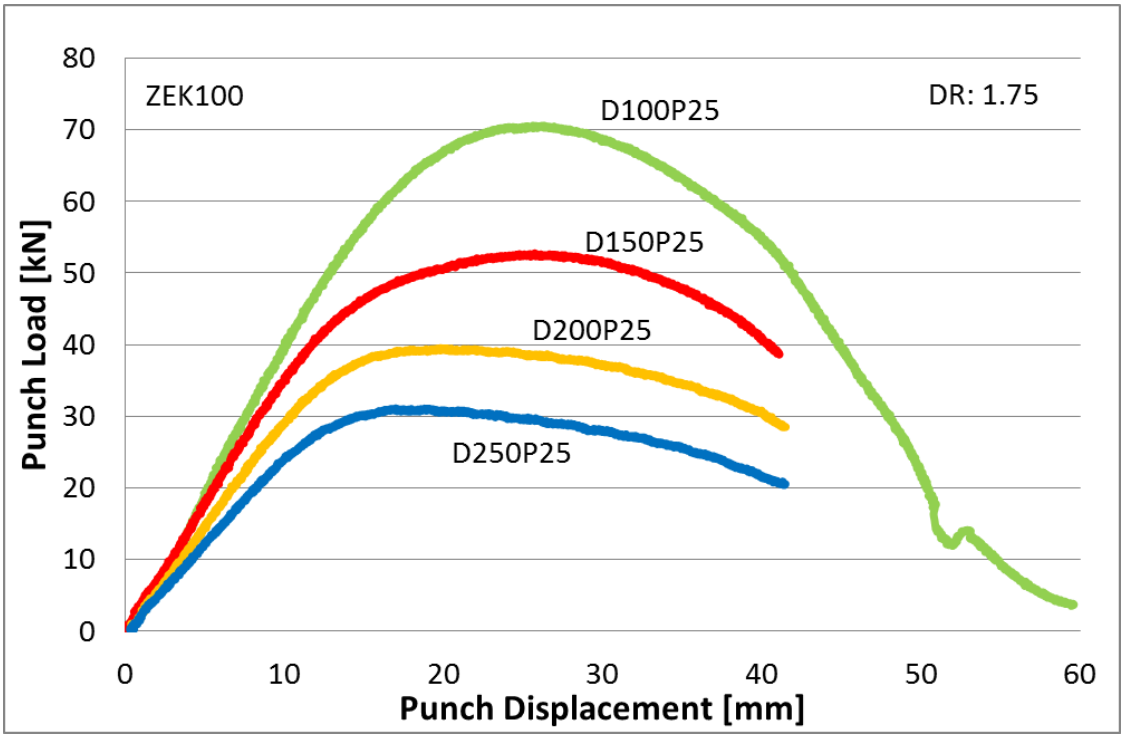
ZEK100
DR: 1.75
D100P25
D150P25
D200P25
D250P25
Punch Load [kN]
Punch Displacement [mm]
0
10
20
30
40
50
60
70
80

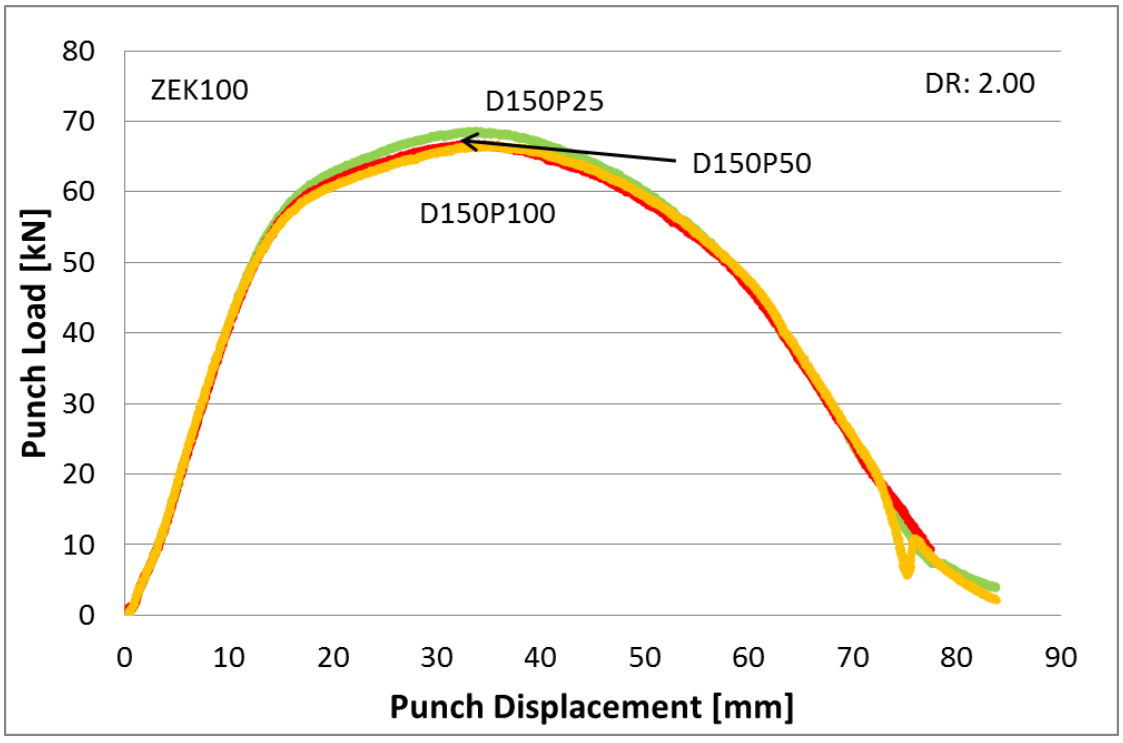
ZEK100
DR: 2.00
D150P25
D150P50
D150P100
Punch Load [kN]
Punch Displacement [mm]
0
10
20
30
40
50
60
70
80
90

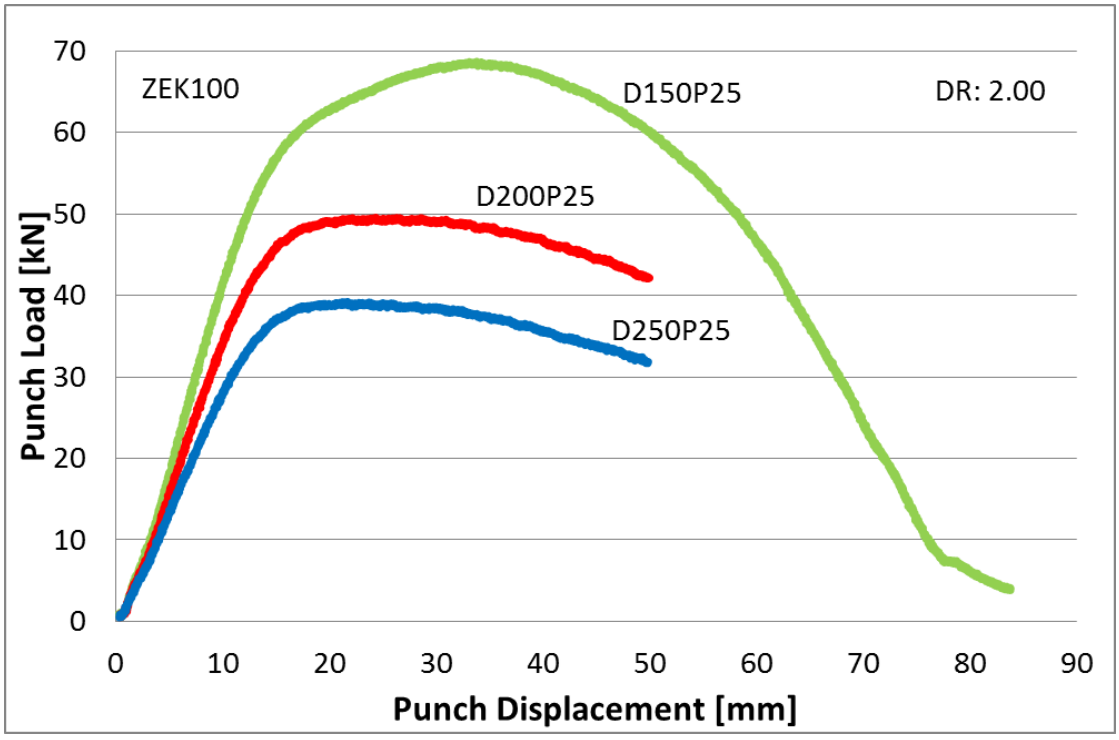
ZEK100
D150P25
DR: 2.00
D200P25
D250P25
Punch Load [kN]
Punch Displacement [mm]
0
10
20
30
40
50
60
70
80
90

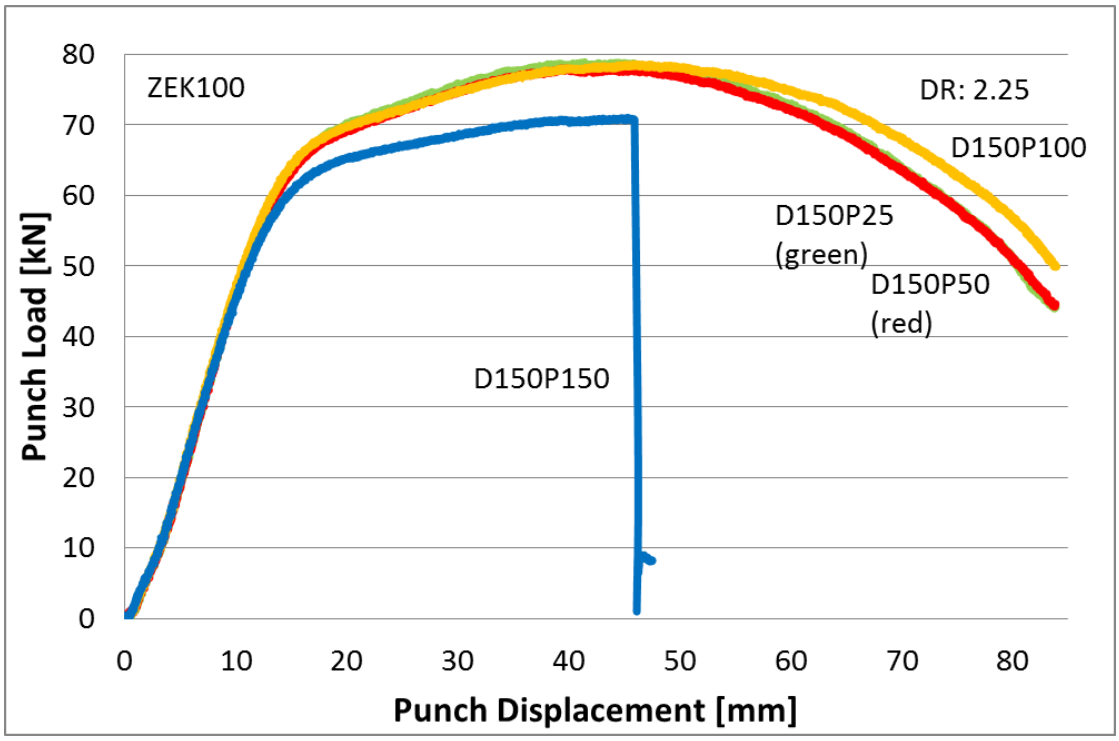
ZEK100
DR: 2.25
D150P100
D150P25
(green)
D150P50
(red)
D150P150
Punch Load [kN]
Punch Displacement [mm]
0
10
20
30
40
50
60
70
80

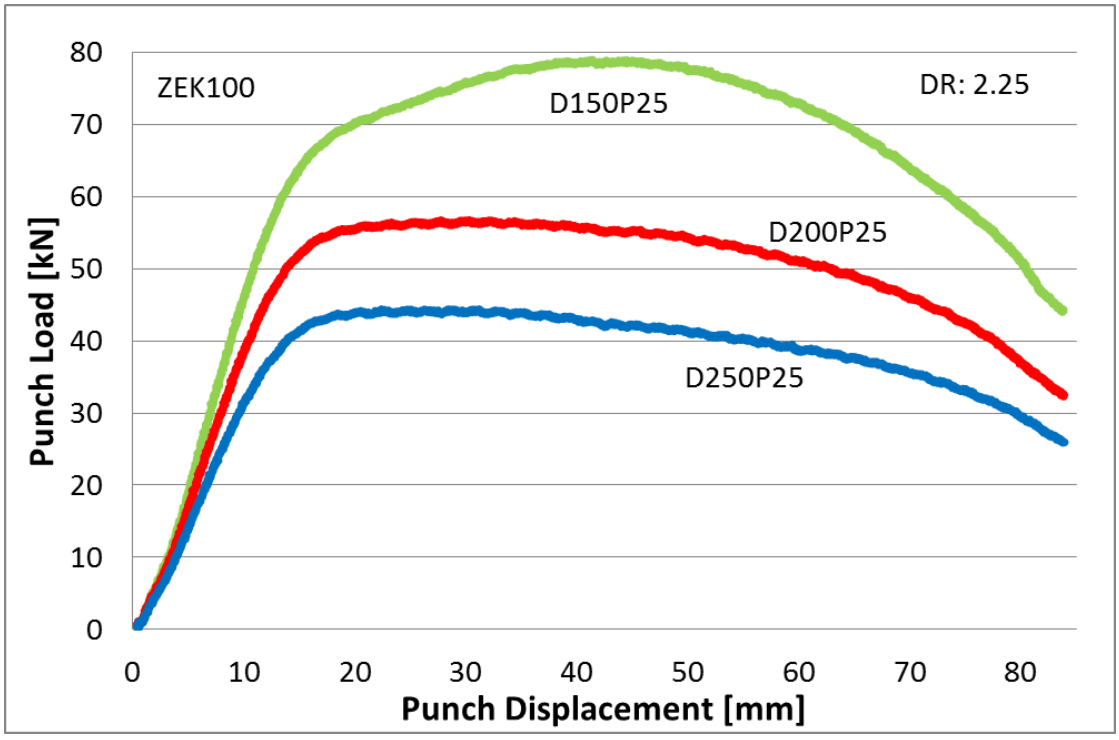
ZEK100
D150P25
DR: 2.25
D200P25
D250P25
Punch Load [kN]
Punch Displacement [mm]
0
10
20
30
40
50
60
70
80

APPENDIX E: ISOTHERMAL EARRING PROFILES FOR ZEK100

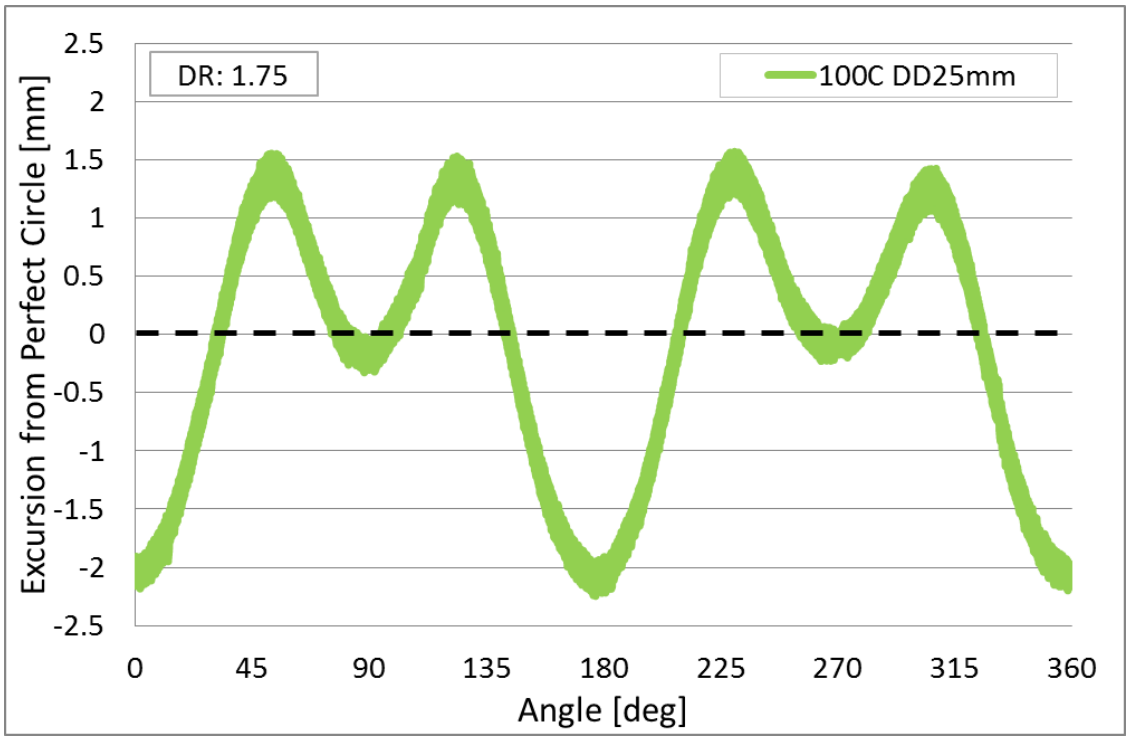

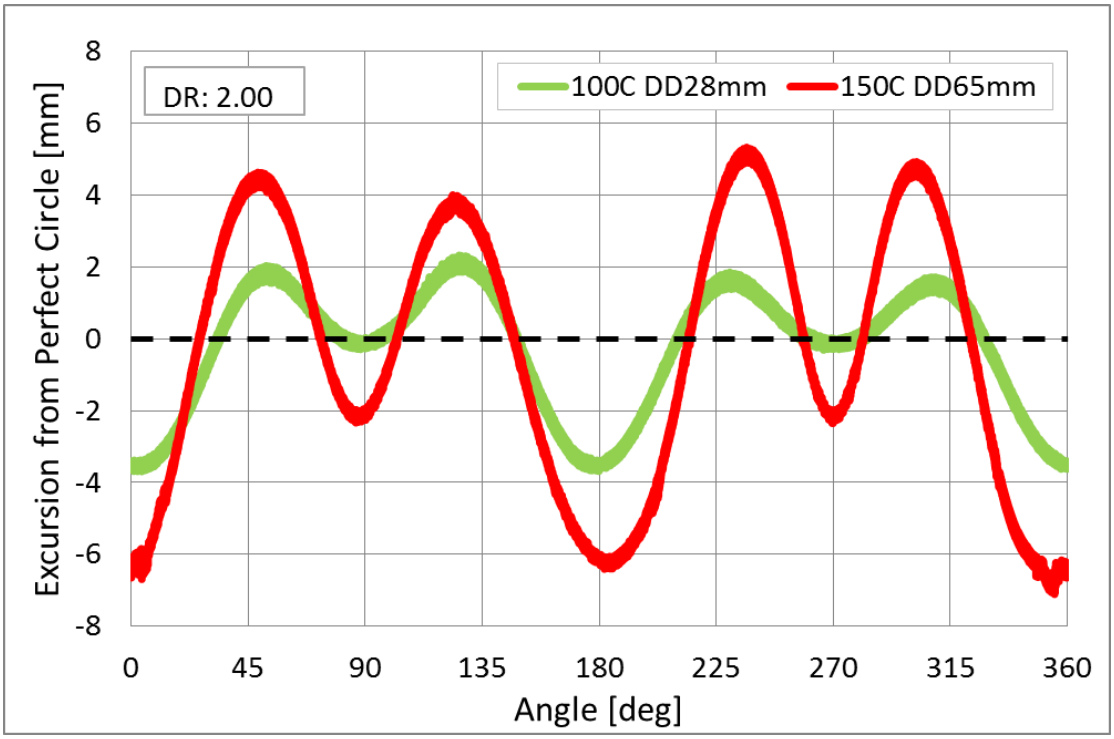

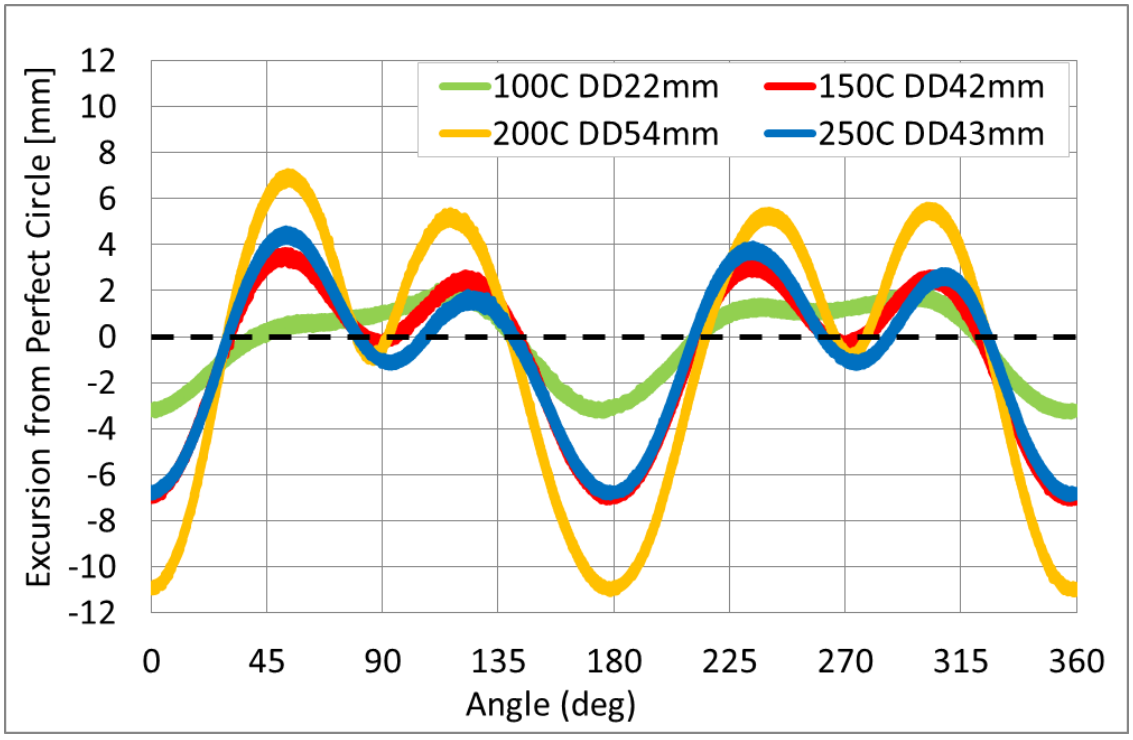
100C DD22mm
150C DD42mm
200C DD54mm
250C DD43mm
Excursion from Perfect Circle [mm]
12
10
8
6
4
2
0
-2
-4
-6
-8
-10
-12
0
45
90
135
180
225
270
315
360
Angle (deg)

APPENDIX F: NON-ISOTHERMAL EARRING PROFILES FOR ZEK100

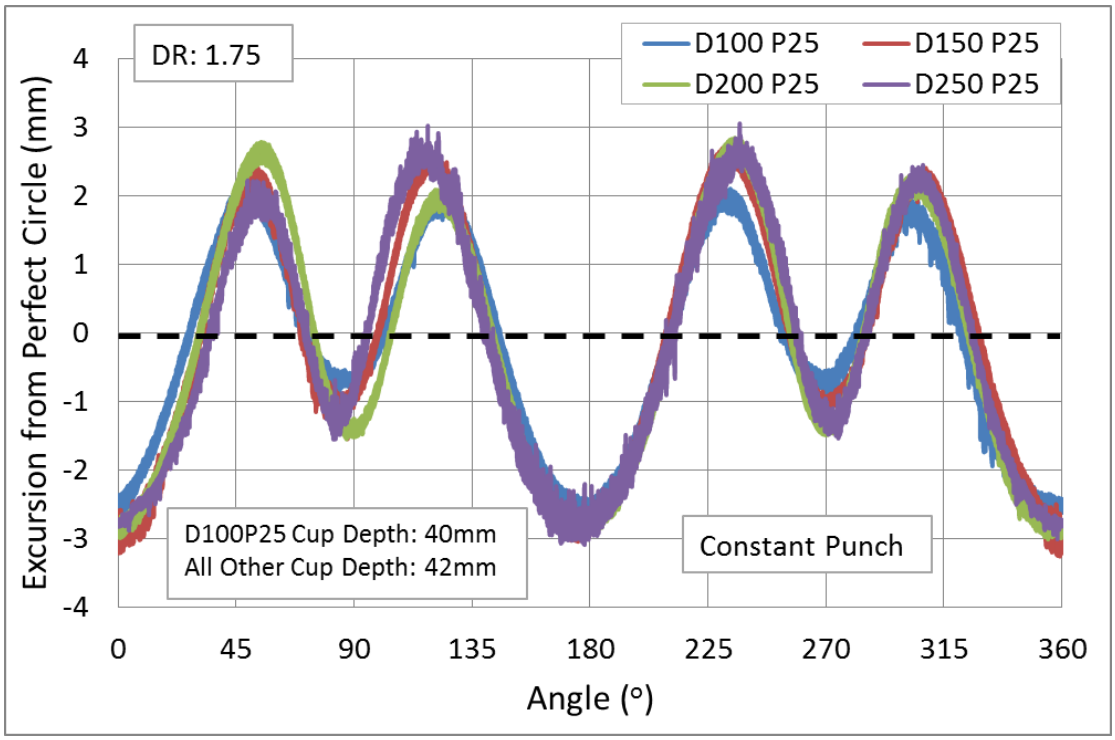

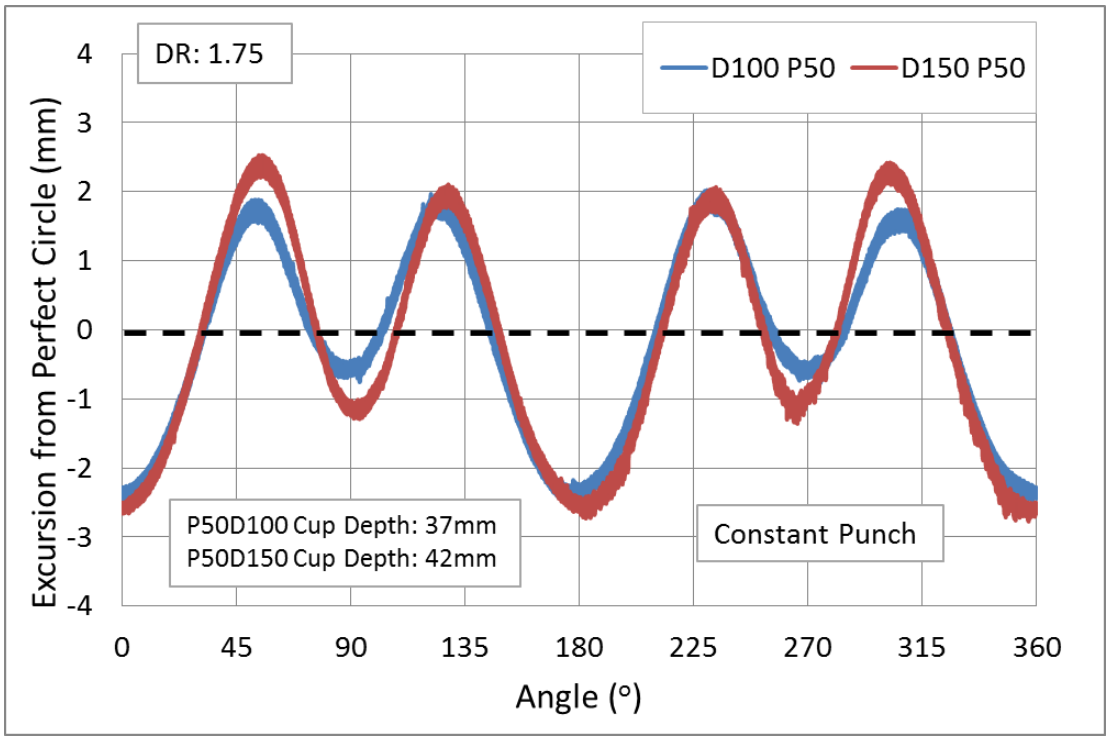

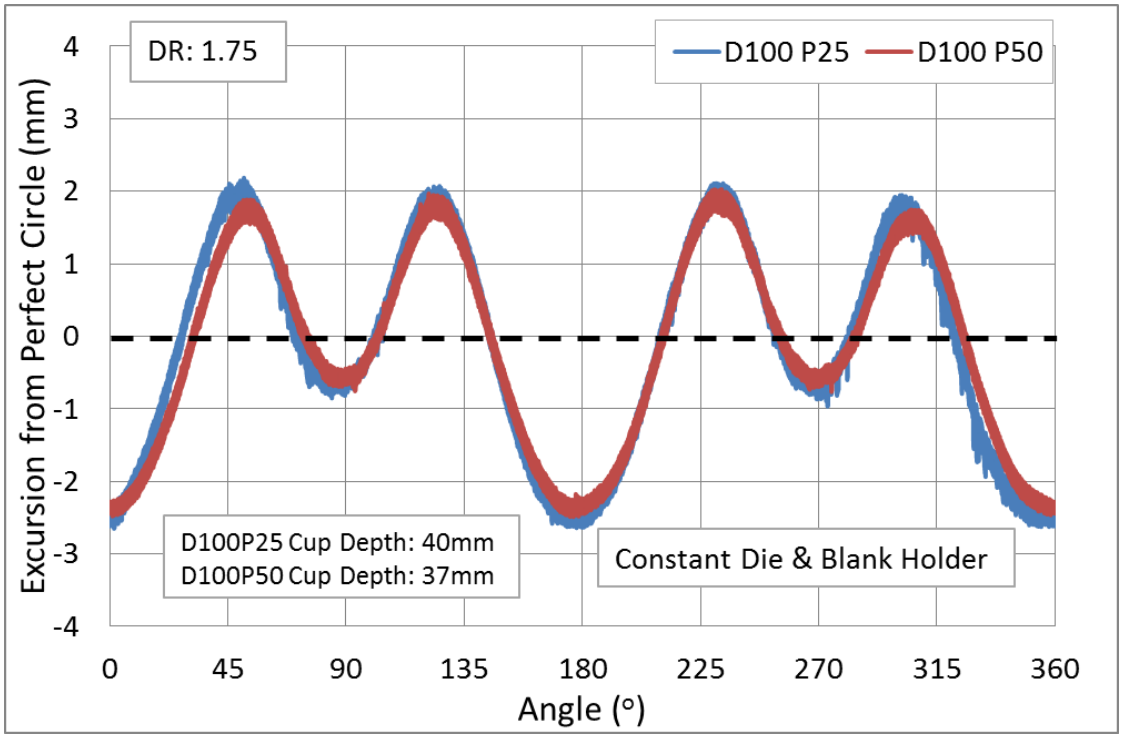
DR: 1.75
D100 P25
D100 P50
Excursion from Perfect Circle (mm)
4
3
2
1
0
-1
-2
-3
-4
D100P25 Cup Depth: 40mm
D100P50 Cup Depth: 37mm
Constant Die & Blank Holder
0
45
90
135
180
225
270
315
360
Angle (°)

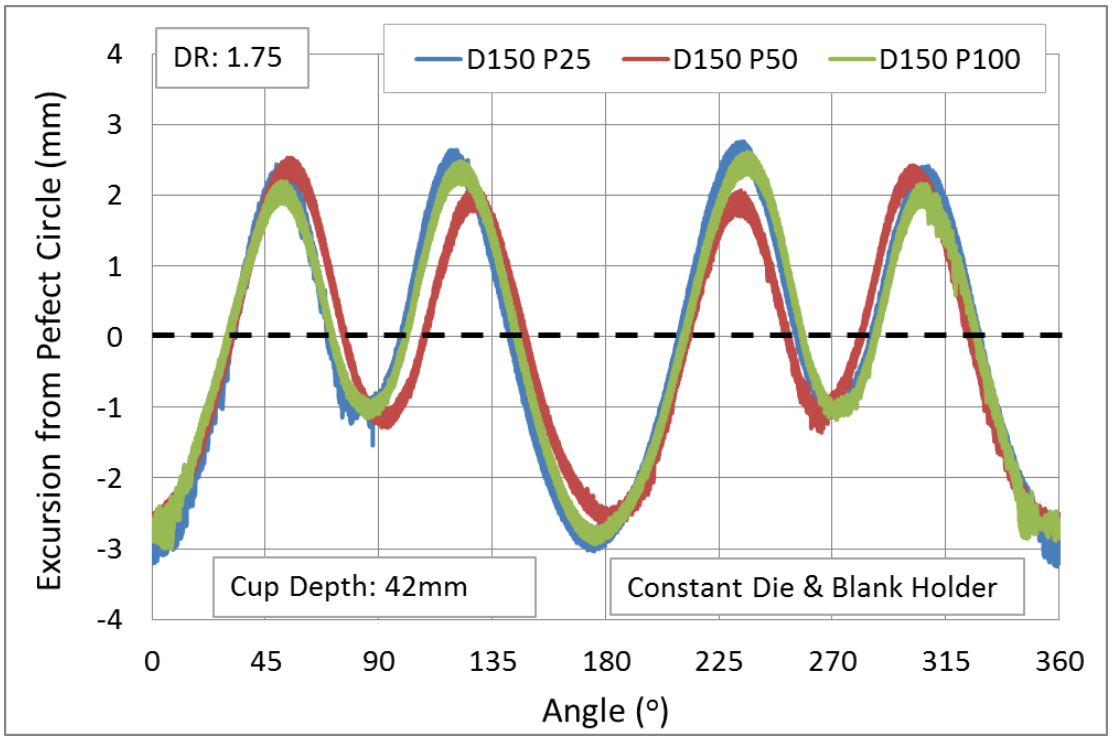
DR: 1.75
D150 P25
D150 P50
D150 P100
Excursion from Pefect Circle (mm)
4
3
2
1
0
-1
-2
-3
-4
Cup Depth: 42mm
Constant Die & Blank Holder
0
45
90
135
180
225
270
315
360
Angle (°)

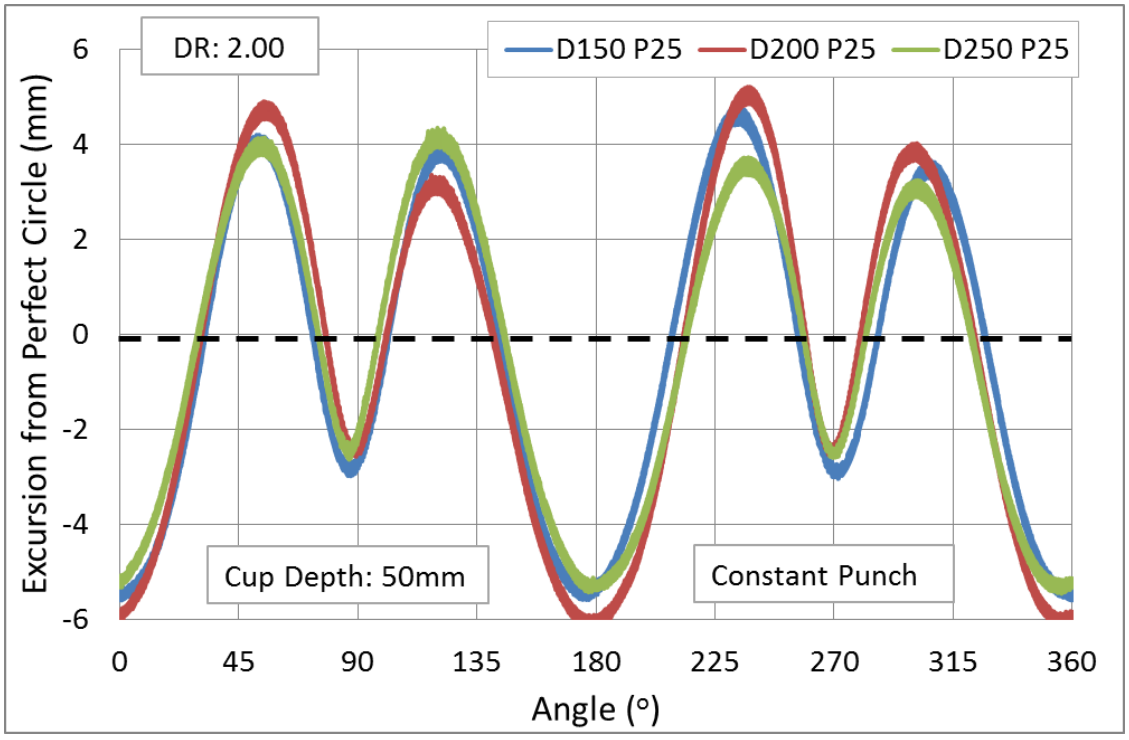
DR: 2.00
D150 P25
D200 P25
D250 P25
Excursion from Perfect Circle (mm)
6
4
2
0
-2
-4
-6
Cup Depth: 50mm
Constant Punch
0
45
90
135
180
225
270
315
360
Angle (°)

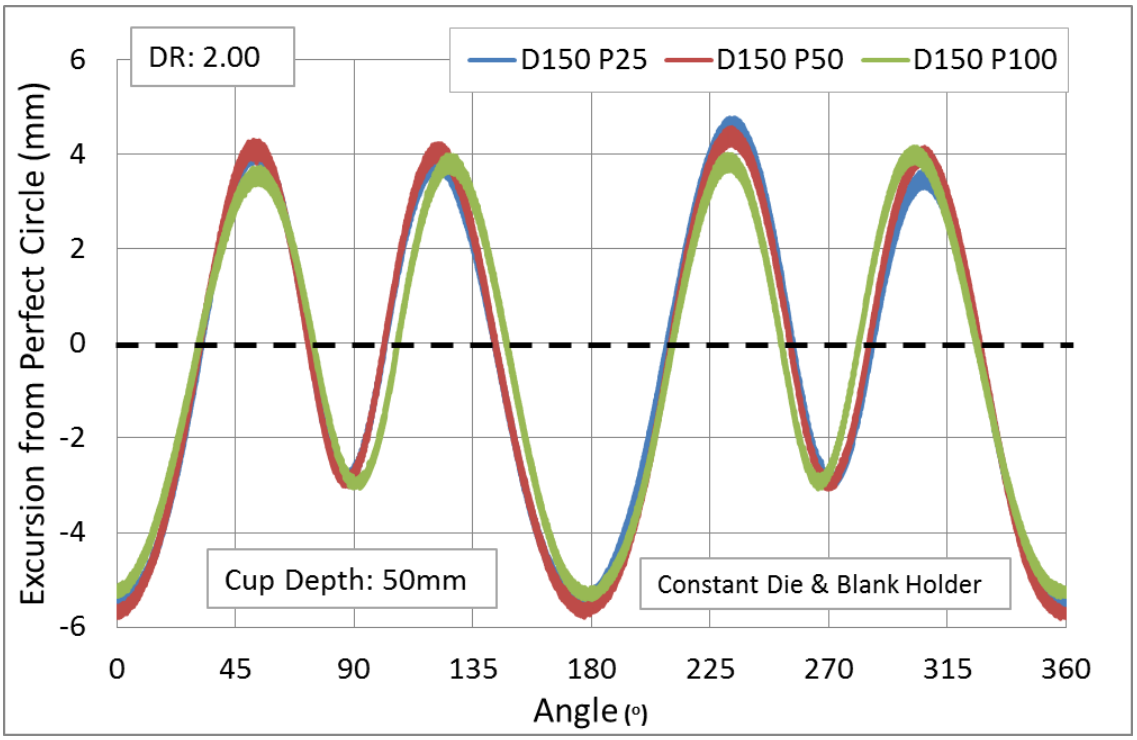
DR: 2.00
D150 P25
D150 P50
D150 P100
Excursion from Perfect Circle (mm)
6
4
2
0
-2
-4
-6
Cup Depth: 50mm
Constant Die & Blank Holder
0
45
90
135
180
225
270
315
360
Angle (°)

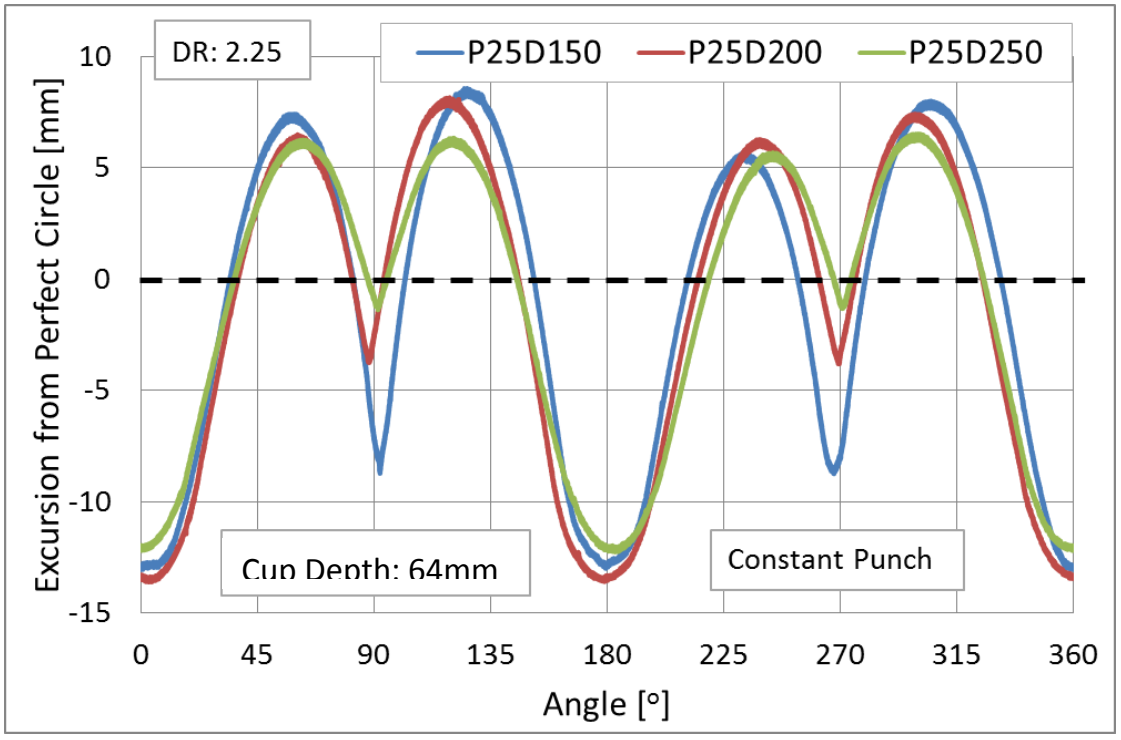
DR: 2.25
P25D150
P25D200
P25D250
Excursion from Perfect Circle [mm]
10
5
0
-5
-10
-15
Cup Depth: 64mm
Constant Punch
0
45
90
135
180
225
270
315
360
Angle [°]

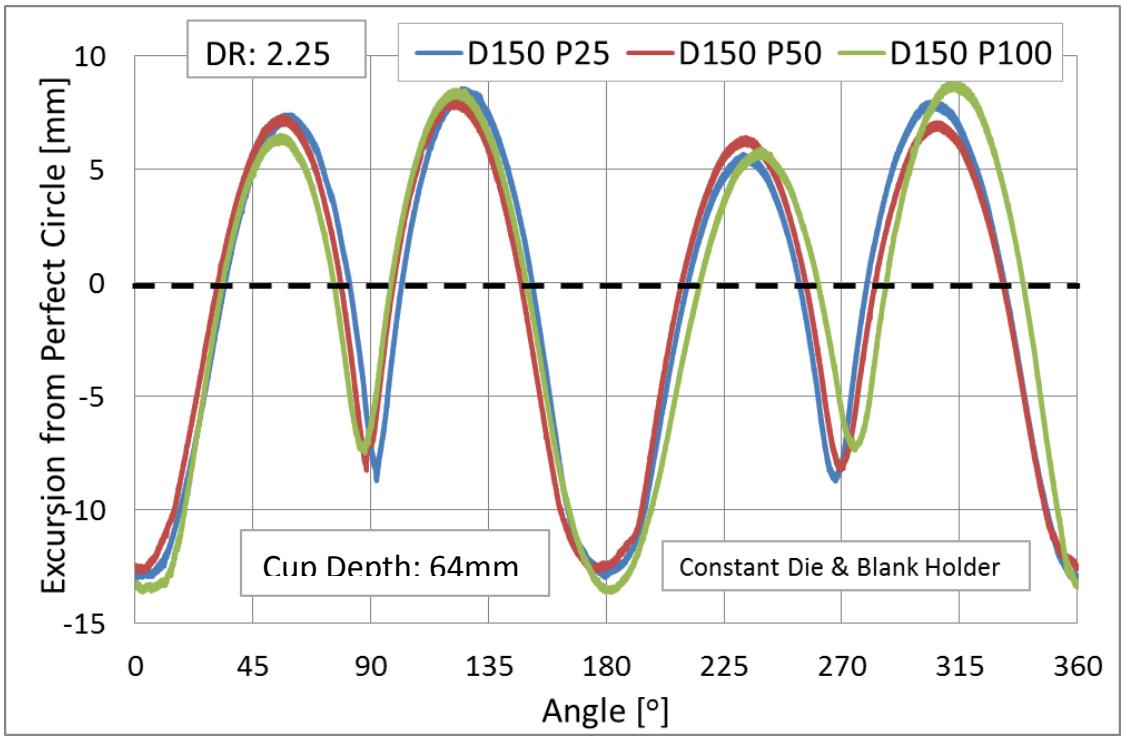
DR: 2.25
D150 P25
D150 P50
D150 P100
Excursion from Perfect Circle [mm]
10
5
0
-5
-10
-15
Cup Depth: 64mm
Constant Die & Blank Holder
0
45
90
135
180
225
270
315
360
Angle [°]

APPENDIX G: ISOTHERMAL STRAIN MEASUREMENTS FOR ZEK100

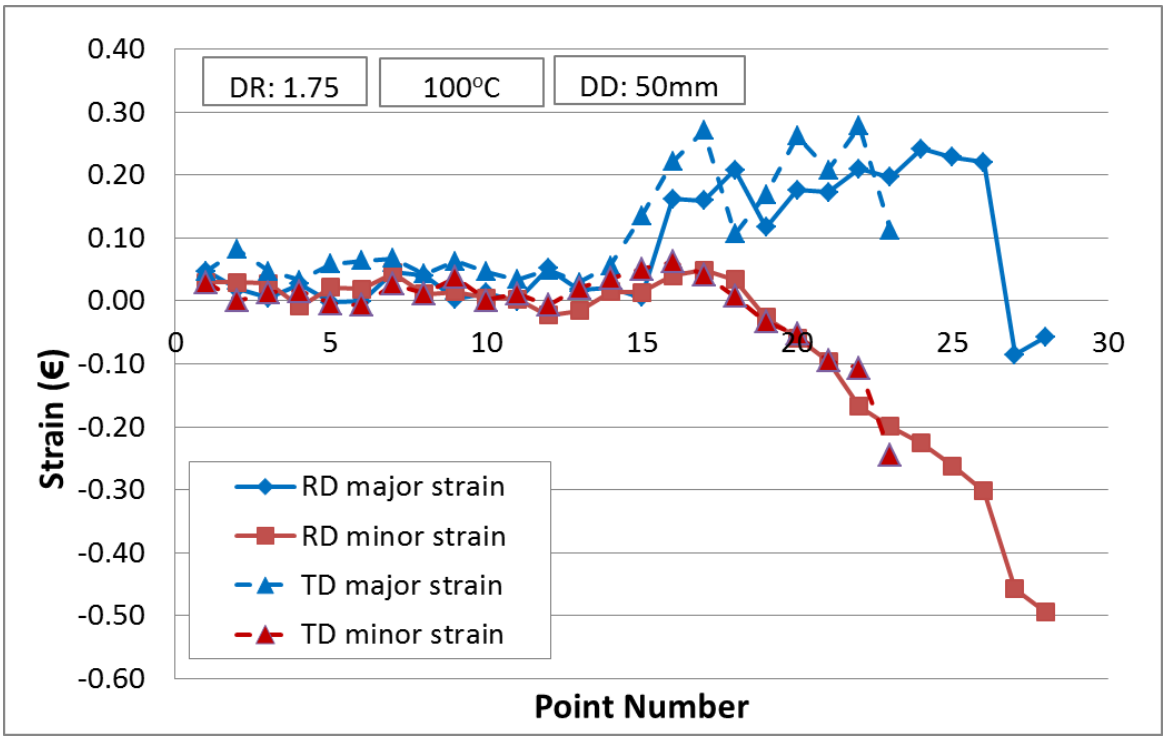

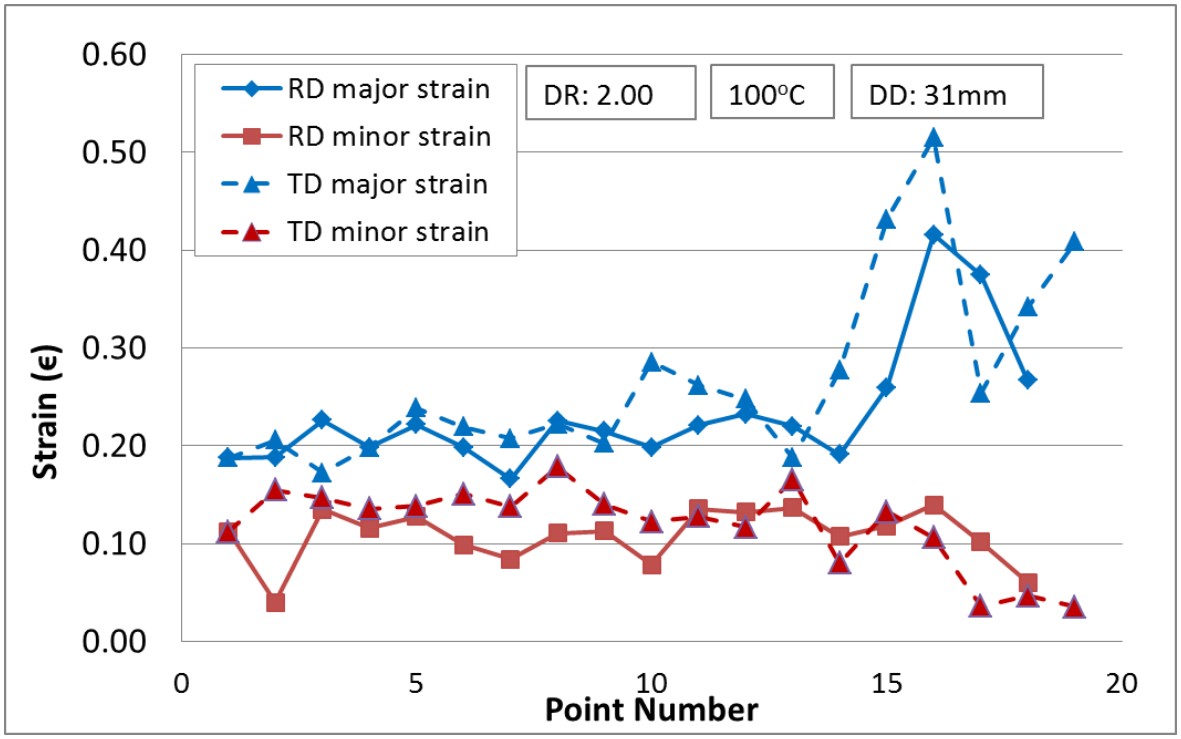

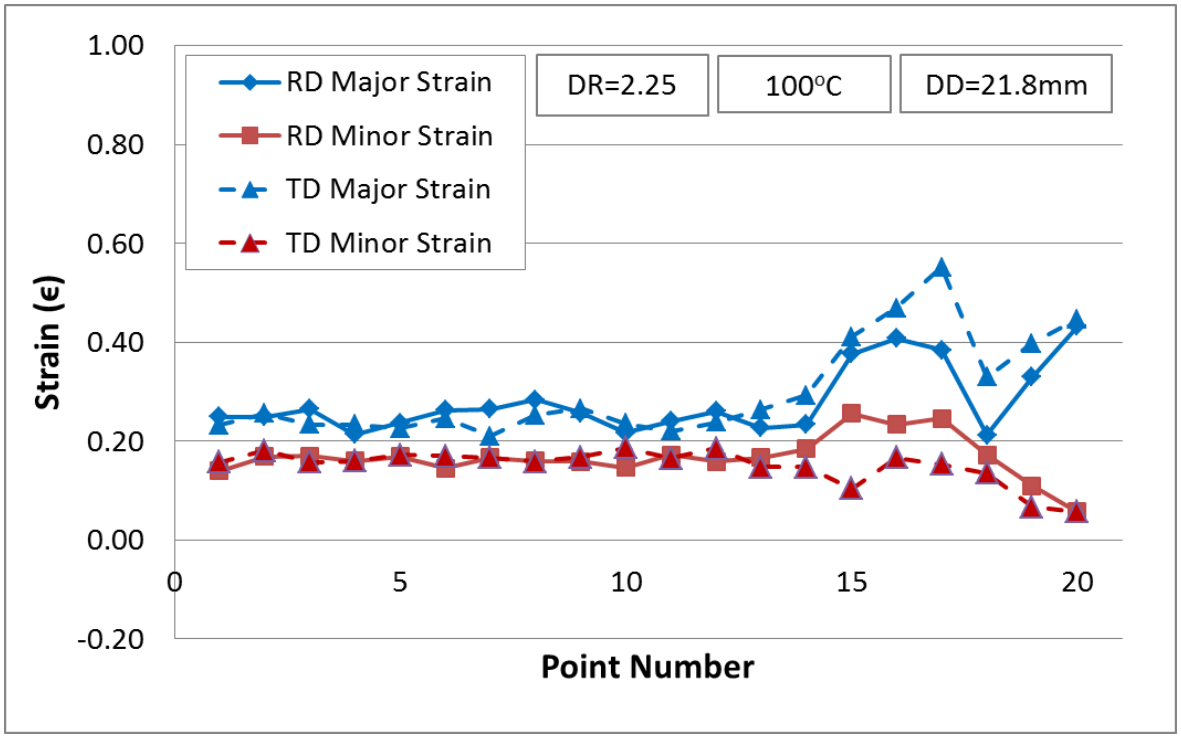
RD Major Strain
RD Minor Strain
TD Major Strain
TD Minor Strain
DR=2.25
100°C
DD=21.8mm
Strain (€)
Point Number
1.00
0.80
0.60
0.40
0.20
0.00
-0.20
0
5
10
15
20

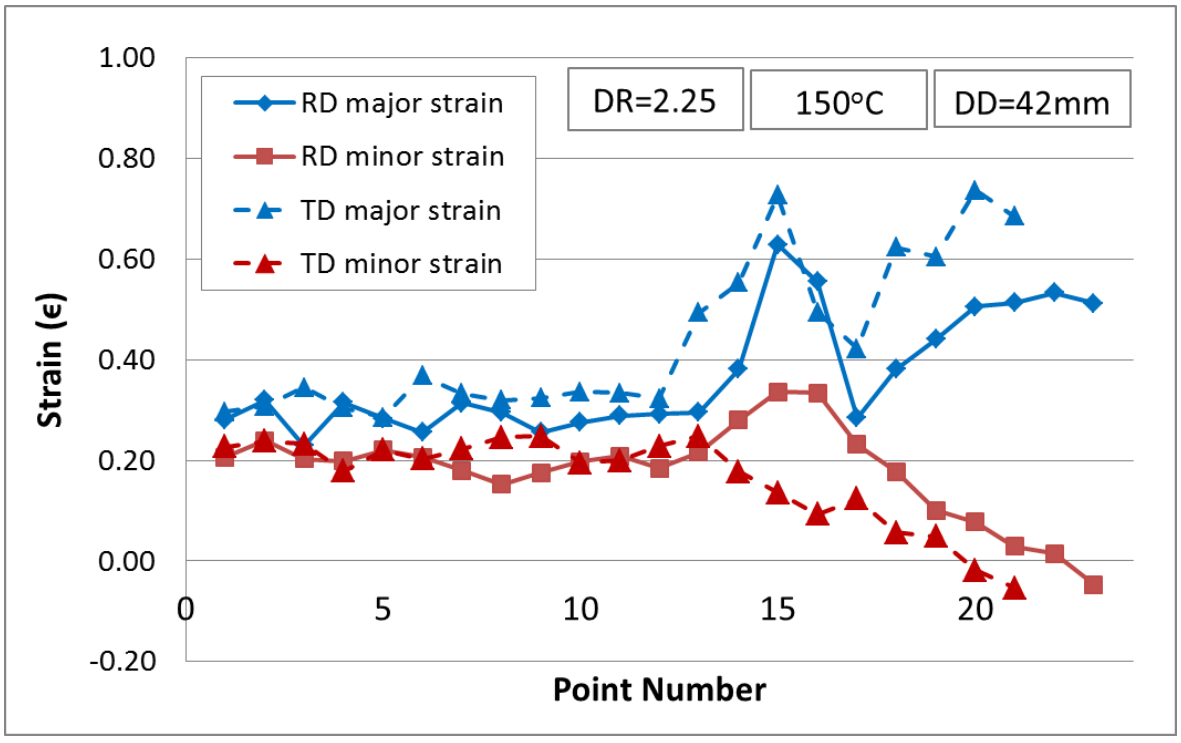
RD major strain
RD minor strain
TD major strain
TD minor strain
DR=2.25
150°C
DD=42mm
Strain (€)
Point Number
1.00
0.80
0.60
0.40
0.20
0.00
-0.20
0
5
10
15
20

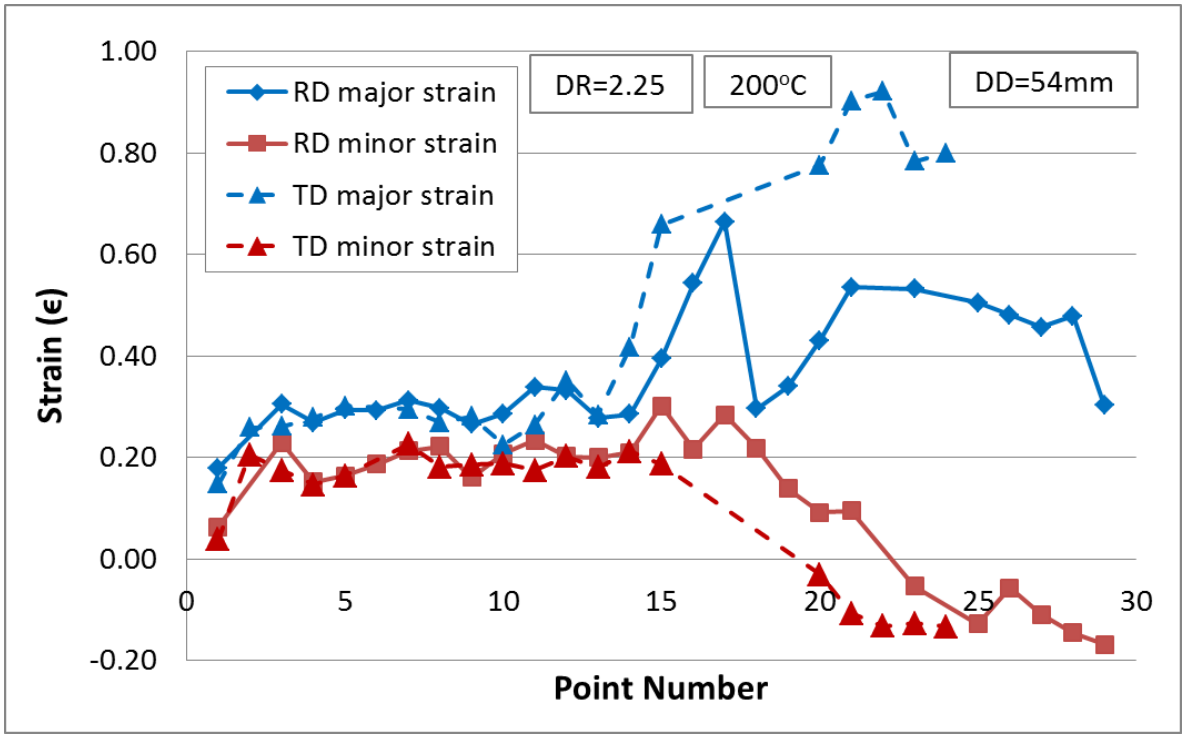
RD major strain
RD minor strain
TD major strain
TD minor strain
DR=2.25
200°C
DD=54mm
Strain (ϵ)
Point Number
1.00
0.80
0.60
0.40
0.20
0.00
-0.20
0
5
10
15
20
25
30

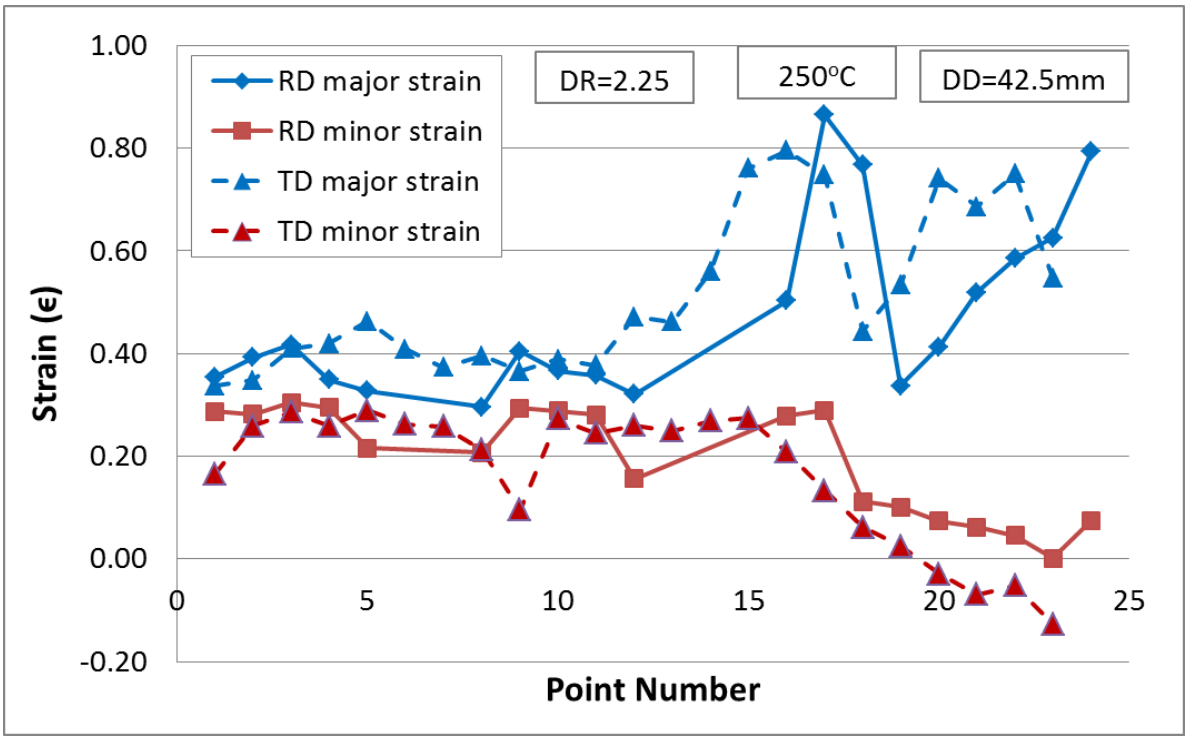
RD major strain
RD minor strain
TD major strain
TD minor strain
DR=2.25
250°C
DD=42.5mm
Strain (ϵ)
Point Number
1.00
0.80
0.60
0.40
0.20
0.00
-0.20
0
5
10
15
20
25

APPENDIX H: ISOTHERMAL THICKNESS PROFILES FOR ZEK100

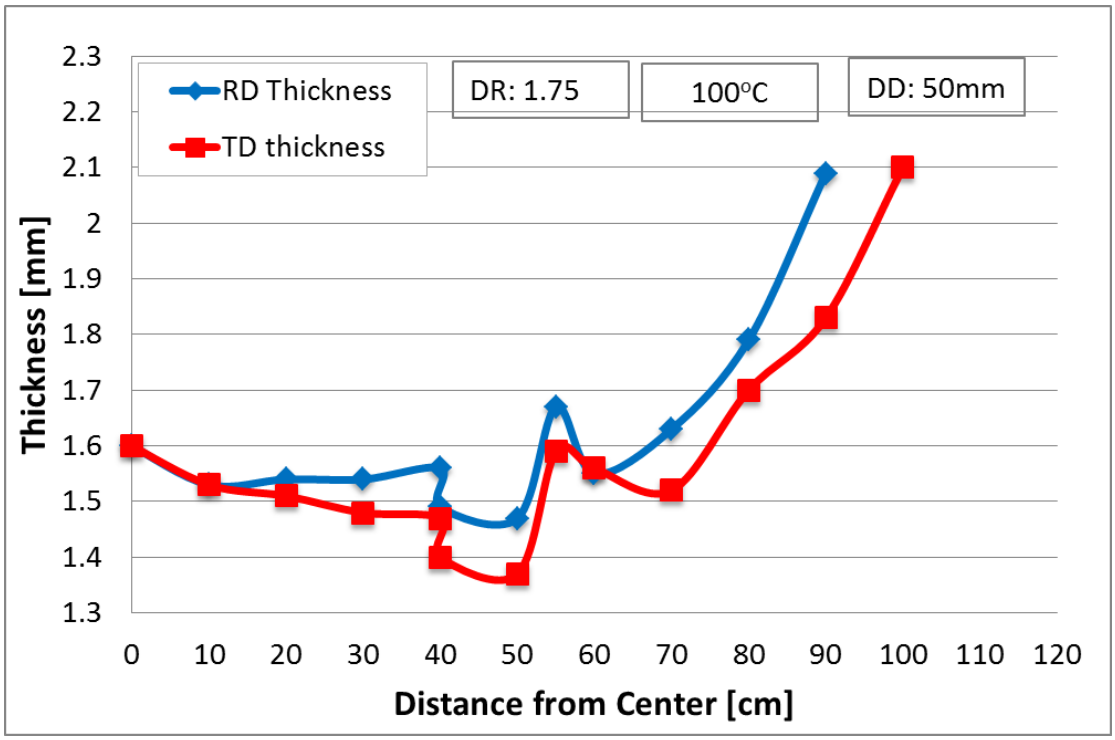

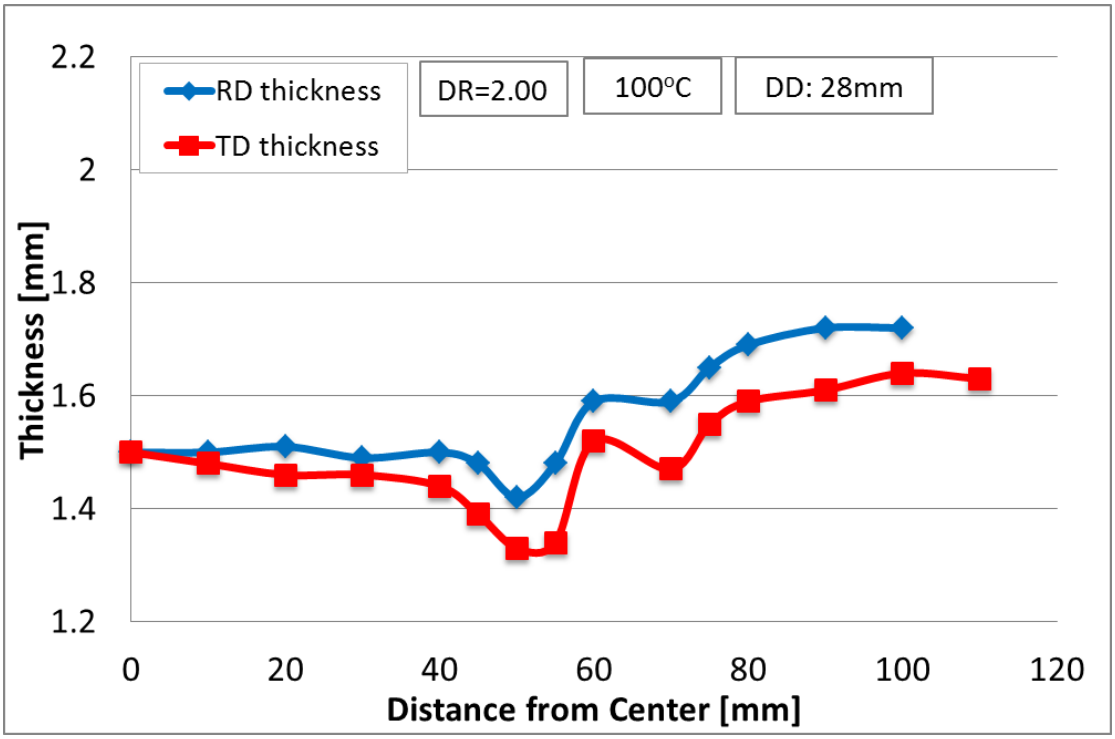

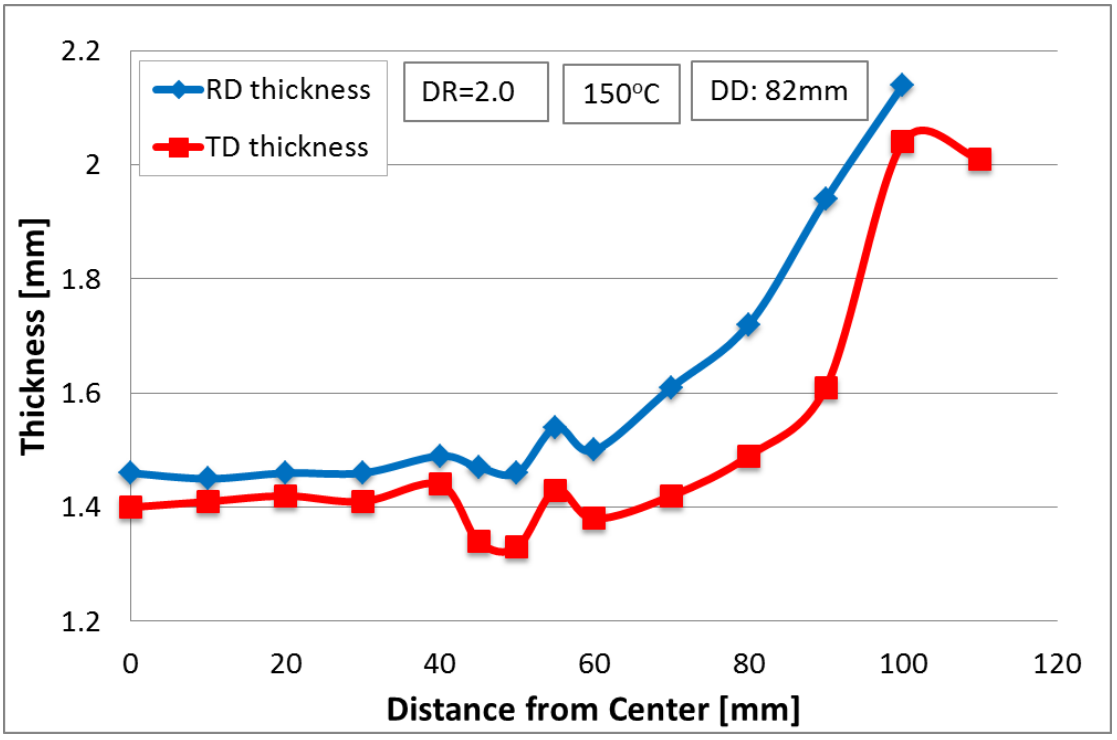
RD thickness
TD thickness
DR=2.0
150°C
DD: 82mm
Thickness [mm]
2.2
2
1.8
1.6
1.4
1.2
0
20
40
60
80
100
120
Distance from Center [mm]

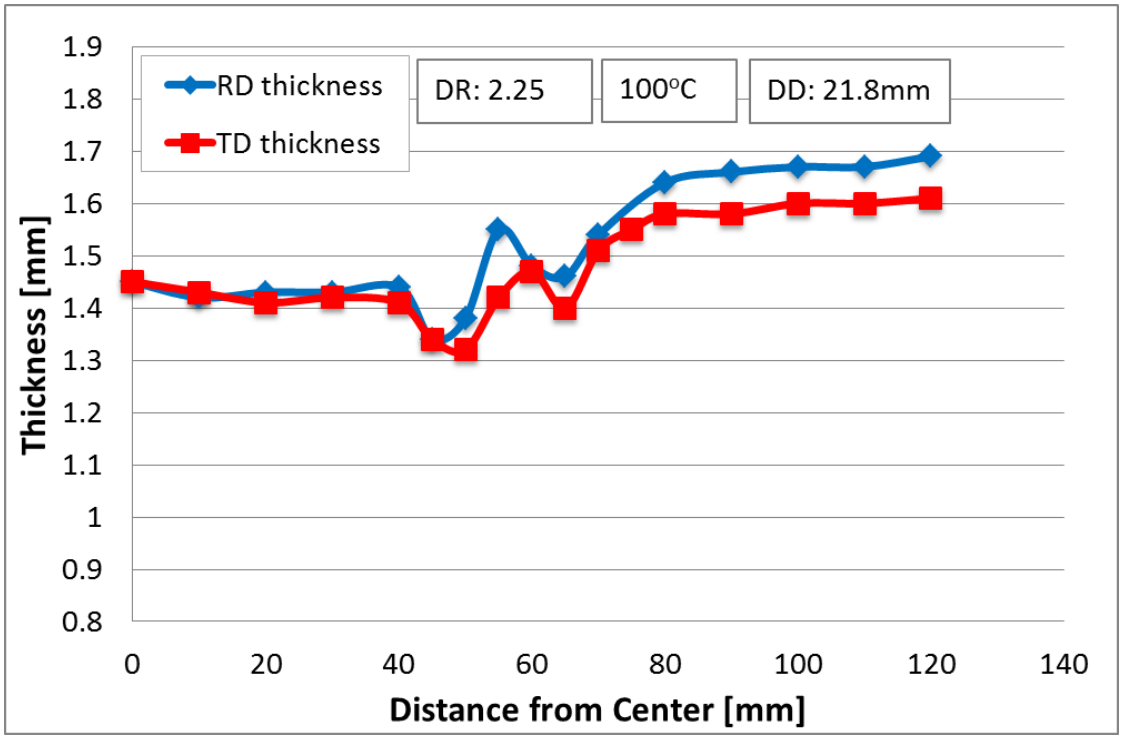
RD thickness
TD thickness
DR: 2.25
100°C
DD: 21.8mm
Thickness [mm]
1.9
1.8
1.7
1.6
1.5
1.4
1.3
1.2
1.1
1
0.9
0.8
0
20
40
60
80
100
120
140
Distance from Center [mm]

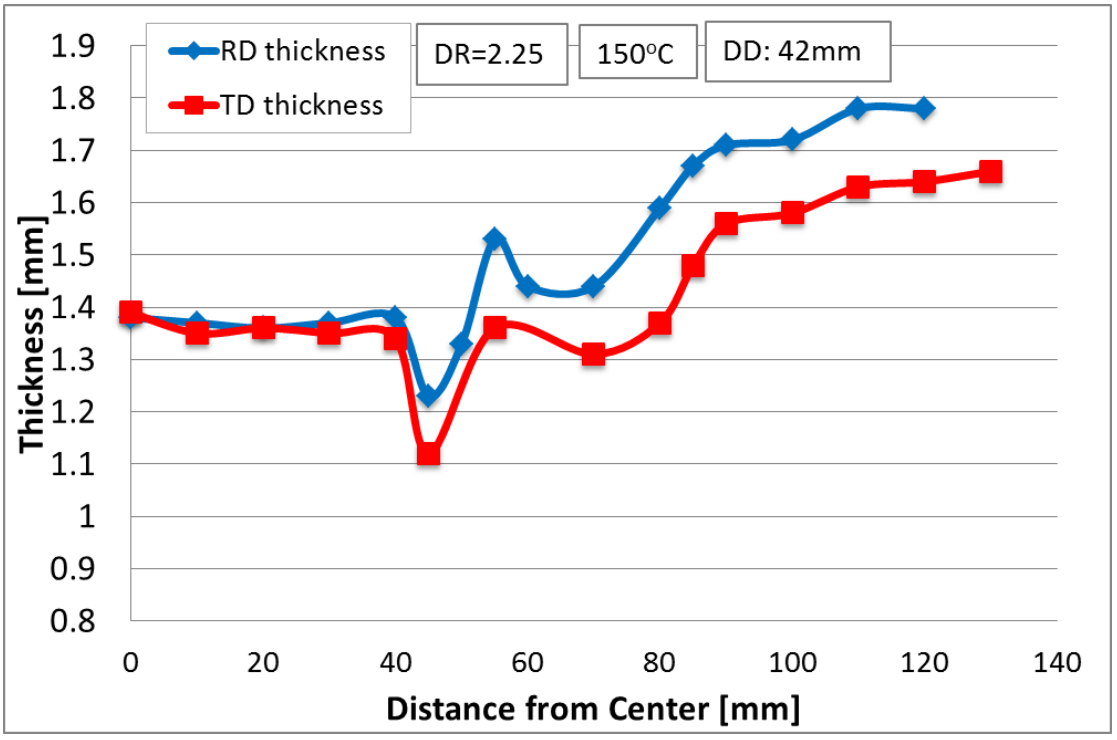
RD thickness
TD thickness
DR=2.25
150°C
DD: 42mm
Thickness [mm]
1.9
1.8
1.7
1.6
1.5
1.4
1.3
1.2
1.1
1
0.9
0.8
0
20
40
60
80
100
120
140
Distance from Center [mm]

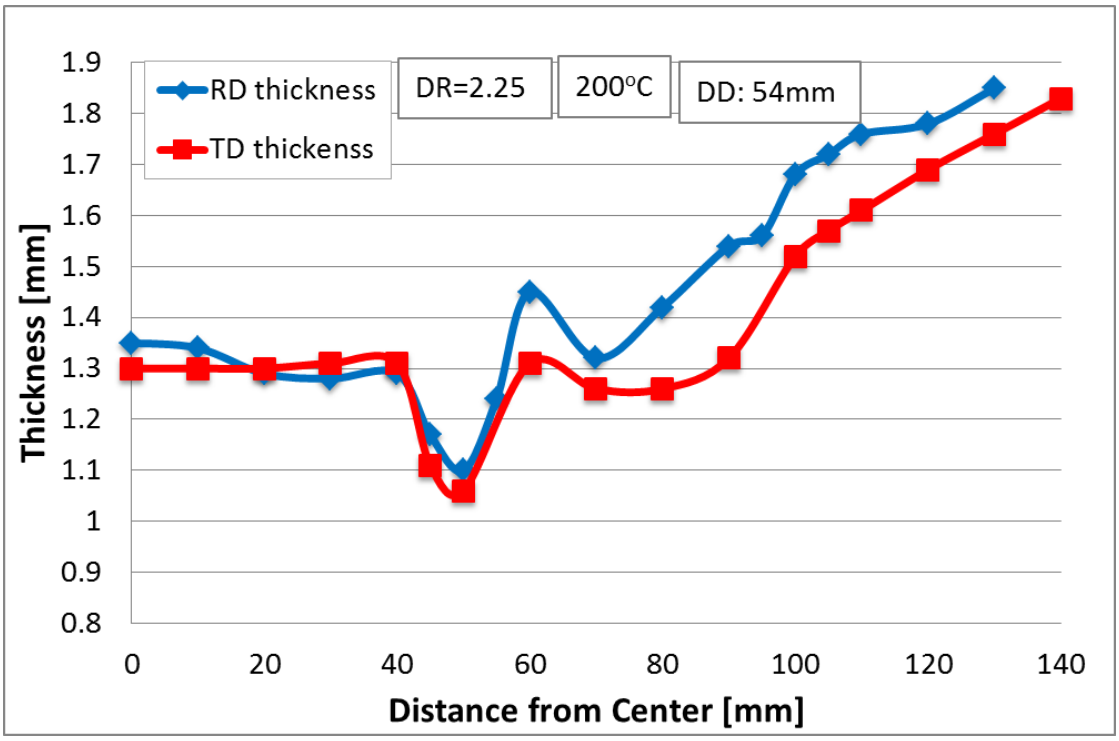
RD thickness
TD thickenss
DR=2.25
200°C
DD: 54mm
Thickness [mm]
1.9
1.8
1.7
1.6
1.5
1.4
1.3
1.2
1.1
1
0.9
0.8
0
20
40
60
80
100
120
140
Distance from Center [mm]

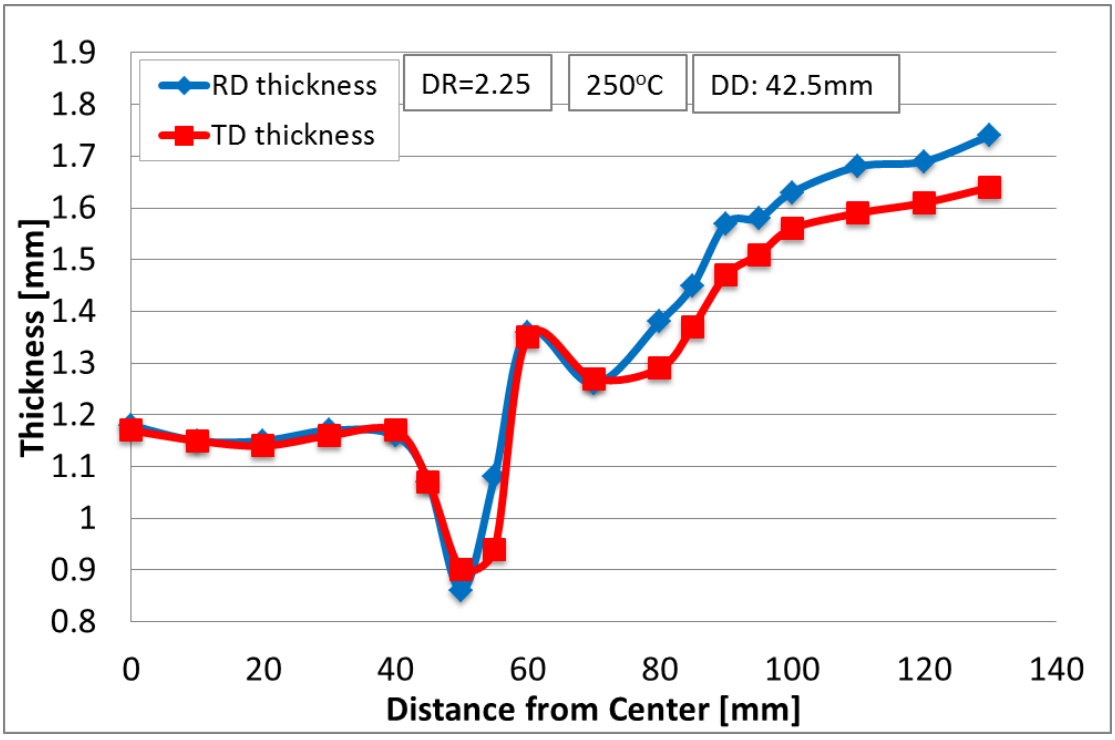
RD thickness
TD thickness
DR=2.25
250°C
DD: 42.5mm
Thickness [mm]
1.9
1.8
1.7
1.6
1.5
1.4
1.3
1.2
1.1
1
0.9
0.8
0
20
40
60
80
100
120
140
Distance from Center [mm]

APPENDIX I: NON-ISOTHERMAL STRAIN MEASUREMENTS FOR ZEK100

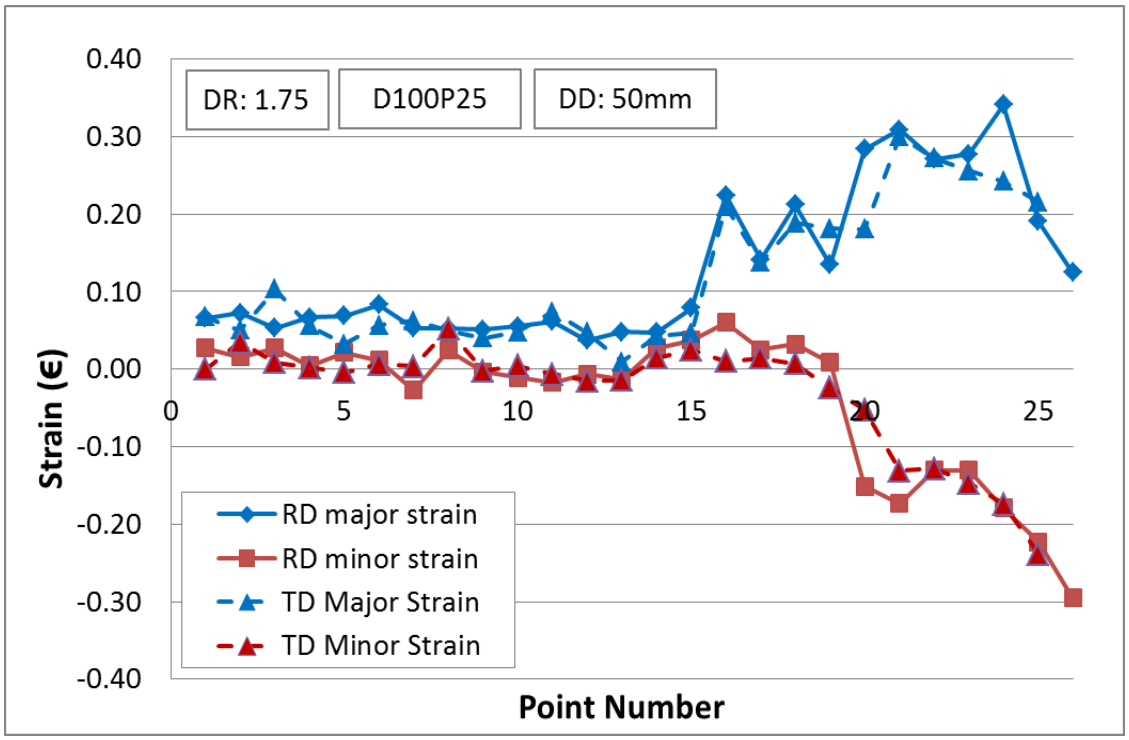

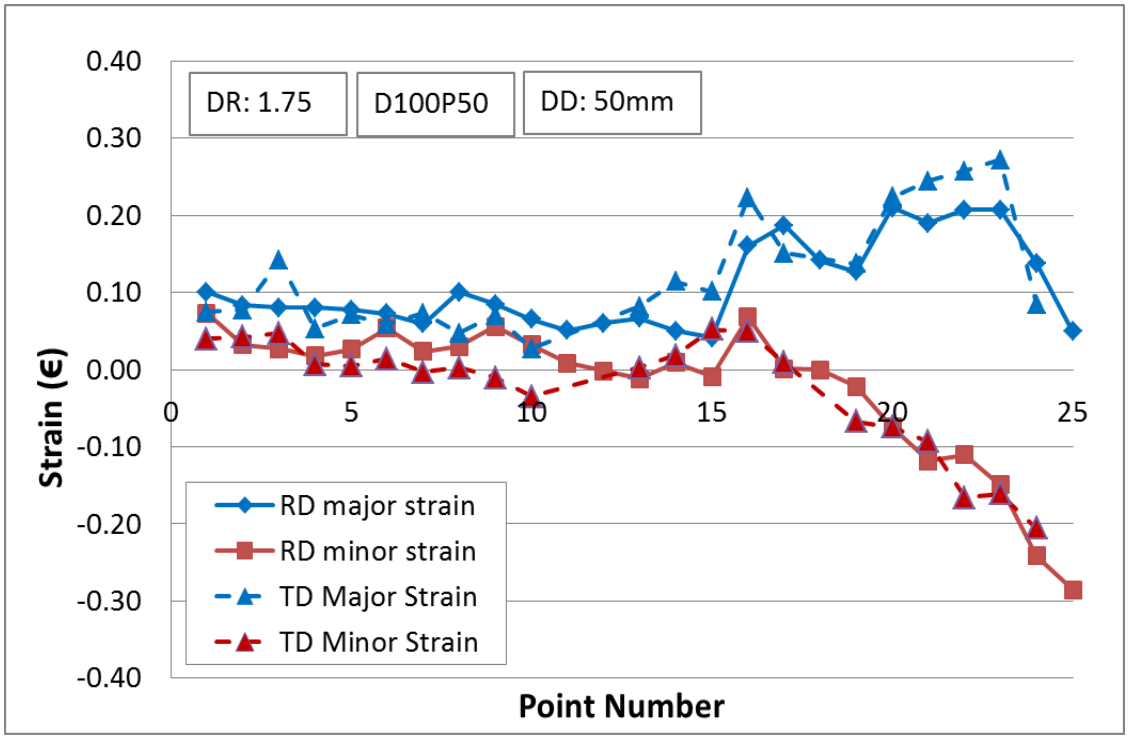

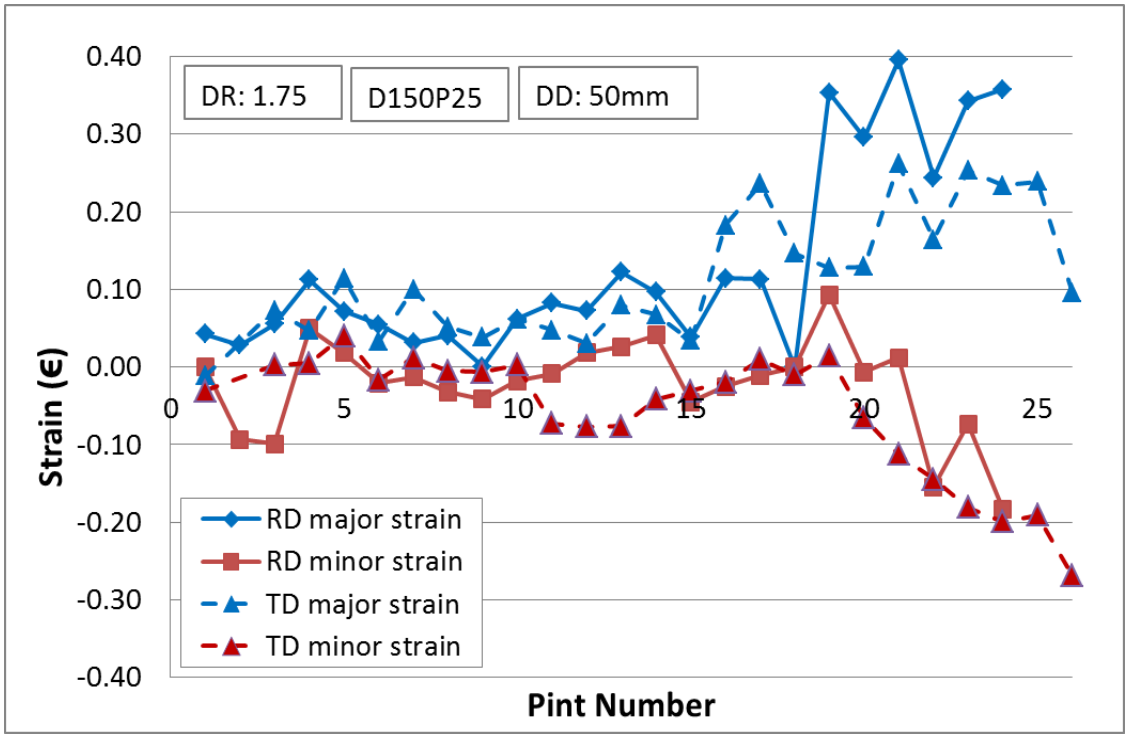
DR: 1.75
D150P25
DD: 50mm
0.40
0.30
0.20
0.10
0.00
-0.10
-0.20
-0.30
-0.40
0
5
10
15
20
25
Strain (€)
RD major strain
RD minor strain
TD major strain
TD minor strain
Pint Number

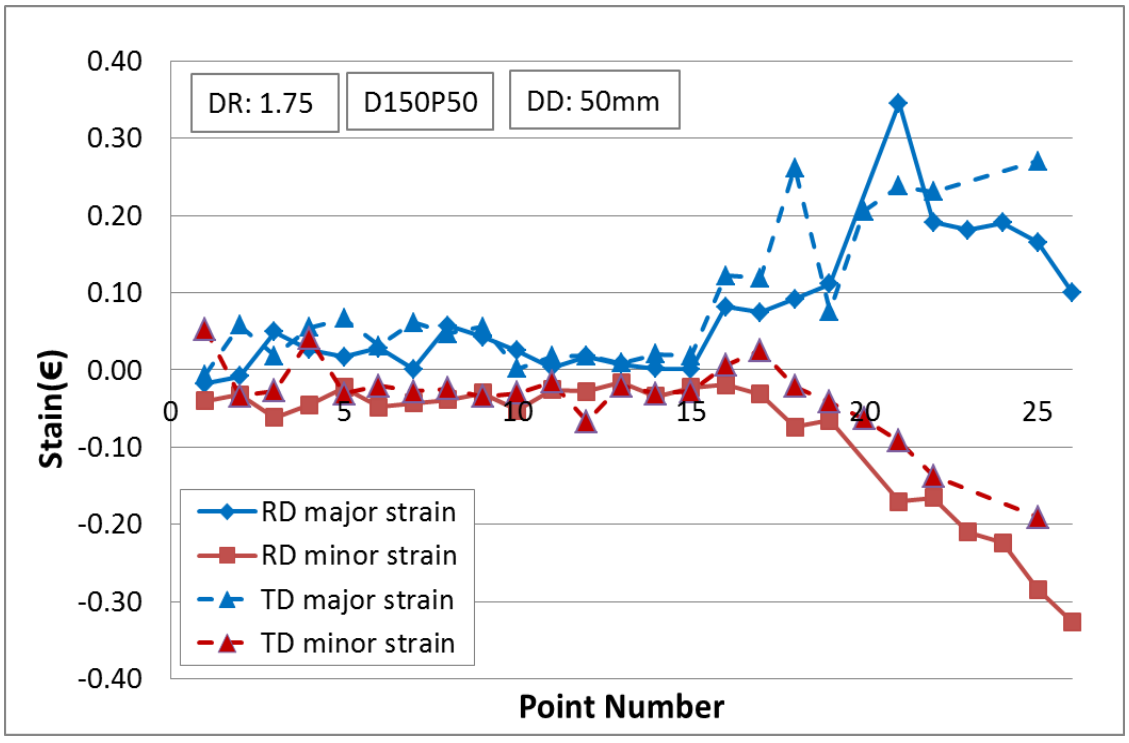
DR: 1.75
D150P50
DD: 50mm
0.40
0.30
0.20
0.10
0.00
-0.10
-0.20
-0.30
-0.40
0
5
10
15
20
25
Stain(€)
RD major strain
RD minor strain
TD major strain
TD minor strain
Point Number

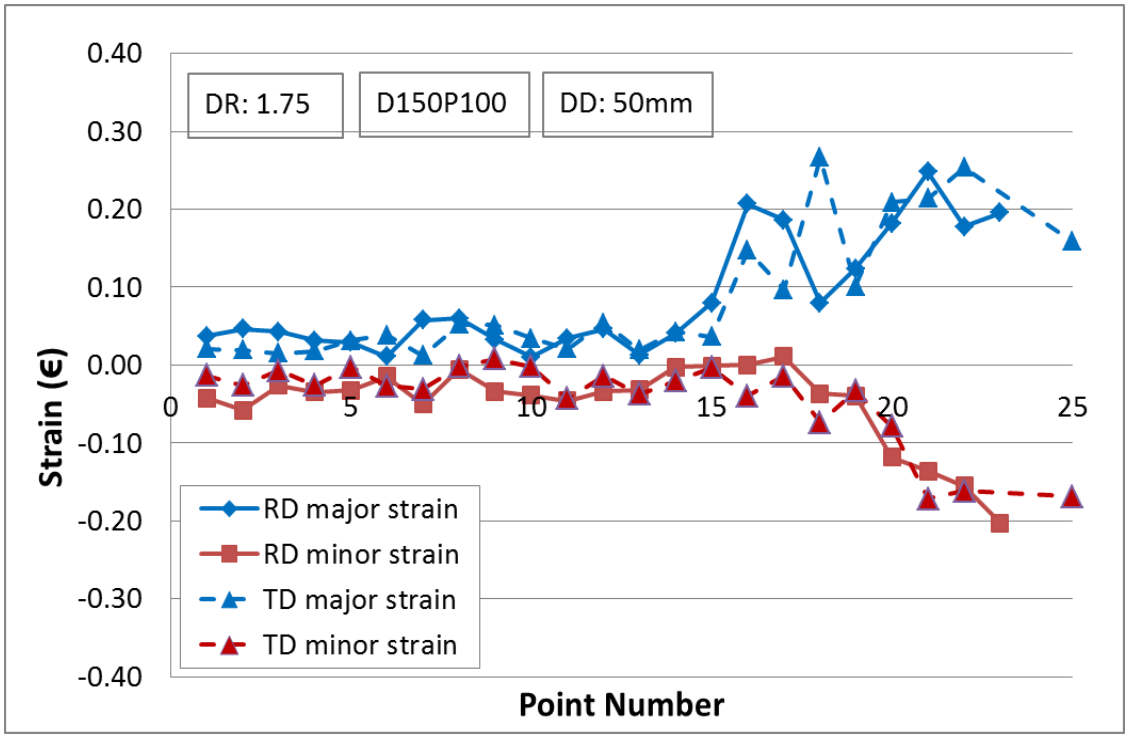
DR: 1.75
D150P100
DD: 50mm
0.40
0.30
0.20
0.10
0.00
-0.10
-0.20
-0.30
-0.40
0
5
10
15
20
25
Strain (€)
RD major strain
RD minor strain
TD major strain
TD minor strain
Point Number

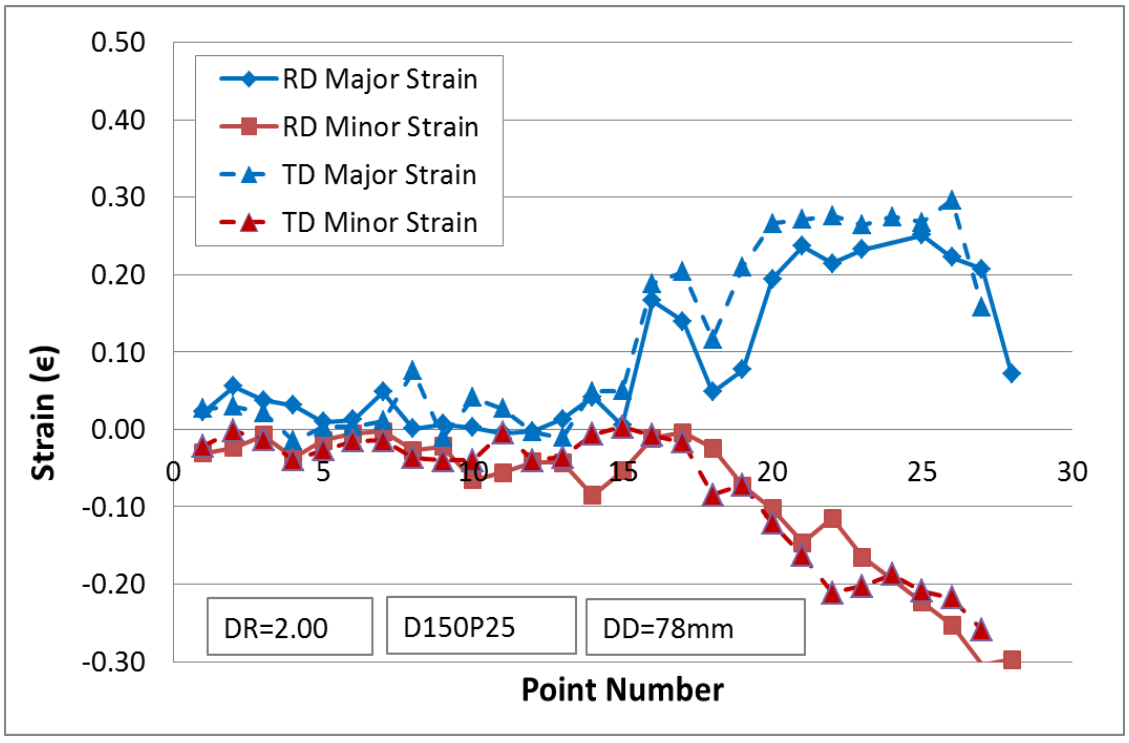
0.50
0.40
0.30
0.20
0.10
0.00
-0.10
-0.20
-0.30
0
5
10
15
20
25
30
Strain (€)
RD Major Strain
RD Minor Strain
TD Major Strain
TD Minor Strain
DR=2.00
D150P25
DD=78mm
Point Number

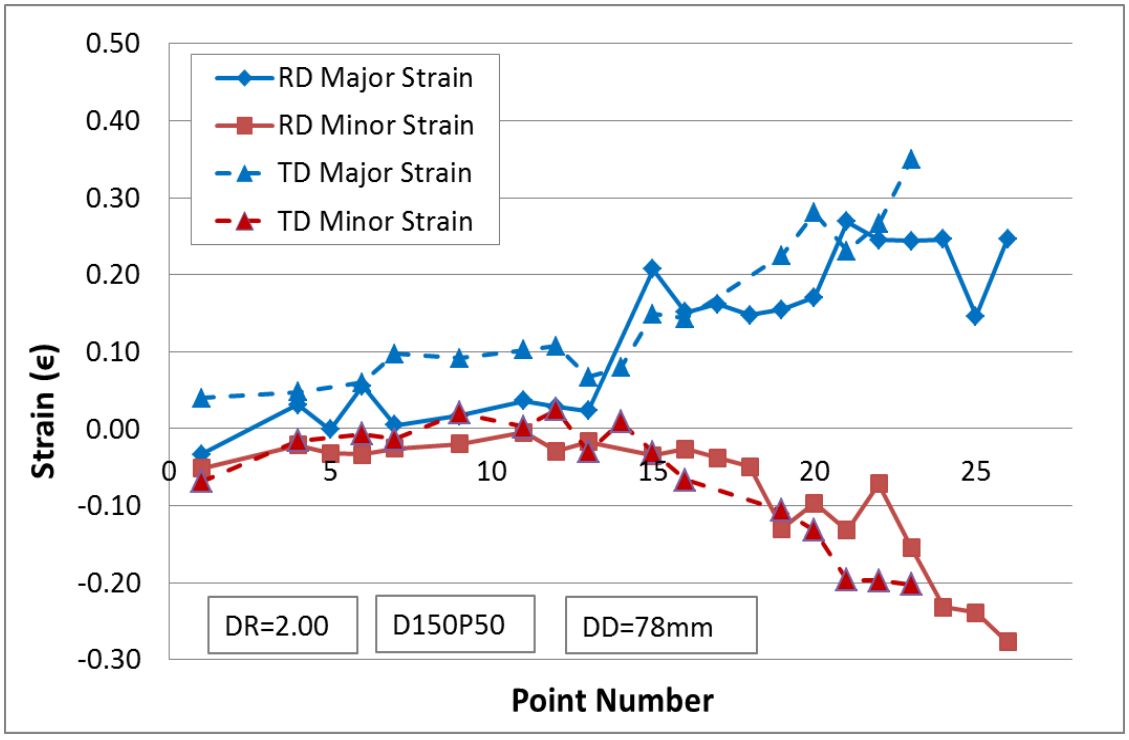
0.50
0.40
0.30
0.20
0.10
0.00
-0.10
-0.20
-0.30
Strain (ϵ)
0
5
10
15
20
25
Point Number
RD Major Strain
RD Minor Strain
TD Major Strain
TD Minor Strain
DR=2.00
D150P50
DD=78mm

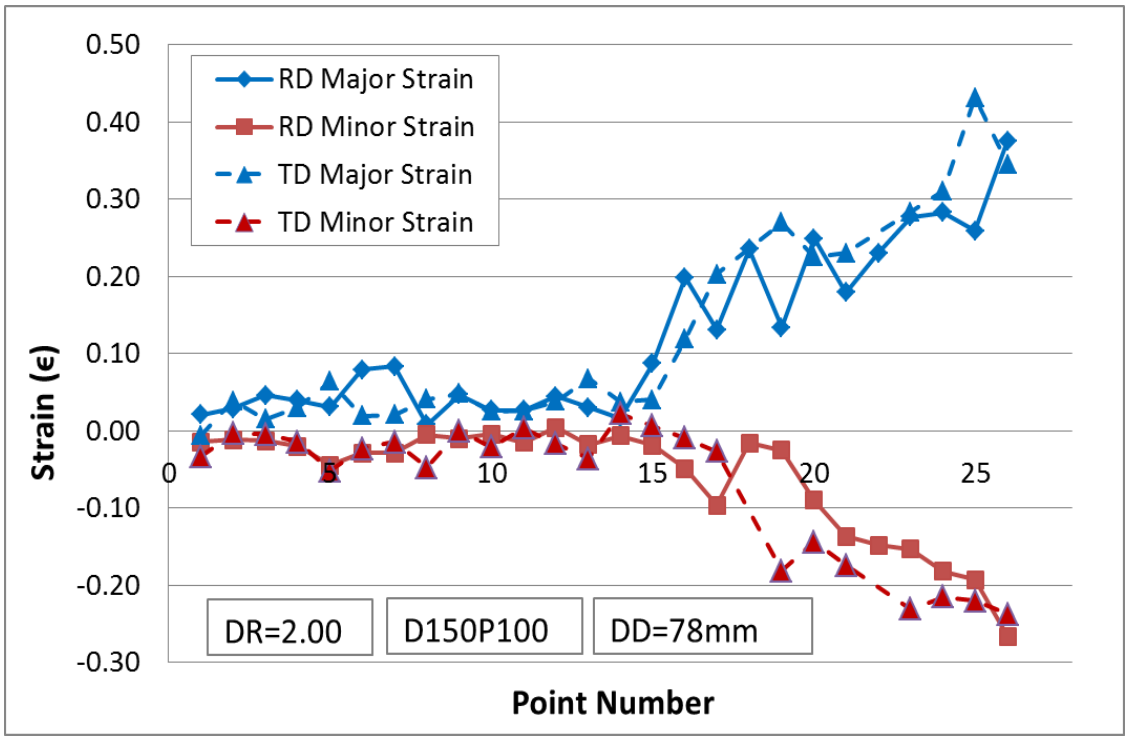
0.50
0.40
0.30
0.20
0.10
0.00
-0.10
-0.20
-0.30
Strain (ϵ)
0
5
10
15
20
25
Point Number
RD Major Strain
RD Minor Strain
TD Major Strain
TD Minor Strain
DR=2.00
D150P100
DD=78mm

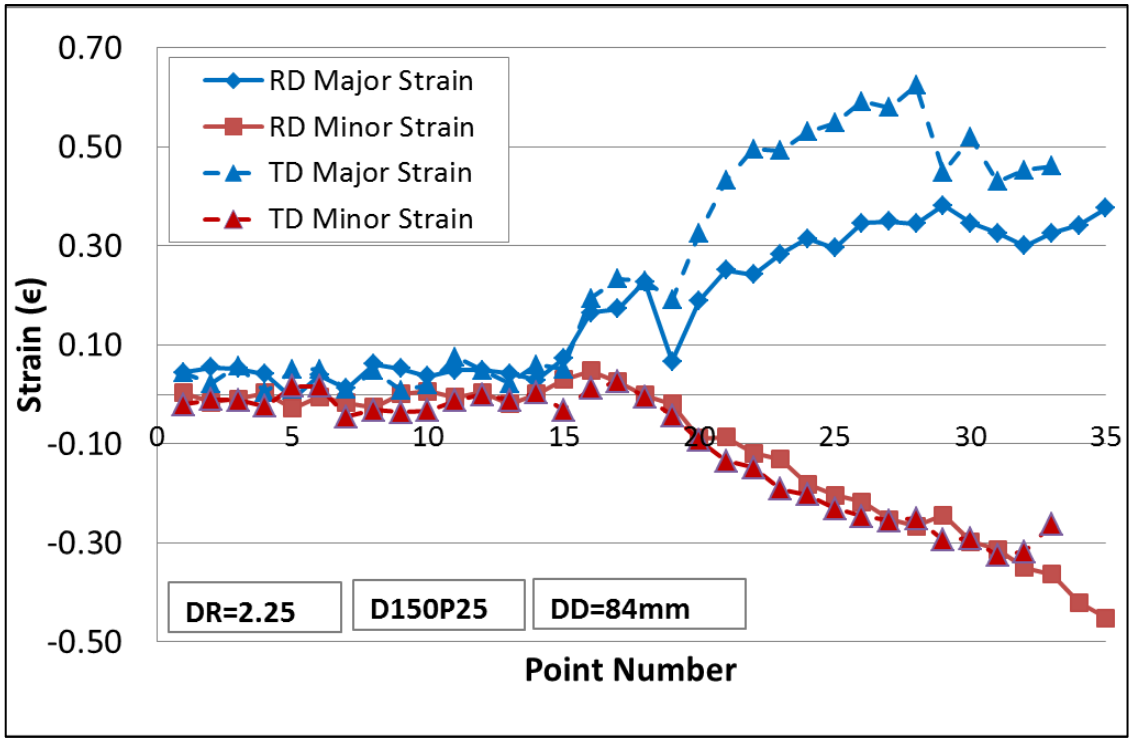
0.70
0.50
0.30
0.10
-0.10
-0.30
-0.50
Strain (€)
RD Major Strain
RD Minor Strain
TD Major Strain
TD Minor Strain
0
5
10
15
20
25
30
35
DR=2.25
D150P25
DD=84mm
Point Number

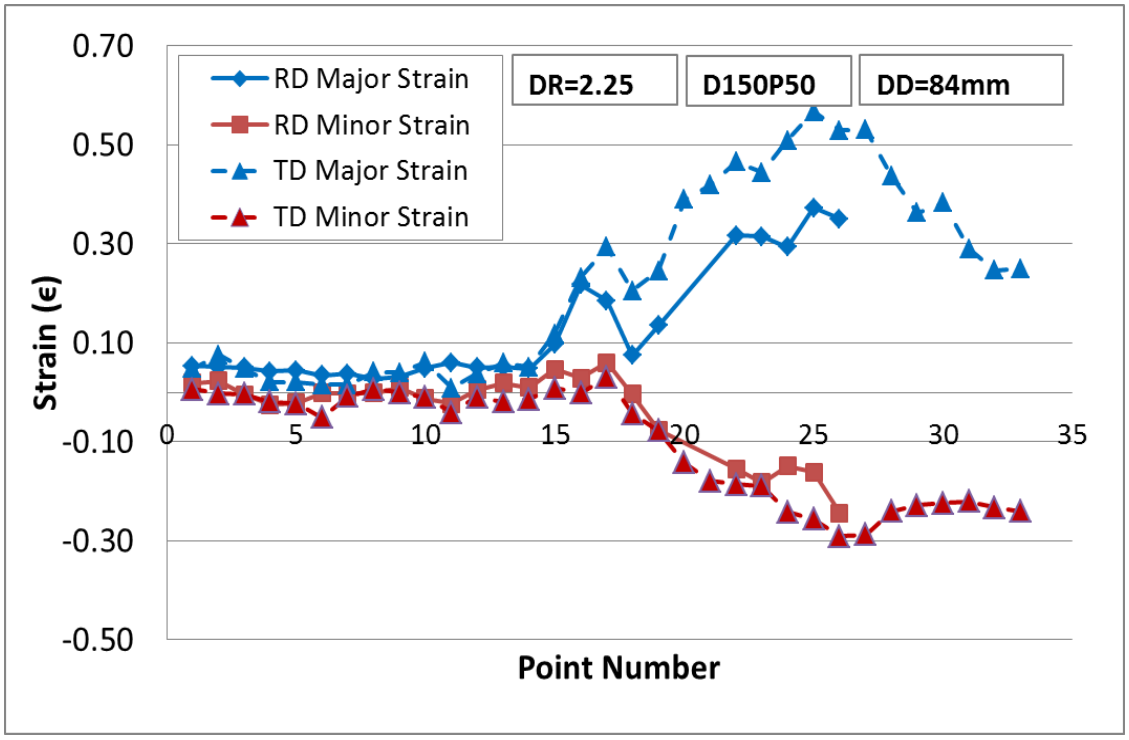
0.70
0.50
0.30
0.10
-0.10
-0.30
-0.50
Strain (€)
RD Major Strain
RD Minor Strain
TD Major Strain
TD Minor Strain
DR=2.25
D150P50
DD=84mm
0
5
10
15
20
25
30
35
Point Number

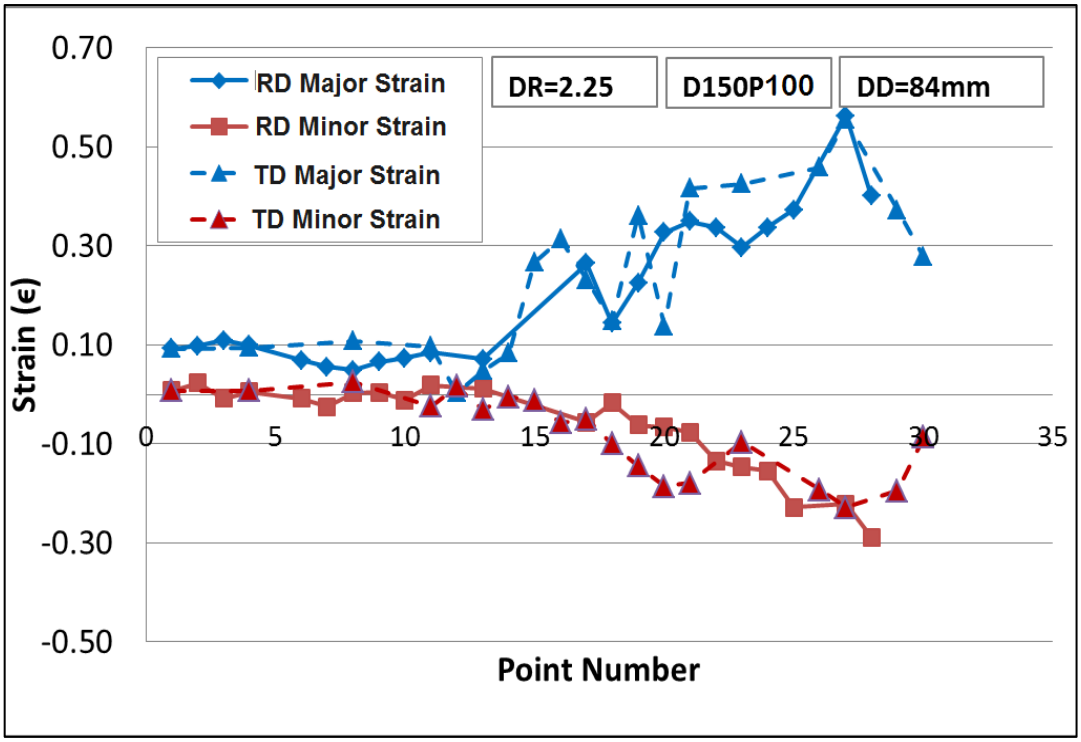
0.70
0.50
0.30
0.10
-0.10
-0.30
-0.50
Strain (ϵ)
0
5
10
15
20
25
30
35
Point Number
RD Major Strain
RD Minor Strain
TD Major Strain
TD Minor Strain
DR=2.25
D150P100
DD=84mm

APPENDIX J: NON-ISOTHERMAL THICKNESS PROFILES FOR ZEK100

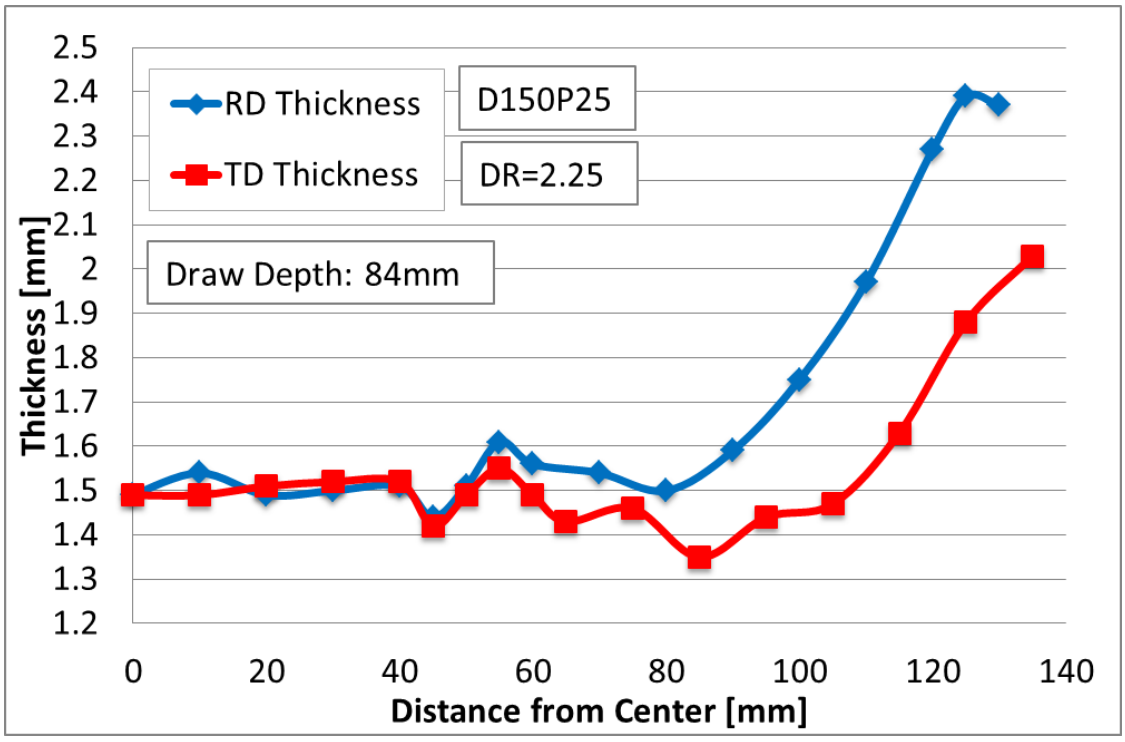

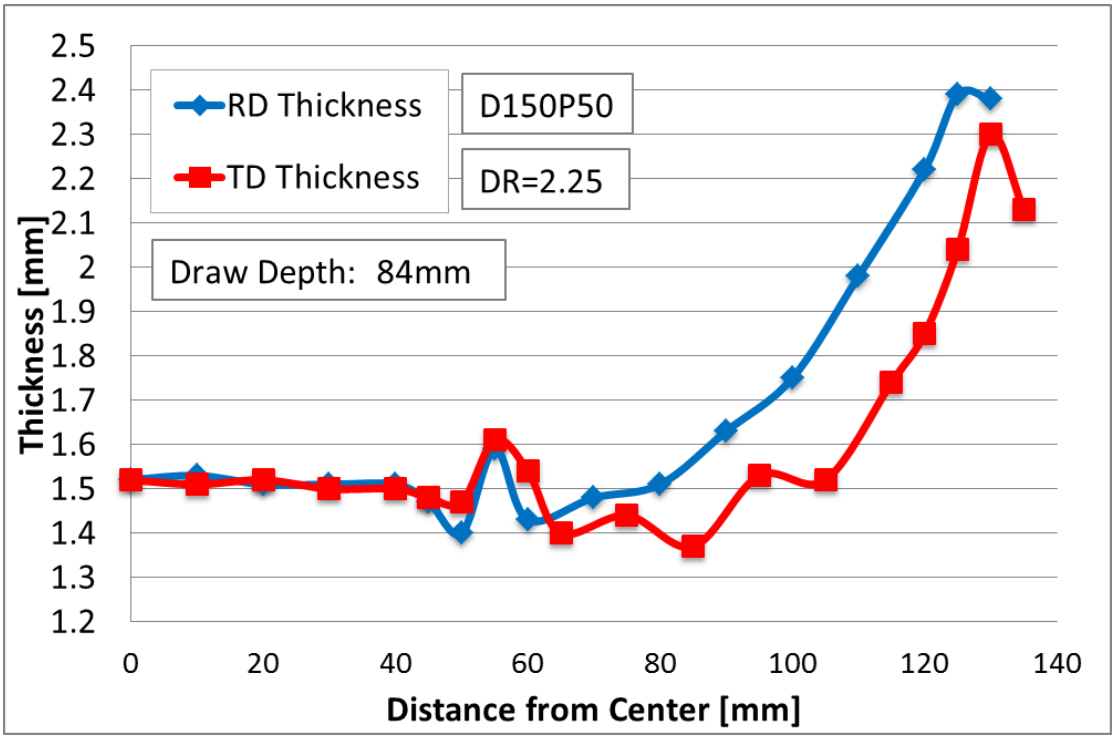

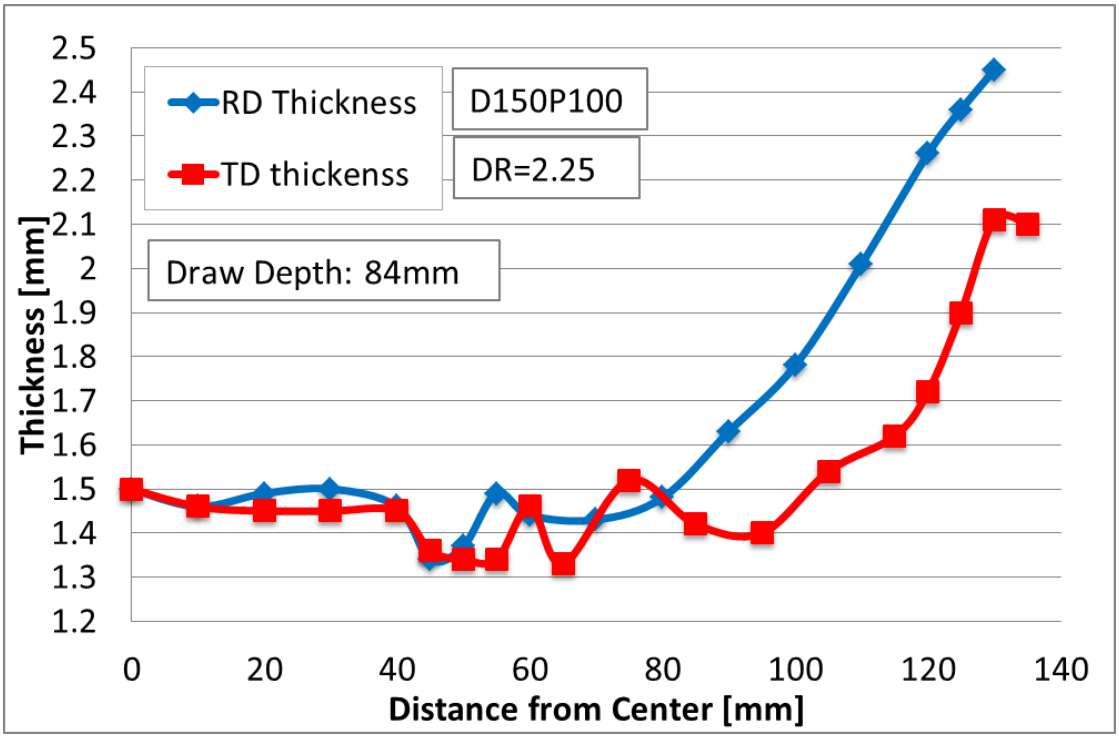
RD Thickness
TD thickenss
D150P100
DR=2.25
Draw Depth: 84mm
Thickness [mm]
Distance from Center [mm]
2.5
2.4
2.3
2.2
2.1
2
1.9
1.8
1.7
1.6
1.5
1.4
1.3
1.2
0
20
40
60
80
100
120
140

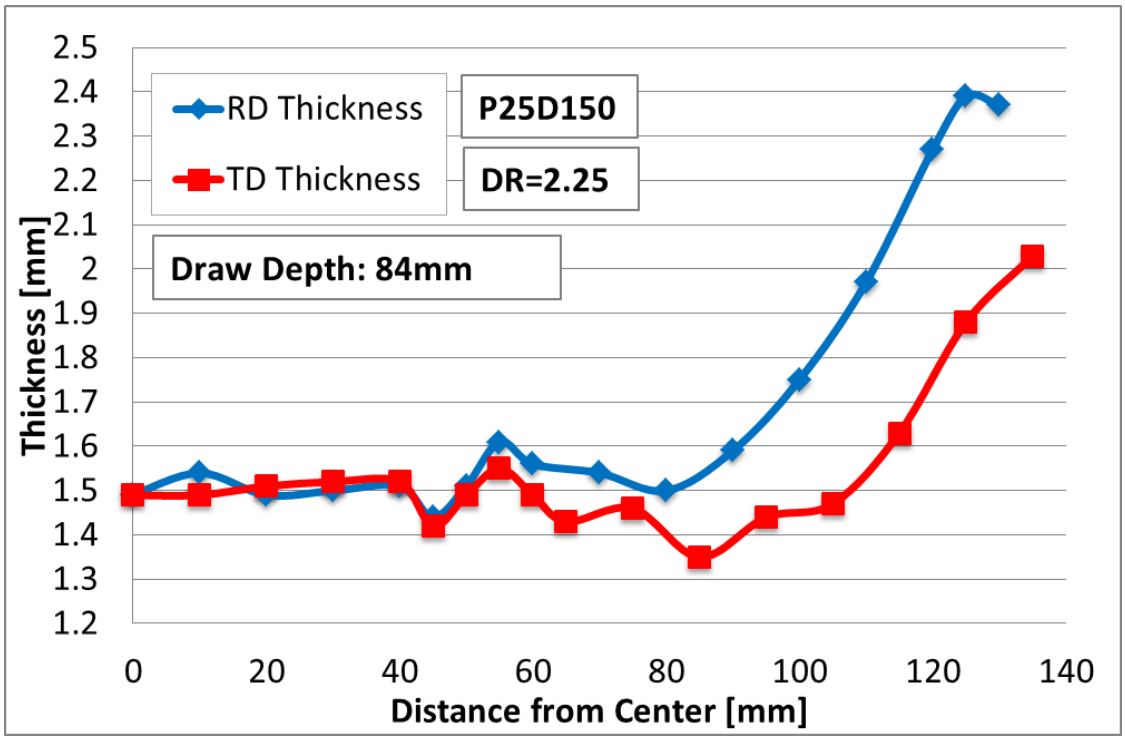
RD Thickness
TD Thickness
P25D150
DR=2.25
Draw Depth: 84mm
Thickness [mm]
Distance from Center [mm]
2.5
2.4
2.3
2.2
2.1
2
1.9
1.8
1.7
1.6
1.5
1.4
1.3
1.2
0
20
40
60
80
100
120
140

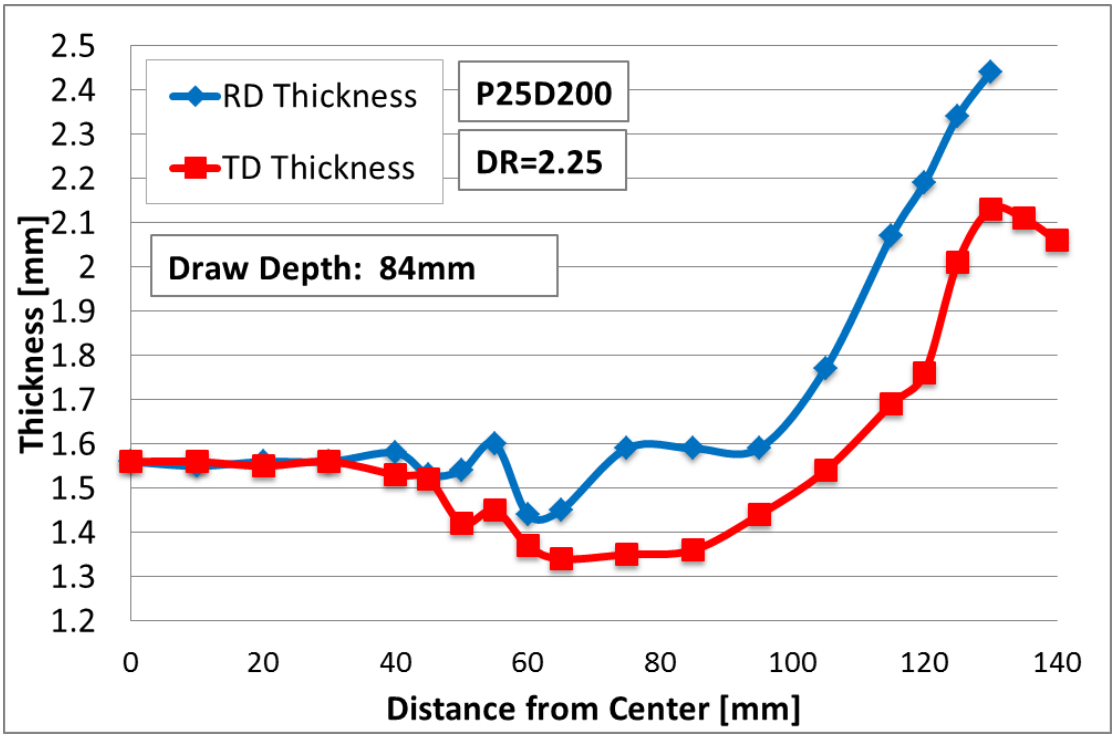
RD Thickness
TD Thickness
P25D200
DR=2.25
Draw Depth: 84mm
Thickness [mm]
Distance from Center [mm]
2.5
2.4
2.3
2.2
2.1
2
1.9
1.8
1.7
1.6
1.5
1.4
1.3
1.2
0
20
40
60
80
100
120
140

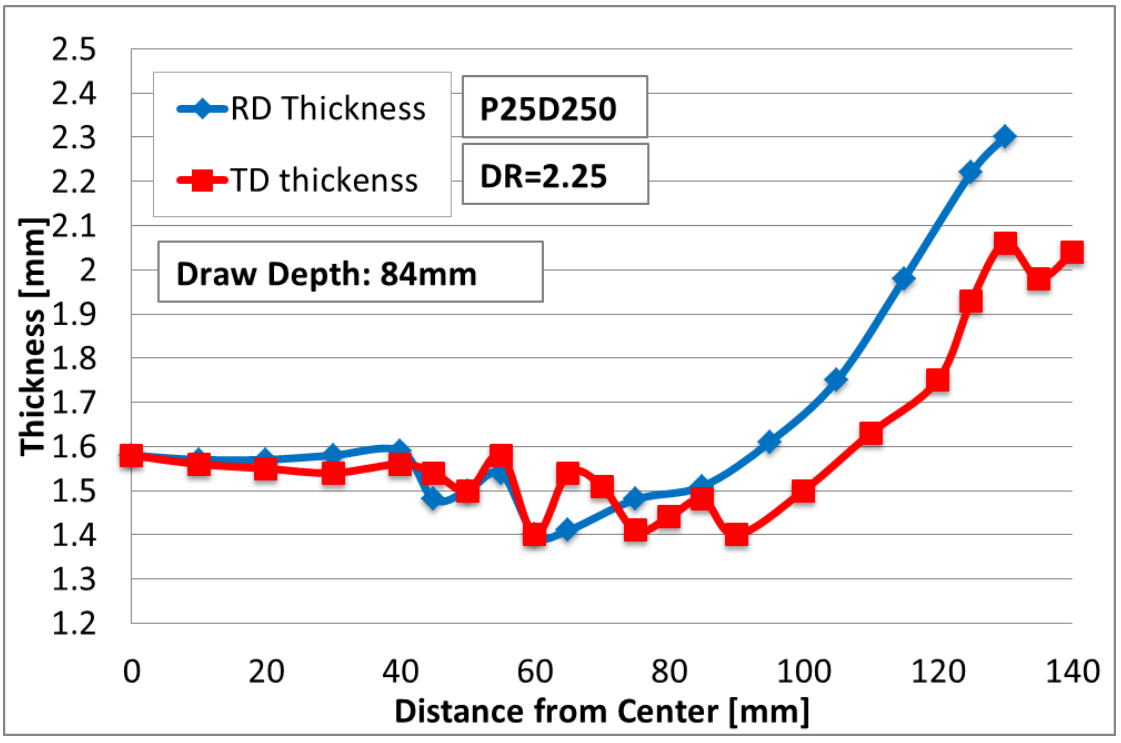
RD Thickness
TD thickenss
P25D250
DR=2.25
Draw Depth: 84mm
Thickness [mm]
Distance from Center [mm]
2.5
2.4
2.3
2.2
2.1
2
1.9
1.8
1.7
1.6
1.5
1.4
1.3
1.2
0
20
40
60
80
100
120
140

APPENDIX K: ZEK100 FORMING LIMIT DIAGRAM ROLLING VS. TRANSVERSE DIRECTION

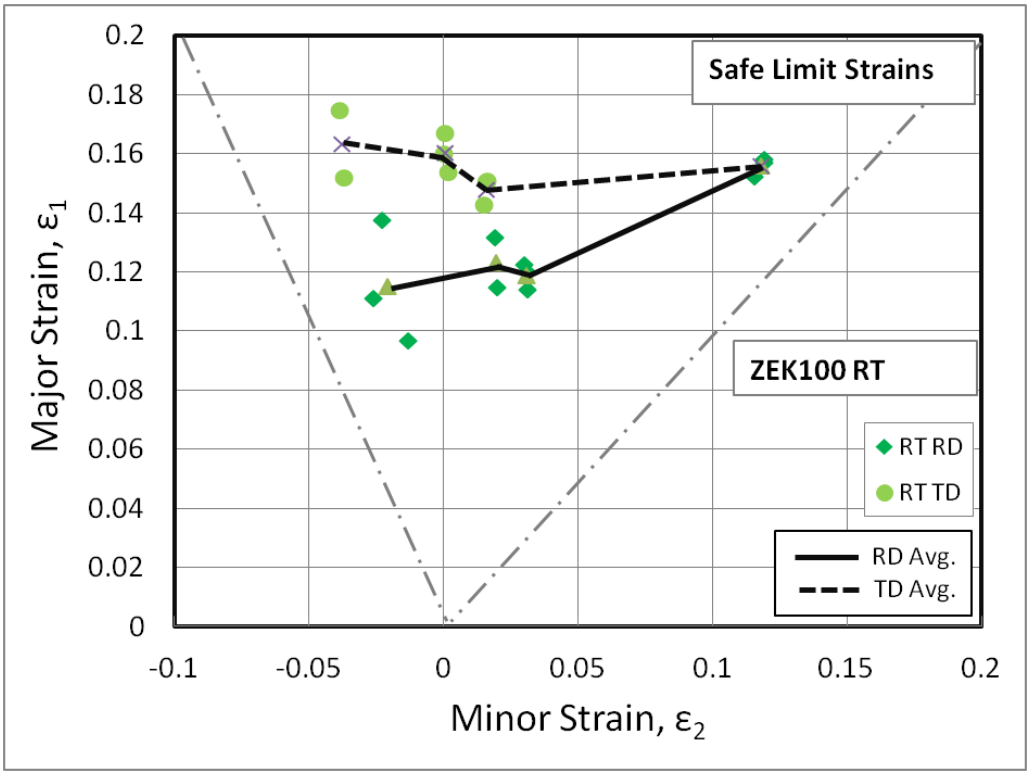

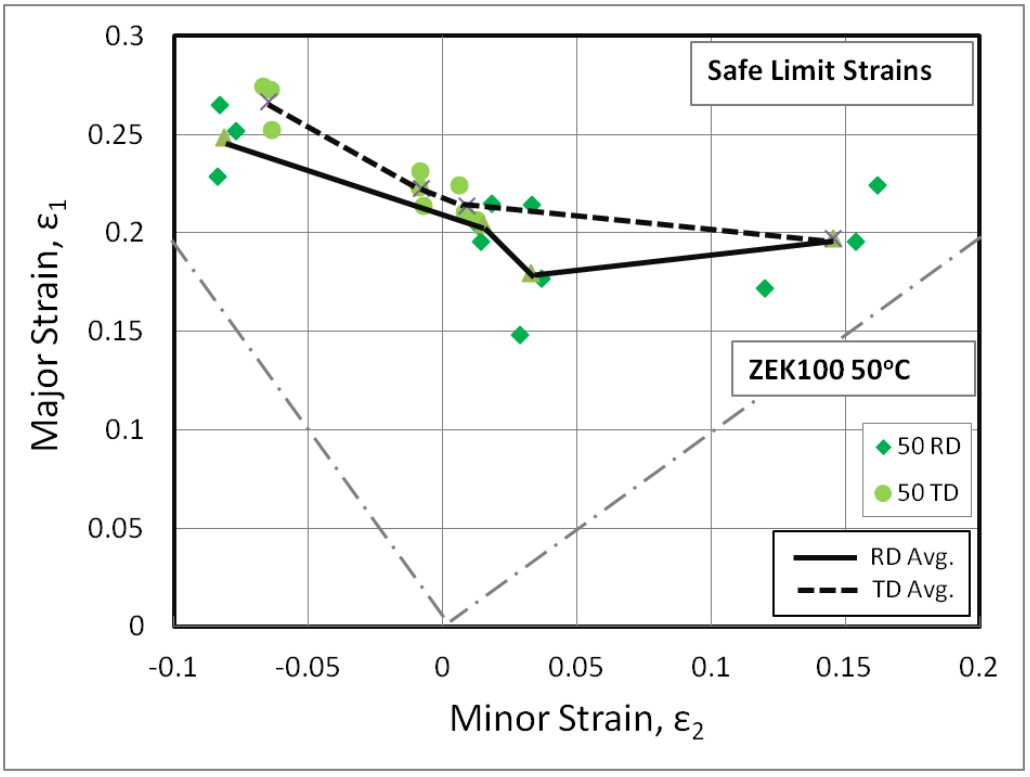

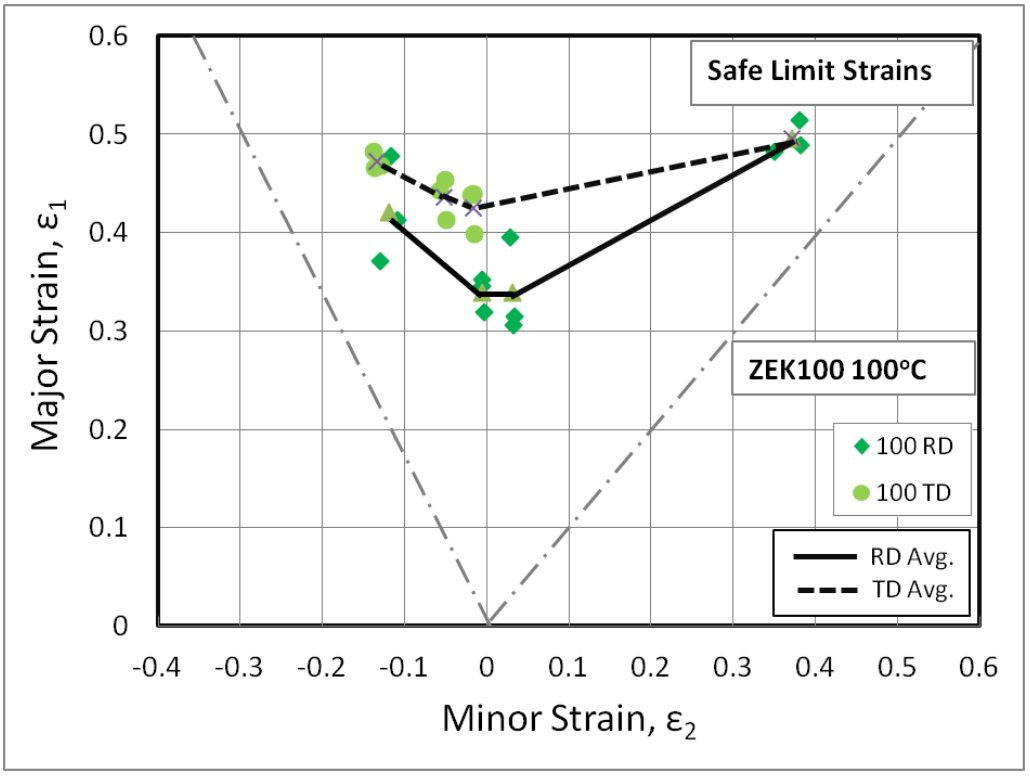
Safe Limit Strains
ZEK100 100°C
100 RD
100 TD
RD Avg.
TD Avg.
Major Strain, ε1
Minor Strain, ε2
0.6
0.5
0.4
0.3
0.2
0.1
0
-0.4
-0.3
-0.2
-0.1
0
0.1
0.2
0.3
0.4
0.5
0.6

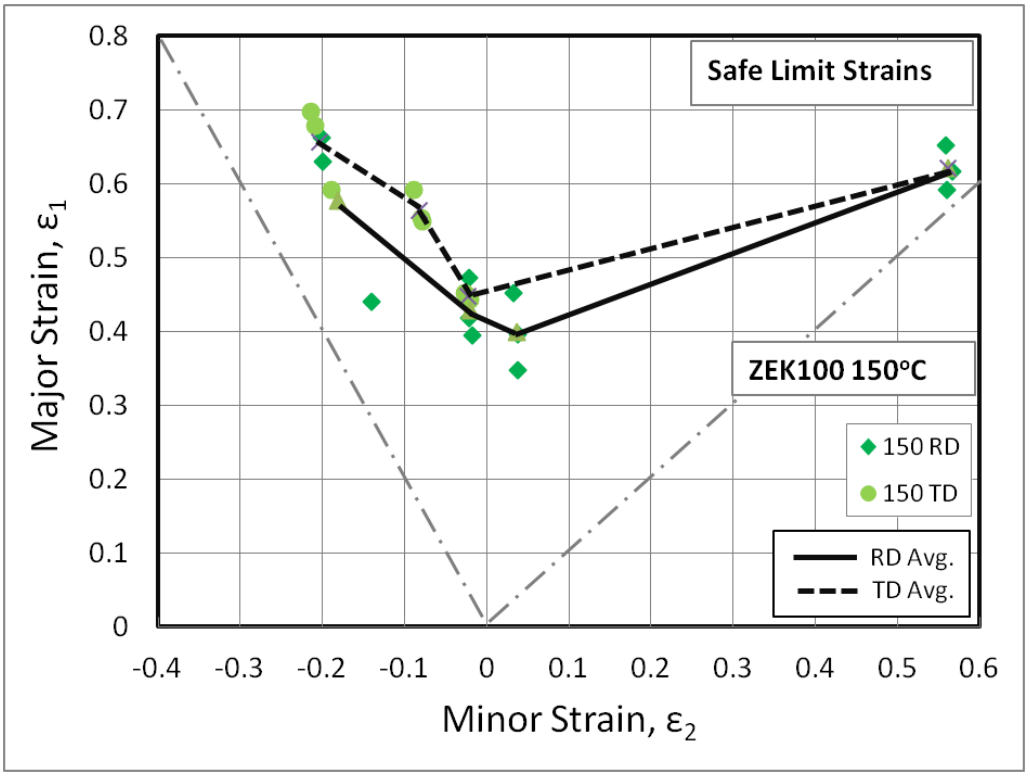
Safe Limit Strains
ZEK100 150°C
150 RD
150 TD
RD Avg.
TD Avg.
Major Strain, ε1
Minor Strain, ε2
0.8
0.7
0.6
0.5
0.4
0.3
0.2
0.1
0
-0.4
-0.3
-0.2
-0.1
0
0.1
0.2
0.3
0.4
0.5
0.6

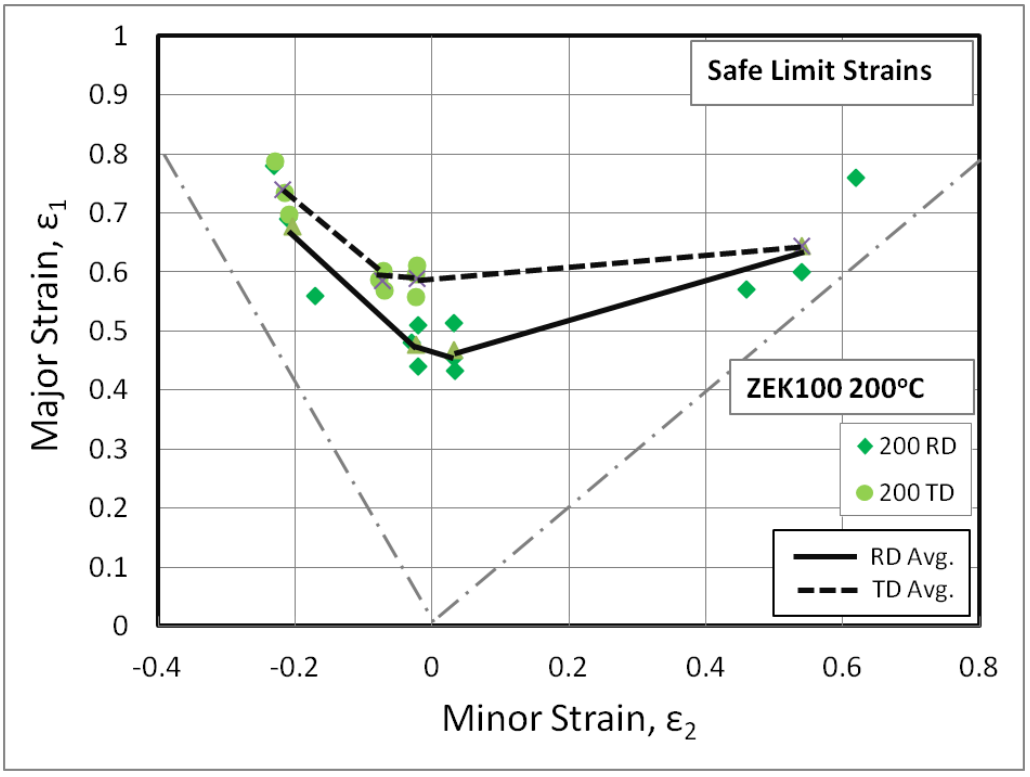
Safe Limit Strains
ZEK100 200°C
200 RD
200 TD
RD Avg.
TD Avg.
Major Strain, ε1
Minor Strain, ε2
1
0.9
0.8
0.7
0.6
0.5
0.4
0.3
0.2
0.1
0
-0.4
-0.2
0
0.2
0.4
0.6
0.8

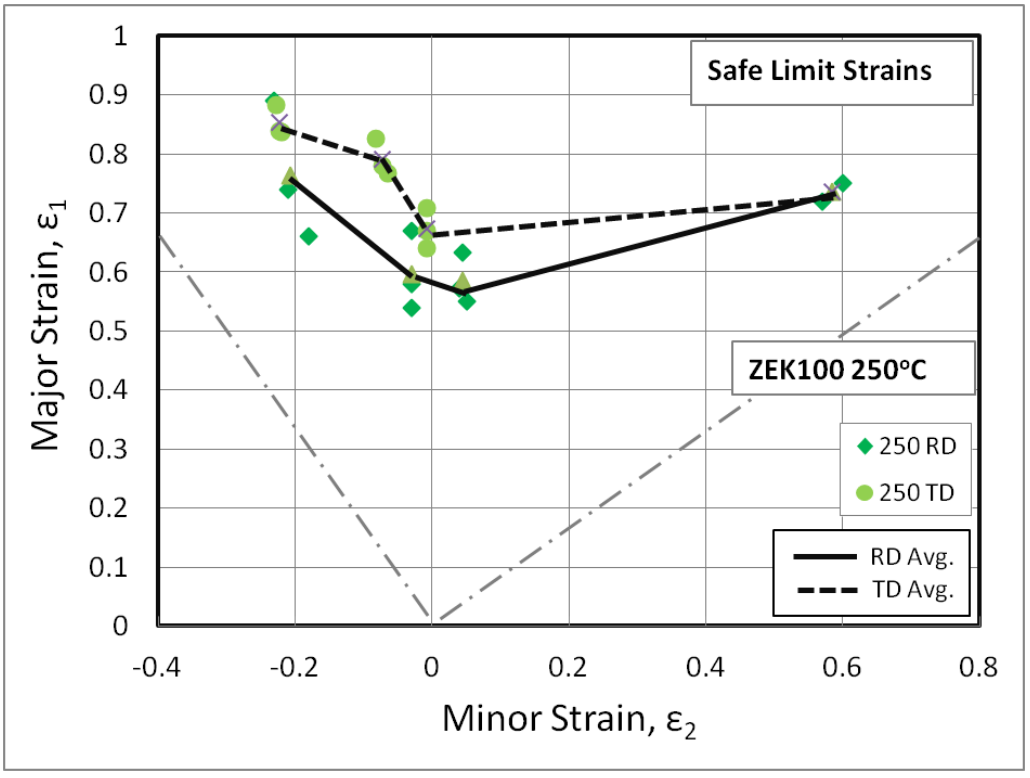
Safe Limit Strains
ZEK100 250°C
250 RD
250 TD
RD Avg.
TD Avg.
Major Strain, ε1
Minor Strain, ε2
1
0.9
0.8
0.7
0.6
0.5
0.4
0.3
0.2
0.1
0
-0.4
-0.2
0
0.2
0.4
0.6
0.8

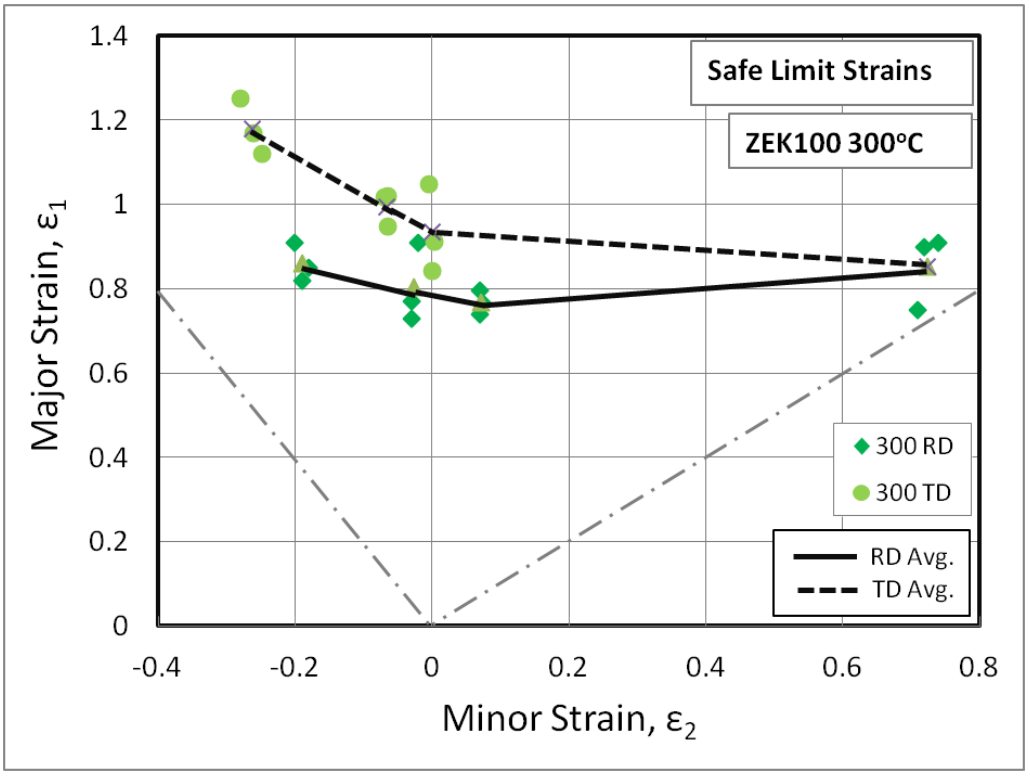
Safe Limit Strains
ZEK100 300°C
300 RD
300 TD
RD Avg.
TD Avg.
Major Strain, ε1
Minor Strain, ε2
1.4
1.2
1
0.8
0.6
0.4
0.2
0
-0.4
-0.2
0
0.2
0.4
0.6
0.8

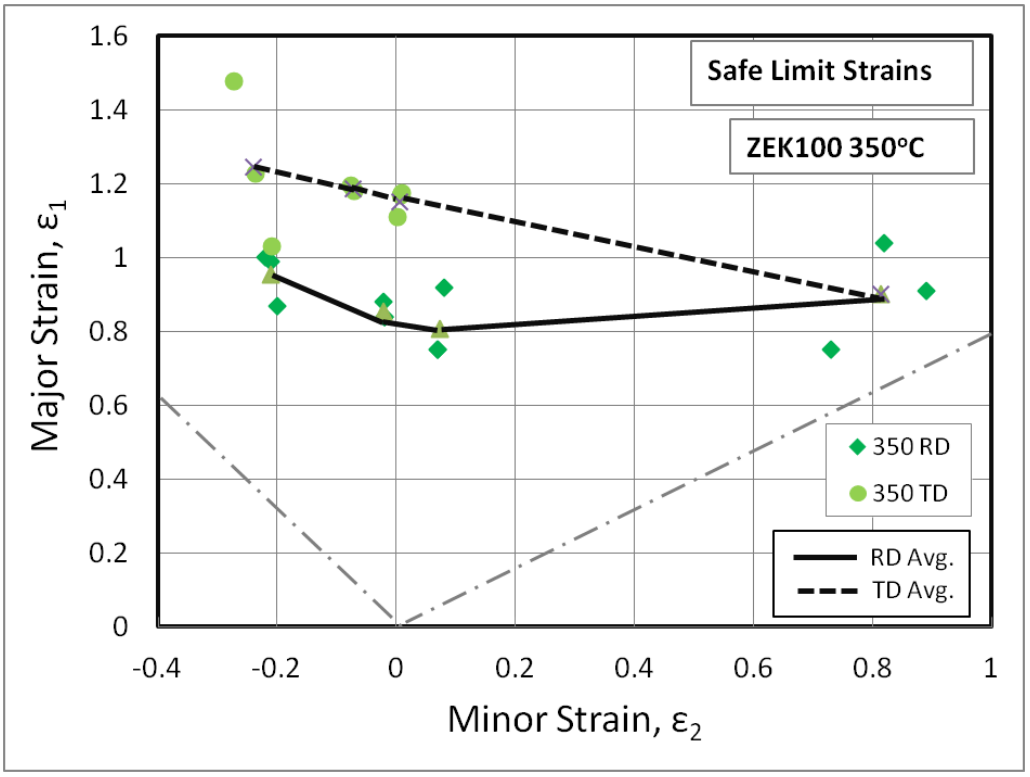
Safe Limit Strains
ZEK100 350°C
350 RD
350 TD
RD Avg.
TD Avg.
Major Strain, ε1
Minor Strain, ε2
1.6
1.4
1.2
1
0.8
0.6
0.4
0.2
0
-0.4
-0.2
0
0.2
0.4
0.6
0.8
1